IBRACON

IBRACON Structures and Materials Journal
Revista IBRACON de Estruturas e Materiais

Editorial

The Brazilian Concrete Institute started its scientific publication in 2005, when two Journals were created: the IBRACON Structural Journal, and the IBRACON Materials Journal. In 2008 these two publications were unified and started the new **IBRACON Structures and Materials Journal.** In that date a new style of cover and diagramming were created, the green-and-yellow pattern. The Journal Volume 1, Number 1, included five articles, published in Portuguese, English and Spanish. In the following years, 2008, 2009 and 2010, four numbers were published in each of these annual volumes, with a total of 20 articles per volume. The 2011-Volume had 5 issue-numbers and 40 articles, the publication of the article in English being mandatory and the publication of a version in Portuguese (or possibly in Spanish) being optional. Since 2012, six issues per volume have been published every two months. Volume 12, from 2019, had 12 articles per issue-number, and consisted of 72 original articles.

This current number (V13, n4) inaugurates a new phase. From now on only articles in English are published and each number may contain 15 articles. Each article is published in continuous flow and is available as soon as approved and diagrammed. The full number is completely closed and made available as soon as all articles are published. Potentially, soon, 90 articles will be published per annual volume.

To celebrate this landmark, a new cover page and diagramming style was created. We must acknowledge Arq. Marcela Noronha P. de O. e Sousa for the courtesy of designing the new cover page. The layout style of the articles now contemplates a pattern with only one column, which facilitates reading on screens, and contains editorial information about the authors and editors. This includes describing each author individual contribution to the scientific article.

The Editorial Board is increasing, moving to have about half of the Associated Editors from outside Brazil, contemplating all continents. We thank our new Associate Editors, all with their extreme scientific excellence and relevance, for the kind acceptance and commitment to serve this Journal:

- Dr. Bruno Briseghella, Fuzhou University, Fujian, China
- Dr. David Oliveira, Jacobs Engineering, Sydney, Australia
- Dr. Leandro F. M. Sanchez, University of Ottawa, Ottawa, Canada
- Dr. Luís Oliveira Santos, Laboratório Nacional de Engenharia Civil, Lisboa, Portugal
- Dr. Marco Di Prisco, Politecnico di Milano, Milan, Italy
- Dr. Mário Jorge de Seixas Pimentel, Universidade do Porto, Porto, Portugal
- Dr. Mark G Alexander, University of Cape Town, Cape Town, South Africa
- Dr. Nigel G. Shrive, University of Calgary, Calgary, Canada
- Dr. Rebecca Gravina, RMIT University, Melbourne, Australia
- Dr. Yury Villagrán Zaccardi, Universidad Tecnológica Nacional Facultad Regional La Plata, Buenos Aires, Argentina

Thank you, and good reading.

The Editors

IBRACON Structures and Materials Journal
Revista IBRACON de Estruturas e Materiais

Contents

Aims and Scope

Aims and Scope

The IBRACON Structures and Materials Journal (in Portuguese: Revista IBRACON de Estruturas e Materiais) is a technical and scientific divulgation vehicle of IBRACON (Brazilian Concrete Institute), published every two months. Each issue has 12 to 15 articles and, possibly, a technical note and/or a technical discussion regarding a previously published paper. All contributions are reviewed and approved by professionals with recognized scientific competence in the area. The IBRACON Structures and Materials Journal is an open access Journal, free of charges for authors and readers.

Objectives

The IBRACON Structures and Materials Journal´s main objectives are:

- Present current developments and advances in concrete structures and materials.
- Make possible the better understanding of structural concrete behavior, supplying subsidies for a continuous interaction among researchers, producers, and users.
- Stimulate the development of scientific and technological research in the areas of concrete structures and materials, through papers peer-reviewed by a qualified Editorial Board.
- Promote the interaction among researchers, constructors and users of concrete structures and materials and the development of Civil Construction.
- Provide a vehicle of communication of high technical level for researchers and designers in the areas of concrete structures and materials.

Submission Procedure

The procedure to submit and revise the contributions, as well as the formats, are detailed in the Journal Website (ismj.org).

The papers and the technical notes are revised by at least two reviewers indicated by the editors. Discussions and replies are accepted for publication after a review by the editors and at least one member of the Editorial Board. In case of disagreement between the reviewer and the authors, the contribution will be sent to a specialist in the area, not necessarily linked to the Editorial Board. Conflict of interests is carefully handled by the Editors.

Contribution Types

The Journal will publish original papers, short technical notes, and paper discussions. Original papers will be accepted if they are in accordance with the objectives of the Journal and present quality of information and presentation. A technical note is a brief manuscript. It may present a new feature of research, development, or technological application in the areas of Concrete Structures and Materials, and Civil Construction. This is an opportunity to be used by industries, companies, universities, institutions of research, researchers, and professionals willing to promote their works and products under development.

A discussion is received no later than 3 months after the publication of the paper or technical note. The discussion must be limited to the topic addressed in the published paper and must not be offensive. The right of reply is granted to the Authors. The discussions and the replies are published in the subsequent issues of the Journal.

The submission file should be in accordance with the paper template available at the Journal Website. It is recommended that the length of the papers does not exceed 25 pages. Where available, URLs for the references should be provided.

The IBRACON Structures and Materials Journal will conduct the review process for manuscripts submitted in English. Titles, abstracts, and keywords are presented in English, and in Portuguese or Spanish. Articles and technical notes are peer-reviewed and only published after approval of the reviewers and the Editorial Board.

Once accepted, an article is typeset according to the journal layout. The author will be required to review and approve the galleys before publishing. At this stage only typesetting errors will be considered.

Internet Access

The IBRACON Structures and Materials Journal Webpage is available at http://ismj.org.

Sponsors

The funds for the maintenance of the Journal are currently obtained from the IBRACON. The Journal is not supposed to be maintained with funds from private sponsorship, which could diminish the credit of the publications.

Photocopying

Copyright

IBRACON

Disclaimer

Papers and other contributions and the statements made or opinions expressed therein are published on the understanding that the authors of the contribution are the only responsible for the opinions expressed in them and that their publication does not necessarily reflect the views of IBRACON or of the Journal Editorial Board.

Editorial Board

IBRACON Structures and Materials Journal
Revista IBRACON de Estruturas e Materiais

ORIGINAL ARTICLE

Hardness correlation length in a self-compacting concrete

Comprimento de correlação da dureza em um concreto autoadensável

Bruna Maria Becker Junges[a] iD
Nadine Machado Ficher[b] iD
Luis Eduardo Kosteski[b] iD
Ederli Marangon[b] iD

[a]Universidade Federal do Pampa – UNIPAMPA, Alegrete, RS, Brasil
[b]Universidade Federal do Pampa – UNIPAMPA, Programa de Pós-graduação em Engenharia, Grupo MAEC, Alegrete, RS, Brasil

Abstract: This paper presents an experimental study of spatial variation of hardness or indentation strength of a self-compacting concrete. With the pourpose of validation, the comparison between the used methodologies with the values obtained by numerical simulation is presented. The correlation length (Lcor) obtained on the semivariogram using a Gaussian model is similar to the numerically simulated value, especially when the distance between the measurements is less than the sought Lcor. Using sclerometry, it was possible to infer that to find the value of concrete correlation length it is necessary to measure nearby points, at ca. 2cm apart. With this scheme, the value of Lcor found is close to the obtained using macro-indentation, a more complex and time-consuming procedure. Finally, for the studied self-compacting concrete, the correlation length is equivalent to a value between 5 to 6 times the maximum aggregate size.

Keywords: spatial distribution, self-compacting concrete, hardness, indentation.

Resumo: Neste trabalho apresenta-se um estudo experimental da variação espacial da dureza ou resistência à indentação de um concreto autoadensável. Inicialmente é apresentada a comparação da metodologia utilizada com os valores obtidos por simulação numérica com o intuito de validação da mesma. O comprimento de correlação (Lcor) obtido do semivariograma utilizando o modelo Gaussiano é próximo ao valor simulado numericamente, especialmente quando a distância entre os pontos medidos é menor que o Lcor procurado. Utilizando esclerometria foi possível concluir que para encontrar o valor do comprimento de correlação do concreto é necessário realizar medições em pontos próximos, na ordem de 2cm. Com esta metodologia, o valor de Lcor encontrado é próximo ao obtido utilizando macro-indentação, procedimento esse mais complexo e demorado. Assim, para o concreto autoadensável em estudo, encontrou-se o comprimento de correlação equivalente a um valor entre 5 a 6 vezes o tamanho máximo do agregado graúdo.

Palavras-chave: distribuição espacial, concreto autoadensável, dureza, indentação.

1 INTRODUCTION

Material behavior is a problem that is under continuous study and, even today, it is a subject that is not yet completely exhausted. Multiscale materials can be considered homogeneous or heterogeneous depending on the level of observation. According to Silva et al. [1], cementitious composites are considered as typical representatives of multiscale materials since they can be treated as homogeneous at the macroscopic level (length scale cm ~ m) and as heterogeneous materials at a more precise level of observation (scale in length nm ~ cm).

This multiscale heterogeneity determines the mechanical performance (stiffness, strength) and degradation (damage, fracture, failure) of cementitious materials [2]. Due to the heterogeneity of the material properties, safety

factors are considered to achieve macroscopic properties with certain safety in engineering design. Current trends in concrete science and engineering seek a better representation of this heterogeneity at various length scales [3].

Classical methods of statistical data analysis generally assume that the realizations of random variables are independent of each other, considering that neighboring observations do not influence each other. Spatial data analysis presents itself as an alternative and/or as a complement to classical data analysis, as this type of analysis considers the correlations between observations [4].

Spatial analysis of data, using geostatistics, has gained momentum since the 1980s in areas other than mining and geology, with great applicability in soil science. This became possible due to the computational ease that made feasible some calculations relatively laborious in this methodology [5]. The applicability and use of geostatistics as a methodology for analyzing data in space or time has been disseminated in various branches of science, involving the areas of social, biological and exact sciences [4].

Local or specific mechanical properties influence the behavior of concrete in its global form, such as its compressive stress, elasticity, creep, and durability, among other factors. The study of the spatial distribution of these properties allows to understand the material behavior at different points on the surface. Following the idea proposed by Constantinides et al. [2], [4], this study can be carried out using a grid of points, in which each point presents the mechanical properties obtained through experimental tests.

Thus, the general objective of this work is to study the spatial distribution of the hardness of a self-compacting concrete and to define a distribution model of the material properties on the analyzed surface, in order to obtain the macroscopic behavior of the material. Geostatistics was used for the spatial analysis of the data, with emphasis on the analysis of the semivariogram for the determination of the spatial dependence of the data. An initial validation through numerical simulation is also presented.

2 MATERIALS AND EXPERIMENTAL PROGRAM

In this section, first the phisics properties of the materials used for the production of self-compacting concrete is shown. The characterization of the materials used for the concrete production and composition were performed by Padoin [6]. Afterwards, the sclerometry and macro-indentation tests of self-compacting concrete are described. Finally, the methodology for the spatial analysis of the data is presented.

2.1 Materials

For this work, a self-compacting concrete developed by Padoin [6] was used to obtain a characteristic compressive strength (fck) of 25 MPa. The water/cement ratio of the concrete was 0.5. Table 1 shows the concrete proportion mixture.

Table 1. Mixture of Self Compacting Concrete.

Materials	kg/m³
Portland Cement	400
Water	200
Superplasticizer additive	2,40
Fine aggregate	731
Coarse aggregate	904

Medium river sand and origin basaltic coarse aggregate was used. These materials were obtained in the city of Alegrete – RS, Brazil.

The granulometric composition of the aggregates was performed according to the procedures established by NBR NM 248 [7], with the maximum diameter of the coarse aggregate being 9.5 mm and the fine aggregate being 2.36 mm.

The determination of the specific mass of the fine aggregate was performed according to procedures described in NBR 9776 [8], obtaining the value of 2.75 g/cm³. For the coarse aggregate, NBR NM 53 [9] was used to determine the specific mass, resulting in a value of 3.19 g/cm³. The Brazilian Portland cement used for the mixture was the CP IV-32, manufactured by the company Votoran. Also, the Sika's ViscoCrete® 5700 superplasticizer additive was added.

The concrete, in its fresh state, had an average spreading diameter of 665 mm and the mixture did not present any segregation, ensuring homogeneity, as shown in Figure 1a. The passing ability was measured using the J Ring, U Box

and V Funnel equipments (according to standard NBR 15823 [10]). The passing ability results were 20 mm for J Ring and 1.5 mm for U box, while the flow time, measured through the V funnel, was found to be 11 seconds.
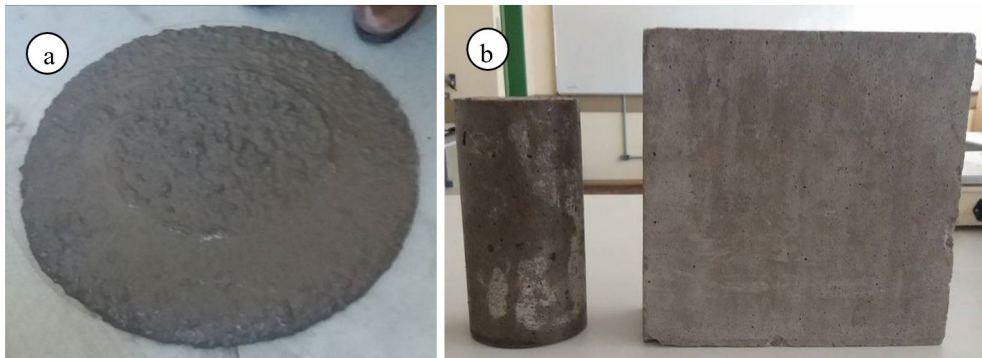
Figure 1. a) Spreading of the concrete in a fresh state and **b)** types of specimens produced.

Cylindrical specimens of dimensions (100x200) mm, prismatic specimens of (250x250x100) mm and (200x200x100) mm were produced to perform the tests. The specimens were molded and cured as described in NBR 5738 [11]. Figure 1b shows the types of specimens produced.

The self-compacting concrete showed, on average (means of 5 specimens), compressive strength at 28 days of 27.67 MPa, with a coefficient of variation (CV) of 3.47%. The tests were performed on an Instron universal machine, with a maximum capacity of 1500 kN, following the procedures described in the NBR 5739 standard [12].

2.2 Sclerometry test

The Schimidt reflection sclerometer was used, with an impact energy of 0.225 mkg and a tip diameter of 15 mm. The reflection sclerometer was calibrated on the standard anvil, as prescribed by NBR 7584 [13]. Particular care during the measurements was considered to ensure that the surface of the tested concrete was dry, clean and regular.

The test was carried out in two ways: first, by following the recommendation of standard NBR 7584 [13]. The self-compacting concrete slab used in the test was (250x250x100) mm. The points were initially defined randomically in the specimen, considering the minimum distances between them and the specimen edges, as shown in Figure 2a. Second, by building a regular mesh of lines every 10 mm on the surface of a (200x200x100) mm plate. However, as the tip of the sclerometer is 15 mm, the impact points were distributed every 20 mm, to not create overlap measurements. The scheme of the mesh in this case can be identified in Figure 2b.
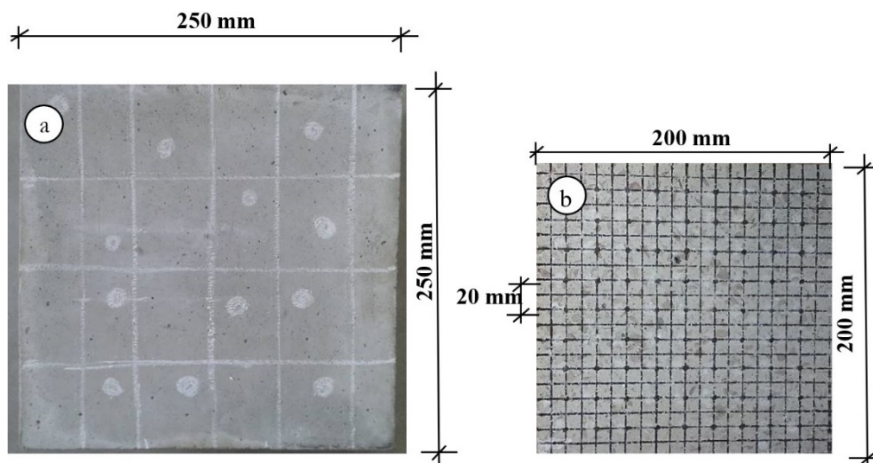
Figure 2. Self-compacting concrete plates used in sclerometry, **a)** for the analysis based on the NBR 7584 standard [13] and **b)** for the analysis of indentation with sclerometer on a regular mesh.

2.3 Macro-indentation tests

For the macro-indentation tests, plates with dimensions of (200x200x100) mm were used, in which 10 mm distant lines were drawn, forming a regular grid with 361 points, as represented in Figure 3a. The concrete plate with the drawn mesh was placed on the plate of the universal testing machine Shimadzu AGS – X, with maximum capacity of 5 kN. The displacement that the material undergoes at each point of the mesh is measured when a compression load of 2000 N is applied. The contact between the machine and the specimen was made through a steel crew with a semi-spherical head, coupled to the machine load cell. The configuration test is shown in Figure 3b.
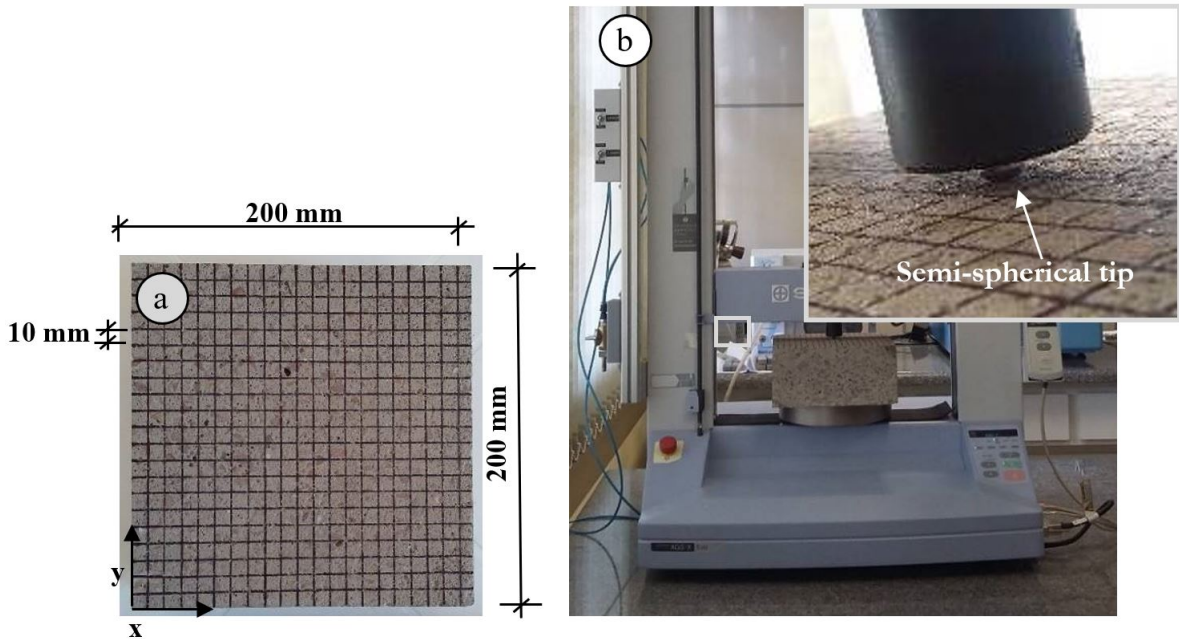
Figure 3. a) Self-compacting concrete plate used in macro-indentation, **b)** configuration of the test and detail of the indenter.

2.4 Spatial an alysis of data

In order to obtain smoother curves in the representation of the spatial distribution of the data, an interpolation by cubic splines was used, both in the Matlab software and in the ArcGis software. In addition, geostatistical data analysis was carried out using semivariograms in the ArcGis software. The semivariograms were modeled using the extension Geostatistical Analyst, with the standard configuration of the ArcGis software. The software generates the semivariograms by means of Kriging interpolation, and supplies the range parameter. Finally, the Gaussian model was used.

3 RESULTS AND DISCUSSIONS

First, the validation of the methodology used by numerical simulation is presented and discussed. In addition, experimental data and spatial analysis of data related to the sclerometry and macro-indentation tests, performed on self-compacting concrete, are presented.

3.1 Validation of the methodology used by numerical simulation

In order to validate the methodology used, the values of correlation length (Lcor) numerically simulated were also measured and analized with the semivariogram.

This verification was based on the proposal of Shinozuka and Deodatis [14], which aims to make the numerical discretization of the correlation length size of a simulated random field independent. This idea is used to introduce variability in the material, for the lattice discrete elements method (LDEM), as explained in [15]–[18]. In this methodology, the domain (3D) is divided into prismatic regions that have correlation lengths as sides, which may be

different in the three Cartesian directions (Lcorx, Lcory, Lcorz). At the vertices of these prisms are the poles (V1 to V8) and random values are assigned with unrelated probability distributions. Subsequently, a linear three-dimensional interpolation is performed to determine the value of the random field corresponding to each point inside the prism.

Using this methodology in a two-dimensional state, pseudo-random values with Weibul type II distribution are simulated through an algorithm implemented in Matlab and the programming used in the LDEM method (see Puglia et al. [18]).

First, a two-dimensional random field with Weibull type II distribution was simulated, with mean 1, coefficient of variation (CV) 30% and correlation length (Lcor) in both directions equal to 1. In Figure 4, the histogram of the values is shown. The average of these simulated values is 0.979 and the CV = 31.3%, both very close to the initial inputs in the program to simulate the random field.

Using the Matlab software, the data matrix was interpolated and the spatial distribution graph of the data, plotted in Figure 5a, was made. With the simulated data, the Gaussian semivariogram model was generated in the ArcGis software. Figure 5b shows the Gaussian model with the obtained range and nugget effect.

Theoretically, the range of the semivariogram is closely linked to the value of Lcor, however, when setting Lcor = 1 in the simulation, this range value (1.907 in Figure 5b) was not obtained in the semivariogram. It is interesting to note that, in this case, the semivariogram has an almost constant graph.

Following the same procedure, random fields with Weibull type II distribution with mean 1, CV = 30%, with Lcor correlation lengths equal to 2, 4 and 6 were simulated. In Figure 6, the spatial distribution histograms of the numerical models are shown togheter with the semivariograms of the numerical analyzes carried out with ArcGis, for the three correlation lengths studied. From Figure 6, it is possible to observe that the range of the semivariogram with the Gaussian model approaches the input value (Lcor) given in the simulation.

From the analyses of Figures 5 and 6, it can be seen that when the distance measured between the points is of the order of Lcor, or greater than this value, the semivariogram appears to be constant from the beginning. The range found with ArcGis software present no relation to the correlation length. On the other hand, when the distance between the measured points is less than Lcor, the semivariogram starts to be constant only after the *range*, a value that corresponds to the simulated correlation length. Also, the smaller the relationship between the distance from the measured points and Lcor, the greater the precision found.

Comparing Figures 5 and 6, it is possible to observe that greater variability is found in the spatial distributions of the data with lower Lcor . Particularly, in Figure 5 there are many peaks and valleys, while in Figure 6, these maximums and minimums are each time more distanced until, with Lcor equal to 6, the data variation is low.

This way of interpolating the data from the values of the simulated poles present the desired theoretical distribution, using the methodology initially proposed by Shinozuka and Deodatis [14]. However, it is important to note that this interpolation method changes the characteristics of the data set, as shown in the comparisons between the histograms in Figures 4 and 6. The average value is close to the desired value, however, the CV varies distinctively: the variation is greater when a smaller number of poles is used in the interpolation.
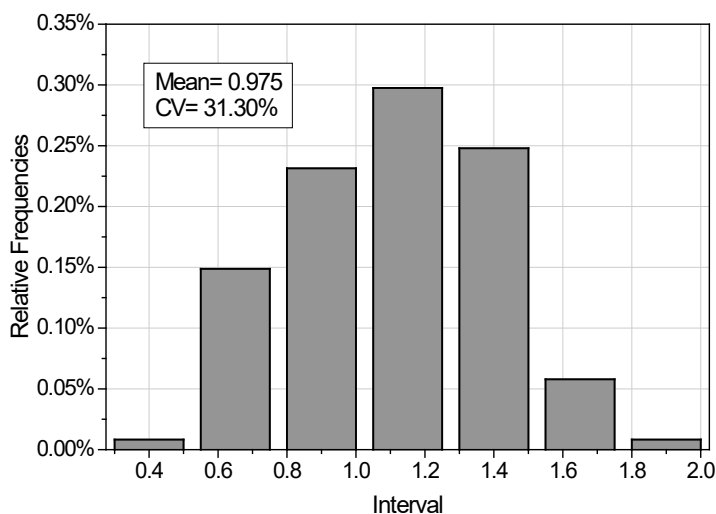
Figure 4. Histogram of the numerical simulation with Lcor = 1.
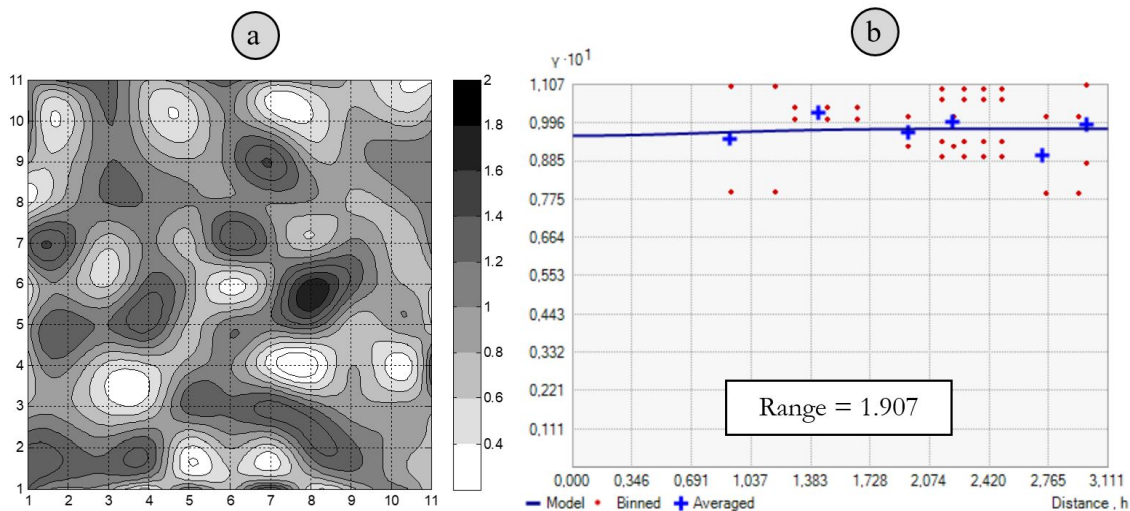
Figure 5. a) Spatial distribution of the numerical simulation with Lcor = 1, **b)** Semivariogram obtained with ArcGis analysis of the numerical simulation with Lcor = 1.
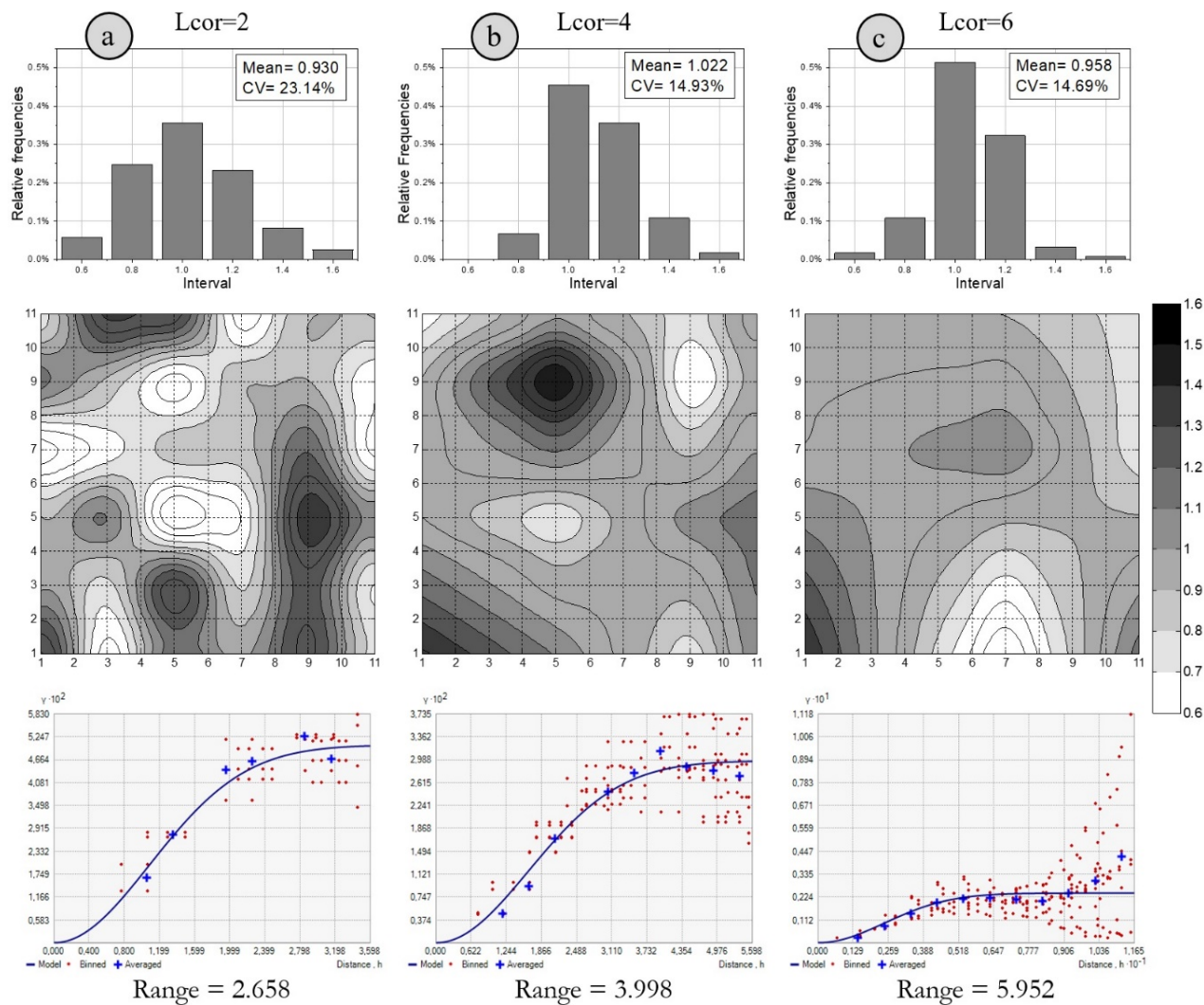
Figure 6. Histogram after the interpolation of the poles, Spatial Distribution and Semivariogram of the numerical simulation with **a)** Lcor = 2, **b)** Lcor = 4 and **c)** Lcor = 6.

4 ANALYSIS OF THE CORRELATION LENGTH USING SCLEROMETRY

4.1 Analysis based on standard NBR 7584 [13]

As the main objective of this work is not to evaluate by sclerometry the strength of the concrete, but to analyze the spatial distribution of the data, all the values obtained in the test were kept.

The sclerometric indices (*SI*) measured in the prismatic specimen (250x250x100) mm, as well as the distances at which the measurements were made, are shown in Table 2. *k* is the correlation coefficient of sclerometric index found in standard NBR 7584 [13].

Table 2. Results of the Sclerometric index established in NBR 7584 [13].

Point N°	x (cm)	y (cm)	*SI*
1	3.25	3.68	29
2	13.69	3.30	34
3	21.87	3.10	32
4	8.33	8.15	32
5	19.15	8.13	34
6	3.76	11.91	34
7	12.45	12.83	32
8	18.75	12.83	38
9	6.48	18.64	31
10	18.03	16.99	28
11	22.05	18.82	30
12	13.87	21.44	28
	Mean		32.00
	k		0.97
	SI_{mean}		31.04

Using the curve adjusted by [19] and following the Equation 1, in which:

$$f_c = 0.026\,SI^{2.044} \tag{1}$$

it is possible to obtain the compressive strength for concrete at 28 days of age, which is equal to 27.79 MPa; this value is very close to what found in the experimental tests (27.68 MPa).

The data histogram of the sclerometric indexes presented in Table 2 are found in Figure 7a. In Figure 7b, the spatial distribution of the hardness is shown, demostrating great variation of the results. With these data, the semivariogram made in ArcGis with Gaussian model reports a constant function, as shown in Figure 7c. This behavior indicates that the size of the correlation length is smaller than the measurements made (on average 7 cm), thus, the Lcor must be less than this value.

4.2 Sclerometer indentation analysis on a regular mesh

As explained in section 2.2, the sclerometric index measurements were taken every 2 cm in both directions (see Figure 2b). Table 3 presents the results obtained in the sclerometry test for the self-compacting concrete plate (200x200x100) mm. It is important to note that the points at the end of the plate were discarded, as they showed distortions in the sclerometric index values. Thus, the average *SI* was 30.56, which corresponds to a compressive strength of 28.22 MPa (Equation 1).

In Figure 8a, the histogram for the sclerometric index data presented in Table 3 can be seen. Figure 8b shows the data spatial distribution on the plate using splines interpolation in the Matlab software, while in Figure 8c it is possible to see the semivariogram obtained with the ArcGis software for the Gaussian model. When comparing the spatial distribution of the measured hardness according to NBR 7584 [13] (Figure 7b) with Figure 8, it is possible to notice in

the latter a greater variation of peaks and valleys at closer distances. This indicates that with this methodology, more spatial variability was found than by following the standard normative.
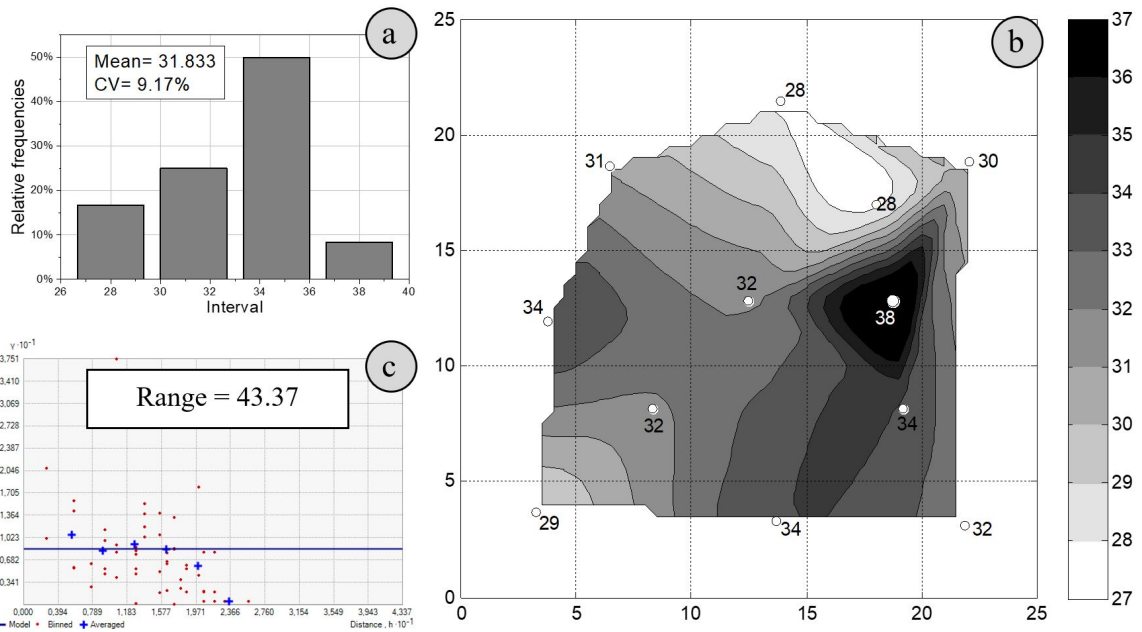
Figure 7. a) Histogram of the sclerometric index data, **b)** Spatial distribution and **c)** semivariogram with Gaussian model.

Table 3. Results of the sclerometric index using the regular 2 cm mesh.

Coordinates	x1	x2	x3	x4	x5	x6	x7	x8	x9
y1	23	34	30	32	28	31	32	28	30
y2	27	27	32	33	30	35	31	30	29
y3	28	29	28	34	33	32	33	28	26
y4	28	31	37	33	37	30	36	30	26
y5	30	37	37	34	32	32	36	32	26
y6	24	30	34	31	32	40	32	34	34
y7	23	32	31	37	35	31	29	28	28
y8	31	29	31	28	26	30	34	28	30
y9	23	26	27	27	30	29	32	25	27

In this case, the semivariogram starts to be constant after the range, 4.79 cm, demonstrating that the value used for the measurements, every 2 cm, can be appropriate for this methodology. This range value represents the correlation length for the concrete under study.

4.3 Macro-indentation test in concrete

Figure 9a shows a scheme of the self-compacting concrete plate (200x200x100) mm used in this test, illustrating the displacements and all points of the mesh measured, as described in section 2.3. Figure 9b reports the data interpolation by splines, performed in the Matlab software; the measurements at the plate borders were discarded, in order to avoid interference from the boundary conditions. The spatial distribution of the displacements shown in Figure 9b has a similar shape to that found by measuring the hardness with the sclerometric index in a 2 cm mesh (Figure 8b). From these data, a semivariogram model was generated in the ArcGis software, presented in Figure 9c. With this analysis, the correlation length was found to be 5.38 cm. Thus, the value found for Lcor is close to that found with the sclerometer, with a difference of approximately 12%.
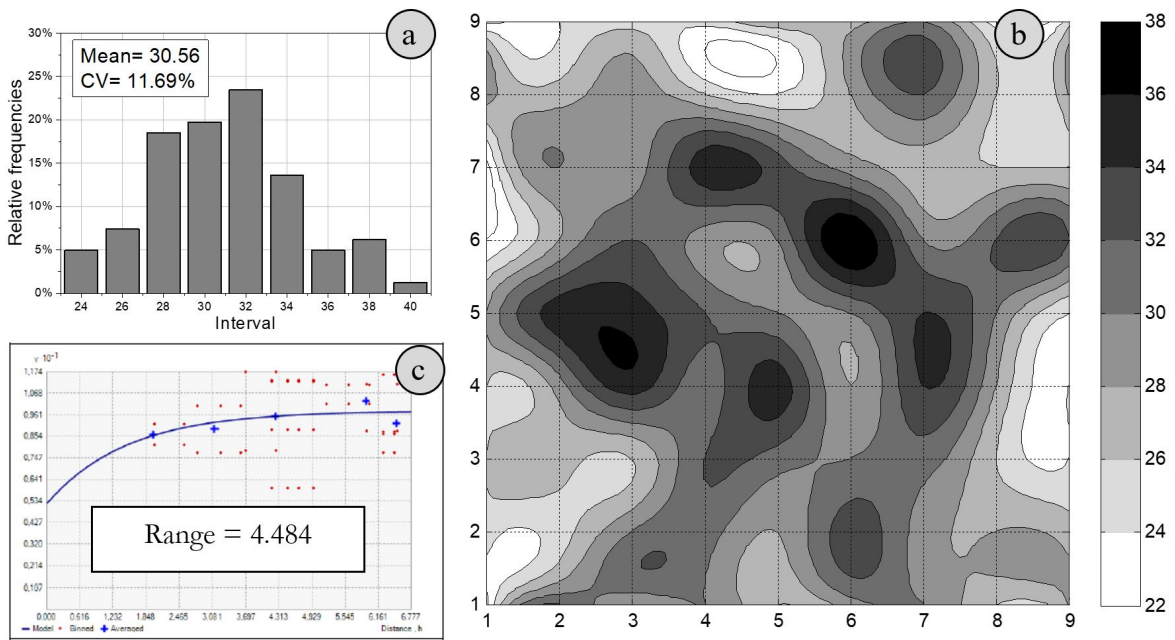
Figure 8. a) Histogram of the sclerometric index data, **b)** Spatial distribution and **c)** semivariogram with Gaussian model.
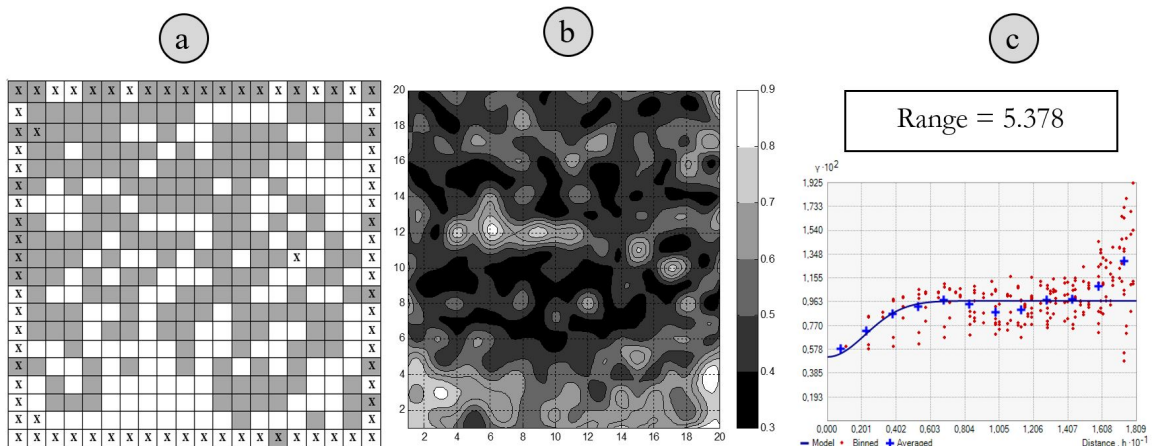
Figure 9. a) Location of points, **b)** Spline interpolation of data in the Matlab software, **c)** semivariogram obtained with ArcGis.

5 CONCLUSIONS

Based on the results, the following conclusions were inferred:

- When comparing the numerical models, it was possible to observe that when a linear interpolation of the simulated data is performed, the form of the distribution adopted initially is also modified, resulting in an average close to the desired value. However, the CV changes noticeably, as well as the shape of the random distribution. The correlation length obtained from the semivariogram with the ArcGis software using the Gaussian model is close to the simulated value;
- The compressive strength of concrete obtained using the correlation equation [19] with the value of the sclerometric index is close to the value obtained experimentally, showing good consistency of the results;
- The correlation length was not successfully obtained from the analysis of self-compacting concrete with a sclerometer, based on the NBR 7584 standard [13], due to the distance between the measurement points, greater than the material Lcor. When analyzing the points using a 2 cm mesh, the semivariogram shows that the correlation length is in the order of 4.8 cm;

- From the semivariogram of the self-compacting concrete macro-indentation analysis it was possible to identify a correlation length of the order of 5.4 cm;
- The correlation lengths (Lcor) measured by both sclerometry and macro indentation are comparable (only 12% difference). It was also possible to identify that the Lcor for this concrete is approximately 5 to 6 times the maximum size of the coarse aggregate (from 4.75 to 5.70 cm; $\phi_{aggregate} = 9.5$ mm). Finally, we believe that this correlation length for concretes will also be influenced by the mortar content and dimension of the coarse aggregates.

Since the results obtained through macro-indentation and sclerometry are similar, the latter method is more indicated, as it is easy to apply and handle. Still, to obtain more reliable results, we suggest to apply measurements at a distance of maximum 2 cm.

ACKNOWLEDGEMENTS

REFERENCES

[1] W. R. L. Silva, J. Němeček, and P. Štemberk, "Nanotechnology and Construction: use of nanoindentation measurements to predict macroscale elastic properties of high strength cementitious composites," *Rev. IBRACON Estrut. Mater.*, vol. 5, no. 3, pp. 284–295, 2012, http://dx.doi.org/10.1590/S1983-41952012000300002.

[2] G. Constantinides, F.-J. Ulm, and K. Van Vliet, "On the use of nanoindentation for cementitious materials," *Mater. Struct.*, vol. 36, no. 3, pp. 191–196, 2003, http://dx.doi.org/10.1007/BF02479557.

[3] G. Constantinides, K. S. Ravi Chandran, F. J. Ulm, and K. J. Van Vliet, "Grid indentation analysis of composite microstructure and mechanics: principles and validation," *Mater. Sci. Eng. A*, vol. 430, no. 1-2, pp. 189–202, 2006, http://dx.doi.org/10.1016/j.msea.2006.05.125.

[4] R. C. Grego and R. S. Vieira, "Variabilidade espacial de propriedades físicas do solo em uma parcela experimental," *Rev. Bras. Ciênc. Solo*, vol. 29, no. 2, pp. 169–177, 2005, http://dx.doi.org/10.1590/S0100-06832005000200002.

[5] L. R. R. Reis, "Utilização da condutividade elétrica para estabelecimento de zonas de manejo em um latossolo amarelo-escuro," M.S. thesis, Prog. Pós-grad. Eng. Agr., Univ. Fed. Viçosa, Viçosa, Brasil, 2005.

[6] D. G. Padoin, "Estudo das propriedades mecânicas e físicas de um traço comercial de concreto autoadensável com e sem substituição de cinza de casca de arroz," M.S. thesis, Prog. Pós-grad. Eng., Univ. Fed. Pampa, Alegrete, Brasil, 2017.

[7] Associação Brasileira de Normas Técnicas, *Determinação da Composição Granulométrica*, NBR NM 248:2003, 2003.

[8] Associação Brasileira de Normas Técnicas, *Agregados – Determinação da Massa Específica de Agregados Miúdos por Meio do Frasco Chapman – Método de Ensaio*, NBR 9776, 1988.

[9] Associação Brasileira de Normas Técnicas, *Agregado Graúdo – Determinação da Massa Específica, Massa Específica Aparente e Absorção de Água*, NBR NM 53, 2009.

[10] Associação Brasileira de Normas Técnicas, *Concreto Autoadensável, Partes 1 a 6*, NBR 15823, 2010.

[11] Associação Brasileira de Normas Técnicas, *Concreto – Procedimento para Moldagem e Cura de Corpos de Prova*, NBR 5738, 2015.

[12] Associação Brasileira de Normas Técnicas, *Concreto – Ensaio de Compressao de Corpos de Prova Cilindrico*, NBR 5739, 2018.

[13] Associação Brasileira de Normas Técnicas, *Concreto Endurecido – Avaliação da Dureza Superficial pelo Esclerômetro de Reflexão – Método de Ensaio*, NBR 7584, 2012.

[14] M. Shinozuka and G. Deodatis, "Simulation of multidimensional gaussian stochastic fields by spectral representation," *Appl. Mech. Rev.*, vol. 49, no. 1, pp. 29–53, 1996, http://dx.doi.org/10.1115/1.3101883.

[15] R. D. Rios, "Aplicações do método dos elementos discretos em estruturas de concreto," Ph.D. dissertation, Univ. Fed. Rio Grande do Sul, Porto Alegre, Brasil, 2002.

[16] L. F. F. Miguel, "Critério constitutivo para o deslizamento com atrito ao longo da falha símica," Ph.D. dissertation, Esc. Eng., Univ. Fed. Rio Grande do Sul, Porto Alegre, Brasil, 2005.

[17] L. F. F. Miguel, L. F. Fadel Miguel, J. D. Riera, J. Kaminski, and R. C. R. Menezes, "Model uncertainty in the assessment of EPS Wind loads in transmission line design," in Proc. Int. Semin. Model. Identif. Struct. Subj. Dyn. Exc. – Emph. Transmiss. Lin., vol. 1, Z. M. C. Pravia, I. Iturrioz, L. F. F. Miguel, L. F. F. Miguel and R. C. R. Menezes, Eds. UPF Editora, Passo Fundo, 2009, pp. 151–173.

[18] V. B. Puglia, I. Iturrioz, J. D. Riera, and L. Kostesteki, "Random field generation of the material properties in the truss-like discrete elemento method," *Mec. Comput. Cilamce-Mecom*, vol. XXIX, pp. 6793–6807, Nov 2010.

[19] M. D. Machado, L. D. Shehata, and I. A. E. M. Shehata, "Curvas de correlação para caracterizar concretos usados no Rio de Janeiro por meio de ensaios não destrutivos," *Rev. IBRACON Estrut. Mater.*, vol. 2, no. 2, pp. 100–123, 2009, http://dx.doi.org/10.1590/S1983-41952009000200001.

Rev. IBRACON Estrut. Mater., vol. 13, no. 4, e13401, 2020

11/11

IBRACON Structures and Materials Journal
Revista IBRACON de Estruturas e Materiais

ORIGINAL ARTICLE

Human comfort assessment of buildings subjected to nondeterministic wind dynamic loadings

Avaliação do conforto humano de edifícios submetidos a carregamentos dinâmicos não determinísticos de vento

Alan Barile[a] ID
Leonardo de Souza Bastos[a] ID
José Guilherme Santos da Silva[a] ID

[a] Universidade do Estado do Rio de Janeiro - UERJ, Faculdade de Engenharia, Programa de Pós-graduação em Engenharia Civil, Rio de Janeiro, RJ, Brasil

Abstract A reliable human comfort assessment depends on the correct description of the wind dynamic loads when compared with studies of natural wind. Thus, in this research work an analysis methodology was developed aiming to generate nondeterministic dynamic wind loadings, based on a power spectral density function and coherence function. This way, aiming to test the developed analysis methodology, a forced vibration dynamic analysis was carried out, based on a three-dimensional finite element model developed to represent a real and existing thirty-storey reinforced concrete building, with total height of 90 m, store height equal to 3 m and rectangular dimensions of 21.50 m by 17.30 m. The dynamic structural response of the investigated building was evaluated, the accelerations at the top of the structure were calculated and the human comfort was verified. The results obtained along this research work indicate that the peak accelerations calculated for periods of recurrence equal to 10 years and 1 year, respectively, overpass the recommended limits proposed by the NBR 6123 and ISO 10137.

Keywords: buildings, wind loads, human comfort, structural dynamics.

Resumo: Uma avaliação confiável do conforto humano depende da descrição correta das cargas dinâmicas de vento, quando comparadas com estudos acerca do vento natural. Assim sendo, neste trabalho de pesquisa foi desenvolvida uma metodologia de análise com o objetivo de gerar cargas dinâmicas não determinísticas de vento, com base no emprego de uma função de densidade espectral de potência e função de coerência. Deste modo, objetivando testar a metodologia de análise proposta, foi realizada uma análise dinâmica de vibração forçada, com base no uso de um modelo tridimensional de elementos finitos desenvolvido para representar um edifício de concreto armado com trinta pavimentos, real e existente, com altura total de 90 m, pé-direito de 3 m e dimensões em planta de 21,50 m x 17,30 m. A resposta estrutural dinâmica do edifício investigado foi avaliada, as acelerações no topo da estrutura foram calculadas, e o conforto humano foi verificado. Os resultados obtidos ao longo deste trabalho de pesquisa indicam que os picos de aceleração calculados para períodos de recorrência de 10 anos e 1 ano, respectivamente, superam os limites recomendados propostos pela NBR 6123 e ISO 10137.

Palavras-chave: edifícios, cargas de vento, conforto humano, dinâmica estrutural.

1 INTRODUCTION

Currently the construction of tall and slender buildings to meet the demand of population growth and the reduction of free spaces in urban areas has resulted in relevant structural problems related to excessive vibrations and human discomfort caused by the dynamic characteristics of the wind. Because of that, it became imperative to study the

interaction between wind and tall buildings, in order to improve structural designs avoiding possible future service limit state problems (Barile [1], Bashor [2], Ferrareto [3], Jiurong [4], and Rist [5]).

Although vibrations caused by the wind in most current design situations do not present risks related to the structural collapse, this kind of dynamic action can cause human discomfort. According to occupant surveys and motion simulators, it is well known that people can develop the sensation of tiredness, low motivation, distraction from work activities and low mood, when subject to wind-induced vibrations (Barile [1], Burton [6], Goto [7],Hansen [8], and Lamb [9], [10]).

Generally, design standards consider the wind effect as static loads, calculated from the average speed without considering the components of the fluctuant part that can induce vibrations on the structural system leading to human discomfort. A more realistic analysis can be carried out considering the dynamic characteristics of the wind (Barile [1], Férnandez [11], Liu [12], [13], and Shinozuka [14]). This way, the spectral representation method can be used based on wind series generated with the fluctuant part of the wind determined as a sum of a finite number of harmonics with randomly generated phase angles. This methodology uses a power spectrum and a coherence function to calculate the amplitude of each harmonic and maintaining resemblance to the natural wind (Franco [15] and Shinozuka [14], [16]). Thus, the wind series can be used to simulate the wind dynamic loadings and a reliable human comfort assessment can be verified based on the accelerations values (Bastos [17], Chávez [18], Oliveira [19], Santos [20] and Steffen [21]).

Thus, in this investigation an analysis methodology was developed (Barile [1]), based on the work of Shinozuka et al. [14], [16], aiming to generate nondeterministic dynamic wind loads considering the power spectrum of Kaimal and the coherence function of Davenport. Having in mind to test the developed analysis methodology, a finite element model was created based on a real and existing design of a thirty-storey reinforced concrete building, with total height of 90 m, store height equal to 3 m and rectangular dimensions of 21.50 m by 17.30 m [22]. Finally, the accelerations at the top of the building were calculated and the human comfort was verified. The results obtained along this investigation indicate that the peak accelerations values calculated for periods of recurrence equal to 10 years and 1 year, respectively, overpass the recommended limits proposed by the Brazilian Standard NBR 6123 [23] and also ISO 10137 Standard [24].

2 NONDETERMINISTIC WIND MODEL

The nondeterministic wind load was developed based on the methodology proposed by Shinozuka et al. [14], [16]; where the fluctuant wind parcel is generated from the sum of a finite number of overlapping harmonics with random phase angles, see Equation 2. The amplitude of each harmonic is obtained through the spectral power density for the wind and the spatial correlation between the wind velocities at distant points horizontally and vertically. This way, the development of the present analysis methodology has considered the power spectral density of Kaimal, see Equation 4 and the Davenport's spatial correlation, see Equation 5.

In this investigation, it was assumed that wind velocity can be divided into a static part and a turbulent part, according to Equation 1, where V_m is the average wind velocity in m/s and v_f is the turbulent part in m/s. The static part is usually obtained using the mean based on an interval of 10 minutes to 1 hour.

$$v(t) = V_m + v_f(t) \tag{1}$$

The turbulent part was obtained based on the "Spectral Representation Method" (Shinozuka et al. [14], [16]). This method consists of generating wind series as a sum of a finite number of superimposed harmonics with random phase angles where the amplitude are calculated using a function that describes a power spectrum and a coherence function for spatial correlation between different points of the investigated structure, see Equation 2.

$$v_j(t) = \sum_{m=1}^{N_p} \sum_{k=1}^{N_\omega} \left| H_{jm}(\omega_k) \right| \sqrt{\Delta_\omega} \cos(\omega t + \phi_k), j = 1,2,3 \dots N_p \tag{2}$$

With reference to Equation 2, N_p is the number of points of the structure used to apply the wind load, N_ω is the number of frequencies used to represent the spectrum, Δ_ω is the frequency increment, ω is the frequency in rad/s, ϕ is a random phase angles evenly distributed in the interval (0-2π). In Equation 2 the H matrix represents the lower part of the cross-spectral density matrix S(ω) [S (ω) = H(ω)* H^T(ω)]. On the other hand, in Equation 3, S represents the spectral density and γ is the coherence function.

$$S_{jk}(\omega) = \sqrt{S_j(\omega) S_k(\omega) \gamma_{jk}(\omega)}, j,k = 1,2,3,\dots,N_p, j \neq k \tag{3}$$

In this research work, the mathematical equation proposed by Kaimal was selected to model the power spectral density of the turbulent part of wind longitudinal velocity at different heights of the building, according to Equation 4.

$$S(\omega) = \frac{2\pi u^{*2}}{\omega} \frac{200n}{(1+50n)^{5/3}}; n = \frac{\omega z}{2\pi V_m(z)} \tag{4}$$

With reference to Equation 4, z is the height, in meters; f is the frequency, in Hz; u* is the shear rate of the fluid, in m/s; and $V_m(z)$ is the average wind velocity at height z, in m/s. The coherence function proposed by Davenport was selected to correlate the floating part of the wind at two different points in the space in the coordinates, (z_1, y_1) and (z_2, y_2), according to Equation 5.

$$Coh(r,n_k) = e^{-f}, f = \frac{n_k \sqrt{C_z^{\,2} \Delta_z^{\,2} + C_y^{\,2} \Delta_y^{\,2}}}{\frac{1}{2}(V_m(z_1) + V_m(z_2))} \tag{5}$$

According to Equation 5, n_k is the frequency in Hz, $V(z_1)$ and $V(z_2)$ are the average wind velocities for heights z_1 and z_2 respectively, in m/s; Δ_z and Δ_y are, respectively, the differences between z_1 and z_2 and between y_1 and y_2, and C_y and C_z are constants which can be used with the value of 10 and 7, respectively. The wind load for each building section (nodes in the FEM), considered in this analysis is obtained using the equation suggested by the Brazilian standard, see Equation 6.

$$F_j(t) = 0.613 v_j^{\,2} C_{aj} A_{eff}, 1,2,3,\ldots,N_p \tag{6}$$

In Equation 6, v represents the calculated velocity for the building structural section (node in the FEM), using the developed analysis, see Equations 15; C_a is a coefficient determined by the design standard NBR 6123 [23] and A_{ef} is the effective area, considered for the node in the building FEM.

It is important to emphasize that the time increment for the resulting signal must be less than twice the maximum frequency adopted to avoid the aliasing phenomenon according to the sampling theorem. Thus, the wind dynamic force applied to the structure is obtained through Equation 6.

Considering the nondeterministic characteristics of the natural wind, the final structural response is obtained through the Monte Carlo Method, where a finite number of analyses are required aiming to obtain the structural response that meets the probabilistic criterion, defined by the structural engineer, based on a statistical analysis. The number of analyses depends on the convergence criterion to obtain the structural response.

In sequence, the power spectrum and the spatial correlation are shown in Figures 1 and 2 for the generated wind velocity signal with duration of 600 seconds, based on the developed analysis methodology. Based on the results presented in Figures 1 and 2, it is possible to see the similarity with the functions used by Kaimal and Davenport.
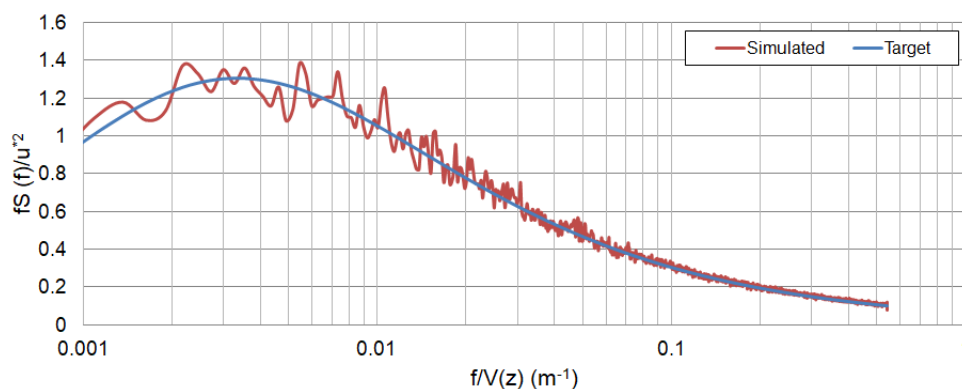
Figure 1. Typical power spectral density of the wind velocity generated for a given position of the structure.
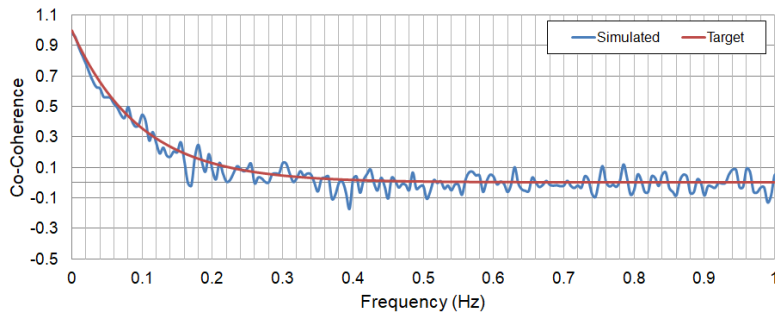
Figure 2. Typical spatial correlation between different points of the structure indicated by the coherence function.

Examples of wind velocities can be seen in Figures 3 and 4, considering three different positions of the structure. It is possible to see that for near, vertical or horizontal distances, the signals present similar characteristics as studied by data obtained from the natural wind and described by the Davenport's correlation function.
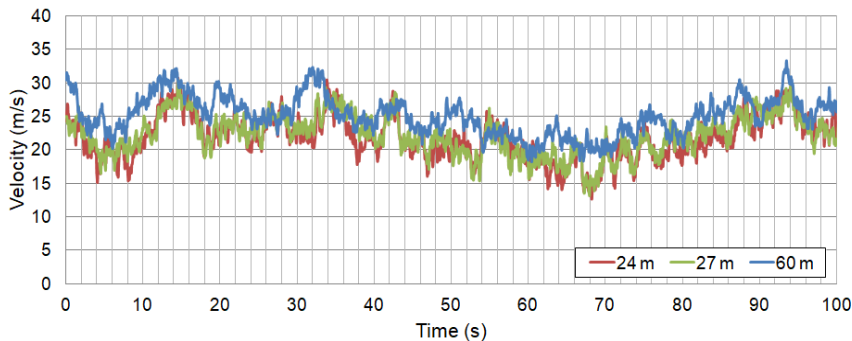
Figure 3. Typical wind speeds for heights of 24 m, 27 m and 60 m for the same horizontal alignment.
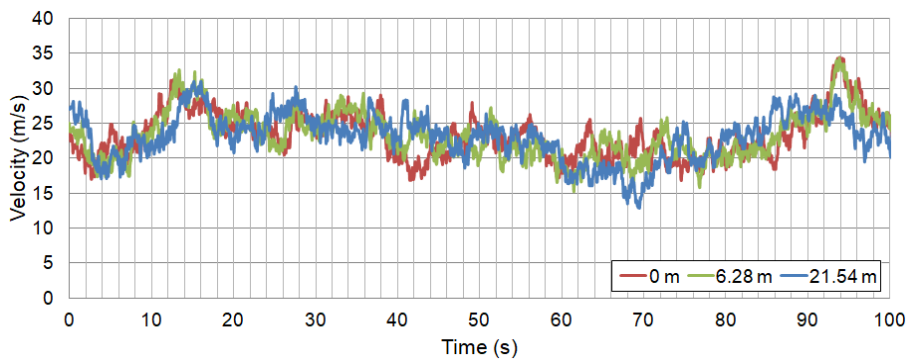
Figure 4. Typical wind speeds for horizontal position of 0, 6.28m and 21.54 m for the same vertical alignment of the building.

3 INVESTIGATED STRUCTURAL MODEL

The investigated building in this research has plant dimensions of 21.50 m by 17.30 m, presents 30 floors, with a height of 3.0 m, total height 90 m, as shown in Figure 5. The structure, made of reinforced concrete, consists of massive concrete slabs with a thickness equal to 18 cm, girders with sections 30x60 cm and columns with sections 30x80 cm in their majority. The structural model does not have girders dividing the internal spans of the slabs, but even so, the periphery beams together with the columns can compose structural frames that contributes to the bracing of the building (Bastos [22]), as illustrated in Figures 5 and 6.

a) Structural floor plant   b) 3D model perspective
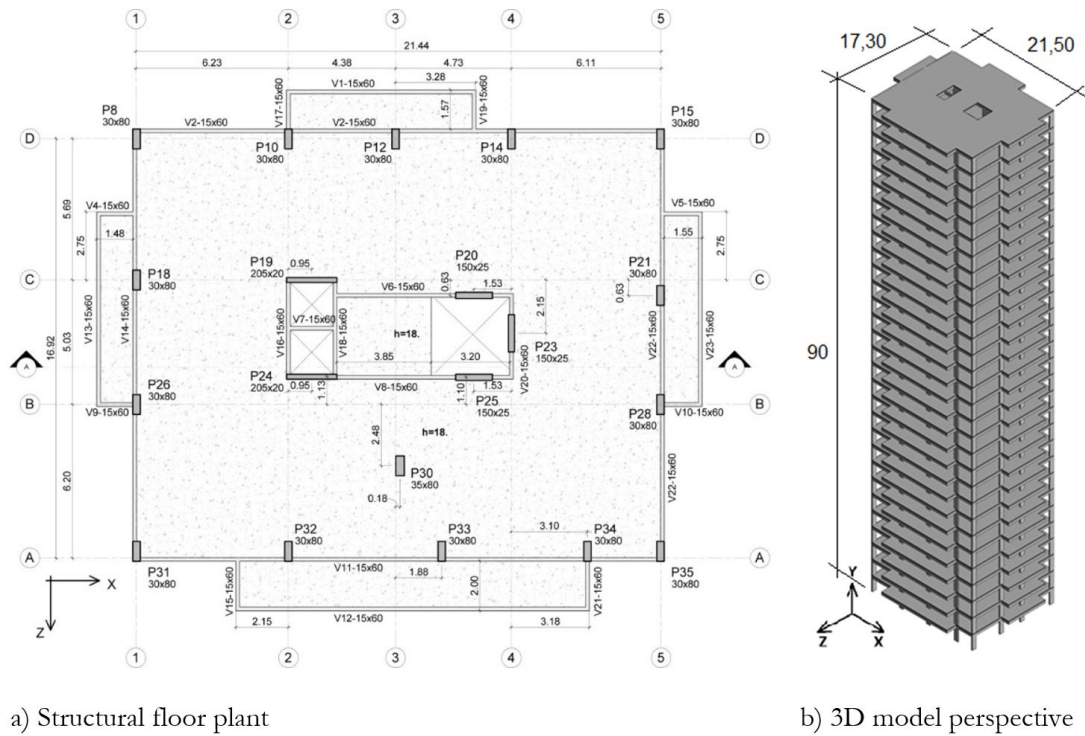
Figure 5. Investigated structural model.
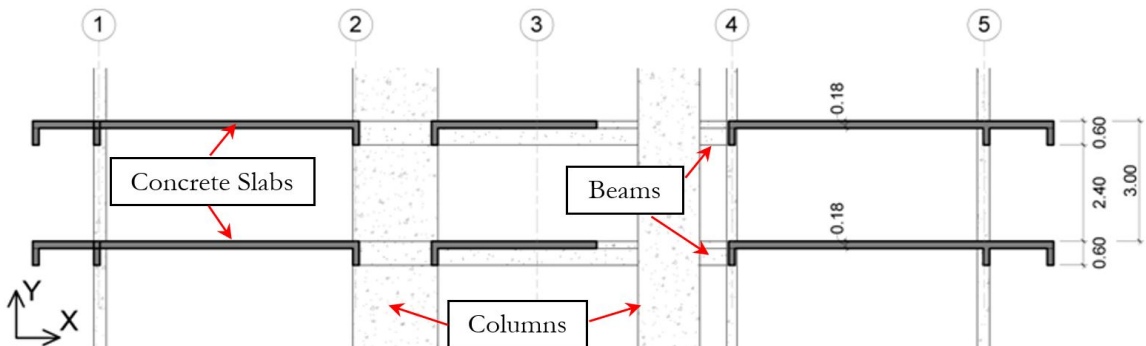
Figure 6. Detail of the concrete slabs thickness and height floor-to-floor.

The structural concrete used has compression strength (f_{ck}) of 45 MPa, Young's modulus (E_{cs}) of 34 GPa, a Poisson's coefficient (v) equal to 0.2 and density (γ_c) of 25 kN/m³. Usual design and permanent loads (1.0 kN/m²) and accidental (1.5 kN/m2) loads were added to the slabs of all floors. The total weight of masonry was distributed evenly over the slabs (2.8 kN/m²).

4 FINITE ELEMENT MODELLING OF THE BUILDING

The proposed numerical model, developed for the reinforced concrete building dynamic analysis, adopted the usual mesh refinement techniques present in finite element method simulations implemented in the ANSYS program (ANSYS, 2009). In this model, the reinforced concrete girders and columns were represented by three-dimensional BEAM44 finite elements, where the effects of bending and torsion are considered. The uniaxial finite element BEAM44 is composed of two nodes and each node with six degrees of freedom (translations and rotations in X, Y and Z directions). The advantage of this element is the possibility of allowing its nodes to be spaced from the centroid axis of the beams, since the slab and the beam are not positioned on the same axis. This eccentricity is considered in the

modelling, because affects the values of the building natural frequencies. On the other hand, the concrete slabs were represented based the SHELL63 finite elements. Four nodes and each node with six degrees of freedom (translations and rotations in X, Y and Z directions) define the shell finite element SHELL63.

The developed numerical model presents an appropriate degree of refinement, aiming to a good representation of the dynamic structural behaviour of the building, see Figure 7. Table 1 presents the characteristics of the numerical model (nodes, elements and degrees of freedom). The support conditions were assumed as a pin-joint, considering that all the building supports were restricted to vertical and horizontal translational and free for rotational displacements.

Table 1 Characteristics of the developed building finite element model.

FEM of the Building	
Number of Nodes	232552
Number of Elements	245880
Number of Degrees of Freedoms (DOF)	1395246
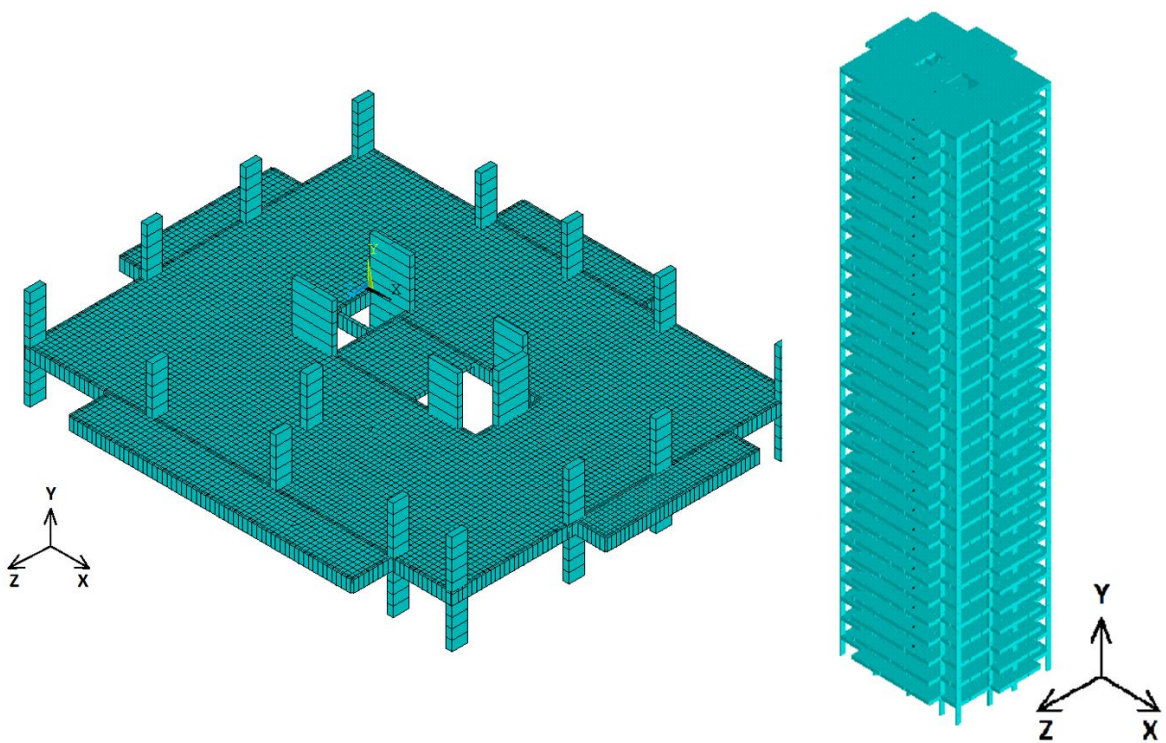
a) FEM: 3D view of typical floor plant   b) FEM: perspective

Figure 7. Finite element model of the investigated building.

5 NATURAL FREQUENCIES AND VIBRATION MODES OF THE BUILDING

The natural frequencies (eigenvalues) and the vibration modes (eigenvectors) of the structure were obtained based on numerical methods of extraction (modal analysis), through a free vibration analysis and using the ANSYS (2009) computational program. The first four vibration modes of the analysed building are shown in Figure 8. The fundamental frequency of 0.25 Hz (f_{01} = 0.25 Hz), obtained through the modal analysis shows the need for dynamic analysis of the building since, as can be seen from the power spectrum presented in Figure 1, the largest transfer of wind energy is concentrated in the region of low frequencies. In order to study the situation that will cause the higher displacements and accelerations, the Z-direction (see Figure 8) was chosen to apply the non-deterministic wind loadings on the structure, since the lowest structural frequency corresponds to the bending around the X axis (see Figure 8).

| 1st Vibration mode ($f_{01} = 0.25$Hz) | 2nd Vibration mode ($f_{02} = 0.26$Hz) | 3rd Vibration mode ($f_{03} = 0.34$Hz) | 4th Vibration mode ($f_{04} = 0.49$Hz) |
| Bending around X-axis | Bending around Z-axis | Torsion around Y-axis | Torsion around Y-axis |
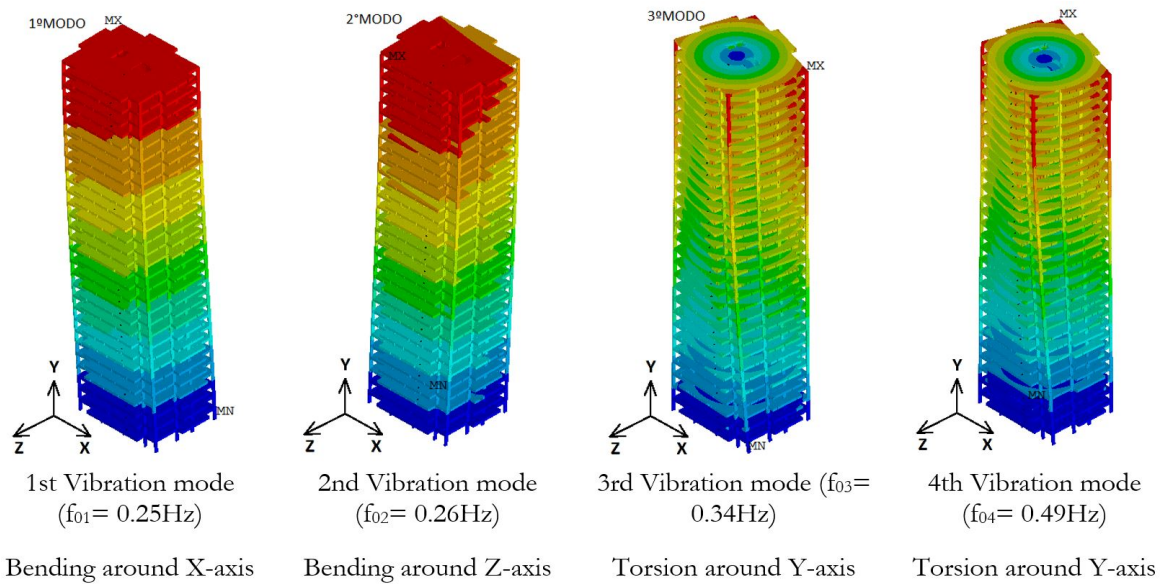
Figure 8. Vibration modes of the investigated building.

6 NONDETERMINISTIC DYNAMIC ANALYSIS

Based on the use of the finite element program ANSYS (2009), forced vibration dynamic analyses were performed on the investigated structural model. In addition to the usual vertical design loads, the nondeterministic wind action was applied on the largest façade of the building [Z-direction, see Figure 7)]. The basic wind speed was determined considering, initially, a time of recurrence of 10 years (NBR 6123 [23]), and after that a period of recurrence equal to 1 year was considered (ISO 10137 [24]). The results of the dynamic analyses were obtained at the top of the building (h = 90 m), when the maximum horizontal translational displacements were analysed, and at the floor of the last building store (h = 87 m), when the maximum accelerations were investigated.

Since the wind dynamic actions considered in this research work have nondeterministic characteristics, it is not possible to predict the response of the structure at a certain instant of time. Thus, a reliable response can be achieved through appropriate statistical treatment, based on the use of Equation 7. This way, considering that the dynamic structural response presents a normal distribution, and based on the calculation of the mean (m) and also the standard deviation (σ), it is possible to obtain the characteristic value ($U_{z95\%}$) that corresponds to a reliability of 95%, meaning that only 5% of the sampled values will exceed this value [9].

$$U_{z95\%} = 1.65\sigma + m \tag{7}$$

In this research work, aiming to attend the period of recurrence of the design standards traditionally used for the human comfort assessment (NBR 6123 [23], ISO 10137 [24]), two wind loading scenarios were considered. The first one with a period of recurrence equal to 10 years, adopted by NBR 6123 [23], and the second considering 1 year of recurrence, according to ISO 10137 [24]. For each scenario, 30 nondeterministic wind series were generated to investigate the dynamic structural behaviour of the analysed building.

The parameters used to generate the wind series are shown in Table 2 Parameters used to generate the nondeterministic wind series. Based on the NBR 6123 [23] recommendations, the basic wind velocity represents the wind for the city of Rio de Janeiro that occurs at least one time in 50 years, with duration of 3 seconds, and the category II is related to open lands in level with few isolated obstacles. The topographic factor S_1 equal to 1 corresponds to a situation of flat terrain that is weakly uneven. The category is used to determine the parameters for the calculation of the factor S_2 that indicates the variation of the velocity according to the height and roughness of the terrain. The probabilistic factor S_3, was obtained in order to satisfy the period of recurrence of 10 years proposed by NBR 6123 [23], and also considering a period of recurrence equal to 1 year, according to ISO 10137 [24]. In both situations, a probability of occurrence equal to 63% is considered. The time duration of 10 minutes (600 seconds) is usually adopted to study wind effects in structures.

Table 2 Parameters used to generate the nondeterministic wind series.

Design Parameters	Recommended Values
Wind Basic Velocity (V_0)	35 m/s
Terrain Category	II
Topographic Factor (S_1)	1
Parameters for Roughness Factor (S_2)	b = 1 and p = 0.15
Probability Factor (S_3)	0.76 (10 years) and 0.53 (1 year)
Time Duration	600 seconds
Time Increment	0.03 seconds

Figures 9 and 10 present a typical example of the wind dynamic force in the time and frequency domain, respectively. It is relevant to observe through the generated wind nondeterministic characteristic, the range of excitation frequencies that represent the harmonics of the signal. It must be emphasized that the fundamental frequency, related to the first vibration mode of the structure (bending around X-axis, see Figure 8), responsible for the higher energy transfer peak of the system in the dynamic analysis was represented in the signal.
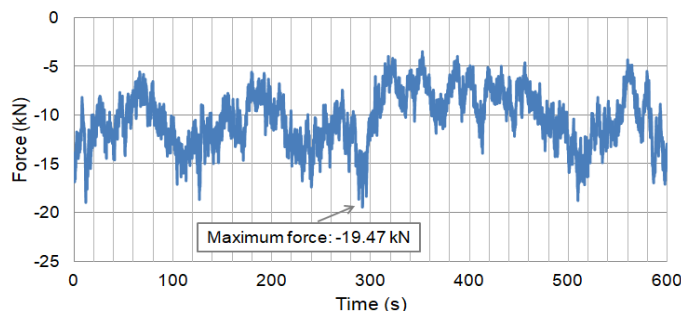
Figure 9. Typical example of nondeterministic wind loading in the time domain (period of recurrence of 10 years).
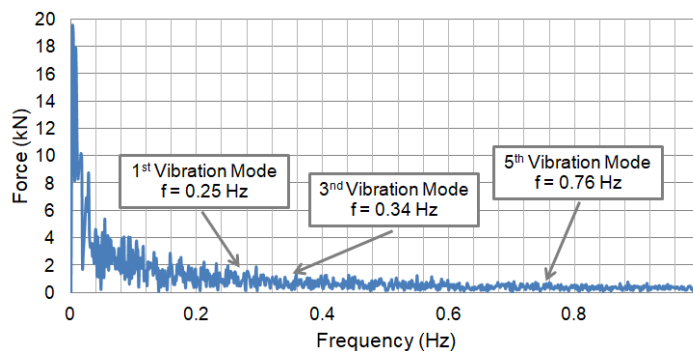
Figure 10. Typical example of nondeterministic wind loading in the frequency domain (period of recurrence of 10 years).

The dynamic structural behaviour of the building over time, when the structure is subjected to non-deterministic wind loadings, can be observed with greater clarity in the next Figures 11 to 13. Figure 11 shows a typical example of the translational horizontal displacements at the top of the structure, over 10 minutes, where it is possible to verify that the maximum horizontal translational displacement value is below the recommended limit proposed by the Brazilian Standard NBR 6118 [25]. In sequence, a typical example of the acceleration result can be seen in Figure 12, attempting to the fact that the maximum acceleration value exceeded the limit proposed by NBR 6123 [23], which would lead to the modification of the structural design, aiming to attend human comfort. After that, Figure 13 illustrates the accelerations in frequency domain, obtained through the Fast Fourier Transform (FFT). It is possible to verify that the main energy transfer peak (greater amplitude of displacement) is associated to resonance related to the building fundamental frequency (first natural frequency: $f_{01} = 0.25$ Hz), corresponding to the first vibration mode (bending around the X-axis, see Figure 8).
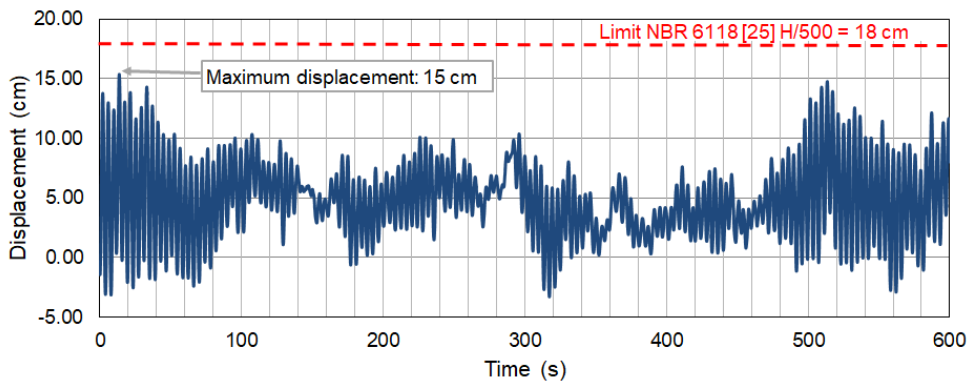
Figure 11. Example of translational horizontal displacement result at 90 meters high (period of recurrence of 10 years).
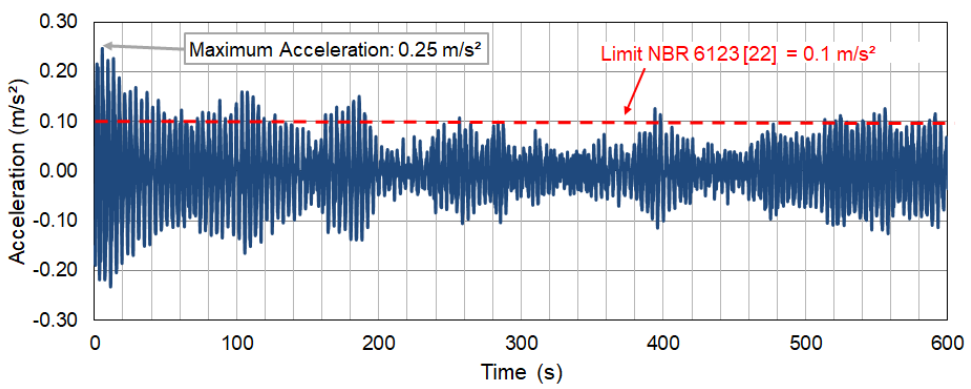
Figure 12. Example of acceleration result at 87 meters high (period of recurrence of 10 years).
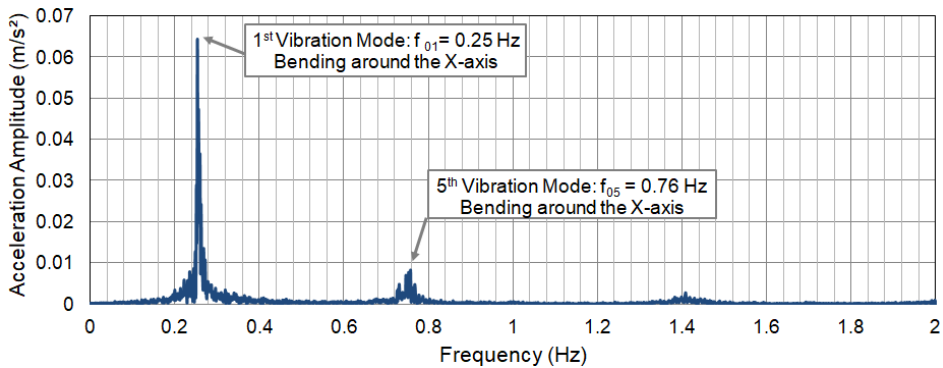
Figure 13. Example of acceleration at 87 meters high in the frequency domain (period of recurrence of 10 years).

As far as the convergence of the numerical results is concerned, Figure 14 illustrates the characteristic horizontal translational displacements ($U_{z95\%}$) at the top of the reinforced concrete building (see Figures 5 and 7), calculated gradually over the results of each series, pointing out to the importance of applying an adequate number of nondeterministic wind series in order to obtain a consistent result.

In sequence of the investigation, having in mind a quantitative analysis of the results, Table 3 presents the maximum translational horizontal displacements and accelerations, respectively, calculated at the top of the building (h = 90m) and at the last floor (h = 87 m), see Figures 5 and 7, considering each nondeterministic wind series applied on the investigated building, and also the mean values (μ), standard deviation (σ) and characteristics values calculated based on the generated 30 series for each investigated scenario [see Equations 1–6].
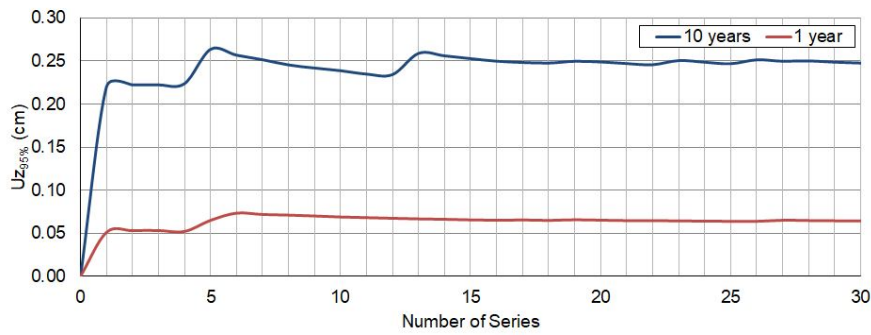
Figure 14. Convergence of the characteristic displacements values considering a period of recurrence equal to 10 years and 1 year.

Table 3 Dynamic structural response of the investigated building: maximum displacements and peak accelerations values.

Nondeterministic Loading Series	Time of recurrence: 10 years		Time of recurrence: 1 year	
	Displacements U_Z (cm)	Accelerations a_p (m/s^2)	Displacements U_Z (cm)	Accelerations a_p (m/s^2)
1	12.13	0.22	5.11	0.07
2	13.93	0.22	4.83	0.08
3	13.44	0.21	4.51	0.08
4	14.99	0.22	4.61	0.07
5	10.10	0.13	6.56	0.10
6	12.03	0.16	7.20	0.10
7	11.25	0.15	5.52	0.09
8	11.71	0.16	5.80	0.09
9	13.42	0.19	4.37	0.07
10	13.13	0.14	4.77	0.09
11	13.83	0.16	4.10	0.06
12	13.73	0.20	5.21	0.08
13	20.44	0.29	4.28	0.07
14	11.78	0.19	5.31	0.08
15	12.37	0.17	4.41	0.07
16	11.99	0.16	3.96	0.06
17	13.81	0.19	5.83	0.09
18	13.84	0.20	4.90	0.07
19	12.67	0.22	6.14	0.09
20	11.32	0.13	4.62	0.06
21	14.02	0.18	4.56	0.08
22	14.02	0.14	5.56	0.09
23	15.37	0.24	5.14	0.07
24	13.01	0.15	5.05	0.08
25	12.34	0.15	5.25	0.08
26	13.43	0.25	5.59	0.07
27	10.38	0.15	6.62	0.11
28	12.77	0.21	4.84	0.07
29	11.64	0.17	5.00	0.07
30	12.93	0.19	5.36	0.08
Mean (m)	13.06	0.18	5.17	0.08
Standard Deviation (σ)	1.80	0.04	0.74	0.01
$U_{z95\%}$	**16.04**	**0.25**	**6.39**	**0.10**

$U_{lim} = 18$ cm (NBR 6118 [25]); $a_{lim} = 0.10$ m/s^2 (NBR 6123 [23]); $a_{lim} = 0.075$ m/s^2 (ISO 10137 [24])

The human comfort criteria can be verified using the peak accelerations values of the nondeterministic signals, see Table 3. The results show peak accelerations (mean maximum values), equal to 0.25 m/s^2 (time of recurrence: 10 years; NBR 6123 [23]), and 0.10 m/s^2 (time of recurrence: 1 year; ISO 10137 [24]), respectively, see Table 3. It must be emphasized that these values overpass the recommended limits proposed by the Brazilian Standard NBR 6123 [23] ($a_p = 0.25$ m/s^2 > $a_{lim} = 0.10$ m/s^2), and ISO 10137 [24] Standard ($a_p = 0.10$ m/s^2 > $a_{lim} = 0.075$ m/s^2), when the building dynamic structural response was considered.

In sequence of the analysis, Figure 15 presents the maximum displacements values [top of the building: h = 90m, see Figures 5 to 7], obtained for each nondeterministic wind series considering, respectively, a period of recurrence equal to 10 years (NBR 6123 [23]) and 1 year (ISO 10137 [24]). It is possible to verify that most of these displacements attend the limit proposed by the standard NBR 6118 [25].
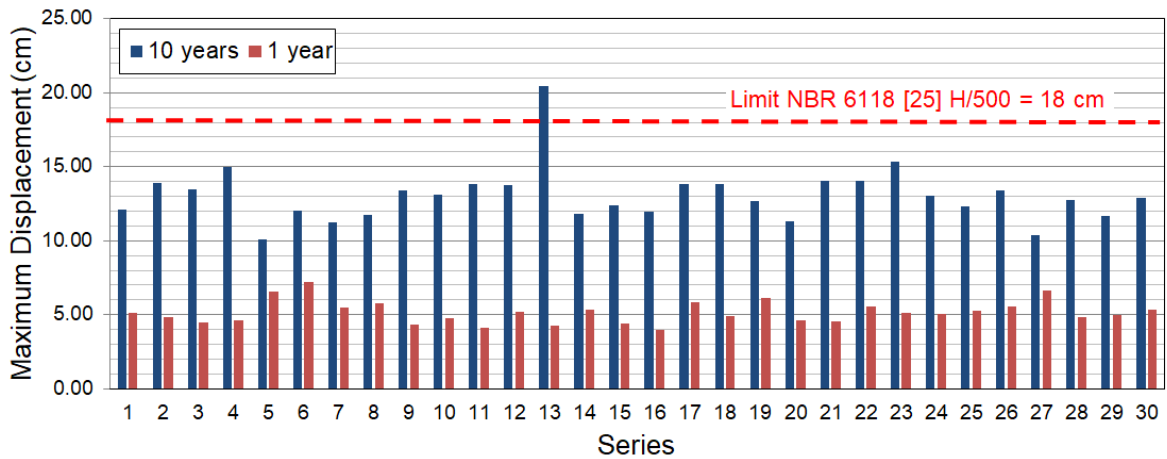
Figure 15. Maximum translational horizontal displacements obtained for each nondeterministic wind series based on a period of recurrence equal to 10 years and 1 year.

Considering the peak accelerations [last floor: h = 87 m, see Figures 5 to 7], Figure 16 clearly shows that these accelerations values are far above the limit of 0.10 m/s^2 (time of recurrence: 10 years), proposed by NBR 6123 [23]. On the other hand, having in mind the limit of 0.075 m/s^2 (period of recurrence: 1 year), obtained according to ISO 10137 [24], in many situations this recommended limit was also surpassed. This way, it can be concluded, having in mind the investigated building with fundamental frequency of 0.25 Hz (f_{01} = 0.25 Hz), that most of the peak accelerations violate the recommended limits for human comfort assessment.
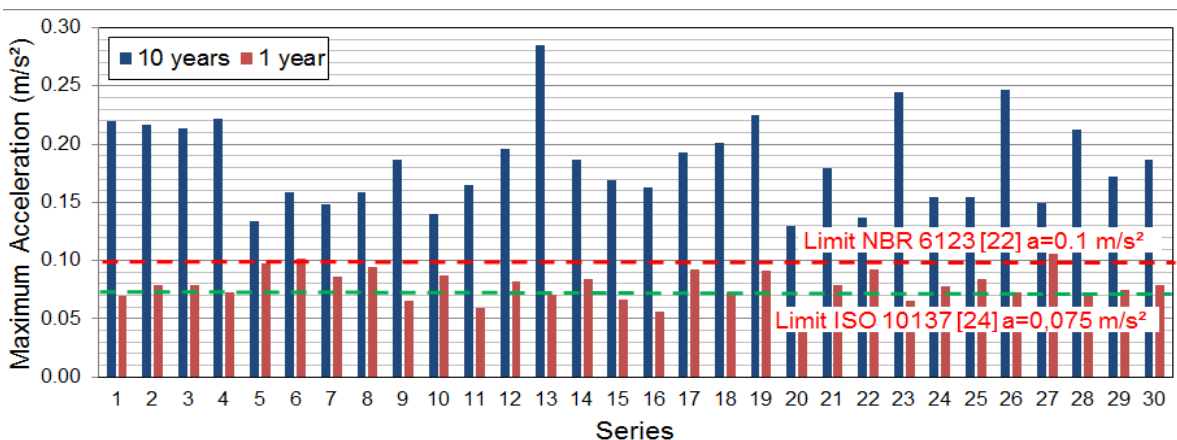
Figure 16. Maximum accelerations values obtained for each nondeterministic wind series considering a period of recurrence of 10 years and 1 year.

7 CONCLUSIONS

This investigation presents the results of a forced vibration dynamic analysis carried out based on a three-dimensional finite element model developed to represent a real and existing residential building (H=90 m), when subjected to non-deterministic wind loads. The turbulent wind velocity was calculated through the summation of a finite number of superimposed harmonics

with random phase angles and the amplitude of each harmonic was determined using a power spectral density function. The human comfort assessment of the building was performed, based on comparisons between the peak accelerations and the recommended limits proposed by the Brazilian Standard NBR 6123 [23] and also ISO 10137 Standard [24].

It can be seen that the power spectrum of the wind velocity is in good agreement with the formula proposed by Kaimal, indicating that the developed analysis methodology leads to a velocity signal close to the natural wind velocity. On the other hand, using the wind velocities of two different points on the structure it was possible to obtain the coherence between their velocities indicating a good agreement with the coherence formula proposed by Davenport.

Based on the results of the modal analysis, the value of 0.25 Hz (f_{01} = 0.25 Hz) was obtained for the fundamental frequency of the structure which, according to the Brazilian design standard NBR 6123 [23], makes the forced vibration analysis necessary.

Displacements and accelerations result values show that although the displacement values are within the limit proposed by the standard NBR 6118 [25], the peak accelerations values surpass the proposed limits of 0.10 m/s^2 (a_p = 0.25 m/s^2 > a_{lim} = 0.10 m/s^2; NBR 6123 [23]: period of recurrence of 10 years) and 0.075 m/s^2 (a_p = 0.10 m/s^2 > a_{lim} = 0.075 m/s^2; ISO 10137 [24]: period of recurrence of 1 year), emphasizing the relevance of the human comfort assessment of tall buildings.

Finally, the authors would like to emphasize the need to continue the research, based on the evaluation of the soil-structure interaction effect and also the masonry infills influence on the dynamic response of the structural model, aiming to contribute with a more realistic assessment of the dynamic structural behaviour and human comfort evaluation of tall buildings.

ACKNOWLEDGEMENTS

REFERENCES

[1] A. Barile, "Development of a methodology for nondeterministic dynamic analysis and human comfort assessment of tall buildings," (in Portuguese), M.S. thesis, Civil Eng. Postgraduate Program., State Univ. Rio de Janeiro, Rio de Janeiro, RJ, Brazil, 2019.

[2] R. Bashor, S. Bobby, T. Kijewski-Correa, and A. Kareem, "Full scale performance evaluation of tall buildings under wind," *J. Wind Eng. Ind. Aerodyn.*, vol. 104-106, pp. 88–97, May/July 2012.

[3] J. A. Ferrareto, "Human comfort in tall buildings subjected to wind-induced motion," (in Portuguese), Ph.D. dissertation, Univ. São Paulo, São Paulo, SP, Brazil, 2017.

[4] W. Jiurong, "Field measurements and numerical study of wind effects on tall buildings," Ph.D. dissertation, City Univ. Hong Kong, Hong Kong, China, 2006.

[5] V. C. Rist, "Methodology for preliminary design of high-rise buildings," M.S. thesis, Lund Univ., Lund, Sweden, 2016.

[6] M. Burton, K. C. S. Kwok, and A. Abdelrazaq, "Wind-induced motion of tall buildings: Design for occupant comfort," *Int. J. of High-Rise Blgd*. vol. 4, no. 1, pp. 1–8, Mar. 2015.

[7] T. Goto, "Studies on wind-induced motion of tall buildings based on occupants reactions," *J. Wind Eng. Ind. Aerodyn.*, vol. 13, pp. 241–252, July 1983.

[8] R. J. Hansen, J. W. Reed, and E. H. Vanmarcke, "Human response to wind-induced motion buildings," *J. Struct. Div.*, vol. 99, pp. 66–74, 1973.

[9] S. M. Lamb, K. C. S. Kwok, and D. Walton, "A longitudinal field study of the effects of wind-induced building motion on occupant wellbeing and work performance," *J. Wind Eng. Ind. Aerodyn.*, vol. 133, pp. 39–51, July 2014.

[10] S. M. Lamb, "The effect of wind-induced tall building motion on occupant comfort, wellbeing and work performance," Ph.D. dissertation, Univ. Western Sydney, Sydney, Australia, 2013.

[11] I. Fernández and V. E. Parnás, "Elements for numerical simulation of wind time series," *Rev. Ing. Constr.*, vol. 32, no. 2, pp. 85–92, Aug 2017.

[12] Z. Liu, W. Liu, and Y. Peng, "Random function based spectral representation of stationary and non-stationary stochastic processes," *Probab. Eng. Mech.*, vol. 45, pp. 115–126, July 2016.

[13] J. Chen, F. Kong, and Y. Peng, "A stochastic harmonic function representation for non-stationary stochastic processes," *Mech. Sys. Sig. Prcsg.*, vol. 96, pp. 31–44, November 2017.

[14] M. Shinozuka and C. M. Jan, "Digital simulation of random process and its application," *J. Sound Vibrat.*, vol. 25, no. 1, pp. 111–128, Apr 1972.

[15] M. Franco *Direct along-wind dynamic analysis of tall structures* (Report, BT/PEF/9303). São Paulo, SP, Brazil: University of São Paulo, 1993.

[16] M. Shinozuka *Stochastic Methods In Structural Dynamics*. Dordrecht: Springer, 1987.

[17] F. J. D. Bastos, "Aerodynamic behaviour of slender structures: gust effect analysis", M.S. thesis, Fac. Eng., Porto Univ., Porto, Portugal, 2008.

[18] E. S. Chávez, "Structural analysis of tall building submitted to floating pressures induced by wind action," (In Portuguese), M.S. thesis, Federal Univ. Minas Gerais, Belo Horizonte, MG, Brazil, 2006.

[19] B. D. Oliveira, "Wind effect as dynamic action on tall buildings," (In Portuguese), M.S. thesis, Fac. Eng. Porto Univ., Porto, Portugal, 2015.

[20] V. H. Santos, "Comparison between the Discrete Method NBR 6123 and the Synthetic Wind Method for multi-storey reinforced concrete buildings," (In Portuguese), M.S. thesis, Federal Univ. Paraná, Curitiba, PR, Brazil, 2018.

[21] F. Steffen, "Wind-induced vibrations in high-rise buildings," M.S. thesis, Lund Univ., Lund, Sweden, 2016.

[22] L.S. Bastos, "Estudo do comportamento estrutural e análise de conforto humano de edifícios de concreto armado", (In Portuguese), M.S. thesis, Civil Eng. Postgraduate Program., State Univ. Rio de Janeiro, Rio de Janeiro, RJ, Brazil, 2015.

[23] Associação Brasileira de Normas Técnicas. *NBR 6123: Forças devidas ao vento em edificações*, 1988.

[24] International Organization for Standardization, *Bases for Design of Structures – Serviceability of Buildings and Walkways Against Vibrations, ISO 10137:2007*, 2007.

[25] Associação Brasileira de Normas Técnicas. *NBR 6118: Projeto de estruturas de concreto - Procedimento*, 2014.

IBRACON Structures and Materials Journal
Revista IBRACON de Estruturas e Materiais

ORIGINAL ARTICLE

Evaluation of external sulfate attack (Na₂SO₄ and MgSO₄): Portland cement mortars containing siliceous supplementary cementitious materials

Avaliação do ataque externo por sulfato (Na₂SO₄ e MgSO₄): argamassas de cimento Portland contendo adições minerais silicosas

Diego Jesus de Souza[a]
Marcelo Henrique Farias de Medeiros[b]
Juarez Hoppe Filho[c]

[a]University of Ottawa – uOttawa, Department of Civil Engineering, Ottawa, ON, Canada
[b]Universidade Federal do Paraná – UFPR, Programa de Pós-graduação em Engenharia de Construção Civil, Curitiba, PR, Brasil
[c]Universidade Federal do Oeste da Bahia – UFOB, Centro das Ciências Exatas e das Tecnologias, Barreiras, BA, Brasil

Abstract: Sulfate attack is a term used to describe a series of chemical reactions between sulfate ions and hydrated compounds of the hardened cement paste. The present study aims to evaluate the physical (linear expansion, flexural and compressive strength) and mineralogical properties (X-ray diffraction) of three different mortar compositions (Portland Cement CPV-ARI containing silica fume and rice husk ash, in both cases with 10% replacement of the cement by weight) against sodium and magnesium sulfate attack (concentration of SO_4^{2-} equal to 0.7 molar). The data collected indicate that the replacing the cement by the two siliceous supplementary cementitious materials (SCMs) generate similar results, both SCMs were able to mitigate the effects of the sodium sulfate attack in both physical and chemical characteristics, however, both materials increase the deterioration (i.e. compressive strength) when exposed to $MgSO_4$ solution.

Keywords: durability, sulfate attack, sodium sulfate, magnesium sulfate.

Resumo: Ataque por sulfato é um termo utilizado para descrever uma série de reações químicas que ocorrem entre os íons de sulfato com os produtos da hidratação do cimento Portland. O presente estudo tem por objetivo avaliar de maneira física (expansão linear, resistência à compressão e tração na flexão) e mineralógica (DRX), três diferentes composições de argamassa, alterando a composição dos finos (CPV – ARI, CPV – ARI com substituição parcial do cimento por 10%, em massa, de sílica ativa, e, CPV – ARI com substituição parcial por sílica de casca de arroz) frente ao ataque por sulfato de sódio, bem como, por sulfato de magnésio (concentração da solução de 0.7 molar). Os resultados obtidos indicam que a substituição parcial do cimento Portland pelas duas diferentes adições, geraram, resultados similares, ambas as adições foram capazes de mitigas os efeitos causados pelo ataque por sulfato de sódio, todavia, frente ao ataque por sulfato de magnésio, ambas as adições apresentaram uma maior degradação quando em comparação com as séries de referência.

Palavras-chave: durabilidade do concreto, ataque por sulfato, sulfato de sódio, sulfato de magnésio.

1 INTRODUCTION

The deterioration of concrete due to sulfate attack is a complex process that has been widely investigated over several decades. Various damage mechanisms including expansion, cracking, spalling, and loss of strength can manifest in concrete exposed sulfate attack. Sulfate attack is a term used to describe a series of chemical reactions between sulfate ions and hydrated compounds of the hardened cement paste [1], [2]. The complex set

of reactions occurs between sulfate ions SO_4^{2-} (coming from the external environment or released by the cement paste after high heating) and the hydrated Portland cement products, such as portlandite $[Ca(OH)_2]$, calcium monosulphoaluminate hydrate (AFm) present in the cement paste [1], [3], [4]. The interaction between SO_4^{2-} ions and hydrated Portland cement products, such as calcium hydroxide, to form gypsum; and, with aluminates, to form ettringite, which can increase the volume in about 1.2 to 2.2 times more than the initial products. Moreover, causing internal stresses in the bulk cement paste, which can form crack resulting in distress of the hydrated cement matrix [2], [5], [6].

An important aspect in studies related to external sulfate attack (ESA) is regarding to the associated cation to SO_4^{2-} (i. e., Na^+, K^+, Mg^{2+}, Ca^{2+}, etc.) since the physical and chemical behaviour of the matter depends on the way in which the atoms interact, all the components in pores solution should be considered in the reaction, some of them can act as a catalyst or actively on the damage [3]–[6]. Several studies indicate that $MgSO_4$ solutions are more aggressive than Na_2SO_4 at the same concentration level [1], [3], [4], [7]–[12]. In sodium sulfate solution the main reaction is between SO_4^{2-} ions and $Ca(OH)_2$, forming gypsum, and then between gypsum and calcium monosulfoaluminate hydrate (AFm) to form secondary ettringite [3], [4], [8], [13], [14]. Magnesium sulfate solutions, besides the formation of gypsum and ettringite, also develop brucite $[Mg(OH)_2]$ (from the reaction between Mg^{2+} and Portlandite) and Magnesium Silicate Hydrate (MSH) due to the decalcification of the C-S-H. MSH has negligible binding capacity and no cementitious properties [9], [12], [15].

The technical importance binder composition with supplementary cementitious materials (SCMs) derives mainly from three aspects: first, the reaction is slow, therefore, the release of heat due to the hydration reactions is also slow. Second, the reactions caused by these materials consume calcium hydroxide, rather than producing them, contributing to the paste resistance to aggressive sulfate solutions. Third, the interaction between amorphous silica, portlandite and water present in the concrete pores leads to the formation of C-S-H [16]–[18].

Siliceous pozzolans, such as Silica Fume (SF) and Rice Husk Ash (RHA), etc. consists nearly exclusively of SiO_2 of fine particle size and a relatively high pozzolanic activity. These materials, especially SF, are widely used to improve the compressive strength, abrasion resistance and durability of concrete [17], [19]–[21]. Besides of these advantages, SF presents some disadvantages, such as cost, may largely increase the drying shrinkage (by self-desiccation and also autogenous shrinkage) and cracking if curing conditions are improper [17], [21]. Although SF improves the rheology of concrete, the high specific surface area of its particles results in an increased water demand. RHA has a similar behaviour in concrete, when compared with SF, according to the literature [22]–[24]. However, RHA can show higher specific surface area due to multilatered, angular, microporous surface and honeycombed structure [25]. However, depending of the amount of carbon on composition of RHA, some particle are able to present some hydrophilic behaviour leading to lack of available water for cement hydration reaction increasing rheological properties of the concrete [25].

As chemical effect on cement hydration, blending of PC higher than 20 wt.% siliceous pozzolans can resulted after longer hydration times in the entire consumption of portlandite with ettringite and C–S–H with a reduced Ca/Si ratio as the only hydrate phase observed [26], [27]. In other words, the use of these materials as cement replacement are beneficial to reduce the sulfate attack [28], [29]. SF as part of the composition of the binder have shown very good results regarding sodium sulfate attack, SF can reduces the penetration rate of sulfate ions, as well as decrease the formation of gypsum and ettringite [30]–[33], however, when exposed to magnesium sulfate solutions the decalcification of C-S-H are more intense, resulting in a loss in strength also higher [11], [29]. This behaviour became even worse when the amount of SF is higher in the composition of the binder, showing losses in strength up to 50% [28].

Some studies [9], [34], [35] have evaluated the resistance to sulfate attack of mortar bars containing the rice husk ash, and, as SF, the durability of the mortars exposed to the Na_2SO_4 solutions was increased, reducing the expansion to very low levels and also, reducing the loss on compressive strength. Which means that RHA has high durability against sodium sulfate attack. For exposure to the $MgSO_4$ solution, RHA also had positive effects on expansion, however, evaluating strength loss, RHA was harmful as the replacement content increased.

The present paper is the third part of a research project to evaluate the sulfate attack on the physical-chemical properties of Portland cement composites, developed at the Federal University of Paraná (Figure 1). Part one and two can be seen in Souza et al. [36] and [37].
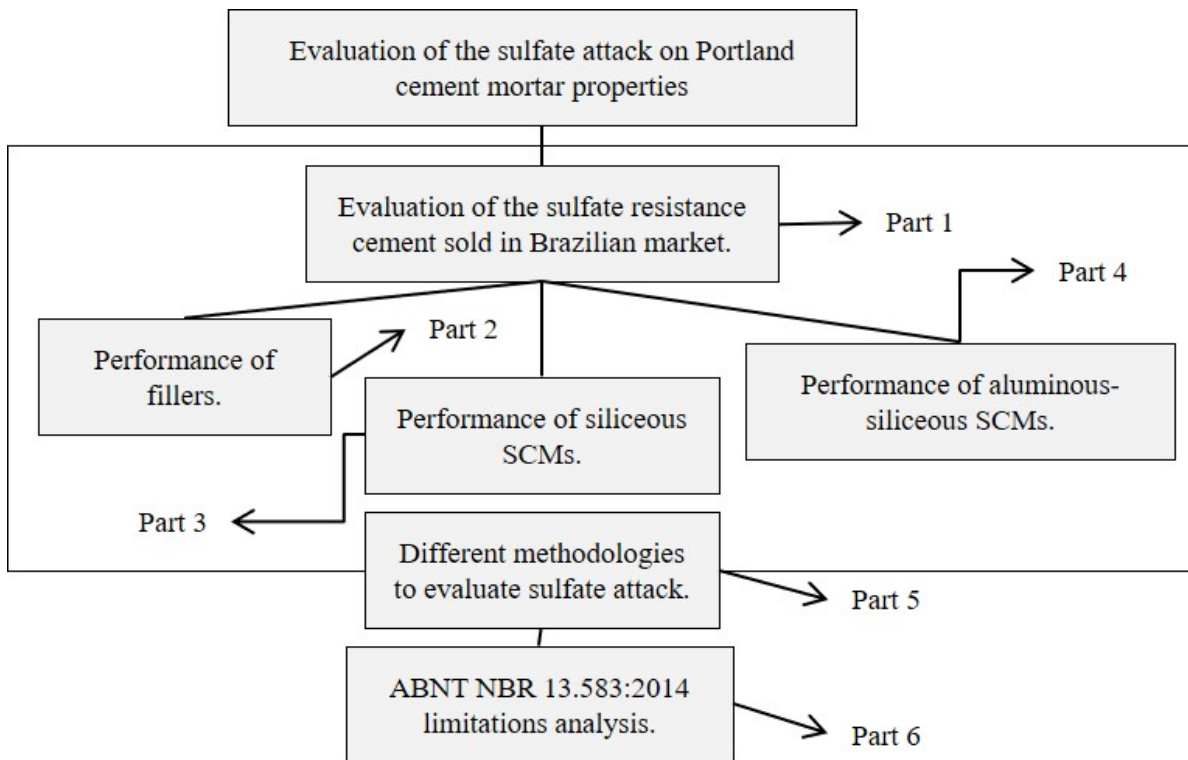
Figure 1: Division of the research project to evaluate sulfate attack on the properties of Portland cement mortars.

2 RESEARCH SIGNIFICANCE

The use of different types of siliceous SCMs with different chemical compositions could also produce different concrete behaviours when exposed to different sulfate salts, affecting cement paste properties differently, which require different remedial actions and mix design depending on the exposure conditions. The present study aims to evaluate the performance of physical and mineralogical properties of three different mortar compositions (PC, with silica fume and rice husk ash) exposed to sodium and magnesium sulfate attack. The approach of the problem will involve the manipulation of two independent variables, the type of binder material used and the aggressive solution of exposure of the mortars.

3 MATERIALS AND METHODS

In order to detect the influence of the cement type on sulfate attack damage degree, the present research has as a main concern, the evaluation of the interference of the sulfate ions in the physical properties intrinsic to the proposed objective.

3.1 Materials

Portland cement with high early age strength CPV - ARI (PC) was used as a control group and replaced partially (10% by weight) by the silica fume and rice husk ash.

The PC alone has no influence of any supplementary cementitious materials (SCM) or even addition of fillers (just clinker + gypsum) on the reference system to be evaluated; however, should be mentioned that the PC has just a small amount of carbonaceous material as allowed by Brazilian's standards (maximum of 10%, according to ABNT NBR 16697 [38]). The Portland cement was characterized by performing loss on ignition; specific gravity and BET tests. Chemical analyses were also performed, using X-ray Fluorescence; and, particle size distribution was measured using laser diffraction in a measurement range of 0.04-500 μm. Table 1 shows the chemical, mineralogical and physical composition of the PC according to the results obtained from the X-ray fluorescence and the physical characteristics of the cement.

Table 1: Chemical composition of the cement

Chemical Composition (%)		Clinker Composition (%)	
CaO	60.97	C_3S	52.00
SiO_2	18.77	C_2S	14.60
Al_2O_3	4.36	C_3A	6.60
Fe_2O_3	2.93	C_4AF	8.91
MgO	3.50	Gypsum	6.71
SO_3	3.12	$CaCO_3$	4.9
Na_2O_{eq}	0.68	Physical Properties	
Free Lime	0.90	BET (m^2/kg)	1,070
Insoluble Res.	0.77	Specific Gravity	3.13
Loss on Ignition	3.55		

In this study, two different types of siliceous SCMs were selected, silica fume (SF) and rice husk ash (RHA). Both materials were characterized for loss on ignition, specific gravity, BET and particle size distribution. The mineralogical properties of the SCMs were also characterized using XRD tests. The analysis was performed from 5º to 75º 2θ, with an angular pitch of 0.02º 2θ and time per step of 1 second. It was used copper anode tube, 40 kV / 30 mA and divergent slit of 1º. Minerals were identified by comparison with the standards of the International Centre for Diffraction Data, ICDD. Finally, the chemical characterization of the samples was performed using X-Ray Fluorescence (XRF) method.

The fine aggregate used for the design of the mortar bars was natural quartz sand with SiO_2 content of 96% and free of contaminants, which means that it is negligible the chemical influence of this material on final results. Finally, the fine aggregate was sieved, and the particle size distribution was fixed as 25% of the total mass of sand between each of the following ranges 0.15-0.30 mm, 0.30-0.60 mm, 0.6-1.2 mm and 1.2-2.4 mm.

3.2 Methods to evaluate sulfate attack

In this section will present the procedures used to evaluate the sulfate attack in different prismatic mortars bars, such as preparing procedure of the samples; solutions; conditions of exposure; length variation test and compressive strength test.

a) Preparing of the sample for mortar bar tests

The degree of sulfate attack on mortars was analyzed in general by two main groups samples:

- Group 1: composed of 36 specimens measuring 25 mm x 25 mm x 285 mm (to evaluate induced expansion), divided into 3 different mix-designs (PC, PC + SF and PC + RHA) and 3 final exposure solutions: Control (water + calcium hydroxide), Na_2SO_4 and $MgSO_4$ solutions;
- Group 2: composed of 108 specimens with dimensions of 40 mm x 40 mm x 160 mm (to evaluate compressive and flexural tensile strength) and divided into 3 compositions and 3 final exposure solutions.

The mortars bars were designed based on Brazilian standard ABNT NBR 13.583/2014 with binder-to-sand ratio of 1.0/3.2, by mass, and water to binder ratio of 0.60 [39]. After casting and moulding, all bars were subject to 48 h in the mold in moist cabinet, later the samples were cured for 12 days in lime water at 23±2 ºC before, finally, immersed in sulfate solutions at 40 ºC, in accordance with ABNT NBR 13.853/2014, for a period of 140 days [40].

b) Exposure solutions

The concentration of anhydrous sodium sulfate, in accordance with ABNT NBR 13.853/2014, was 100g of Na_2SO_4/L of solution (0.704 mol/L); which means that the concentration of SO_4^{2-} (also 0.704 mol/L) can be defined as 67,630 ppm (67.63 g/L). Fixing the total amount of sulfate ions, the magnesium sulfate solution was prepared as 0.704 mol/L as well, (84.74g of $MgSO_4$/L of solution). Finally, the solution volume-to-samples volume ratio was fixed as 4.0/1.0 [13], [14], [36], [41], along the whole exposure period.

c) Length variation

The evaluation of the induced expansion followed NBR 13.583/2014, after the first and second curing procedures (48 h and 12 days, respectively), the samples had their initial lengths measured just before the exposure to the final solutions.

The measurements were performed after 2, 4, 6, 8, 10, 15 and 20 weeks of exposure. For this purpose, the samples were placed at the micrometre, always with the same face upwards, and the measurements were taken always referring to the smaller length indication identified by the apparatus after 360° rotation of the bar. The individual expansion or shrinkage of the samples are given by the difference between the value measured at the corresponding exposure time and the initial reading minus the difference of the same group of samples exposed to the lime-water solution, divided by its initial length and multiplied by 100.

d) Compressive and flexural tensile strength.

The tests of flexural tensile and compression strength were made at times of exposure of 0; 2; 6; 10; and, 20 weeks. ABNT NBR 13.279 recommendations were followed, and the tests were carried out in an equipment with a load capacity of 100 kN, and the tensile strength tests were performed in the bars before the compression.

For the flexural tensile strength test the load application rate was 50 ± 10 N/sec until failure, thus, the strength was calculated according to ABNT NBR 13.279 [42].

In compressive strength test, 6 specimens were obtained after tensile tests of 3 samples and the load application rate was 505 ± 5 N/sec until failure, thus, the strength was calculated.

4 RESULTS AND DISCUSSIONS

4.1 Physical and chemical characterization of the silica fume and rice husk ash

Table 2 reports the chemical compositions measured by XRF and the results of BET specific surface area, LOI and the specific gravity of the mineral additions.

Table 2. Chemical and physical properties of the Silica Fume and Rice Husk Ash

	Silica Fume	Rice Husk Ash
CaO	0.19	0.43
SiO_2	92.35	88.47
Al_2O_3	2.21	2.72
Fe_2O_3	0.05	0.05
MgO	-	-
SO_3	1.52	1.55
K_2O	0.94	1.46
Insoluble Residue	0.04	0.49
Loss on Ignition	2.7	4.84
BET (m^2/g)	20.24	14.69
Specific Gravity	2.18	2.12

Both SCMs have higher surface specific area and lower specific gravity than PC, the surface specific area of the SF is 18.9 times higher than the cement and the RHA, 13.7 times. In general, the SF and RHA have very similar chemical composition, the major differences between the SCMs are the total amount of SiO_2, 4% bigger in the SF samples, for the RHA the content of K_2O and Loss on Ignition (LOI) are higher in comparison with SF. Both values can be explained by the fabrication processes of the rice and RHA, the soil treatment to enhance quality and rice production can it be the major indicator that increases the potassium content. On the other hand, the burning process during RHA fabrication can induce to high contamination of carbon in the RHA. An example of that is the differences in the coloration of the sample before and after the LOI test, correlated to the loss of CO_2, as indicated in Figure 2.
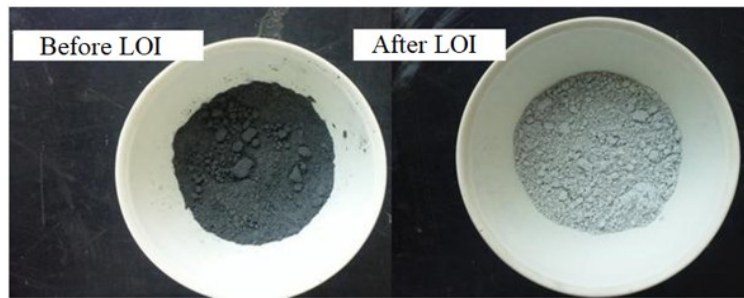
Figure 2: RHA samples before and after loss on ignition test

The XRD patterns of the SF and RHA, respectively, are shown in Figure 3. As indicated, silica fume has distinguishing amorphous halo, characteristic of its high pozzolanic reactivity, with almost any crystallinity. Moreover, RHA also presented partial amorphous minerals, the patterns resulting from the X-ray diffraction indicates crystallinity of its predominant phase, cristobalite. The distinguished molecular amorphous arrangement of the SF, indicating almost any crystallinity, in summation with the considerably higher specific surface area and lower particle size distribution (Figure 4) than the RHA, suggest that this material also present higher pozzolanic reactivity [13], [14], [36], [43].
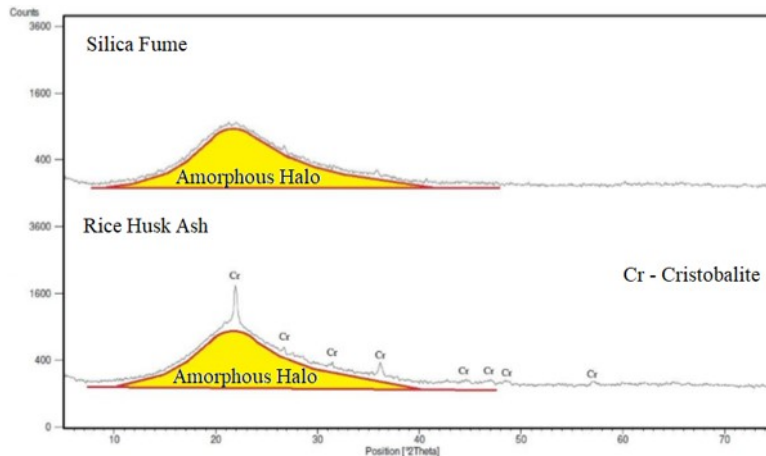
Figure 3: X-ray diffractograms of the silica fume and rice husk ash.
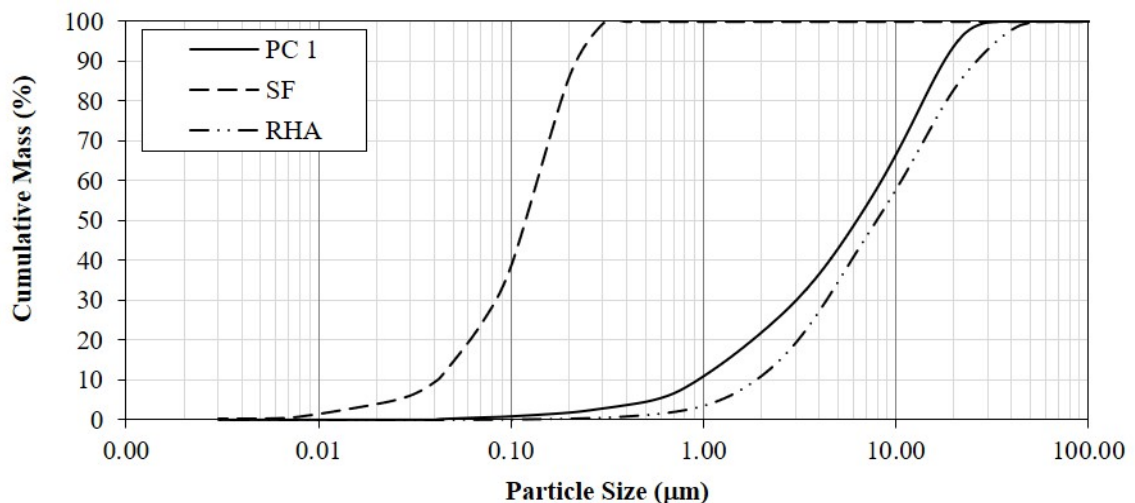
Figure 4: Particle size distribution of the CPV - ARI, silica fume and rice husk ash

In Figure 4, the particle size distributions of the cement and the SCMs are presented. The RHA has D50 equal to 8 μm, higher than the cement average, around 6 μm. However, SF showed an average particle size of 0.12 μm (52 times smaller than Portland cement). Indicating that the SF can also influence, significantly, the nucleation and hydration of the cement particles, changing the hydration kinetics of the cement [44]–[46].

4.2 Length variation analysis

The results of the analysis of length variation of the samples over the 20 weeks of exposure (140 days) in both aggressive solutions are presented in Figure 5.
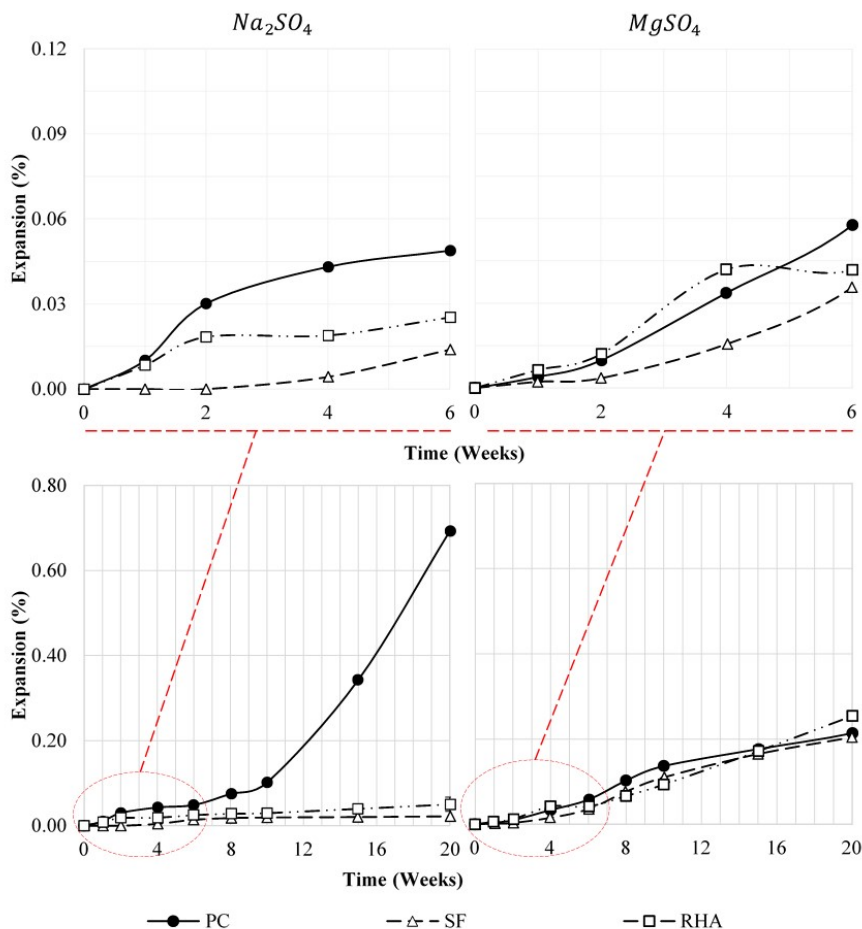
Figure 5: Expansion of the mortar bars ARI, SF and RHA exposed to solutions of Na_2SO_4 and $MgSO_4$ (0.7 mol/L) for 42 and 140 days (6 and 20 weeks).

It should be noted that NBR 13.583 does not specify a value to which a composition can be considered resistant or not to sulfate attack since it is only a comparative analysis. However, according to Marciano [47], compositions with expansion equal to or less than 0.030% at the 42 days of exposure (6 weeks) may be considered resistant to sodium sulfate. However, considering that SO_4^{2-} content in solution was kept constant at 0.704 M, it was observed that all groups of samples had expansion higher than 0.03% when exposed to $MgSO_4$, on the other hand, at sodium sulfate solution both siliceous SCMs had induced expansion lower than the maximum determined by Marciano [47], leading to conclude that, at least for short periods of exposure, both supplementary cementitious materials are the best options for both Na_2SO_4 and $MgSO_4$ exposure.

The comparative analysis between the averages results, Tukey's test, for 6 weeks of exposure, can be seen in Figure 6. Due to the exposure to $MgSO_4$ at the 42nd day, all samples can be considered as statically equal, independent

of the composition of the binder material, the behaviour of the sample were similar, regarding the induced expansion. Therefore, the decision-making should be based on the economic and non-technical benefits for these cases (when the analysis is based on NBR 13.583, at 42 days of exposure). On the other hand, when soaked in Na_2SO_4 solution, both SCMs mitigated, significantly, the sulfate attack, in about 48% for SF and 80% for RHA in comparison with CPV – ARI samples. As above mentioned, the expansion of mortars bars exposed to magnesium sulfate was more intense until the 42nd day. This behaviour is associated with the higher solubility of $MgSO_4$ when compared to Na_2SO_4, which results in a higher sulfate ions content in the solution.

Along the 140 days of exposure, the excessive formation of brucite and gypsum, the pH of the mortar pores solution begins to decrease, since such materials have much lower solubility than the portlandite, therefore, releasing less OH^-. Consequently, the pH of the solution tends to decrease until levels where it can destabilize the C - S - H, which starts to release calcium ions to elevate pH. However, besides this process, the decalcification of hydrated calcium silicate, forming M - S - H that does not have any binder capacity. Moreover, the release of calcium ions by the C-S-H can react with the sulfate ions and precipitate as gypsum, decreasing more the pH and increasing the damage in the mortar bars. The groups of mortar SF and RHA with lower portlandite contents due to its highly pozzolanic reactivity [13] initially also presented gel formation on the surface of the samples, however, with a noticeably smaller amount, but, during 140 days of exposure, the formation of the gel was almost interrupted. Then, it was noted the occurrence of dissolution of the surface layers of the samples in the solution (Figure 7a and b).

The excessive formation of gel observed on the surface of the CPV – ARI samples exposed to $MgSO_4$ (Figure 7c). According to the literature [3], [8], [11], [28], [48], [49], is the first product of the interaction between magnesium sulfate and Portland cement hydration products is brucite (magnesium hydroxide), in which the electron affinity of the magnesium ion replaces the calcium ions in the portlandite particles. According to the authors, such material is presented as a gel filling the voids of the mortar and it can precipitate on the surface along with the gypsum and compositions of hydrated magnesium sulfate. Therefore, such visual indication of the interaction between the cementitious material and the aggressive solution could indicate higher expansion of the bars, but this did not occur. Such gel formation has an influence on delaying the expansion process, since it decreases the diffusivity of sulfate ions in the mortar samples. To analyze such statement, for the present study, pH measurements were carried out along the analyzed periods of exposure, and Figure 8 presents the comparative pH along the evaluation between three studied solutions (i.e. control, sodium sulfate and magnesium sulfate).

On the other hand, both highly reactive pozzolans presented, in general, considerably resistance to linear expansion due to the sodium sulfate attack at 140 days of exposure, being considered statistically equivalent as seen in Figure 9. Both SCMs obtained, on average, 94% less expansion than CPV – ARI. Therefore, it is evaluated that the morphological characteristics as the fineness of the particles, besides, of course, its amorphous structure, contributed to the good performance, favoring the packing of particles and the consumption of more portlandite, which favors the formation of new CSH particles. Likewise, making available less $Ca(OH)_2$ to react with SO_4^{2-} ions, in which, as above mentioned, enhance the surface deterioration of the samples due to the exposure to $MgSO_4$.
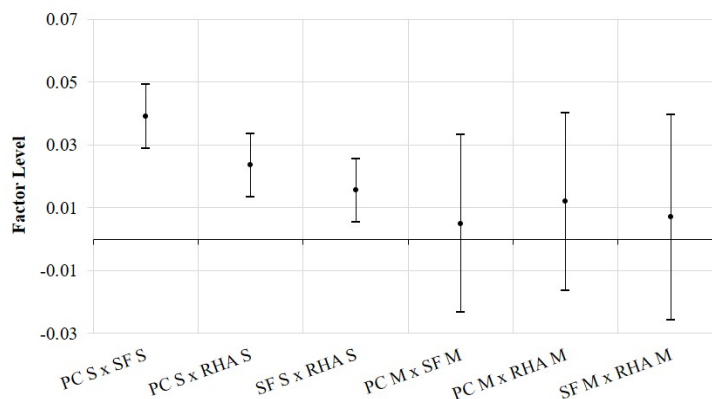
Figure 6: Comparative analysis of the averages, Tukey's test, for 6 weeks of exposure among the series studied, for a significance level of 5% (S-sodium sulfate and M-Magnesium sulfate).
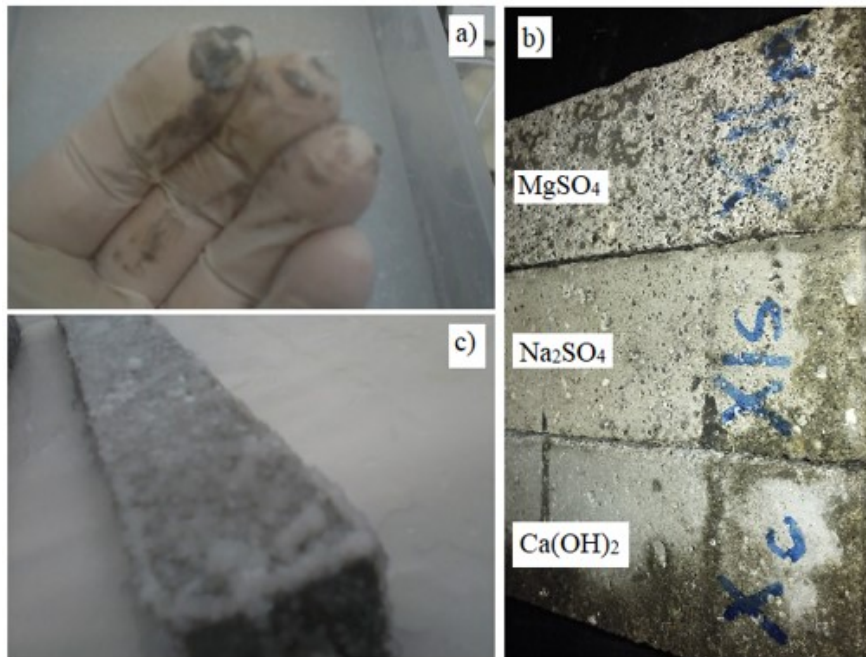
Figure 7: Samples of mortar bars after 140 days of exposures to sulfate solutions, a) indication of the disaggregated material from the SF and RHA samples due to the exposure to MgSO$_4$, b) surface degradation of the SF mortars due to MgSO$_4$ and c) indication of the surface gel formed due to MgSO$_4$.
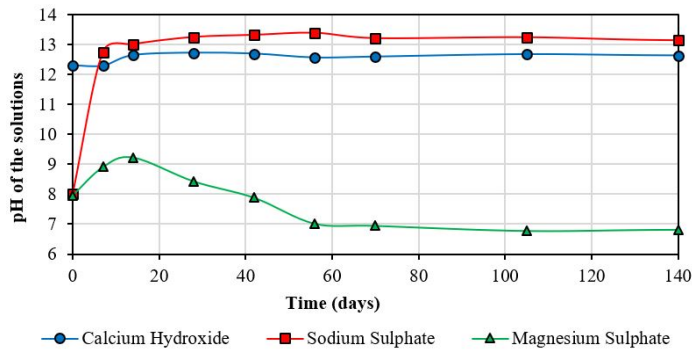
Figure 8: Comparative pH analysis of Ca(OH)$_2$, Na$_2$SO$_4$ and MgSO$_4$ solutions over 20 weeks (140 days).
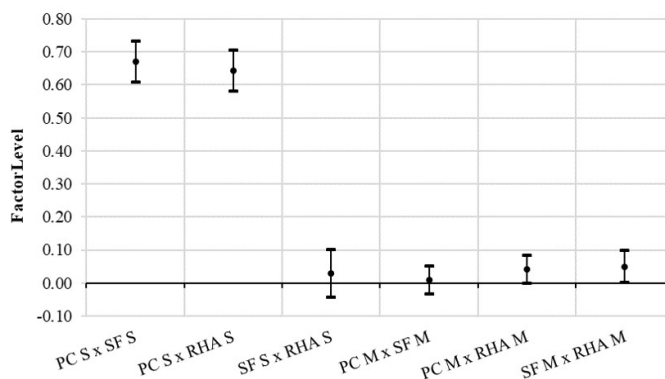
Figure 9: Comparative analysis of the averages, Tukey's test, for 20 weeks of exposure among the series studied, for a significance level of 5% (S-sodium sulfate and M-Magnesium sulfate).

4.3 Mineralogical analysis

The obtained diffractograms for all series for each exposure conditions can be seen in Figure 10, Figure 11 and Figure 12. Compared to calcium hydroxide exposure solution, it can be observed that PC, SF, and RHA presented a higher intensity the peaks related to ettringite crystals (E) for exposure in both sulfate solutions, as well as consumption of the portlandite.
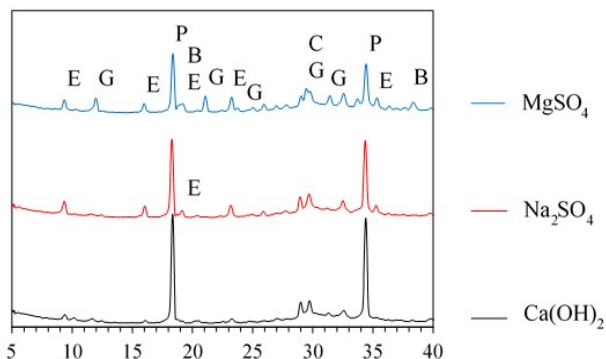
Figure 10: CPV-ARI diffractograms after 20 weeks of exposure to $Ca(OH)_2$, Na_2SO_4 and $MgSO_4$. Monocarboluminate (A), brucite (B), calcite (C), ettringite (E), gypsum (G) and portlandite (P).
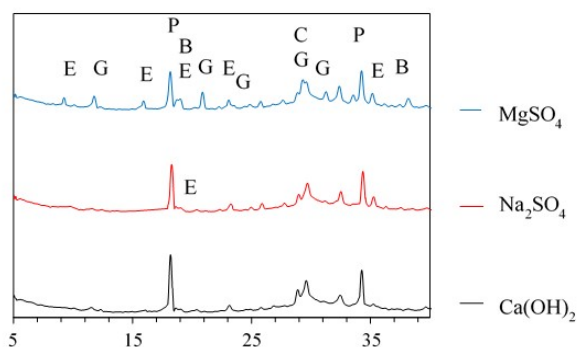
Figure 11: SF diffractograms after 20 weeks of exposure to $Ca(OH)_2$, Na_2SO_4 and $MgSO_4$. Monocarboluminate (A), brucite (B), calcite (C), ettringite (E), gypsum (G) and portlandite (P).
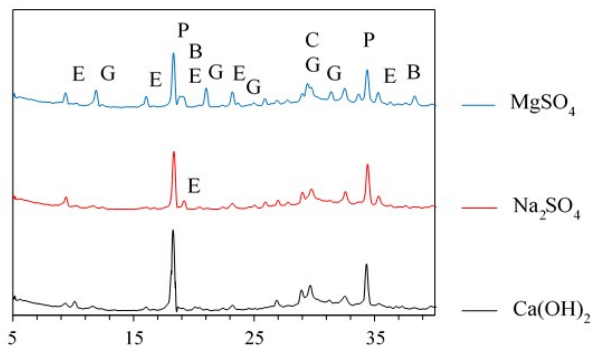
Figure 12: RHA diffractograms after 20 weeks of exposure to $Ca(OH)_2$, Na_2SO_4 and $MgSO_4$. Monocarboluminate (A), brucite (B), calcite (C), ettringite (E), gypsum (G) and portlandite (P).

SF and RHA mortar samples have their mineralogical composition relatively close to each other, both are highly siliceous materials and with low aluminate contents, in about 2% of the mass. Then, their behaviour under sulfate attack are similar in both aggressive solutions. For calcium hydroxide exposure solution, RHA present on its XRD patterns, small peaks related to the formation of ettringite, indicating the presence of the remaining primary ettringite.

For the exposure to the magnesium sulfate solution, SF and RHA groups presented similar counts than the CPV-ARI for ettringite formation at 9.14° 2θ, and, at the same time, slightly higher peaks of gypsum (peak at 12.00° 2θ), indicating that the alkaline reserve consumption in the pozzolanic reaction may have contributed with the decalcification of the C-S-H particles, producing more M-S-H (not possible to identify with XRD), releasing calcium to react with SO_4^{2-} ions to form gypsum. Moreover, as observed in the exposure to the calcium hydroxide solution, the group with the SCMs showed significant consumption of portlandite, indicating the occurrence of an intense pozzolanic activity, specially considering the replacement of the cement by 10% by mass.

4.4 Mechanical properties

The compressive and tensile strength are essential parameter to be considered regarding the degree of sulfate attack [11], [50], as well as the flexural strength which gives important data regarding the microcrack propagation within the cement paste [51], [52]. Is common in the literature that samples exposed to the sodium sulfate solutions have their strength increased at an initial exposure time and then, for a long time of exposure, there are strength loss (Figure 13 and Figure 14). The statistical analysis of the obtained data can be seen in Figure 15 and Figure 16.

In general, the influence of the aggressive solutions increases the flexural in the samples. It is also seen that both aggressive solutions showed similar behavior in the samples according, for example, to the results obtained by Huang et al. [53]. Supplementary cementitious materials, in general, can reduce the porosity of the cementitious matrix and the interfacial transition zone (ITZ). This fact leads to an improvement in both compressive and tensile strengths, with the last being on smaller scale until there is an increase in the cement hydration products present in the ITZ. Moreover, while there are high levels of portlandite in this region, the tensile strength will remain unchanged. Thus, the addition of the SCMs can cause a significant increase of the strength since there is formation of more C-S-H particles in this region, then, the interference of the ITZ in the strength of the mortar starts to decrease.

It can be seen in Figure 13 and Figure 14 that the samples exposed to the calcium hydroxide solution, in general, increase the strength (flexural or compressive) as a function of time, even though showing some variations in 6 and 10 weeks. Moreover, it is assumed that the bars did not developed cracks at the evaluation period, as expected since the mortars remained in ideal conditions of curing. On the other hand, when subjected to sulfate solutions, CPV – ARI, for example, show even higher increase in strength over time, until certain point at which micro-cracking begins, then the losses in strength starts. CPV-ARI showed earlier degradation due to the exposure to sodium sulfate solution and slower damaging processes when exposed to magnesium sulfate attack. Indicating, in this case, that Na_2SO_4 was more aggressive to this composition. However, SF and RHA samples presented opposite behavior when than CPV-ARI samples. In other words, SF and RHA delayed the micro-crack starting point for exposure to sodium sulfate but accelerated the degradation when exposed to magnesium sulfate, at least for measurement of compressive strength.

As well known, the tensile strength is more sensitive to any crack formation in the concrete, mortars, etc, different authors [6], [54], [55] stated that, does not matter the mechanism of deterioration of the concrete, if there is crack formation there is reduction in the capacity of the concrete on tensile stresses. However, considering the expansion levels and the flexural strength results seems that the groups of samples containing SF and RHA did not developed crack, at least, during the period of evaluation. Yet, the compressive strength results indicate significant losses for both composition when exposed to $MgSO_4$.

The Ca/Si ratio of the samples varied due to the replacement of the cement by the highly siliceous SCMs. According to Tikalsky et al. [56], Bellmann and Stark [57] and Lothenbach et al. [19], the decrease in this ratio implies in a reduction in the amount of portlandite after hydration, therefore, the composition can be more resistant to sodium sulfate attack. On the other hand, for magnesium sulfate attack, such reduction results in a composition more susceptible to the damage [3], [8]. Thus, for both cases, what was seen was, precisely, a behavior of the samples according to information obtained in the literature.

In general, it is observed during the 20 weeks of exposure that the individual behavior of each series distinguishes between both aggressive solutions, indicating, once again, that the cations associated with the sulfate ions also influence the degree of the attack. For example, the SF and RHA groups presented at 20 weeks just a little variation in strength when exposed to Na_2SO_4 and can be considered as highly resistant to attack by this type of sulfate. However, the same series when exposed to $MgSO_4$ showed high losses in compressive strength, about 8.6% for RHA and 9.8% for SF, corresponding to losses of 5.4 MPa and 5.9 MPa, respectively. This loss of compressive strength is associated with the decomposition of C-S-H particles, and, consequently, formation of M-S-H, which have little or no binder capacity.
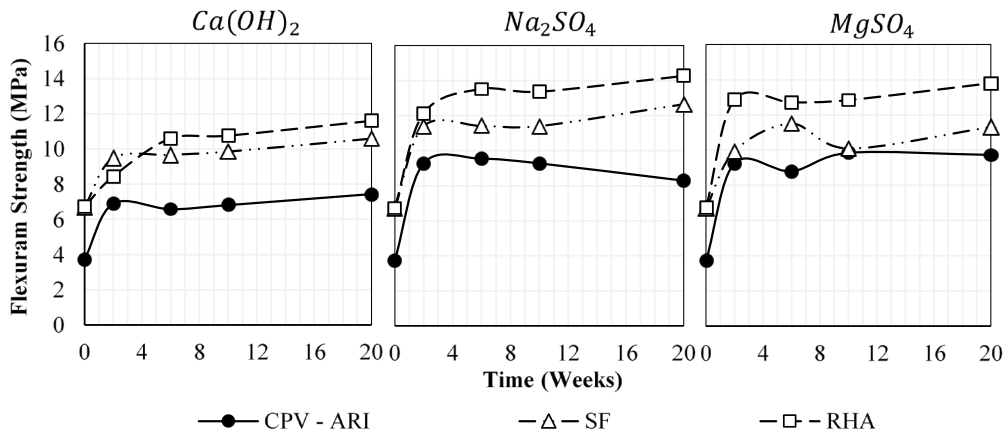
Figure 13: Flexural Tensile strength of the samples up to 20 weeks of exposure in the three different solutions [Ca(OH)₂, Na₂SO₄ e MgSO₄].
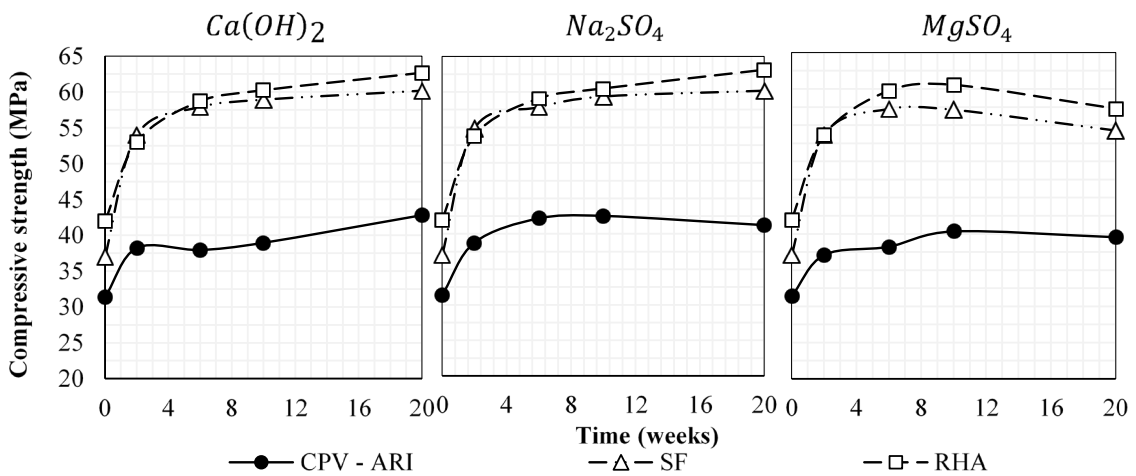
Figure 14: Compressive strength of the samples up to 20 weeks of exposure in the three different solutions [Ca(OH)₂, Na₂SO₄ e MgSO₄].
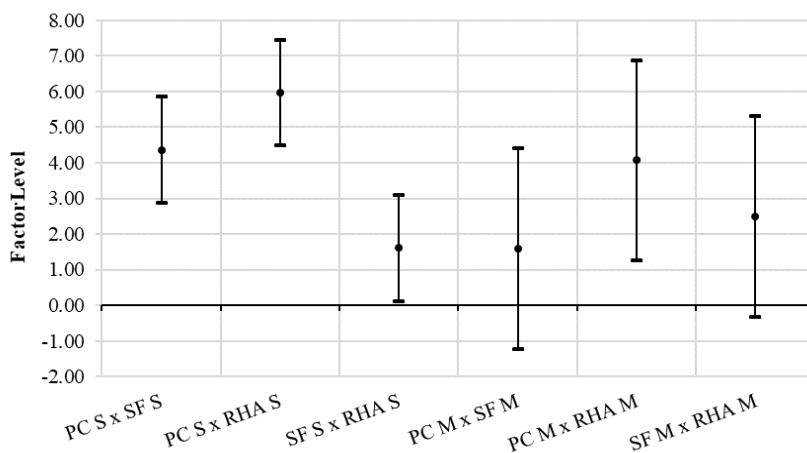
Figure 15: Comparison between averages of Flexural strength losses (Tukey test for a significance level of 5%) of the same series for different aggressive solutions (S - sodium sulfate and M - magnesium sulfate) for 20 weeks of exposure.
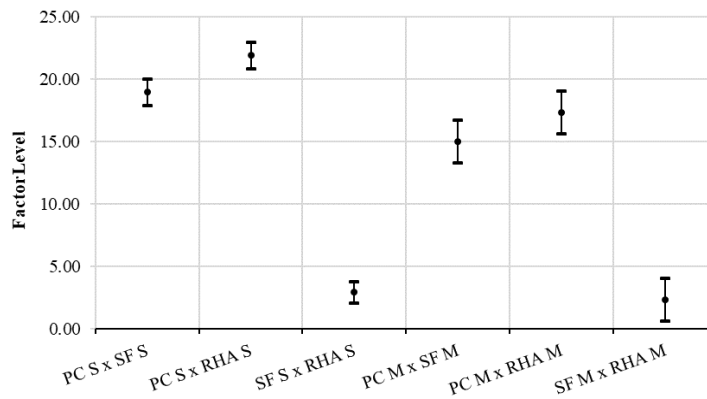
Figure 16: Comparison between averages of compressive strength losses (Tukey test for a significance level of 5%) of the same series for different aggressive solutions (S - sodium sulfate and M - magnesium sulfate) for 20 weeks of exposure.

Likewise, these results are reliable with the theory and experiments analyzed in the literature, such as those of Santhanam et al. [8], Diab et al. [11], that is, the loss in compressive strength is much more significant than the actual expansion of the samples containing higher amount of reactive SiO_2 when exposed to magnesium sulfate attack. These results bring important information regarding the degradation of the sulfate attack, especially when it makes a parallel with real concrete structures since these are always projected based on compressive strength. At the same time, such degradation was not observed for linear dimensional expansion, so it was confirmed that "quantify" sulfate attack only using one-dimensional behavior can lead to errors in decision-making to define the materials to be used at the field.

5 CONCLUSIONS

Based on the results of this experimental investigation under tidal environment, the following conclusions are drawn:

- The partial replacement (10% by mass) of the cement by supplementary cementing materials in the mortars mitigated significantly the induced expansion due to sodium sulfate attack. The exposure to magnesium sulfate solution did not show the same behaviour, the use of SF and RHA were statistically similar to the control group;
- When exposed to sodium sulfate attack, the pH increased along time and has an influence on the test results (i.e. length variation and mechanical analysis), since higher pH maintains the stability of CSH and Ettringite particles. For $MgSO_4$ the pH decreases to values close to 7, affecting the stability of the CSH, reducing, significantly the compressive strength of the SF and RHA;
- Comparing the expansion caused by both sulfate solutions, at short (i.e. 6 weeks as per NBR 13,583) and long-term (i.e. 20 weeks) exposure conditions, $MgSO_4$ developed higher expansion levels than sodium sulfate attack for both mortars made of PC plus SCMs. Yet, for the control group made only by PC, the long-term exposure to Na_2SO_4 lead to a much higher induced-expansion than $MgSO_4$;
- Sulfate attack tests with long exposure period, such as 20 weeks or more, are important to better understand and characterize degradation processes of Portland cement composites due to different types of sulfate (sodium sulfate attack, magnesium sulfate attack, etc.);
- Finally, it was clear from the obtained results the importance of knowing, precisely the type of sulfate to which the cementitious material will be exposed. In other words, groups of samples considerable resist to Na_2SO_4 had higher damage when exposed to $MgSO_4$. This reinforces, once again, that the approach to classify the capacity of each binder composition if is resistant of not to sulfate attack is always dependent of the different types of sulfate solutions present in the environment.

REFERENCES

[1]   N. M. Al-Akhras, "Durability of metakaolin concrete to sulfate attack," *Cement Concr. Res.*, vol. 36, no. 9, pp. 1727–1734, 2006, http://dx.doi.org/10.1016/j.cemconres.2006.03.026.

[2]   P. K. Mehta and P. J. M. Monteiro, *Concrete: Microstructure, Properties, and Materials*, 3rd ed. New York, NY, USA: McGraw-Hill, 2013.

[3]   M. Santhanam, M. D. Cohen, and J. Olek, "Mechanism of sulfate attack: a fresh look. Part 2: proposed mechanisms," *Cement Concr. Res.*, vol. 33, no. 3, pp. 341–346, 2003, http://dx.doi.org/10.1016/S0008-8846(02)00958-4.

[4]   A. Neville, "The confused world of sulfate attack on concrete," *Cement Concr. Res.*, vol. 34, no. 8, pp. 1275–1296, 2004, http://dx.doi.org/10.1016/j.cemconres.2004.04.004.

[5]   P. J. M. Monteiro and K. E. Kurtis, "Time to failure for concrete exposed to severe sulfate attack," *Cement Concr. Res.*, vol. 33, no. 7, pp. 987–993, 2003, http://dx.doi.org/10.1016/S0008-8846(02)01097-9.

[6]   W. Müllauer, R. E. Beddoe, and D. Heinz, "Sulfate attack expansion mechanisms," *Cement Concr. Res.*, vol. 52, pp. 208–215, 2013, http://dx.doi.org/10.1016/j.cemconres.2013.07.005.

[7]   M. Santhanam, M. D. Cohen, and J. Olek, "Sulfate attack research - Whither now," *Cement Concr. Res.*, vol. 31, no. 6, pp. 845–851, 2001, http://dx.doi.org/10.1016/S0008-8846(01)00510-5.

[8]   M. Santhanam, M. D. Cohen, and J. Olek, "Mechanism of sulfate attack: a fresh look. Part 1: summary of experimental results," *Cement Concr. Res.*, vol. 32, no. 6, pp. 915–921, 2002, http://dx.doi.org/10.1016/S0008-8846(02)00724-X.

[9]   B. Chatveera and P. Lertwattanaruk, "Evaluation of sulfate resistance of cement mortars containing black rice husk ash," *J. Environ. Manage.*, vol. 90, no. 3, pp. 1435–1441, 2009, http://dx.doi.org/10.1016/j.jenvman.2008.09.001.

[10] K. Behfarnia and O. Farshadfar, "The effects of pozzolanic binders and polypropylene fibers on durability of SCC to magnesium sulfate attack," *Constr. Build. Mater.*, vol. 38, pp. 64–71, 2013, http://dx.doi.org/10.1016/j.conbuildmat.2012.08.035.

[11] A. M. Diab, A. E. M. Awad, H. E. Elyamany, and A. E. M. Abd Elmoaty, "Guidelines in compressive strength assessment of concrete modified with silica fume due to magnesium sulfate attack," *Constr. Build. Mater.*, vol. 36, pp. 311–318, 2012, http://dx.doi.org/10.1016/j.conbuildmat.2012.04.075.

[12] N. Saca and M. Georgescu, "Behavior of ternary blended cements containing limestone filler and fly ash in magnesium sulfate solution at low temperature," *Constr. Build. Mater.*, vol. 71, pp. 246–253, 2014, http://dx.doi.org/10.1016/j.conbuildmat.2014.08.037.

[13] J. Hoppe Fo., D. J. Souza, M. H. F. Medeiros, E. Pereira, and K. F. Portella, "Concrete attack by sodium sulfate: mineral additions as a mitigation tool," *Ceramica*, vol. 61, pp. 168–177, 2015, http://dx.doi.org/10.1590/0366-69132015613581905.

[14] D. J. Souza, L. Y. Yamashita, F. Dranka, M. H. F. Medeiros, and R. A. Medeiros-Junior, "Repair Mortars Incorporating Multiwalled Carbon Nanotubes: Shrinkage and Sodium Sulfate Attack," *J. Mater. Civ. Eng.*, vol. 29, no. 12, pp. 1–12, 2017, http://dx.doi.org/10.1061/(ASCE)MT.1943-5533.0002105.

[15] M. D. Cohen and A. Bentur, "Durability of Portland cement-silica fume pastes in magnesium sulfate and sodium sulfate solutions," *ACI Mater. J.*, vol. 85, pp. 148–157, 1988.

[16] M. C. G. Juenger and R. Siddique, "Recent advances in understanding the role of supplementary cementitious materials in concrete," *Cement Concr. Res.*, vol. 78, pp. 71–80, 2015, http://dx.doi.org/10.1016/j.cemconres.2015.03.018.

[17] E. Ghafari, S. A. Ghahari, H. Costa, E. Júlio, A. Portugal, and L. Durães, "Effect of supplementary cementitious materials on autogenous shrinkage of ultra-high performance concrete," *Constr. Build. Mater.*, vol. 127, pp. 43–48, 2016, http://dx.doi.org/10.1016/j.conbuildmat.2016.09.123.

[18] P. K. Mehta and P. J. M. Monteiro, *Concrete Microstructure, Properties and Materials*. . New York, NY, USA: McGraw-Hill, 2017.

[19] B. Lothenbach, K. Scrivener, and R. D. Hooton, "Supplementary cementitious materials," *Cement Concr. Res.*, vol. 41, no. 12, pp. 1244–1256, 2011, http://dx.doi.org/10.1016/j.cemconres.2010.12.001.

[20] S. W. Tang, Y. Yao, C. Andrade, and Z. J. Li, "Recent durability studies on concrete structure," *Cement Concr. Res.*, vol. 78, pp. 143–154, 2015, http://dx.doi.org/10.1016/j.cemconres.2015.05.021.

[21] S. W. Tang et al., "The review of pore structure evaluation in cementitious materials by electrical methods," *Constr. Build. Mater.*, vol. 117, pp. 273–284, 2016, http://dx.doi.org/10.1016/j.conbuildmat.2016.05.037.

[22] A. L. G. Gastaldini, M. P. Da Silva, F. B. Zamberlan, and C. Z. Mostardeiro No., "Total shrinkage, chloride penetration, and compressive strength of concretes that contain clear-colored rice husk ash," *Constr. Build. Mater.*, vol. 54, pp. 369–377, 2014, http://dx.doi.org/10.1016/j.conbuildmat.2013.12.044.

[23] H. Kizhakkumodom Venkatanarayanan and P. R. Rangaraju, "Effect of grinding of low-carbon rice husk ash on the microstructure and performance properties of blended cement concrete," *Cement Concr. Compos.*, vol. 55, pp. 348–363, 2015, http://dx.doi.org/10.1016/j.cemconcomp.2014.09.021.

[24] J. Prasara-A and S. H. Gheewala, "Sustainable utilization of rice husk ash from power plants: a review," *J. Clean. Prod.*, vol. 167, pp. 1020–1028, 2017, http://dx.doi.org/10.1016/j.jclepro.2016.11.042.

[25] R. K. Sandhu and R. Siddique, "Influence of rice husk ash (RHA) on the properties of self-compacting concrete: a review," *Constr. Build. Mater.*, vol. 153, pp. 751–764, 2017, http://dx.doi.org/10.1016/j.conbuildmat.2017.07.165.

[26] J. L. García Calvo, A. Hidalgo, C. Alonso, and L. Fernández Luco, "Development of low-pH cementitious materials for HLRW repositories: resistance against ground waters aggression," *Cement Concr. Res.*, vol. 40, no. 8, pp. 1290–1297, 2010, http://dx.doi.org/10.1016/j.cemconres.2009.11.008.

[27] G. Le Saoût, E. Lécolier, A. Rivereau, and H. Zanni, "Chemical structure of cement aged at normal and elevated temperatures and pressures, Part II: low permeability class G oilwell cement," *Cement Concr. Res.*, vol. 36, no. 3, pp. 428–433, 2006, http://dx.doi.org/10.1016/j.cemconres.2005.11.005.

[28] S. T. Lee, H. Y. Moon, and R. N. Swamy, "Sulfate attack and role of silica fume in resisting strength loss," *Cement Concr. Compos.*, vol. 27, no. 1, pp. 65–76, 2005, http://dx.doi.org/10.1016/j.cemconcomp.2003.11.003.

[29] D. Bonen, "A microstructural study of the effect produced by magnesium sulfate on plain and silica fume-bearing Portland cement mortars," *Cement Concr. Res.*, vol. 23, no. 3, pp. 541–555, 1993, http://dx.doi.org/10.1016/0008-8846(93)90004-S.

[30] M. J. Shannag and H. A. Shaia, "Sulfate resistance of high-performance concrete," *Cement Concr. Compos.*, vol. 25, no. 3, pp. 363–369, 2003., http://dx.doi.org/10.1016/S0958-9465(02)00049-5.

[31] E. Ganjian and H. S. Pouya, "Effect of magnesium and sulfate ions on durability of silica fume blended mixes exposed to the seawater tidal zone," *Cement Concr. Res.*, vol. 35, no. 7, pp. 1332–1343, 2005, http://dx.doi.org/10.1016/j.cemconres.2004.09.028.

[32] M. I. Khan and R. Siddique, "Utilization of silica fume in concrete: review of durability properties," *Resour. Conserv. Recycling*, vol. 57, pp. 30–35, 2011, http://dx.doi.org/10.1016/j.resconrec.2011.09.016.

[33] M. F. Najjar, M. L. Nehdi, A. M. Soliman, and T. M. Azabi, "Damage mechanisms of two-stage concrete exposed to chemical and physical sulfate attack," *Constr. Build. Mater.*, vol. 137, pp. 141–152, 2017, http://dx.doi.org/10.1016/j.conbuildmat.2017.01.112.

[34] P. Chindaprasirt, P. Kanchanda, A. Sathonsaowaphak, and H. T. Cao, "Sulfate resistance of blended cements containing fly ash and rice husk ash," *Constr. Build. Mater.*, vol. 21, no. 6, pp. 1356–1361, 2007, http://dx.doi.org/10.1016/j.conbuildmat.2005.10.005.

[35] B. Chatveera and P. Lertwattanaruk, "Durability of conventional concretes containing black rice husk ash," *J. Environ. Manage.*, vol. 92, no. 1, pp. 59–66, 2011, http://dx.doi.org/10.1016/j.jenvman.2010.08.007.

[36] D. J. Souza, M. H. F. Medeiros, and J. Hoppe Fo., "Evaluation of the SR Portland cement against sodium and magnesium sulfate attack: a physical and comparative analysis of mortars," *Rev. IBRACON Estrut. Mater.*, vol. 11, no. 5, pp. 1053–1075, 2018, http://dx.doi.org/10.1590/s1983-41952018000500009.

[37] D. J. Souza, M. H. F. Medeiros, and J. Hoppe Filho, "Evaluation of external sulfate attack (Na$_2$SO$_4$ and MgSO$_4$): Portland cement mortars containing fillers," *Rev. IBRACON Estrut. Mater.*, vol. 13, no. 3, pp. 644–655, 2020, http://dx.doi.org/10.1590/s1983-41952020000300013.

[38] Associação Brasileira de Normas Técnicas, *Cimento Portland - Requisitos* , ABNT NBR 16697:2018, 2018.

[39] Associação Brasileira de Normas Técnicas, *Cimento Portland – Determinação da variação dimensional de barras de argamassa de cimento Portland expostas à solução de sulfato de sódio*, ABNT NBR 13583:2014, 2014.

[40] Associação Brasileira de Normas Técnicas, *Cimento Portland — Determinação da variação dimensional de barras de argamassa de cimento Portland expostas à solução de sulfato de sódio*, ABNT NBR 13.853/2014, 2014.

[41] M. H. F. Medeiros, D. J. Souza, J. Hoppe Fo., C. S. Adorno, V. A. Quarcioni, and E. Pereira, "Red-clay waste and limestone filler added in Portland cement composite: effects on sulfate attack and alkali-silica reaction," *Rev. Mat.*, vol. 21, pp. 282–300, 2016, http://dx.doi.org/10.1590/S1517-707620160002.0028.

[42] Associação Brasileira de Normas Técnicas, *Argamassa para assentamento e revestimento de paredes e tetos - Determinação da resistência à tração na flexão e à compressão*, ABNT NBR 13.279, 2005.

[43] D. J. Souza, "Capacidade de adições minerais em mitigar o ataque por sulfatos de sódio e magnésio em argamassas de cimento Portland," M.S. thesis, Univ. Fed. Paraná, Curitiba, PR, 2016.

[44] P. Lawrence, M. Cyr, and E. Ringot, "Mineral admixtures in mortars," *Cement Concr. Res.*, vol. 33, no. 12, pp. 1939–1947, 2003, http://dx.doi.org/10.1016/S0008-8846(03)00183-2.

[45] M. Cyr, P. Lawrence, and E. Ringot, "Efficiency of mineral admixtures in mortars: Quantification of the physical and chemical effects of fine admixtures in relation with compressive strength," *Cement Concr. Res.*, vol. 36, no. 2, pp. 264–277, 2006, http://dx.doi.org/10.1016/j.cemconres.2005.07.001.

[46] M. Cyr, P. Lawrence, and E. Ringot, "Mineral admixtures in mortars: Quantification of the physical effects of inert materials on short-term hydration," *Cement Concr. Res.*, vol. 35, pp. 719–730, 2005, http://dx.doi.org/10.1016/j.cemconres.2004.05.030.

[47] Z.A. Marciano, "Desenvolvimento de um método acelerado para avaliação da resistência de argamassas de cimento Portland expostas à solução de sulfato de sódio," M.S. thesis, Univ. São Paulo, São Paulo, SP, 1993.

[48] D. Bonen and M. D. Cohen, "Magnesium sulfate attack on portland cement paste-I. Microstructural analysis," *Cement Concr. Res.*, vol. 22, no. 1, pp. 169–180, 1992, http://dx.doi.org/10.1016/0008-8846(92)90147-N.

[49] Z. Makhloufi, S. Aggoun, B. Benabed, E. H. Kadri, and M. Bederina, "Effect of magnesium sulfate on the durability of limestone mortars based on quaternary blended cements," *Cement Concr. Compos.*, vol. 65, pp. 186–199, 2016, http://dx.doi.org/10.1016/j.cemconcomp.2015.10.020.

[50] W. Ouyang, J. Chen, and M. Jiang, "Evolution of surface hardness of concrete under sulfate attack," *Constr. Build. Mater.*, vol. 53, pp. 419–424, 2014, http://dx.doi.org/10.1016/j.conbuildmat.2013.11.107.

[51] E. F. Irassar, M. González, and V. Rahhal, "Sulfate resistance of type V cements with limestone filler and natural pozzolana," *Cement Concr. Compos.*, vol. 22, no. 5, pp. 361–368, 2000, http://dx.doi.org/10.1016/S0958-9465(00)00019-6.

[52] E. F. Irassar, "Sulfate resistance of blended cement: prediction and relation with flexural strength," *Cement Concr. Res.*, vol. 20, no. 2, pp. 209–218, 1990, http://dx.doi.org/10.1016/0008-8846(90)90073-7.

[53] Q. Huang, C. Wang, C. Yang, L. Zhou, and J. Yin, "Accelerated sulfate attack on mortars using electrical pulse," *Constr. Build. Mater.*, vol. 95, pp. 875–881, 2015, http://dx.doi.org/10.1016/j.conbuildmat.2015.07.034.

[54] S. Zhao, F. Hu, X. Ding, M. Zhao, C. Li, and S. Pei, "Dataset of tensile strength development of concrete with manufactured sand," *Data Brief*, vol. 11, pp. 469–472, 2017, http://dx.doi.org/10.1016/j.dib.2017.02.043.

[55] A. Hillerborg, M. Modéer, and P. E. Petersson, "Analysis of crack formation and crack growth in concrete by means of fracture mechanics and finite elements," *Cement Concr. Res.*, vol. 6, no. 6, pp. 773–781, 1976, http://dx.doi.org/10.1016/0008-8846(76)90007-7.

[56] P. J. Tikalsky, D. Roy, B. Scheetz, and T. Krize, "Redefining cement characteristics for sulfate-resistant Portland cement," *Cement Concr. Res.*, vol. 32, no. 8, pp. 1239–1246, 2002, http://dx.doi.org/10.1016/S0008-8846(02)00767-6.

[57] F. Bellmann and J. Stark, "Prevention of thaumasite formation in concrete exposed to sulfate attack," *Cement Concr. Res.*, vol. 37, no. 8, pp. 1215–1222, 2007, http://dx.doi.org/10.1016/j.cemconres.2007.04.007.

Rev. IBRACON Estrut. Mater., vol. 13, no. 4, e13403, 2020

16/16

IBRACON Structures and Materials Journal
Revista IBRACON de Estruturas e Materiais

ORIGINAL ARTICLE

Thermomechanical analysis of reinforced concrete columns exposed to fire

Análise termomecânica de pilares de concreto armado em situação de incêndio

Matheus Wanglon Ferreira[a]
Luiz Carlos Pinto da Silva Filho[a]
Mauro de Vasconcellos Real[b]

[a]Universidade Federal do Rio Grande do Sul – UFRGS, Escola de Engenharia, Programa de Pós-graduação em Engenharia Civil, Porto Alegre, RS, Brasil
[b]Universidade Federal do Rio Grande – FURG, Escola de Engenharia, Rio Grande, RS, Brasil

Abstract: A three-dimensional (3D) transient numerical model for thermomechanical analysis developed with Finite Element Method (FEM) using the software ANSYS 19.1 is exposed in this paper. The proposed model aims to predict the structural behavior of reinforced concrete columns in a fire situation since it is known that high temperatures significantly reduce their mechanical resistance. For this, the main factors that govern their structural behavior should be considered. Analyses obtained by the proposed model were validated with results from experimental data, evidencing a good correlation between numerical and experimental fields.

Keywords: termomechanical analysis, fire, finite element method, high temperature, reinforced concrete.

Resumo: Um modelo numérico transiente tridimensional (3D) para análises termomecânicas, criado através do método dos elementos finitos (MEF) com o auxílio do software ANSYS 19.1, é apresentado neste trabalho. O modelo proposto tem por objetivo predizer o comportamento estrutural de pilares de concreto armado em situação de incêndio, pois é sabido que a temperatura elevada reduz significativamente a sua capacidade resistente. Assim, os principais fatores que governam o comportamento estrutural em altas temperaturas devem ser levados em consideração. As análises obtidas com o modelo criado foram confrontadas e validadas com resultados oriundos de ensaios laboratoriais, evidenciando boa correlação entre o campo numérico e o experimental.

Palavras-chave: análise termodinâmica, fogo, método dos elementos finitos, alta temperatura, concreto armado.

1 INTRODUCTION

Over the years, mainly due to disasters caused by severe fires in buildings, industrial pavilions, tunnels and other civil engineering works, many research groups have been focusing on evaluating the behavior of structural elements exposed to fire.

Specifically, in Brazil, there are various researches conducted in this area, published through dissertations, theses, and several journal articles. To illustrate it, Silva [1] carried out his thesis evaluating steel structures exposed to fires and continued to contribute with many works on fire safety [2], [3]. Carla Costa, for instance, had important cooperation in designing reinforced concrete elements in fire situations [4], [5].

In the state of Rio Grande do Sul, Lemos [6], through his dissertation, created a computational code able to perform a numerical study of reinforced concrete structures under high temperatures by the finite element method. In addition, Kirchhof [7]

developed during her Doctorate at the Structural Models and Testing Laboratory (LEME-UFRGS), a numerical and experimental study analyzing how the water content influence on explosive spalling phenomena in concretes exposed to elevated temperatures. Finally, Bolina [8] presented results of the experimental tests carried out at its Performance/UNISINOS, evaluating the influence of durability requirements on fire safety through prototypes of prefabricated reinforced concrete columns.

Moreover, many studies involving numerical models of structures exposed to fire using the software ANSYS, in the national scenario, was developed by researches of USP - São Carlos, including thermomechanical analyses in steel structures [9] and [10], concrete-filled steel columns [11], composite steel and concrete beams [12], composite concrete and timber beams [13], among others.

It is known that columns of a building structure are the main responsible for its integrity, hence the need to predict their structural behavior in harmful situations through analytical, numerical and experimental methods. Experimental testing is the best way to understand the behavior of these structures. However, laboratory procedures are often limited in quantity due to high costs and time demands. Thus, the development of numerical models, calibrated with experimental data, allows expanding the knowledge with more agility and resource-saving.

1.1 Objectives

The current study aims to evaluate, through an advanced calculation model using the finite element method (FEM), reinforced concrete columns behavior in fire situations considering geometric nonlinearity and the elastoplastic regime of the materials. This work was elaborated with the aid of ANSYS 19.1 software [14] where columns models were exposed to a standard temperature-fire curve recommended by ISO 834 [15].

The expectation at the end of the study, by validating the thermomechanical model created with consistent experimental data present in the bibliography, is to conclude that the proposed model can offer good responses and enables several applications and analyses for future researches involving this thematic.

2 METHODOLOGY – PROPOSED NUMERICAL MODEL

In this work, a three-dimensional numerical model was created using ANSYS 19.1 software [14] to carry out transient thermomechanical analyses, that is, evaluations considering the variability of the parameters in accordance with temperature increase. In order to do this, the coupling of two engineering analyses fields was necessary: thermal and mechanical.

It must be observed that the processing time of all models presented in this work will be indicated in their respective subitems related to results. Besides, all simulations were performed with the aid of an Intel Xeon E3-1225 v5 3.30 GHz Processor, 8.00 GB installed memory, and Intel HD Graphics P530.

2.1 Thermal analysis

Firstly, through purely thermal analysis, was achieved the thermal gradient evolution in the structure. Such a study was performed by exposing columns to the standard fire curve ISO 834 [15]. This curve, expressed according to Equation 1, represents a typical building fire whose combustible material considered is cellulosic. Figure 1 shows the evolution of temperature as a function of time in accordance with the curve mentioned above.
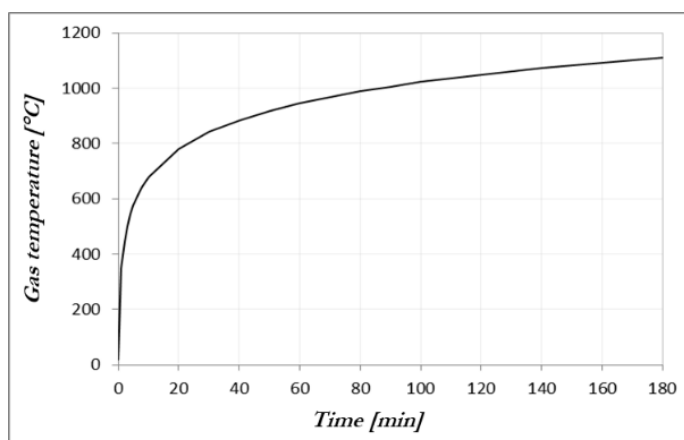
Figure 1. Standard temperature-time curve suggested by ISO 834 [8].

$$\boldsymbol{\theta_g} - \boldsymbol{\theta_{g0}} = 345 \cdot \log \cdot (8 \cdot \boldsymbol{t} + 1) \tag{1}$$

Where:

θ_g is the gas temperature [°C];

θ_{g0} is the gas temperature at time t=0, i.e., room temperature [20 °C];

t is the time [h].

2.1.1 Thermal properties

Proceeding the analysis, some thermal properties of steel and concrete were required, such as specific heat, thermal conductivity; density; and emissivity. The ABNT NBR 14323:2013 [16] allows the adoption of simplified values. However, for the current study, knowing that the constituent materials have a significant variation of their properties when exposed to fire, the values suggested in Annex C of ABNT NBR 15200:2012 [17] and in Annex E of ABNT NBR 14323:2013 [16] was chosen. It is worth noting that the values prescribed above are in accordance with Eurocode [18].

Finally, among the thermal properties required, the specific mass was defined. For steel, ABNT NBR 14323:2013 [16] indicates that the value of 7850 kg/m³ can be considered regardless of temperature. According to Lomba [19], such consideration is attributed to the fact that steel has a stable and well-defined microstructure at elevated temperatures. For concrete, in turn, the Annex C of ABNT NBR 15200:2012 [17] points out that specific mass is influenced by water loss; thus, it varies with increasing temperature.

2.1.2 Discretization of the structure into finite elements

In order to simulate the thermal response, reinforced concrete columns are discretized using three different types of elements available in ANSYS 19.1 internal library [14]. To represent solid materials, the elements SOLID70 and LINK33 were used. To enable the application of fire boundary conditions, SURF152 was used overlaid onto a heated surface of 3D thermal solid elements.

SOLID70 is an eight nodes element used for three-dimensional applications and LINK33 is a bar element with only two nodes, both having the temperature as a single degree of freedom, at each node. It allows the element capability to simulate thermal conductivity, being the solid element applicable to concrete simulation and the bar element applicable to steel. SURF152, in its turn, is a thermal surface effect element that is defined by four to nine nodes with the possibility of using an extra node. The function of the extra node, located away from the base element, is to be a logical point for the fire curve application. The objective of surface elements is to simulate heat transfers by convection and radiation. For that, material properties such as emissivity and convection heat transfer coefficient should be assigned.

Thus, with the mentioned discretization, it is possible to encompass the three main heat transfer mechanisms. Fire exposed surfaces contribute to the temperature rise by convection and radiation through the SURF152 element, while internal temperature conduction capability is attributed by SOLID70 and LINK33 elements.

In addition, depending on the structural arrangement of each model, if possible, the principle of symmetry is used, reducing computational costs and analysis time. For better understanding, Figure 2 presents a generic model created as described above.

The thermal analysis results consist of determining temperatures at each node of the mesh. It is also noteworthy that, according to the analyses realized, the temperature remains uniform longitudinally while in the structure cross-section, the temperature variation was observed. It is important to emphasize that materials properties are assigned according to the average temperature of elements, calculated from the temperature of each element node. This approach to average the nodal values is used in both thermal and thermomechanical analysis defined in the next subitem.

2.2 Thermomechanical analysis

The thermomechanical simulation is performed using coupled fields analysis offered by ANSYS 19.1 [14]. Such work consists of using thermal outputs (nodal temperatures) as inputs in the structural analysis through the command LREAD. The nodal temperatures are applied as body forces on the nodes, as showed in the flowchart presented in Figure 3. It is important to note that, for the right operation in the interest of field coupling, the mesh of the second analysis (in this case, thermomechanical) must be identical to the mesh defined in the first process (thermal). This methodology ensures the correct imposition of input data on each node of the model.

To create the thermostructural model is required that at first, a simpler analysis must be performed at room temperature. The objective is to quickly certify that the criteria established in the model design are working well. After

that, it is possible to proceed safely for structural analysis in a fire situation, where the material mechanical properties, as well as the discretization of the model, must be appropriately assigned.
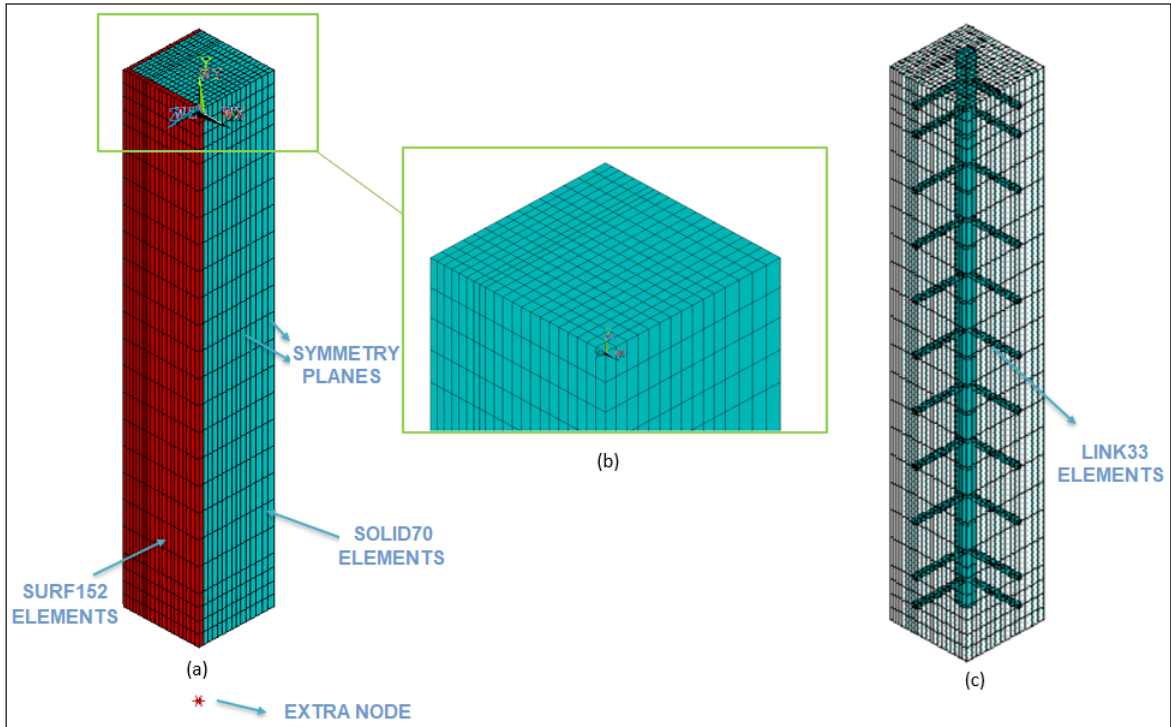
Figure 2. (a) Generic thermal model, (b) mesh detail (c) arranging of longitudinal and transversal reinforcement.
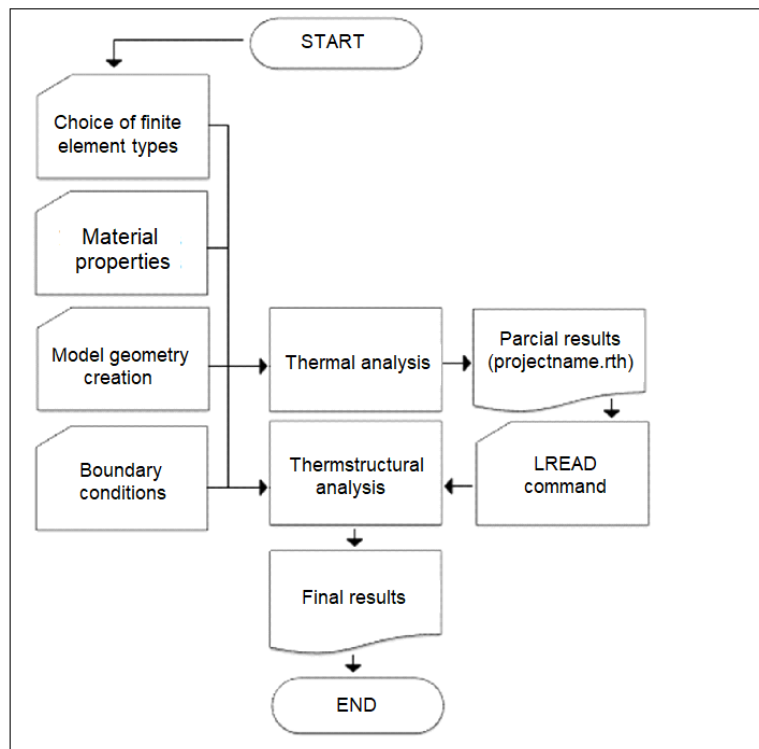
Figure 3. Coupled analysis flowchart.

Rev. IBRACON Estrut. Mater., vol. 13, no. 4, e13404, 2020

4/14

2.2.1 Thermomechanical properties

The temperature-dependent properties required are specific thermal strain, compressive strength, tensile strength, modulus of elasticity, and the stress-strain diagram of the materials. The specific thermal strains of steel and concrete are determined by Annex E of ABNT NBR 14323: 2013 [16] and Annex C of ABNT NBR 15200: 2012 [17] respectively.

For steel, the variation of the characteristic yield strength and the modulus of elasticity with the increase in temperature are obtained by decreasing the values corresponding to ambient temperature by reduction factors, $\kappa_{s,\theta}$ and $\kappa_{Es,\theta}$ respectively. The reduction coefficients, distinguished for steel CA-50 and CA-60, can be found in ABNT NBR 15200: 2012 [17].

For concrete, in its turns, the mean tensile strength (f_{ctm}) and the modulus of elasticity at room temperature (E_{ci}) are calculated from the mean compressive strength obtained in the laboratory (f_{cm}) according to Equations 2 and 3 suggested by the Fib Model Code [20]. The variation of the properties with the increase in temperature, as in the case of the steel properties, are obtained by decreasing the value at room temperature through the reduction factors $\kappa_{t,\theta}$, $\kappa_{cE,\theta}$ and $\kappa_{c,\theta}$ present in tabular form in ABNT NBR 15200:2012 [17]. According to Eurocode [18], the values of $\kappa_{cE,\theta}$ must be obtained from $\kappa_{c,\theta}$, as indicated in Equation 4. It is noteworthy that the Brazilian standards do not inform how to proceed with the $\kappa_{cE,\theta}$ calculation, which justifies the adoption of the recommendation made by European code. Moreover, differently from national technical standardization, Eurocode [18] suggests different values for concretes consisting predominantly of siliceous aggregates from those composed of calcareous aggregates.

$$f_{ctm} = 0,3 \cdot \left(f_{cm} - \Delta f \right)^{2/3} \tag{2}$$

$$E_{ci} = 21500 \cdot \alpha_E \cdot \left(\frac{f_{cm}}{10} \right)^{1/3} \tag{3}$$

$$\kappa_{cE,\theta} = \left(\kappa_{c,\theta} \right)^2 \tag{4}$$

Where:
Δf is equal to 8 MPa;
α_E is a coefficient, being 1.0 for silica concrete and 0.9 calcareous.

Finally, stress-strain relations to be used for both materials were defined. For the steel was attributed a perfect elastoplastic model with bilinear constitutive law, respecting Hooke's law to the point of deformation corresponding to the yield strength, followed by a straight line to the point of the ultimate tensile strength (Figure 4).
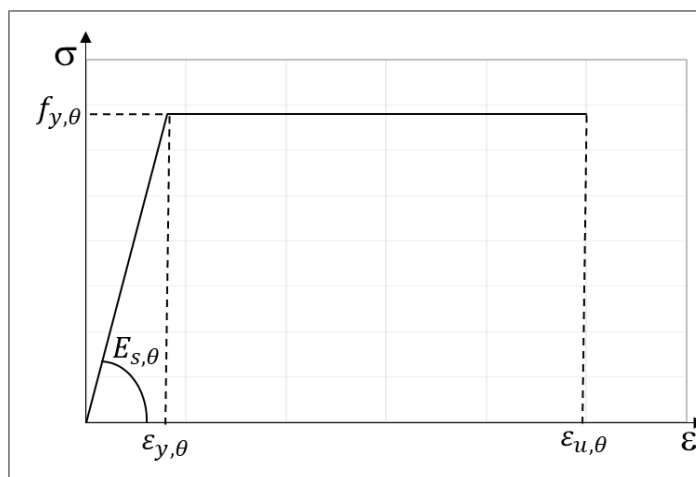
Figure 4. Generic perfect elastoplastic bilinear constitutive law for steel in function of the temperature.

To simulate the behavior of concrete, several studies ([21], [22], [23], among others) used the diagram proposed by Eurocode [18] (Equation 5). However, Lemos [6], opts for the model indicated by fib [20]. Moreover, as pointed out by Araújo [24], the relation of fib [20] represents in a better way the behavior of reinforced concrete. Therefore, in the current study, it was decided to analyze the structures at both room temperature and fire situation through the two mentioned diagrams. It was noteworthy that the curve suggested by fib [20] was idealized for room temperature and it was necessary to adjust the parameters as a function of temperature. The original formulation can be found in the cited reference, and the adapted formulation can be observed in Equation 6 below.

$$\sigma_{c,\theta} = \frac{3 \cdot \varepsilon_{c,\theta} \cdot f_{cm,\theta}}{\varepsilon_{c1,\theta} \cdot \left(2 + \left(\frac{\varepsilon_{c,\theta}}{\varepsilon_{c1,\theta}} \right)^3 \right)} \qquad [5]$$

$$\frac{\sigma_{c,\theta}}{f_{cm}} = - \left| \frac{\left(\frac{E_{ci,\theta}}{E_{c1,\theta}} \right) \cdot \left(\frac{\varepsilon_{c,\theta}}{\varepsilon_{c1,\theta}} \right) - \left(\frac{\varepsilon_{c,\theta}}{\varepsilon_{c1,\theta}} \right)^2}{1 + \left(\left(\frac{E_{ci,\theta}}{E_{c1,\theta}} \right) - 2 \right) \cdot \left(\frac{\varepsilon_{c,\theta}}{\varepsilon_{c1,\theta}} \right)} \right|, |\varepsilon_{c,\theta}| \le |\varepsilon_{cu1,\theta}| \qquad [6]$$

Where:
$\sigma_{c,\theta}$ is the uniaxial compressive stress in the concrete as a function of temperature [MPa];

$\varepsilon_{c,\theta}$ is the total specific linear deformation in the concrete at a given temperature [dimensionless];

$\varepsilon_{c1,\theta}$ is the total specific linear strain in the concrete at peak compression stress as a function of temperature [dimensionless];

$\varepsilon_{cu1,\theta}$ is the ultimate specific linear strain in the concrete as a function of temperature [dimensionless];

$E_{ci,\theta}$ is the initial tangent modulus of elasticity of concrete as a function of temperature [MPa];

$E_{c1,\theta}$ is the secant modulus of elasticity of concrete as a function of temperature [MPa].

The schematic representation of the stress-strain relation proposed by fib [20] can be visualized in a general way in Figure 5. The strain values used for steel and concrete diagrams calculations were extracted from ABNT NBR 15200:2012 [17] and Eurocode [18].
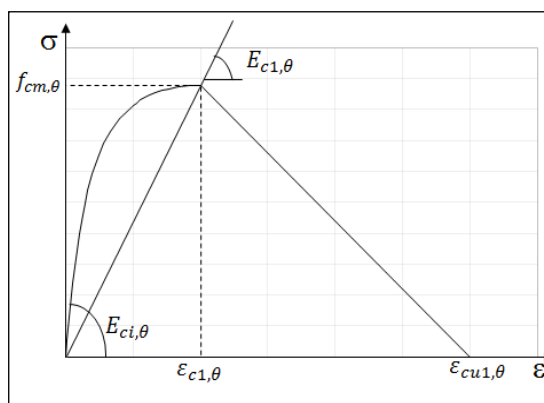
Figure 5. Generic concrete constitutive relation under compression in function of the temperature.

2.2.2 Discretization of the structure into finite elements

To proceed with the modeling, elements compatible with those defined in item 2.1 were adopted. In this case, SOLID65 and LINK180 elements were used and there was no need to maintain the surface element for mechanical boundary conditions. The element SOLID65 used to represent concrete as well as the solid element previously

described, was a three-dimensional element with eight nodes, but with three degrees of freedom per node. The LINK180 element was a two-node bar element with a degree of freedom per node capable of simulating the compressive and tensile stresses on reinforcing steel bars.

2.2.3 Concrete failure modes

The material model predicts concrete failure considering cracking and crushing effects [14]. These phenomena, being crushing the most important for a central compression column, imply a significant strength loss of the structural member, leading it to the failure. In the numerical model developed with ANSYS 19.1, through the SOLID65 element, according to ANSYS [14], the failure envelope proposed by Willam and Warnke [25] could be defined. The envelope aims to consider the crushing and cracking effects of concrete, performing a fundamental role in defining its behavior. The failure criterion due to a multiaxial stress state could be expressed according to Equation 7.

$$\frac{F}{f_c} - S \geq 0 \qquad\qquad [7]$$

Where:

F is a function of the principal stress state [MPa];

f_c is uniaxial crushing strength of concrete [MPa];

S is a continuous failure surface.

In order to define the failure surface, five parameters are required: ultimate uniaxial compressive strength, ultimate uniaxial tensile strength (f_t), ultimate biaxial compressive strength (f_{cb}) and ultimate compressive strength for a state of biaxial and uniaxial compression superimposed on hydrostatic stress state (f_1 and f_2). The relative magnitudes of the principal stresses in the octahedral plane are described using the angle of similarity (η) and functions r_1 and r_2, as shown in Figure 6. The three-dimensional failure surface resulting from the main stress state is presented in Figure 6 and the detailed mathematical formulation can be consulted on [25].
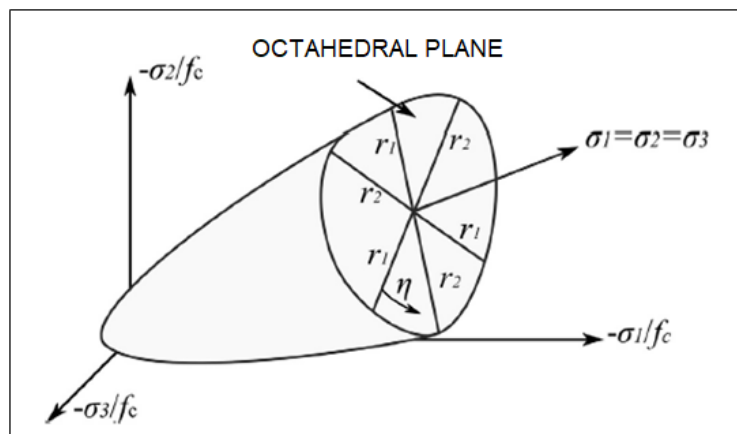
Figure 6. Three-dimensional failure envelope for cracking and crushing of concrete ($\sigma_1\sigma_1$, $\sigma_2\,\sigma_2$ and $\sigma_3\sigma_3$ are principal stresses). Adapted from: Kumar and Kodur [23].

According to ANSYS [14], it is possible to inform only two inputs (f_t and f_t) for the failure envelope calculation if sufficient experimental data is not available. The other parameters are determined according to software default values: f_{cb} =1.2 f_c , f_1 =1.45 f_c e f_2 =1.725 f_c .

In the case of an element cracking, a plane of weakness was introduced in a direction normal of the crack face that meets the criterion. In order to incorporate the element stiffness reduction due to cracking, additional parameters are required. These parameters consist of shear transfer coefficients for an open (β_t) and a closed crack (β_c). The values range from 0 to 1, with 0 representing a smooth crack (complete loss of shear transfer) and 1 representing a rough crack

Rev. IBRACON Estrut. Mater., vol. 13, no. 4, e13404, 2020

7/14

(no loss of shear transfer). For the present work, as in Kumar and Kodur [23], the values of 0.53 and 0.98 for open and closed cracks were adopted.

The ANSYS documentation [14] informs the difficulty of solution convergence in cases where concrete cracking and crushing are simultaneously considered. Thus, it is possible to adopt only one failure mode, assigning the value of -1 for which it is intended to be disregarded. Based on this statement and on the experience acquired from the analyses performed during the development of this work, it was decided to consider only the concrete cracking through the Willam and Warnke model [25].

Crushing, in turn, is related to concrete strength imposed on the material stress-strain diagram. Therefore, concrete crushing was considered when the element was not able to resist the stress state originated from mechanical and thermal loading anymore.

3 VALIDATION OF NUMERICAL MODEL AT ROOM TEMPERATURE

In order to create a consistent numerical model, room temperature analyses were performed for reference before proceeding with coupled fields. To this end, the study elaborated by Ramos and Giongo [26] was chosen to evaluate the criteria adopted in the model developed in the current study.

3.1 Brief description of the experimental program

Ramos and Giongo [26] analyzed 16 normal strength columns considering variation in the following parameters: geometric dimensions of the structural element, longitudinal reinforcement ratio, transverse reinforcement spacing and configuration. Tests were performed on a servo-controlled hydraulic machine which allows the application of load under displacements control. The monitoring of the reinforcement deformations was conducted through electric strain gauges fixed on the steel bars and on the column faces. The deflectometers that were positioned on the column faces measured displacements derived by the compressive force. Further details on the procedures adopted in this experimental program can be obtained by consulting the above reference.

3.2 Numerical model aspects

For validation, columns models P1-10-120 and P1-12,5-100 extracted from Ramos and Giongo [26] were chosen, which will be renamed in this article as Column 1 and Column 2 respectively. The information required to perform the mechanical analysis is shown in Table 1.

Table 1 Studied columns parameters.

Parameter	Column 1	Column 2	Column 3
Experimental test developed by	Ramos and Giongo [26]	Ramos and Giongo [26]	Wu and Lie [27] Zhu and Lie [28]
Column reference designation	P1-10-120	P1-12.5-100	Column 3
Dimensions (width x height x length) - cm	20 x 20 x 120	20 x 20 x 100	30.5 x 30.5 x 350
Concrete cover - cm	1.5	1.5	4.8
Longitudinal reinforcement	4 φ 10 mm	4 φ 12.5 mm	4 φ 22 mm
Reinforcement ratio - %	0.79	1.23	1.66
Stirrups	φ 5 c. 12 cm	φ 6.3 c. 10 cm	φ 8 c. 30.5 cm
Concrete mean compressive strength - MPa	23,7	27,1	23,4
Steel yield strength - MPa	611	561	340
Aggregate type	Siliceous	Siliceous	Siliceous
Experimental column ultimate force - kN	1072	1292	-
Experimental failure time of column on fire - min	-	-	109

With the purpose of simulating the same pillar conditions found in the experimental test, the structure was modeled respecting actual dimensions. However, since the columns present double symmetry, only a quarter of their volume

Rev. IBRACON Estrut. Mater., vol. 13, no. 4, e13404, 2020

8/14

was modeled according to the generic model shown in Figure 7. To ensure an appropriate simulation, nodes present in the symmetrical plane had their movement restricted in the perpendicular direction.

Also, rigid body motions were restricted at nodes belonging to the structure base. For nodes belonging to the top, only translation in the load application direction is allowed. The distributed load was applied to the nodes of the upper structure section. Furthermore, extremely rigid plates were placed at the top and bottom of the model allowing uniform loading on the nodes and avoiding localized plastic deformations due to different displacement between them.

The mesh used for analysis was done manually, dividing the cross-sectional region of the covering and concrete core in a manner such that the element longest side does not exceed 1 cm. These details can be seen in Figure 7.
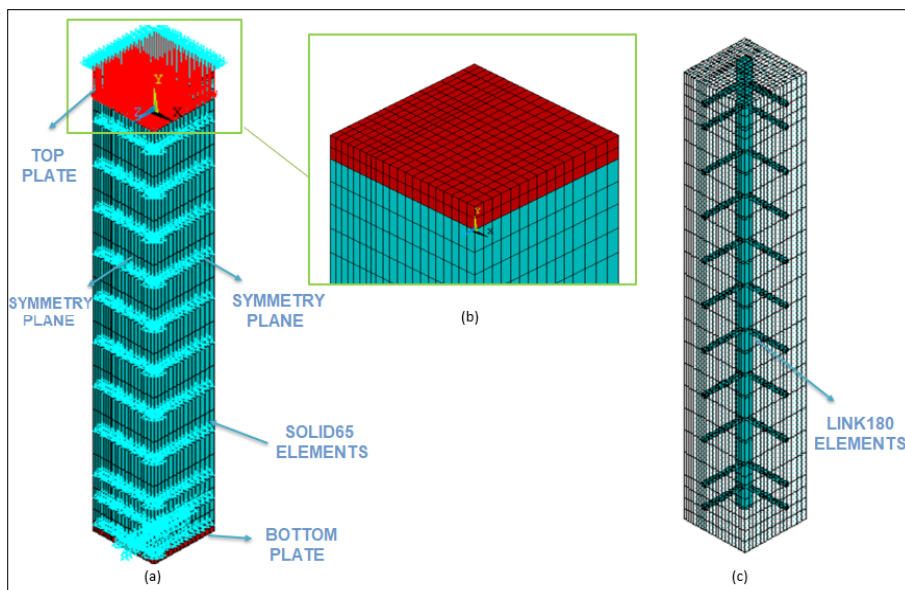
Figure 7. (a) Generic mechanical/thermomechanical model (b) top plate detail (c) arranging of longitudinal and transversal reinforcement

About the solution options adopted, it is important to point out that loading was applied incrementally, dividing the total load into sub-steps. Each load sub-step starts with the last complete sub-step value and proceeds linearly until the end. This way of load application is called [14] as ramped load and must be enabled with KBC command, 0. Additionally, geometric nonlinearity was considered through NLGEOM, ON command. The convergence criteria adopted for force and displacement were 5% of the vector norm. The solution was given through the full Newton-Raphson iterative method.

3.3 Validation results

The first analysis performed with Column 1 was the behavior of different stress-strain diagrams. Figure 8 shows a good difference between the curves proposed by European Committee For Standardization [18] and Federation Internationale du Béton [20], and the latter showed a behavior closer to that found in the experimental field at room temperature.

Figure 9 indicates an even greater agreement on the reinforced concrete column behavior when subjected to axial compression. As for the rupture force, Column 1 through numerical simulation presented an ultimate force of 1049 kN, representing an error of only 2.19% when compared to experimental test. The numerical model for Column 2, in its turn, presented an ultimate force equivalent to 1376.25 kN, which represents an error of 6.52%. In the face of it, the strategy adopted and described in item 2 can be regarded as satisfactory, obtaining consistent results for performed analyses and allowing to advance to the thermomechanical model. It should be noted that the processing time for Column 1 was 6 min 10 sec, while Column 2 required 6 min 43 sec.
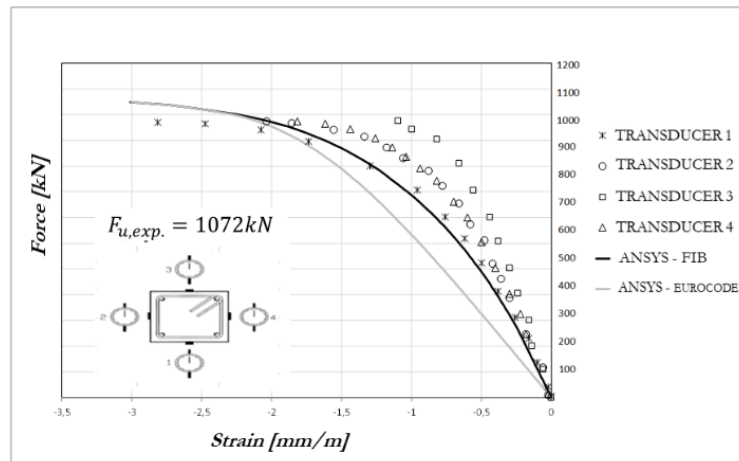
Figure 8. Comparison of Column 1 results.
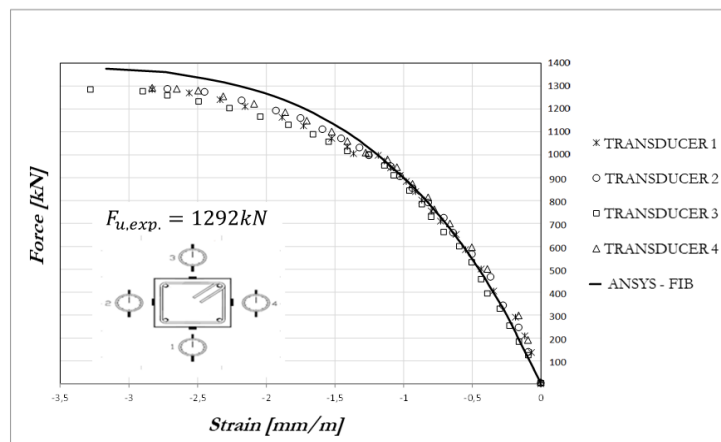
Figure 9. Comparison of Column 2 results.

4 VALIDATION OF THE THERMOMECHANICAL NUMERICAL MODEL

The numerical model was compared with results obtained by experimental tests conducted by Wu and Lie [27] and by analytical results presented in a later study published by Zhu and Lie [28] using the same columns. Thus, it is verified, with both experimental and analytical results, the proposed model validity and effectiveness in predicting the reinforced concrete columns thermomechanical behavior.

4.1 Brief description of the experimental program

Wu and Lie [27] conducted an experimental program including seven fire-exposed reinforced concrete columns, the aim of this study was to provide practical and real data to validate calculation methods that were being developed at the time. The columns were built with siliceous and calcareous aggregates, and the parameter studied were structural elements geometric dimensions and load types (centered and eccentric).

The experiments were carried out by exposing the columns to fire, fixed at the top and bottom, in a specially built furnace to evaluate preloaded columns. For centered loading, the prescribed load is applied by a hydraulic jack located under the column. After stabilization of deformation caused by loading, the structural element is exposed to fire in a controlled manner following the standard curve recommended by ISO 834 [15] which remains unchanged until the present days.

Concrete and steel temperatures were obtained using Type K Thermocouples (Cromel/Alumel) located at points of interest previously defined. The column axial displacements were measured by transducers that monitored the hydraulic

Rev. IBRACON Estrut. Mater., vol. 13, no. 4, e13404, 2020

10/14

jack motion during the test with an accuracy of 0.002 mm. More information about the procedures and instruments adopted in the experimental program can be obtained at Wu and Lie [27].

4.2 Brief description of the analytical method

The analytical method defined by Zhu and Lie [28] consists of different steps, involving, besides temperature calculation, calculation of mean deformations, and resistance capacity presented by columns in a fire situation.

First, temperatures were defined by subdividing the cross-sectional structure domain using the Finite Difference Method. The number of elements was set to allow that they can be arranged in a triangular mesh within the section boundaries. The methods used to derive the heat transfer equation and determine temperatures in reinforced concrete columns have been published in previous work [28].

In a second moment, the authors present the methodology used to determine strains, stresses, and strength of columns. Where the previously used triangular mesh was replaced by a square one. To obtain the column strength, the authors used a method based on a load-deflection analysis, idealizing columns, which are fixed at the ends during the tests, as pin-ended with a reduced length. From the curvature, the column strength is determined for each temperature. Strains were given for concrete and steel as the sum of mechanical strain, thermal expansion properties and elements curvature. With the values of strains, through material stress-strain relation, it was finally possible to determine the stresses acting on the structure. Further information about methods and parameters adopted for analytical calculation could be found in Zhu and Lie [28].

4.3 Numerical model aspects

In order to proceed with validation, Column 3 presented in Wu and Lie [27] and Zhu and Lie [28] was selected. The necessary information related to the column characteristics and properties can be seen in Table 1. The motivation in choosing such a column is given by analytical results demonstrated greater agreement with experimental ones.

For thermal analysis, the structure faces that will be exposed to fire and the time-temperature curve adopted are the only boundary conditions required. As discussed in section 3.2, Column 3 of [27] also allows the adoption of double symmetry. Therefore, only faces that do not represent symmetry planes are exposed to fire (see example in Figure 2). The material emissivity assigned was 0.7, and the convective heat transfer coefficient adopted was 25 W/(m^2.k).

The standard fire indicated by ISO 834 [15] was applied incrementally, i.e., every time step of fire, the software calculates the nodal temperature evolution. The thermal analysis uses an explicit default method to solve the problem differential equations (TRNOPT, FULL). Besides, it is noteworthy that the convergence criterion adopted for temperature was 1% of the vector norm.

The load applied to the column top section before starting the temperature rise was 1180 kN, and the other thermomechanical model aspects are identical to those presented in item 3.2. The only difference is the addition of LREAD command after mechanical loading, thus obtaining the influence of temperature rise on the preloaded column (see item 2.2).

4.4 Validation results

The present subitem exposes, results obtained by the proposed thermomechanical numerical model. These results include temperature rise in concrete structure according to the depth measured from concrete face at cross-section midline - 12 mm, 38 mm, 63 mm and 152 mm - (Figure 10), longitudinal bars temperature (Figure 11) and, finally, thermomechanical analysis represented by the column axial displacement during the time of fire exposure (Figure 12). Note that, for subtitling purposes, the names EXP were used for experimental results (item 4.1), CALC for those calculated analytically (item 4.2), and ANSYS for those obtained with the software aid (item 4.3).

Figures 10 and 11 show the convergence in temperature values during the standard fire. It is noteworthy that the numerical model provides, for steel, values corresponding almost exactly with those found experimentally, evidencing the satisfactory representativity obtained by computational simulation.

Figure 12 presents a new comparative analysis between numerical models using stress-strain diagrams suggested by Eurocode [18] and Fib Model Code [20]. In contrast to item 3.3, when dealing with high temperatures, the relation proposed by European code presents a behavior closer to that found in experimental data.

The thermomechanical validation shown in Figure 12, although numerical simulation presents a higher axial displacement, shows especially an important concordance on general column behavior when exposed to fire. Furthermore, it indicates 103 min fire resistance, differing approximately 5.8% of the value found in the laboratory (109 min), showing that

the numerical model is in favor of safety. It is important to note that the processing time for Column 3 thermal analysis was 35 min 46 sec, while for thermomechanical analysis, it was necessary 2h 47 min 20 sec.

It should be emphasized that, according to the experimental program description exposed in item 4.1, the columns are preloaded and subsequently exposed to fire. Thus, before observing a structure expansion due to the increase in temperature, there is a negative axial displacement (compression). However, this initial compressive displacement was neglected because the experimental test, as well as numerical model objective, is to analyze the structural behavior during the fire.
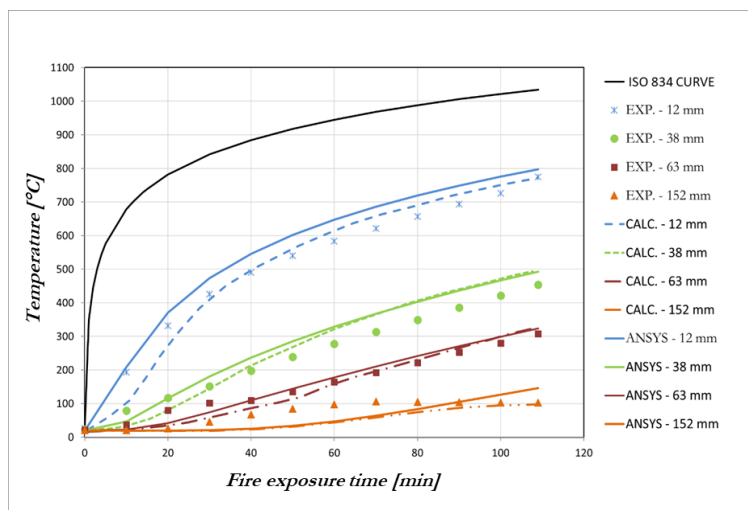
Figure 10. Comparison between experimental (EXP.), calculated (CALC.), and numerical values (ANSYS) of Column 3 temperature evolution at concrete points.
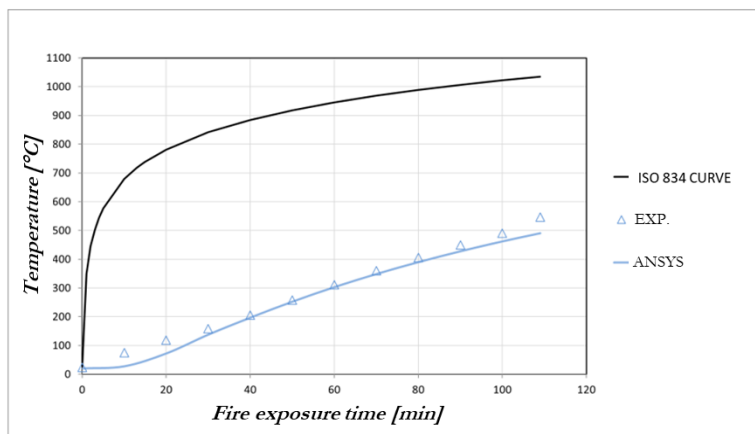
Figure 11. Comparison between experimental (EXP.) and numerical values (ANSYS) of Column 3 temperature evolution at longitudinal steel bars.

Additionally, Figure 12 also reveals that there is a divergence of approximately twice the column displacement when comparing the final values obtained between Eurocode relation [18] and the experimental data. This difference can be attributed to the high concrete theoretical capacity of deformation at high temperatures specified by current standards, according to the thermomechanical properties already mentioned in item 2.2.

To conclude thermomechanical result analysis, the structure specific strain (axial) is used as a parameter. This, in turn, represents the relation between the variation of axial displacement and column length. For Column 3, which length is 3.5 m, a divergence in the axial strain of only 0.0005 m/m or 0.5 mm/m is observed. This difference can be considered

not representative when considering all thermomechanical variables involved and the complexity of determining reinforced concrete structures behavior when exposed to high temperatures.
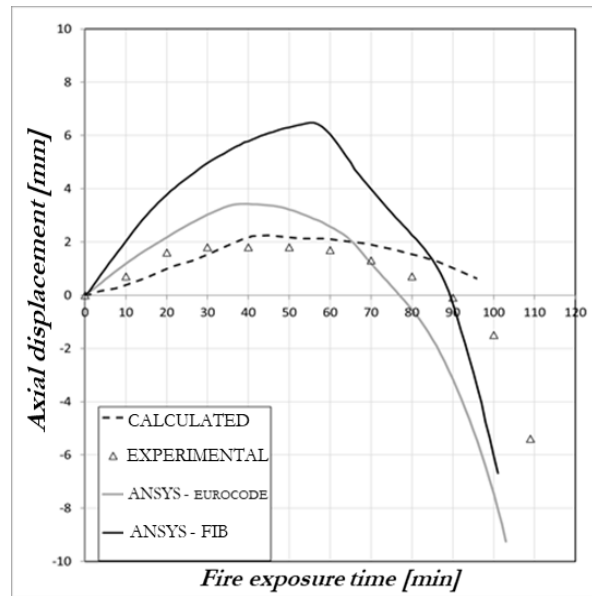
Figure 12. Comparison of Column 3 axial displacement.

5 CONCLUSIONS

This paper shows that the concrete constitutive law proposed for fib [20] better represented the behavior of the material at room temperature. However, it was found that increasing temperatures, simulations using the stress-strain relation specified by Eurocode [18] achieved the best results when compared to experimental data.

Moreover, it is concluded at the end of research that the proposed numerical model based on the finite element method, according to validations and comparisons made with experimental results, can predict the reinforced concrete columns thermomechanical behavior when exposed to fire.

It is also noted that the methodology presented here enables a wide range of studies in the building fire area, allowing adaptation of the created model to study other structures such as beams, slabs, and frames. The current study also allows us to expand the knowledge by parametric analyses of temperature influence on structural members with different dimensions, concrete cover, steel bar diameters, aggregate types, moisture content, among others.

ACKNOWLEDGMENTS

REFERENCES

[1] V. P. Silva, "Estruturas de aço em situação de incêndio," Ph.D. dissertation, Esc. Politéc., Univ. São Paulo, São Paulo, SP, 1997.

[2] V. P. Silva, S. B. Silva, U. D. Carlo, A. I. Seito, A. A. Gil, and F. D. Pannoni, *A Segurança Contra Incêndios no Brasil*. São Paulo: Projeto Editora, 2008.

[3] V. P. Silva, *Projeto de Estruturas de Concreto em Situação de Incêndio*. São Paulo: Blücher, 2012.

[4] C. N. Costa and V. P. Silva, "Estruturas de concreto em situação de incêndio," in *Ann. XXX Jornadas Sul-Americanas de Engenharia Estrutural*, Brasília, DF, 2002.

[5] C. N. Costa, "Dimensionamento de elementos de concreto armado em situação de incêndio," Ph.D. dissertation, Dep. Eng. Estrut. Geot., Esc. Politéc., Univ. São Paulo, São Paulo, SP, 2008.

[6] P. S. B. Lemos, "Estudo de estruturas de concreto sob altas temperaturas através do método dos elementos finitos," M.S. thesis, Esc. Eng., Univ. Fed. Rio Grande do Sul, Porto Alegre, RS, 2011, 148 p.

[7] L. D. Kirchhof, "Estudo teórico-experimental da influência do teor de umidade no fenômeno de spalling explosivo em concretos expostos a elevadas temperaturas," Ph.D. dissertation, Esc. Eng., Univ. Fed. Rio Grande do Sul, Porto Alegre, RS, 2010.

[8] F. L. Bolina, "Avaliação experimental da influência dos requisitos de durabilidade na segurança contra incêndio de protótipos de pilares pré-fabricados de concreto armado," M.S. thesis, Univ. Vale do Rio dos Sinos, São Leopoldo, RS, 2016.

[9] R. Regobello, "Análise numérica de seções transversais e de elementos estruturais de aço e concreto em situação de incêndio," M.S. thesis, Esc. Eng. São Carlos, Univ. São Paulo, São Carlos, SP, 2007.

[10] E. F. A. Kimura, "Análise termoestrutural de pilares de aço em situação de incêndio," M.S. thesis, Esc. Eng. São Carlos, Univ. São Paulo, São Carlos, SP, 2009.

[11] R. T. Santos, "Modelos numéricos de pilares mistos curtos de seções circulares de aço preenchidos com concreto em situação de incêndio," M.S. thesis, Esc. Eng. São Carlos, Univ. São Paulo, São Carlos, SP, 2009.

[12] T. I. Kotinda, " Modelagem numérica de vigas mistas aço-concreto simplesmente apoiadas: ênfase ao estudo da interface laje-viga," M.S. thesis, Esc. Eng. São Carlos, Univ. São Paulo, São Carlos, SP, 2006.

[13] F. P. D. Fernandes, "Análise numérica de vigas mistas de madeira e concreto em situação de incêndio," M.S. thesis, Esc. Eng. São Carlos, Univ. São Paulo, São Carlos, SP, 2018.

[14] ANSYS, *Mechanical APDL Version 19.2*. Canonsburg, PA: ANSYS Inc., 2018.

[15] International Organization for Standardization, *Fire Resistance Tests: Elements of Building Construction – Part 1.1 – General Requirements For Fire Resistance Testing*, ISO 834, 1999.

[16] Associação Brasileira de Normas Técnicas, *Dimensionamento de Estruturas de Aço de Edifícios em Situação de Incêndio – Procedimento*, NBR 14323, 2013.

[17] Associação Brasileira de Normas Técnicas, *Projeto de Estruturas de Concreto em Situação de Incêndio*, NBR 15200, 2012.

[18] European Committee For Standardization, *Eurocode 2: Design of Concrete Structures – Part 1.2 – General Rules – Structural Fire Design*, EN 1992-1-2, 2004.

[19] N. C. F. Lomba, "Resistência residual de vigas de betão armado após incêndio," M.S. thesis, Dep. Eng. Civ., Univ. Aveiro, Aveiro, 2011.

[20] Federation Internationale du Béton, *Model Code 2010, vol. 1* (Bulletin FIB 55). Lausanne: FIB, 2010.

[21] S. Bratina, B. Cas, M. Saje, and I. Planinc, "Numerical modelling of behavior of reinforced concrete columns in fire and comparison with Eurocode 2," *Int. J. Solids Struct.*, vol. 42, pp. 5715–5733, 2005.

[22] A. Balaji, P. Nagarajan, and M. Pillai, "Validation of Indian standard code provisions for fire resistance of flexural," *Songklanakarin J. Sci. Technol.*, vol. 37, no. 2, pp. 183–192, 2015.

[23] P. Kumar and V. K. R. Kodur, "Modeling the behavior of load bearing concrete walls under fire exposure," *Constr. Build. Mater.*, vol. 154, pp. 993–1003, 2017.

[24] J. M. Araújo, *Curso de Concreto Armado*, 4. ed. Rio Grande: Dunas, 2014.

[25] K. J. Willam and E. P. Warnke, "Constitutive model for triaxial behavior of concrete," in Proc. Inter. Assoc. Bridg. Struct. Eng. Conf., Bergamo, Italy, 1974, 174 p.

[26] R. F. Ramos and J. S. Giongo, "Pilares de concreto armado sob ação centrada com resistência do concreto de 25 MPa," *Cad. Engenharias Estrut. Sao Carlos*, vol. 7, no. 27, pp. 59–92, 2005.

[27] H. J. Wu and T. T. Lie, *Fire Resistance of Reinforced Concrete Columns: Experimental Studies* (Institute for Research in Construction Internal Report 632). Ottawa: National Research Council Canada, 1992.

[28] H. L. Zhu and T. T. Lie, *Fire Resistance Evaluation of Reinforced Concrete Columns* (Institute for Research in Construction Internal Report 639). Ottawa: National Research Council Canada, 1993.

Rev. IBRACON Estrut. Mater., vol. 13, no. 4, e13404, 2020

14/14

IBRACON Structures and Materials Journal
Revista IBRACON de Estruturas e Materiais

ORIGINAL ARTICLE

Incorporation of recycled aggregates from construction and demolition waste in paver blocks

Desempenho de blocos de concreto com incorporação de agregados reciclados provenientes de resíduos de construção e demolição

Cinthia Maia Pederneiras[a]
Maria Del Pilar Durante[a]
Ênio Fernandes Amorim[b]
Ruan Landolfo da Silva Ferreira[c]

[a]Universidade Federal do Rio Grande do Norte – UFRN, Natal, RN, Brasil
[b]Instituto Federal do Rio Grande do Norte – IFRN, Natal, RN, Brasil
[c]Instituto Federal de Educação, Ciência e Tecnologia de Pernambuco – IFPE, Pesqueira, PE, Brasil

Abstract: The consumption of natural resources and energy increased proportionally with the growth of the world population and its economic level. There was an increasing exponential consumption of natural resources, which implied an increase in environmental impacts. The construction sector is responsible for a very significant production of construction and demolition waste (CDW). Thus, there is a concern in search of a more sustainable final disposal. Many studies have been investigated the development of new materials with the incorporation of recycled aggregates from CDW. This paper presents a study of performance evaluation of concrete blocks produced with CDW. For that purpose, an experimental campaign was performed, including a characterization of the aggregates used. The incorporation of 100% of fine and coarse recycled aggregates. The mixtures were designed according to the condition of the aggregate (dry, washed or saturated). The performance of these blocks was evaluated in terms of mechanical strength and water absorption. Some additional tests were also performed to deeper analyze of the microstructure of these blocks. To assess the durability of the concrete blocks, a full-scale road was built. The results were very positive, since there were no significant differences between the modified concrete blocks and the reference sample (0% of the CDW). The modified block with fine aggregate presented the best performance of all the blocks, concerning mechanical strength. In addition, the performance of concrete blocks with washed recycled aggregates had a better performance compared to the others. The results obtained were satisfactory for the application of the blocks in the streets with low movement and low load.

Keywords: recycled aggregates, construction and demolition waste, paver blocks.

Resumo: O consumo de recursos naturais e energia aumentou proporcionalmente com o crescimento da população mundial e seu nível econômico. Houve um consumo exponencial crescente de recursos naturais, o que implicou em um aumento nos impactos ambientais. O setor da construção é responsável por uma produção muito significativa dos resíduos de construção e demolição (RCD). Dessa forma, evidencia-se uma preocupação em busca de destino final mais sustentável, com isso muitos estudos estão sendo feitos a fim de desenvolver novos produtos com a substituição de recursos naturais por RCD. Este trabalho pretende analisar o comportamento de blocos de concreto produzidos com RCD. Para isso, foi realizado um programa experimental, incluindo uma caracterização dos agregados utilizados. A substituição foi de 100% de agregados naturais miúdos e graúdos por agregados reciclados. As misturas foram projetadas de acordo com a condição do agregado (seco, lavado ou saturado). O desempenho destes blocos foi avaliado em termos de resistência mecânica e absorção de água. Alguns testes extras também foram formulados para entender a microestrutura desses blocos. Para avaliar a durabilidade dos blocos de pavimentação, foi realizada uma estrada em escala real. Os resultados da pesquisa foram muito positivos, uma vez que não houve diferenças significativas entre os blocos de concreto modificados e a amostra de referência (0% do RCD). Em termos mecânicos, o concreto modificado com agregado miúdo foi o que apresentou o melhor desempenho de todos

os blocos. Além disso, o desempenho de blocos de concreto usando agregados reciclados lavados foi melhor em comparação com os outros. Os resultados obtidos foram satisfatórios para a aplicação dos blocos em ruas de baixo movimento e baixa carga.

Palavras-chave: agregados reciclados, resíduos de construção e demolição, blocos de pavimentação.

1 INTRODUCTION

The construction industry has been considered one of the most waste producer and consumer of natural resources. This environmental concern encouraged the current trend of using recycled aggregates from construction and demolition waste for production of cementitious materials.

According to the Brazilian Association for Recycling of Construction and Demolition Waste (ABRECON) [1], in Brazil in the year of 2015 the estimated production of waste was approximately 85 million m^3. The amount of recycled CDW was an average of 5 million m^3.

The use of CDW as recycled aggregates is one of the most feasible solution. Several studies have been published about the use of recycled aggregate as replacement of natural sand. In this study, the performance of concrete blocks for interlocked paving with the incorporation of CDW as recycled aggregate is analyzed.

Researches have been developed to evaluate the use of recycled aggregates in concrete. From the literature, it can be verified that the materials produced with recycled aggregates achieve the required standards and specifications. Although, in some cases, there is a decrease in the mechanical strength. Particularly in the manufacture of concrete blocks [2]–[8], pre-cast cementitious products [9] and bricks [10].

Nonetheless, some authors have demonstrated an improvement on the mechanical properties of these materials with the use of recycled aggregate. Penteado et al. [11] observed an increase in compressive strength of the concrete blocks with recycled fine aggregates when compared to the reference blocks. Evangelista and Brito [12] justified these better results due the presence of non-hydrated cement particles in the recycled aggregate, which could contribute to a better bond between the cement paste and aggregates, due to their higher porosity. Rodriguez et al. [8] and Leite [13] studied the mechanical performance of concrete produced with recycled aggregates and obtained similar results.

On the other hand, the type of recycled aggregate affects differently the performance of the materials. Thus, Bravo et al. [14] highlighted an increase in impact resistance when coarse recycled aggregates were used in concrete blocks. Braga et al. [15] pointed out that the incorporation of fine recycled aggregates from CDW can increase the mechanical strength of the concrete due to the non-hydrated cement particles in the recycled material.

Bear in mind that the loss of mechanical strength is a limiting factor for the use of recycled aggregates, and it is higher when the water/cement ratio is lower [8], [16]. Notwithstanding the foregoing, some authors justified the increase of compressive strength in concrete with fine recycled aggregates due the pozzolanic effect of the fine particles [17], [18]

The higher content of fines in the recycled aggregates can improve the transition zone between the cementitious matrix and the aggregate, which contributes to a greater compactness of the concrete [19]. According to Lovato et al. [20] the fines particles provide a better packaging. As the recycled aggregate has higher absorption it promotes a greater adhesion between the cement paste and the aggregate, through the absorption of the paste and the precipitation of the crystals of hydration in the pores of the aggregate.

Another characteristic of the recycled aggregate that affects the concrete behavior is the presence of old mortar particles adhered to the grains. This could be related to a higher water absorption, higher porosity and lower resistance of the modified concrete [21]–[23].

In this research, the recycled aggregates were used in three different conditions, such as dried, washed and saturated. Rodrigues et al. [24] suggested to wash the aggregates to discard the fraction below 0.063mm, which can improve the quality of the recycled concrete produced. Poon et al. [25] recommended to saturate the recycled aggregate before mixing with the cement. This can reduce the water absorption of the aggregates.

Therefore, this research intends to analyze the performance of the concrete blocks with different conditions of the recycled aggregate.

1.1 Justification

Considering the environmental impacts, it has been developed several researches about the use of recycled aggregates from CDW. Therefore, this study presents a feasible product with the incorporation of recycled aggregate from CDW.

2 MATERIALS AND EXPERIMENTAL PROGRAM

2.1 Materials

The following materials were used in this research: cement, sand, additive and water.

2.1.1 Cement

The binder used was cement type CP II-Z-RS, mainly used for the precast industry. The physical, mechanical and chemical properties are presented in Table 1.

Table 1. Characteristics of CP II-Z-RS.

Physical characteristics	
Density (g/cm^3)	3.0
Blaine specif. area (cm^2/g)	4362
Initial set (min)	139
Final set (min)	191
Chemical characteristics	
Al2O3	4.41
CaO	68.68
Fe2O3	2.35
K2O	1.26
MgO	2.70
SiO2	14.71
TiO2	0.33
SO3	5.48

2.1.2 Aggregates

Both aggregates (fine and coarse) were separated in terms of their size, by sieving. The recycled aggregates were collected according to NBR NM 26 [26], dried in an oven (105 ± 5 °C) for 48 hours and then cooled to the room temperature. After this procedure, they were submitted to the characterization tests. The fine fraction was sieved to remove particles over 4.75mm. The coarse aggregate was sieved to remove particles over 12.5mm and smaller than 4.75mm.

2.1.3 Additive

The additive used was SikaPaver HC-10.

2.2 Aggregates characterization

The characterization tests were performed for natural and recycled aggregates (fine and coarse). The physical tests: size distribution [27], dry bulk density [28], [29], water absorption by capillarity [30], abrasion resistance Los Angeles [31], the superficial area of the fines of the aggregates determined from the physical adsorption of the nitrogen on the materials by the Brunauer-Emmett-Teller (BET) method, these analyzes were performed by the BEL JAPAN model BELSORP-mini II.

The chemical analysis was performed by the EDX-720 X-ray fluorescence spectrometer Shimadzu in a vacuum atmosphere and the semi-quantitative method was developed. The micrographs were obtained from Hitachi model TM-3000.MEV equipment. The X-ray diffractogram was performed for the mixed recycled aggregate sample. The equipment used was Shimadzu model XRD - 7000. The specimen with a particle size of less than 0.15 mm were submitted to the test, using Cu - Kα radiation, with accelerated voltage 40 kV and 30 mA current, with a 2θ scan of 5 ° to 80 ° and speed of 5°/ min.

2.3 Mixes proportions

Table 2 presents the mortars specification. Table 3 shows the mixes compositions.

Table 2. Mixes' composition.

Mixes	Mixes' composition	Recycled Aggregates Condition
FNCN	Fine Natural Aggregate + Coarse Natural Aggregate	-
FNCRD	Fine Natural Aggregate + Coarse Recycled Aggregate	Dried
FNCRW	Fine Natural Aggregate + Coarse Recycled Aggregate	Washed
FNCRS	Fine Natural Aggregate + Coarse Recycled Aggregate	Saturated
FRCND	Fine Recycled Aggregate + Coarse Natural Aggregate	Dried
FRCNW	Fine Recycled Aggregate + Coarse Natural Aggregate	Washed
FRCRD	Fine Recycled Aggregate + Coarse Recycled Aggregate	Dried
FRCRW	Fine Recycled Aggregate + Coarse Recycled Aggregate	Washed

Table 3. Mix proportions of concrete (kg/m3).

Mixes	Cement	Water	Natural sand	Recycled sand	Natural gravel	Recycled gravel
FNCN	199.7	76.8	1716.8	-	533.8	-
FNCRD	197.4	75.9	1696.8	-	-	440.3
FNCRW	197.4	75.9	1696.8	-	-	440.3
FNCRS	197.4	75.9	1696.8	-	-	440.3
FRCND	198.6	76.4	-	1649.6	530.8	-
FRCNW	198.6	76.4	-	1649.6	530.8	-
FRCRD	196.3	75.5	-	1630.6	-	437.9
FRCRW	196.3	75.5	-	1630.6	-	437.9

It was investigated the use of fine and coarse recycled aggregates under three conditions: dried, washed and saturated. In order to verify the influence of its condition on the properties of the concrete blocks produced.

Dried condition: the recycled aggregates were introduced into the mixture as they are produced in the plant.

Washed condition: the recycled aggregates were washed for removal of the pulverulent material, the sieve used in the wash was #200 (0.075mm). After that the recycled aggregates were dried before adding in the mix.

Saturated condition: the recycled aggregates were immersed in water for 24 hours before being mixed for the production of the blocks. However, the saturated fine recycled aggregates did not obtain the required consistency, discarding this possibility. Thus, only the recycled coarse aggregates were saturated.

2.4 Tests

The production of the blocks was performed in a real scale inside a precast plant. The dimensional tolerance analysis of the blocks was according to NBR 9781 [32]. The standard refers to the dimensions of the block as 10x20x6cm (width x length x thickness), admitting 3 cm of tolerance.

The compressive strength was evaluated at the ages of 7, 14, 28 and 365 days with six blocks for each sample, according to NBR 9781 [32]. The standard requires that two auxiliary boards for the compressive strength test must be circular, with a diameter of 85 mm and a minimum thickness of 20 mm, made of steel.

Water absorption at 28 and 365 days with three blocks of each composition was analyzed. For the anaysis of water absorption, the test was carried out according to NBR 9781 [32].

2.5 Evaluation of real-scale interlocked blocks

To evaluate the performance in the field, a real-scale experimental stretch of interlocked paving was performed with the blocks produced. The prototype was built in the Recycling Plant, which provided the recycled aggregates. The segment was divided into parts for evaluation of each composition, in order to analyze the functional performance of the blocks.

3 RESULTS AND DISCUSSIONS

3.1 Aggregates characterization

Figure 1 shows the size distribution curve of the sand. The recycled sand presented a curve of differentiated size of particles, which enhance the packaging.
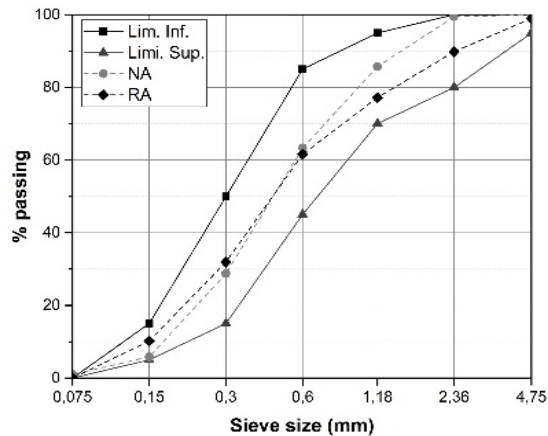
Figure 1. Size distribution of natural and recycled fine aggregate. NA = Natural Aggregate. RA = Recycled Aggregate.

The size distribution of the coarse recycled aggregate is similar to that the natural aggregate, as can be observed in Figure 2. The compactness of the concrete affects directly the mechanical behavior. It can be observed that the recycled sand presents a better size distribution, which could improve the mechanical resistance.
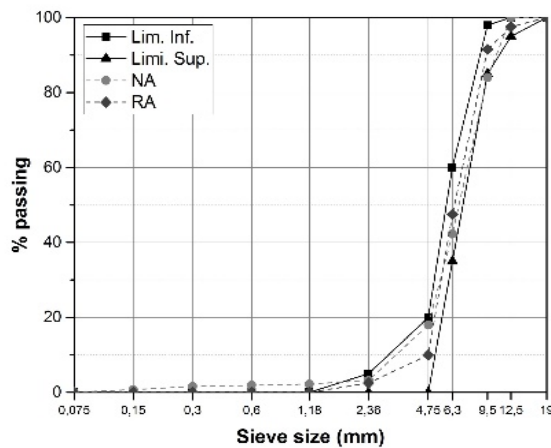
Figure 2. Size distribution of natural and recycled coarse aggregate. NA = Natural Aggregate. RA = Recycled Aggregate.

Table 4 shows the results of the physical tests of natural and recycled fine aggregates. The density of the recycled aggregate is lower when compared to the natural aggregate, while the water absorption has significantly higher values. These characteristics, in general, are attributed to the old mortar adhered to the particle [21], [22], [33].

Rev. IBRACON Estrut. Mater., vol. 13, no. 4, e13405, 2020

5/13

Table 4. Fine aggregates characteristics.

	Natural Sand	Recycled Sand
Fineness Modulus	2.17	2.27
Bulk density (kg/m^3)	1490	1440
Dry density (kg/m^3)	2620	2510
Fine content (%)	1.00	7.00
Surface area	1.227	3.547

In general, recycled aggregates present lower density than natural aggregates. This fact could be attributed to their heterogeneity due to the waste´s composition. Thus, the density of the recycled materials tends to be lower than those of conventional mortar and concrete [8].

According to the standard for determining the content of powdery materials in aggregates (NBR 7219) [34] the maximum values of materials passing through the 0.075mm sieve is 5%. A higher content of fine particles in the mix can affect the required kneading water, which implies a reduction in the mechanical resistance of the concrete produced, as well as, a decrease in abrasion resistance [35]. This may affect negatively the concrete, due to the higher water consumption and the presence of clay minerals.

In this research, the recycled fine aggregates obtained 7% of particles passing through the #200 sieve. This amount of dust can affect the bond between the aggregate and the paste, which may weaken the transition zone. Washing is a technique used to remove the pulverulent material from the recycled aggregates, since the content of fines correlates directly with the water absorption of the aggregates, due to the greater surface area of the materials. The reduction of the very fines particles decreases the water/cement ratio, which can influence the workability and improve the properties of the hardened concrete.

The results obtained in the laser granulometry (BET) test for the fines material showed the recycled aggregates with greater surface area, corroborating with other studies [19], [36]. This could be explained by a surface more irregular and porous. As a consequence of this, the recycled aggregate can provide a strengthening of the interfacial transition zone between the cementitious matrix and the aggregates.

Table 5 presents the results of the tests performed with the coarse aggregates. The Los Angeles abrasion resistance analyses the quality of the material. It is identified the resistance to fragmentation by shock and friction of the particles. The resistance of the recycled aggregate is not the same as the material that originated it, because the crushing process weakens the particle, which causes the cracks inside the recycled aggregate.

Table 5. Coarse aggregates characteristics.

	Natural Gravel	Recycled Gravel
Bulk density (kg/m^3)	1390	1160
Dry density (kg/m^3)	2610	2060
Fine content (%)	1.00	4.00
Los Angeles	25	49
Water absorption (%)	1.00	8.00

Table 6 shows the chemical analyzes of the natural and recycled aggregates.

Table 6. X Ray fluorescence test results.

Samples	Al2O3	CaO	Fe2O3
NA	12.10	4.65	8.99
RA	10.18	29.80	8.90

NA = Natural Aggregate. RA = Recycled Aggregate.

The recycled aggregates present a chemical composition similar to that found in other studies that analyzed the recycled aggregates [22], [37], [38].

The main elements found in the recycled aggregates are oxides of silica, calcium, aluminum and iron, originating mainly from hydrated cementitious compounds (concretes and mortars), as well as materials of ceramic origin [39]. It is important

to highlight the presence of sulfur oxide (SO3) in the recycled aggregate, since this chemical element can cause gradual loss of mechanical resistance and affect the durability of materials produced with this type of aggregates [40].

The results of the images obtained by SEM for the natural and recycled aggregates are shown in Figures 3 and 4.
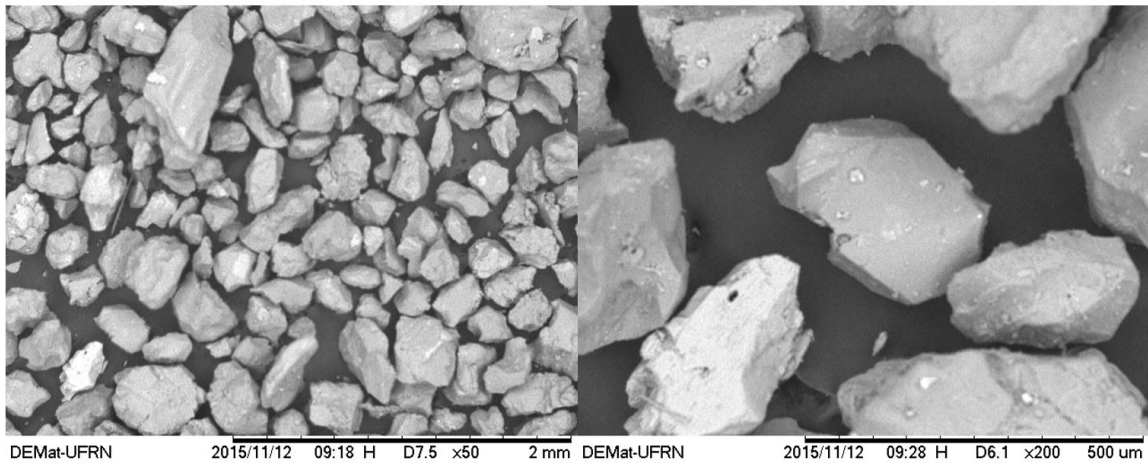
Figure 3. SEM image of obtained natural aggregate sample.
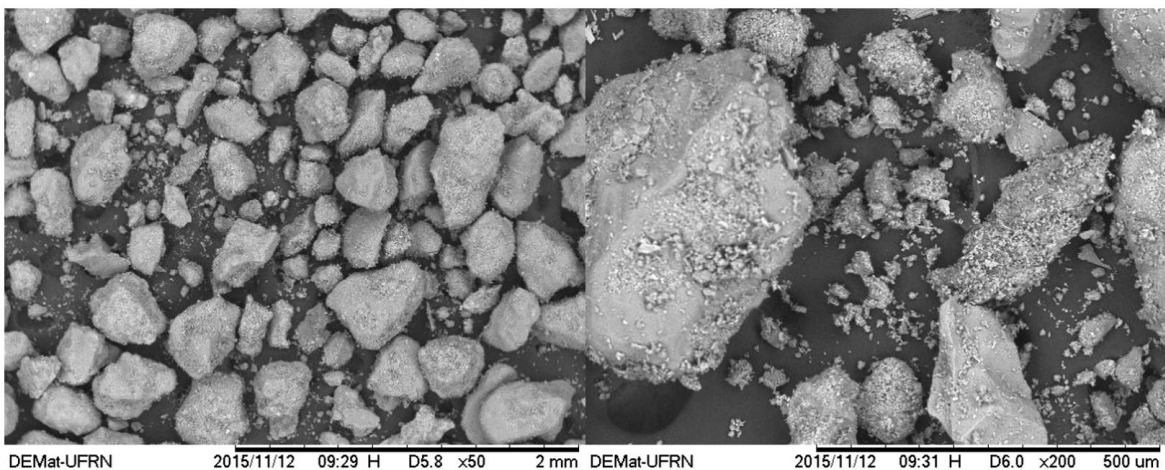
Figure 4. SEM image of obtained recycled aggregate sample.

The particles of the natural aggregates present regular texture and size. However, the recycled aggregates present irregular shape and size, with more defined edges, which can be attributed to the CDW crushing process to obtain these aggregates.

The particles of the recycled aggregates also present a roughened porous surface, which may be due to the old mortar adhered to the particles, corroborating with the micrographs presented by other authors [23], [41], [42]. The rough surface of the particle can improve the adhesion between the particles and the cementitious matrix, increasing the mechanical resistance.

Figure 5 shows the main crystalline phases of the recycled aggregate. In agreement with the results of the chemical composition, the recycled aggregate presents silicates (quarzt; feldspars-albite and microcline; mica-muscovite and clay mineral-kaolinite), sulfates (gypsite) and carbonates (calcite).

The mineralogical composition of the recycled aggregate originated from the variety of original components (concrete, mortar, and ceramics), and is consistent with other published studies [10], [23], [24], [27], [39], [40].
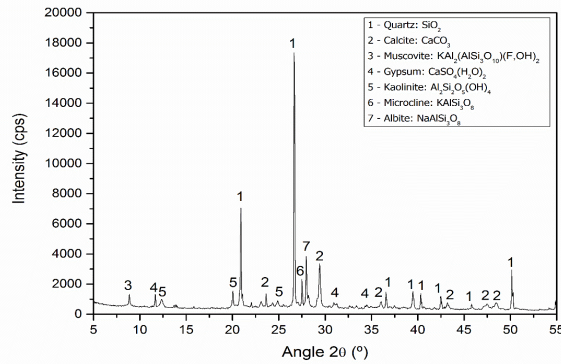
Figure 5. Diffractogram of the recycled aggregate.

3.2 Blocks characterization

Table 7 present the results obtained of water absorption and compressive strength of the concrete blocks. These results are discussed individually in the following sections.

Table 7. Properties of concrete blocks.

Samples	Water absorption (%)				Compressive strength (MPa)							
FNCN	28 d	SD	365 d	SD	7 d	SD	14 d	SD	28 d	SD	365 d	SD
FNCRD	4.0	0.1	2.0	0.14	10.97	0.25	11.6	0.88	13.12	0.87	18.1	0.33
FNCRW	7.0	0.48	6.0	0.24	7.41	0.69	9.26	1.01	9.72	0.77	14.28	0.55
FNCRS	6.0	0.158	5.0	0.38	9.11	0.38	10.66	0.98	12.22	0.54	16.58	0.48
FRCND	8.0	0.25	5.0	0.54	8.2	0.54	10.6	0.65	13.56	0.59	19.23	0.59
FRCNW	3.0	0.36	2.0	0.41	11.57	0.87	12.96	0.67	15.2	0.67	24.35	0.77
FRCRD	4.0	0.58	3.0	0.33	15.71	0.59	17.35	0.77	22.16	0.55	27.34	0.99
FRCRW	6.0	0.12	5.0	0.21	9.85	0.25	10.29	0.88	11.13	0.34	15.34	1.05

Legenda: d = days; SD = Standard deviation

3.2.1 Water absorption

The Brazilian standard NBR 9781 [32] based on ASTM C 936-1 [43], requires an average water absorption results of less than or equal to 5%, with individual values not exceeding 7% being accepted. Figure 6 shows the values of the absorption rate of the blocks at 28 and 365 days.
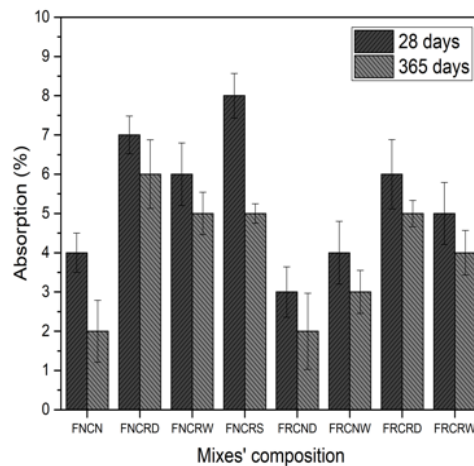
Figure 6. Absorption of water from the blocks at 28 and 365 days.

The samples with dried recycled sand and natural coarse aggregate obtained the lowest rate of water absorption at 28 days. The recycled sand with high powder content may have caused a better packaging of the particles in the concrete, which contributes to a better compactness of the block. The continuous size distribution of recycled sand may have influenced a lower rate of water absorption.

At 28 days, the concrete blocks produced with washed recycled aggregate achieved the requirements of the standard, obtained the water absorption rate less than or equal to 5% beyond the reference. On the other hand, the blocks produced with natural sand and recycled coarse aggregates obtained an average water absorption higher than 5%.

The reference block had the lowest volume of voids and, consequently, the highest density. Blocks with natural sand and dried coarse recycled aggregate showed a higher absorption rate as greater voids indices. However, the block with natural sand and washed coarse recycled obtained a lower rate of water absorption. It is emphasized that the washing procedure changed the water absorption rate of the block with coarse recycled aggregate.

The blocks produced with recycled sand presented water absorption similar to the block with natural aggregates. As for the blocks with washed fine recycled aggregates, it was observed that they obtained higher absorption results than the blocks with dried recycled.

3.2.2 Compressive strength

Figure 7 shows the results obtained in the compressive strength of all specimens at 7, 14, 28 and 365 days. The best mechanical strength at 28 and 365 days was the modified concrete produced with washed recycled sand and natural coarse aggregate.
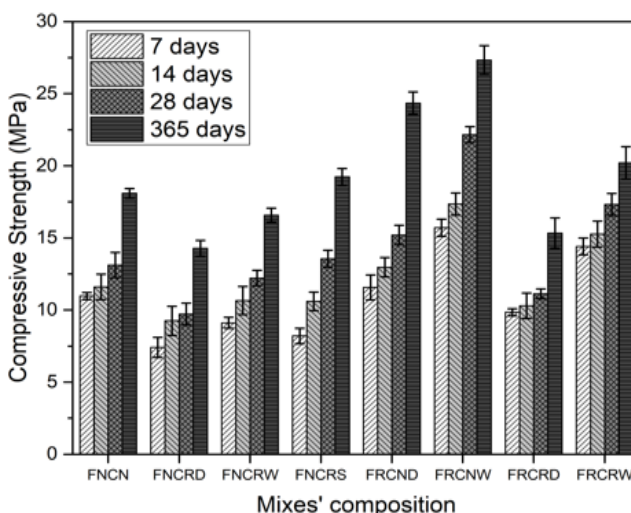
Figure 7. Comparison of the compressive strength of the blocks tested.

Blocks with recycled sand presented a better mechanical performance compared to the reference concrete block. Vieira and Dal Molin [44] also followed the same trend. There was an increase in the compressive strength with 100% recycled sand and 0% recycled coarse aggregate. This better performance could also be attributed to a chemical factor due to a possible pozzolanic effect of the very fine material.

Figure 8 presents the results of the compressive strength of the blocks by the fine and coarse aggregates used. Figure 8 shows the increment in compressive strength of the blocks produced with fine recycled aggregates when compared to the others.
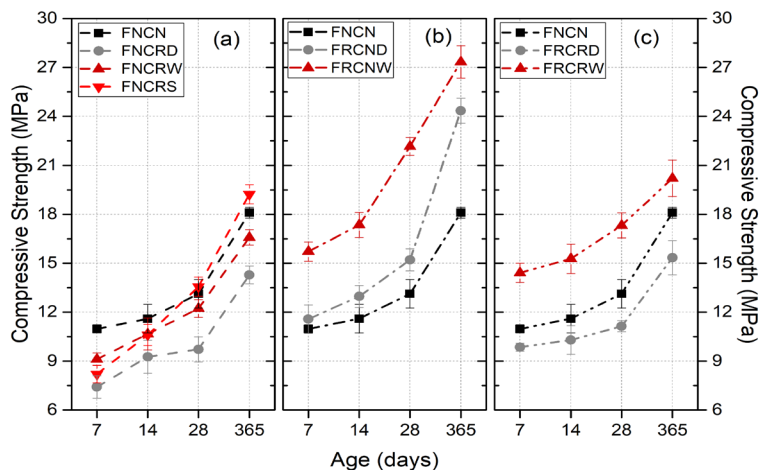
Figure 8. Compressive strength of the blocks tested by fine and coarse aggregates.

Leite et al. [45] also found that the concrete blocks with fine recycled aggregates presented pozzolanic activity indexes, which may be associated to the increase of compressive strength in concretes with high content of sand replacement at advanced ages. Khatib [17] verified the increase of compressive strength from 28 to 90 days in concrete with fine recycled aggregate and justified this effect by the possible pozzolanic activity of the fines.

Cabral et al. [19] also verified that the use of the fine recycled aggregate increased the compressive strength of the concrete. Possible reasons for this effect were the pozzolanic reactions, which improve the interfacial transition zone of the matrix, the roughness of the particles. It reinforces the bonds between the cement paste and the aggregates, and the water absorbed by the particles may be available for continuous hydration of the cement. These results were also pointed out by other authors [12], [18], [46].

In general, the mechanical strength present significant improvements with the incorporation of fines, due to both the filler effect, due to a filling of voids by the very fine particles, which increase the compactness of the concrete. Braga et al. [15] pointed out that with the replacement of fine aggregate, in addition to the filler effect, it occurs the hydraulic effect of non-hydrated cement on the recycled material. Thus, the strength may depend on the type of fines and the amount of replacement.

From the results obtained in this research and from other authors [20], [47] it is evident that the use of recycled aggregates in concrete does not significantly affect the compressive strength. However, it is essential to consider the characterization and treatment of recycled aggregates. Leite et al. [45] found that the use of recycled aggregate in concrete replacing the natural aggregate, mainly for low water/cement ratios is feasible.

The concrete produced with coarse recycled aggregates presented a decrease of compressive strength when compared to the reference blocks. At 365 days, obtained reduction of 21% and 8%, with dried and washed aggregates, respectively. Vieira and Dal Molin [44] and Poon and Chan [2] also found a reduction of mechanical resistance with the replacement of 100% of coarse recycled aggregates.

For the manufacture of precast concrete a lower water/cement factor is required, which may present difficulty in the workability of the mixture. Thus, it is necessary to take into consideration that recycled aggregates can absorb part of the kneading water. Thus, the decrease of mechanical strength with recycled aggregate can be attributed to the water/cement ratio, the higher water absorption and the lower density of the recycled aggregates.

The performance of the concrete with recycled aggregate depends mainly on the cement consumption and the water/cement ratio. The decrease of compressive strength can be attributed to factors such as low resistance and density of the recycled aggregate and higher water absorption, which implies negatively in the workability and consequently in the mechanical resistance.

3.2.3 Analysis of the experimental section

The interlocking pavement road was analyzed after one year of being used. In general, the pavement indicated good functionality and its in use, supporting the demanded load.

Visually, in the reference blocks can notice no evidence of broken edges. The blocks produced with recycled fine aggregate also exhibit similar behavior as the reference block. However, blocks produced with coarse recycled aggregate presented higher damages.

In order to evaluate the mechanical performance of the specimens, the compressive strength was analyzed in blocks with total replacement of fine and coarse recycled aggregates (FRCRD / FRCRW), the results are presented in Figure 9. It was observed a reduction in the mechanical performance. Blocks produced with dried recycled aggregates obtained an average of 9.87MPa, a reduction of 34.2% when compared to the results obtained of the same samples kept 365 days inside the laboratory conditions.
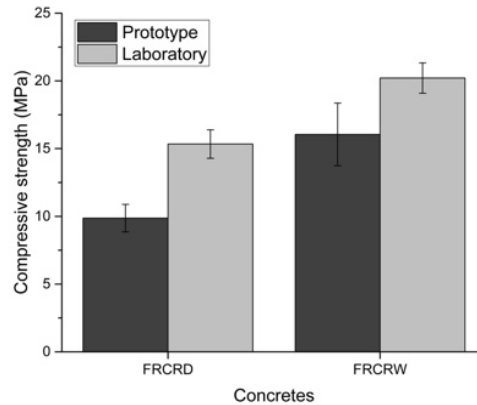
Figure 9. Comparison between the compressive strength of the blocks produced in the laboratory and in the field.

The blocks produced with washed recycled aggregates presented a compressive strength of 16.05MPa, which means a reduction of 27% according to the resistance at 365 days. The decrease in mechanical strength can be attributed to the load borne by the parts during this period. In general, the pavement indicated good functionality and is in use in the plant itself, supporting the demanded load.

4 CONCLUSIONS

Modified blocks with the incorporation of recycled sand presented a better performance comparing to the reference concrete. On the other hand, blocks with the incorporation of coarse aggregates presented several drawbacks.

Blocks produced with washed recycled aggregates presented better results in all properties. The removal of the powdery material provided greater compressive strength.

The visual aspects of the modified blocks in the experimental full-scale presented slightly more damaged than the reference blocks.

Blocks produced with recycled aggregates could be used for low-load road, such as sidewalks, gardens and streets.

ACKNOWLEDGEMENTS

REFERENCES

[1] Associação Brasileira para Reciclagem de Resíduos da Construção Civil e Demolição. "*Recycling of Construction and Demolition Waste in Brazil, Statistics Reports 2014-2015*." São Paulo: ABRECON, 2015. Accessed: Feb. 15, 2018. [Online]. Available: http://www.abrecon.org.br/pesquisa_setorial/

[2] C. S. Poon and D. Chan, "Feasible use of recycled concrete aggregates and crushed clay brick as unbound road sub-base," *Constr. Build. Mater.*, vol. 20, pp. 578–585, 2006.

[3] J. Yang, Q. Du, and Y. Bao, "Concrete with recycled concrete aggregate and crushed clay bricks," *Constr. Build. Mater.*, vol. 25, pp. 1935–1945, 2011.

[4] M. N. Soutsos, K. Tang, and S. G. Millard, "Use of recycled demolition aggregate in precast products, phase II: concrete paving blocks," *Constr. Build. Mater.*, vol. 25, pp. 3131–3143, 2011.

[5] F. Lopez-Gayarre, C. Lopez-Colina, M. A. Serrano, and A. Lopez-Martínez, "Manufacture of concrete kerbs and floor blocks with recycled aggregate from C&DW," *Constr. Build. Mater.*, vol. 40, pp. 1193–1199, 2013.

[6] M. M. Sabai, M. G. D. M. Cox, R. R. Mato, E. L. C. Egmond, and J. J. N. Lichtenberg, "Concrete block production from construction and demolition waste in Tanzania," *Resour. Conserv. Recycling*, vol. 72, pp. 9–19, 2013.

[7] J. Xiao, L. Li, L. Shen, and C. S. Poon, "Compressive behaviour of recycled aggregate concrete under impact loading," *Cement Concr. Res.*, vol. 71, pp. 46–55, 2015.

[8] C. Rodriguez et al., "The incorporation of construction and demolition wastes as recycled mixed aggregates in non-structural concrete precast pieces," *J. Clean. Prod.*, vol. 127, pp. 152–161, 2016.

[9] F. Ozalp, H. D. Yilmaz, M. Kara, O. Kaya, and A. Sahin, "Effects of recycled aggregates from construction and demolition wastes on mechanical and permeability properties of paving stone, kerb and concrete pipes," *Constr. Build. Mater.*, vol. 110, pp. 17–23, 2016.

[10] M. Contreras et al., "Recycling of construction and demolition waste for producing new construction material (Brazil case study)," *Constr. Build. Mater.*, vol. 123, pp. 594–600, 2016.

[11] C. S. G. Penteado, E. V. Carvalho, and R. C. C. Lintz, "Reusing ceramic tile polishing waste in paving block manufacturing," *J. Clean. Prod.*, vol. 112, pp. 514–520, 2016.

[12] L. Evangelista and J. Brito, "Durability performance of concrete made with fine recycled concrete aggregates," *Cement Concr. Compos.*, vol. 32, no. 1, pp. 9–14, 2010.

[13] M. A. Leite, "Evaluation of mechanical properties of concretes produced with recycled aggregates of construction and demolition wastes," Ph.D. dissertation, Univ. Fed. Rio Grande do Sul, Porto Alegre, 2001.

[14] M. Bravo, J. Brito, J. Pontes, and L. Evangelista, "Mechanical performance of concrete made with aggregates from construction and demolition waste recycling plants," *J. Clean. Prod.*, vol. 99, pp. 59–74, 2015.

[15] M. Braga, J. Brito, and R. Veiga, "Reduction of the cement content in mortars made with fine concrete aggregates," *Mater. Struct.*, vol. 47, no. 1, pp. 171–182, 2014.

[16] C. Medina, W. Zhu, and T. Howind, "S_anchez de Rojas, M.I., Frías, M. Influence of mixed recycled aggregate on the physical e mechanical properties of recycled concrete," *J. Clean. Prod.*, vol. 68, pp. 216–225, 2014.

[17] J. M. Khatib, "Properties of concrete incorporating fine recycled aggregate," *Cement Concr. Res.*, vol. 35, no. 4, pp. 763–769, 2005.

[18] S. Laserna and J. Montero, "Influence of natural aggregates typology on recycled concrete strength properties," *Constr. Build. Mater.*, vol. 115, pp. 78–86, 2016.

[19] A. E. B. Cabral, V. Schalch, D. C. C. Dal Molin, and J. L. D. Ribeiro, "Mechanical properties modeling of recycled aggregate concrete," *Constr. Build. Mater.*, vol. 24, no. 4, pp. 421–430, 2010.

[20] P. S. Lovato, E. Possan, D. C. C. Dal Molin, A. Masuero, and J. Ribeiro, "Modeling of mechanical properties and durability of recycled aggregate concretes," *Constr. Build. Mater.*, vol. 26, pp. 437–447, 2012.

[21] M. Etxeberria, E. Vázquez, A. Marí, and M. Barra, "Influence of the amount of recycled coarse aggregates and production process on properties of recycled aggregate concrete," *Cement Concr. Res.*, vol. 27, no. 5, pp. 735–742, 2006.

[22] M. Pepe, R. D. Toledo Fo., E. A. Koenders, and E. Martinelli, "Alternative processing procedures for recycled aggregates in structural concrete," *Constr. Build. Mater.*, vol. 69, pp. 124–132, 2014.

[23] L. Evangelista, M. Guedes, J. de Brito, A. C. Ferro, and M. F. Pereira, "Physical, chemical and mineralogical properties of fine recycled aggregates made from concrete waste," *Constr. Build. Mater.*, vol. 86, pp. 178–188, 2015.

[24] F. Rodrigues, M. Carvalho, L. Evangelista, and J. Brito, "Physical-chemical and mineralogical characterization of fine aggregates from construction and demolition waste recycling plants," *J. Clean. Prod.*, vol. 52, pp. 438–445, 2013.

[25] C. S. Poon, S. C. Kou, and L. Lam, "Use of recycled aggregates in molded concrete bricks and blocks," *Constr. Build. Mater.*, vol. 16, pp. 281–289, 2002.

[26] Associação Brasileira de Normas Técnicas, *Aggregates – Sampling*, NBR NM 26, 2001.

[27] Associação Brasileira de Normas Técnicas, *Aggregates – Sieve Analysis of Fine and Coarse Aggregates*, NBR NM 248, 2003.

[28] Associação Brasileira de Normas Técnicas, *Aggregate Determination of the Unit Weight and Air-void Contents*, NBR NM 45, 2006.

[29] Associação Brasileira de Normas Técnicas, *Fine Aggregates – Determination of the Bulk Specific Gravity and Apparent Specific*, NBR NM 52, 2009.

[30] Associação Brasileira de Normas Técnicas, *Coarse Aggregates – Determination of the Bulk Specific Gravity, Apparent Specific Gravity and Water Absorption*, NBR NM 53, 2009.

[31] Associação Brasileira de Normas Técnicas, *Small-size Coarse Aggregates – Test Method for Resistence to Degradation by Los Angeles Machine*, NBR NM 51, 2001.

[32] Associação Brasileira de Normas Técnicas, *Concrete Paving Units – Specification and Test Methods*, NBR 9781, 2013.

[33] M. S. Juan and P. A. Gutiérrez, "Study on the influence of attached mortar content on the properties of recycled concrete aggregate," *Constr. Build. Mater.*, vol. 23, no. 2, pp. 872–877, 2009.

[34] Associação Brasileira de Normas Técnicas, *Aggregates – Determination of Powder Content*, NBR 7219, 1987.

[35] P. K. Mehta and P. J. M. Monteiro, *Concreto: Microestrutura, Propriedades e Materiais*, 3rd ed. São Paulo: Ibracon, 2013.

[36] R. Silva, J. Brito, and R. K. Dhir, "Performance of cementitious rendering and masonry mortars containing recycled aggregates from construction and demolition wastes," *Constr. Build. Mater.*, vol. 105, pp. 400–415, 2016.

[37] E. Limbachiya and A. Marrocchino, "Kouloris. Chemical-mineralogical characterization of coarse recycled concrete aggregate," *Waste Manag.*, vol. 27, pp. 201–208, 2007.

[38] M. Stefanidou, E. Anastasiou, and G. Filikas, "Recycled sand in lime-based mortars," *Waste Manag.*, vol. 34, pp. 2595–2602, 2014.

[39] S. C. Angulo, C. Ulsen, V. M. John, H. Kahn, and M. A. Cincotto, "Chemical-mineralogical characterization of C&D waste recycled aggregates from São Paulo, Brazil," *Waste Manag.*, vol. 29, pp. 721–730, 2009.

[40] P. S. Martínez, M. G. Cortina, F. F. Martínez, and A. R. Sánchez, "Comparative study of three types of fine recycled aggregates from construction and demolition waste (CDW), and their use in masonry mortar fabrication," *J. Clean. Prod.*, vol. 118, pp. 162–169, 2016.

[41] M. S. K. Behera, A. K. Bhattacharyya, R. Minocha, S. Deoliya, and S. Maiti, "Recycled aggregate from C&D waste & its use in concrete. A breakthrough towards sustainability in construction sector: a review," *Constr. Build. Mater.*, vol. 68, pp. 501–516, 2014.

[42] J. Li and E. Yang, "Macroscopic and microstructural properties of engineered cementitious composites incorporating recycled concrete fines," *Cement Concr. Compos.*, vol. 78, pp. 33–42, 2017.

[43] American Society for Testing and Materials, *Specification for Solid Concrete Interlocking Paving Units*, ASTM 936-1, 2016.

[44] G. Vieira and D. Dal Molin, "Resistência e durabilidade de concretos produzidos com agregados reciclados provenientes de resíduos de construção e demolição," *Eng. Civ. UM.*, vol. 19, pp. 5–18, 2004.

[45] F. C. Leite, R. S. Motta, K. L. Vasconcelos, and L. Bernucci, "Laboratory evaluation on recycled construction and demolition waste for pavements," *Constr. Build. Mater.*, vol. 25, pp. 2972–2979, 2011.

[46] V. Corinaldesi and G. Moriconi, "Behaviour of cementitious mortars containing different kinds of recycled aggregate," *Constr. Build. Mater.*, vol. 23, no. 1, pp. 289–294, 2009.

[47] J. Brito, R. K. Dhir, and R. V. Silva, "Properties and composition of recycles aggregates from construction and demolition waste suitable for concrete production," *Constr. Build. Mater.*, vol. 65, pp. 201–217, 2015.

Rev. IBRACON Estrut. Mater., vol. 13, no. 4, e13405, 2020

13/13

IBRACON Structures and Materials Journal
Revista IBRACON de Estruturas e Materiais

ORIGINAL ARTICLE

Application of the rebound test for the technological control of concrete hollow-core slabs

Aplicação do ensaio de esclerometria para o controle tecnológico de lajes alveolares de concreto

Vladimir Guilherme Haach[a]   iD
Mariana Acioli do Carmo Paiva[a]   iD

[a]Universidade de São Paulo – USP, Escola de Engenharia de São Carlos, Departamento de Estruturas, São Carlos, SP, Brasil

Abstract: Hollow-core slabs are precast elements produced with very dry concrete, which hinders the molding of cube or cylindrical specimens normally used for the technological control of the material. This paper addresses the use of the rebound test for the technological control of concrete applied to hollow-core slabs. An experimental program divided into two phases was developed. In the first phase, three concrete mixtures were produced and compressive and rebound tests were performed in cylindrical and prismatic specimens for 6 hours to 28 days for the obtaining of a correlation curve. In the second phase, a hollow-core slab was built with one of the concrete mixtures used and the same tests were applied. The results showed the rebound number correlates well with the compressive strength, which confirms the possible application of the test for the technological control of the concrete used in the construction of hollow-core slabs.

Keywords: non-destructive tests, rebound, hollow-core slab, technological control.

Resumo: As lajes alveolares são elementos pré-fabricados produzidos com concreto muito seco, o que dificulta a moldagem de amostras cúbicas ou cilíndricas normalmente utilizadas para o controle tecnológico do material. Este artigo aborda o uso do ensaio de esclerometria para o controle tecnológico do concreto aplicado em lajes alveolares. Um programa experimental dividido em duas fases foi desenvolvido. Na primeira fase, três misturas de concreto foram produzidas e testes de compressão e esclerometria foram realizados em amostras cilíndricas e prismáticas por 6 horas a 28 dias para a obtenção de uma curva de correlação. Na segunda fase, foi construída uma laje alveolar com uma das misturas de concreto utilizadas e os mesmos testes foram aplicados. Os resultados mostraram que o índice esclerométrico se correlaciona bem com a resistência à compressão, o que confirma a possível aplicação do teste para o controle tecnológico do concreto utilizado na construção de lajes alveolares.

Keywords: ensaios não destrutivos, esclerometria, laje alveolar, controle tecnológico.

1 INTRODUCTION

The constant demand for the rationalization of civil construction increases the application of structural systems with a higher level of industrialization. Precast concrete elements have gained space in the construction scenario due to the advantages they offer, as speed, competitiveness, time and cost control, durability and safety. Hollow-core slabs have been distinguished by their versatility in civil construction, since they can be supported by masonry, steel, precast or cast-in-place concrete structures. They have been widely applied as floors and loadbearing walls of residential, commercial and industrial buildings, as well as bridge decks [1]. As a consequence, extensive research has been conducted towards a deeper

understanding of their behavior regarding different aspects, as subjection to fire and blast loading [2], [3], fiber strengthened [4], [5], and behavior as a composite section with cast-in-place concrete topping [6], [7].

Hollow core slabs are prestressed elements and, although they can be manufactured in fixed molds, the most common production processes are extrusion and sliding molding [8]. The time spent between the cast and the prestress transference is approximately 24 hours, therefore, the technological control of the concrete must be performed at early ages. According to Mehta and Monteiro [9], the early age covers an insignificant amount of time (2 days after production) in the total life of the concrete. However, deficiencies in the characteristics of fresh concrete may influence the end product and reduce its service life. The evaluation of the concrete properties over the early ages is a concern not only in the manufacture of hollow core slabs, but also in other civil engineering works, as construction of massive concrete elements [10], [11], application of shotcrete [12], [13], [14], production of other precast concrete elements [15], [16] and construction of concrete pavements [17]–[19].

The manufacture of hollow core slabs by extrusion involves the application of a very dry concrete to the elements at a 0.30 to 0.40 water/cement ratio (w/c) [8]. Such values are close to the required w/c for the hydration of cement and ensure a concrete of high compressive strength and lower porosity. Its low slump hinders the molding of cube or cylindrical specimens normally used for the technological control of the material. BSI [20] indicates non-destructive tests (NDTs) as useful tools for increasing the confidence level of destructive tests. Azenha et al. [21] continuously monitored the evolution of elastic modulus of a prefabricated beam through modal analysis. Haach and Juliani [22] evaluated the possible application of ultrasonic tests for the technological control of concrete of hollow-core slabs in the production phase and concluded UPV tests can be an interesting alternative for use in precast concrete industries.

PCI [23] also points NDTs may supplement, but not replace, cylinder tests for the evaluation of the compressive strength of concrete and recommends the rebound test as the more common method. The rebound method has been one of the oldest NDTs applied to concrete structures to date. Its principle is based on the correlation between surface hardness measured by a rebound number and the compressive strength of the concrete. PCI [23] highlights the most important criterion is the correlation between rebound number and compressive strength. The literature reports several empirical relations developed from experimental data [24]–[29]. Pascale et al. [30] studied nondestructive tests (UPV, rebound hammer, probe penetration, etc.) applied to high-strength concrete representing the regression curves by power functions as Equation 1, where f_c is the estimated cube strength in MPa, x is the nondestructive parameter typical of the method used and α and β are parameters obtained by the ordinary least-squares method applied to the experimental data.

$$f_c = \alpha x^{\beta} \tag{1}$$

Mohammed et al. [31] studied the behavior of concrete containing crumb rubber as a replacement of fine aggregate and proposed an exponential relationship between compressive strength and rebound number. Szilágyi et al. [32] proposed a phenomenological constitutive model (SBZ-model) formulated for the surface hardness of concrete based on the time-dependent development of the capillary pore system of the hardened cement paste. The authors demonstrated its applicability for CEM I 42.5 N, CEM II/A-V 42.5 N and CEM III/B 32.5 N cements in a 0.38 to 0.60 range of water/cement ratio and 7 to 180 days of concrete. Tsioulou et al. [33] evaluated the mechanical characteristics of ultra-high performance fibre-reinforced concrete (UHPFRC) and proposed linear, power and exponential relationships between compressive strength and rebound number. Völgyi and Farkas [34] highlighted the non-destructive testing functions developed for vibrated concrete are not applicable for dry concrete, since the results of rebound tests strongly depend on the properties of the microenvironment of the material. Völgyi and Farkas [34] studied spun-cast concrete elements produced at low water/cement ratios. In general, the limitations of all proposed formulations regarding the influence of variables, as smoothness of test surface, size, shape, and rigidity of the specimens, moisture and type of cement and aggregates, lead to a high coefficient of variation [35].

Since NDT is an easy, quick and inexpensive test, researchers continue proposing improvements and new applications for the rebound test method [30], [36], [37].

This paper discusses the possible advantages and limitations of the use of the rebound hammer for improving the technological control of the concrete used in the manufacture of hollow core slabs.

2 EXPERIMENTAL PROGRAM

The experimental program was divided into two phases. The first involved the evaluation of three different concrete mixtures through compressive and rebound tests for the obtaining of the variation in the concrete behavior during the hardening process and correlation curves between compressive strength and rebound number. In the second phase, a

hollow-core slab was built in the laboratory with one of the concrete mixtures tested in the previous phase for the evaluation of the applicability of the rebound test for the technological control of the concrete in those elements.

2.1 Properties of materials

Type III Portland cement of high early strength specified according to the ASTM C150 [38] classification, sand and gravel were used in the preparation of the concrete. Sand has 2.4 mm maximum size and 1.95 fineness modulus, whereas gravel has 12.7 mm maximum size and 6.84 fineness modulus. Figure 1 displays the particle size distribution for sand and gravel and Table 1 shows some physical properties of the materials. The standard procedure described in ASTM C192 [39] was applied to the mixtures. Three different compositions of concrete (M1 to M3) were produced, according to Table 2. The mixtures were defined through a 100 mm slump and three different binder/aggregate ratios (1:3.5; 1:5.0 and 1:6.5). The dry mortar ratio defined by Equation 2, shown in Oliveira et al. [40], was set to 51%. Only one batch of concrete was produced for each mixture.
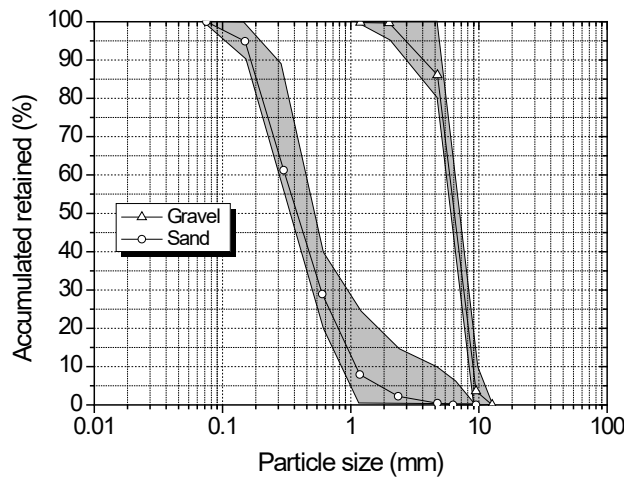
Figure 1 – Grading curve of aggregates.

Table 1 – Properties of materials.

	Cement	Sand	Gravel
Bulk density (kg/m^3)	1171	1565	1498
Density (kg/m^3)	3070	2625	2804

Table 2 – Compositions of concrete (kg/m^3).

ID	Cement	Sand	Gravel	Water	Water/cement ratio
M1	484.6	630.0	1066.2	227.8	0.47
M2	378.8	780.4	1113.8	227.3	0.60
M3	295.0	834.6	1141.5	224.2	0.76

$$D(\%) = \frac{1 + sand}{1 + sand + gravel} \tag{2}$$

2.2 Test specimens

In the first phase of this research, cylindrical specimens of 100 mm diameter and 200 mm height and prismatic specimens of 150 mm × 150 mm × 500 mm were molded according to ABNT NBR 5738 [41]. The former was removed from the molds after 7 hours, whereas prismatic specimens were kept inside the metallic molds for avoiding any possible

damage during manipulation due to their weight. Forty-five cylindrical and eight prismatic specimens were molded from each concrete mixture and kept in the laboratory environment during all tests. Compressive and rebound tests were performed at thirteen different ages between 8 hours and 24 hours after the concrete batch and at 7 and 28 days.

In the second phase, hollow-core slabs of 500 mm × 100 mm cross section dimensions and 2000 mm length were built with concrete mixture M1, as shown in Figure 2. Four longitudinal bars of 6.3 mm diameter with 500 MPa nominal yield strength were placed at the top of the slab from the edge to the mid-span on one side for evaluations of their influence on the results regarding presence of reinforcements. A welded mesh composed of 4.2 mm diameter wires with uniform spacing of 10 cm was used at the bottom of the slabs to avoid damages during the transport of the model. Thirty cylindrical specimens were also molded with the hollow-core slab for the evaluation of the compressive strength of the concrete at different ages. Hollow cores were generated by PVC tubes positioned in the formwork and removed after the curing of the concrete.
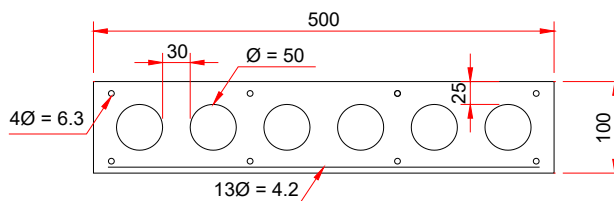
Figure 2 – Geometrical properties of hollow-core slabs. (*Note: units in mm*).

2.3 Compressive tests

Compressive tests were performed in cylindrical specimens according to ASTM C39/C39M [42]. Neoprene pads of 70 durometer hardness were used on top and bottom of the specimens for providing a uniform load distribution during the test, according to ASTM C1231 [43]. Three specimens were tested at each age.

2.4 Rebound tests

Rebound tests were applied to the prismatic specimens in the first phase and on the hollow-core slab in the second phase, according to ASTM C805/C805M [44]. Although the standard recommends 10 measurements under the same nominal condition, the rebound number was calculated as the mean of sixteen readings at each age with a 30mm-spacing between impact points for improving the accuracy of the results. In both phases, the steel plunger of the rebound hammer was positioned in the gravity direction. As the readings were performed with the rebound hammer always in the same position, no correction factors were applied to the rebound number.

In the first phase, 32 impacts were applied on the top face of the prisms ensuring readings of two ages per prismatic specimen. The prisms were kept directly supported on the floor of the laboratory.

In the second phase, ten 150 mm transversal bands were defined on top of the hollow-core slab for the rebound tests. Five bands were positioned on the half slab with reinforcements (named BR) and five bands were placed on the half slab without reinforcements (named BW). Similarly to the first phase, the readings of two ages per band were performed.

3 EXPERIMENTAL RESULTS

The analyses and discussions of the results were also divided into two parts, according to the experimental program. The results of the first phase are showed and discussions on the evolution of the rebound number and compressive strength over time and the correlation curve between those properties were developed. The results of the rebound and compressive tests performed in a hollow core slab are provided and highlight the difficulties and differences in the technological control of the structural member and specimens used in the first phase.

3.1 Phase I – Evaluation of cylindrical and prismatic specimens

Compressive strength and rebound number were measured in cylindrical and prismatic specimens, respectively, for three different concrete mixtures. Table 3 shows the mean values and the coefficients of variation (C.V.) of the results. The rebound

number was null at the first three ages for the three concrete mixtures due to the small hardness of the concrete surface and as expected, it showed a higher dispersion than the compressive strength with C.V.s in the 3.37% to 14.65% range against 1.97% to 17.21% range for the compressive strength. The mean value of the C.V.s of the rebound number was almost twice the C.V.s of the compressive strength. Such a variation did not seem to be influenced by the specimen age.

Table 3 – Test results of the first phase of the experimental program.

ID	Age (hours)	Rebound Number		Compressive Strength	
		Mean	C.V. (%)	Mean (MPa)	C.V. (%)
M1	8.5	-	-	2.76	9.85
	9.5	-	-	4.54	6.07
	11.5	15.88	10.51	8.38	3.06
	12.5	19.33	8.45	11.54	3.95
	13.5	19.13	8.29	12.90	1.97
	14.5	19.69	10.11	14.18	5.07
	15.5	20.31	7.57	15.69	5.92
	16.5	20.63	7.89	17.17	1.79
	17.5	22.31	6.89	18.23	5.12
	18.5	21.44	8.16	18.79	4.88
	21.5	21.38	8.35	21.06	3.42
	22.5	22.00	5.98	21.89	2.88
	23.5	22.75	8.72	23.97	11.57
	168	26.88	8.69	46.39	7.35
	672	28.07	10.64	52.56	11.17
M2	9.0	-	-	2.92	17.21
	11.0	-	-	4.68	5.42
	12.0	10.56	14.65	5.26	6.82
	14.0	11.75	12.62	7.58	11.75
	15.0	12.13	12.00	8.19	3.07
	16.0	13.75	13.14	8.91	6.06
	17.0	15.81	10.89	9.67	3.51
	18.0	16.13	8.44	10.15	2.00
	19.0	15.27	13.21	11.13	10.91
	20.0	16.69	11.10	11.47	2.54
	22.0	16.94	11.90	13.30	8.07
	23.0	16.88	10.57	14.24	2.87
	24.0	18.31	14.48	15.40	7.73
	168	25.47	10.69	26.86	7.73
	672	26.38	7.31	33.33	3.46
M3	10.5	-	-	1.53	5.45
	11.5	-	-	1.79	5.01
	13.5	-	-	2.40	7.91
	14.5	-	-	2.90	6.02
	15.5	-	-	3.32	3.03
	16.5	10.13	3.37	3.61	2.40
	17.5	10.19	5.34	4.07	6.42
	18.5	11.69	12.77	4.33	8.21
	19.5	12.31	10.15	5.30	10.42
	22.5	13.44	10.51	7.43	5.59
	23.5	13.00	11.92	7.70	2.68
	24.5	15.06	9.22	8.93	3.52
	168	22.88	9.15	24.45	4.62
	672	28.69	10.24	31.21	3.23

The monitoring of the evolution of compressive strength of the concrete during the production process of precast elements is fundamental for the prestress transference operation and demolding of the elements. Fib Bulletin 55 [45] proposes an exponential equation for the prediction of the compressive strength ($f_c(t)$) at age t (in days), from the

strength at 28 days ($f_c(28)$), see Equation 3. The equation is valid for ages between 3 and 28 days and s depends on the strength class of cement and hardening characteristics - its value for type III cement is 0.2.

$$f_c(t) = \beta_c(t)f_c(28) \rightarrow \beta_c(t) = exp\left\{s\left[1 - (28/t)^{0.5}\right]\right\} \tag{3}$$

An exponential function (Equation 4) based on fib equation was fit to the results of compressive strength over 672 hours - 28 days (Figure 3). The coefficient of determination R^2 was higher than 0.97 for all mixes. R^2 for the fib equation applied to concrete mixtures M1, M2 and M3 was 0.67, 0.74 and 0.89, respectively. The fib equation reasonably predicted the compressive strength of all mixtures at 7 days and 28 days, as shown in Figure 3a. However, it overestimated the compressive strength in the first 24 hours (Figure 3b).
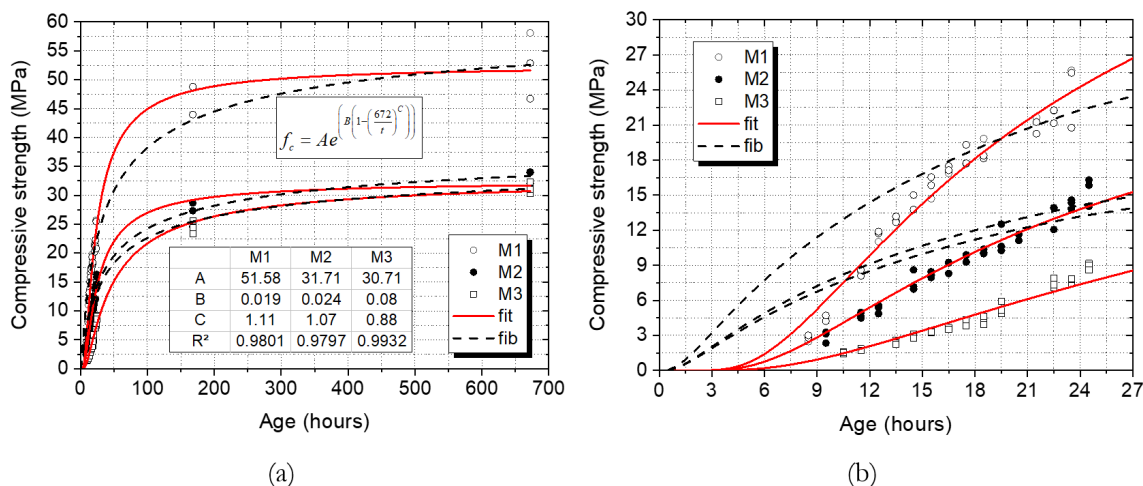
Figure 3 – Variation in the compressive strength over time: (a) during 28 days and (b) during 24 hours

$$y(t) = A\xi(t) \rightarrow \xi(t) = exp\left\{B\left[1 - (28/t)^C\right]\right\} \tag{4}$$

where $y(t)$ is the compressive strength or rebound number and A, B and C are coefficients obtained by the ordinary least-squares method applied to the experimental data.

All compressive strength data in Figure 4 were normalized by the value at 28 days, since the fib proposition considers only the effect of cement type on the variation of compressive strength over age, (Equation 3), and all concrete mixtures were produced with the same cement type. A high dispersion is observed in the first 24 hours and indicates the material proportions significantly influence the variation in the compressive strength at early ages.

As the proposition here is to apply rebound tests to supplement the technological control of concrete used in hollow-core slabs, the evolution of rebound number over time was also analyzed. Rebound and compressive tests showed a similar behavior (Figure 5 and Figure 6). The exponential curve represented by Equation 4 seems to express the variations in both properties and the proportions of the materials clearly influenced the variation in the rebound number at early ages. Coefficients A, B and C in Equation 4 can express this dependence on the concrete composition. The cement type probably contributes to variations in such coefficients, as pointed out in the expressions presented in fib Bulletin 55 (2010). Variations in coefficients B and C strongly influenced the curve behavior in the first hours. Both parameters B and C define the strength gain of the material (Figure 7).

Compressive strength, f_c, and rebound number, RN, highly correlated with coefficients of determination R^2 higher than 0.95 for all concrete mixtures. A power expression, as Equation 1 used by Pascale et al. [30], was the curve, which best represented the relation between both properties (Figure 8), see Equation 5.
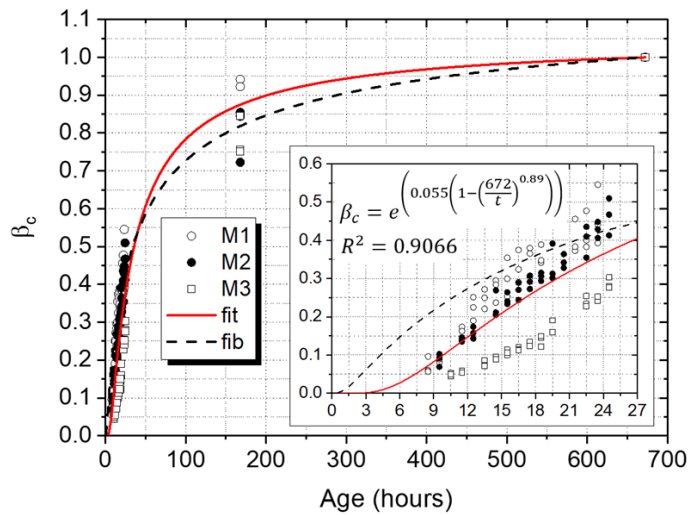
Figure 4 – Variation in the normalized compressive strength over age.

(a)

(b)
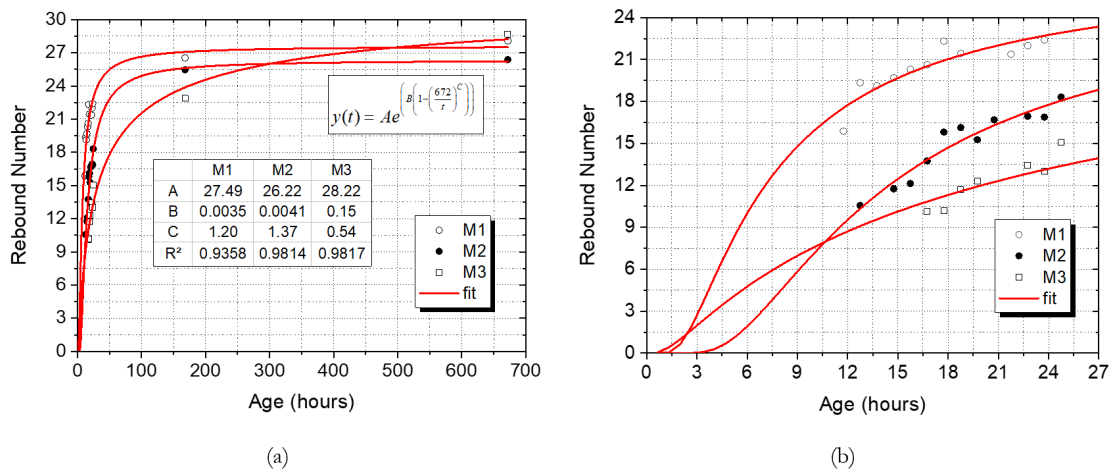
Figure 5 – Variation in the rebound number over age: (a) over 28 days and (b) over 24 hours.
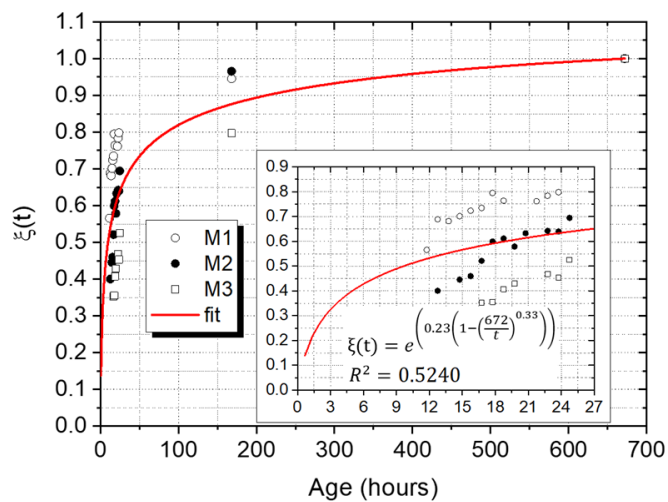
Figure 6 – Variation in the normalized rebound number over age.

Rev. IBRACON Estrut. Mater., vol. 13, no. 4, e13406, 2020

7/14
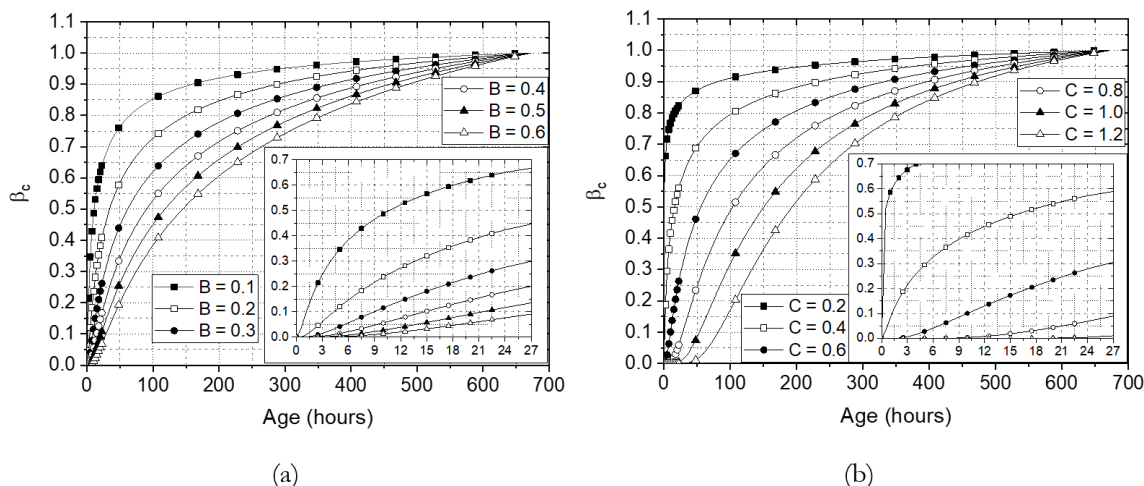
Figure 7 – Variation in coefficient β$_c$ with the constants: (a) B variable and C = 0.5 and (b) C variable and B = 0.2.
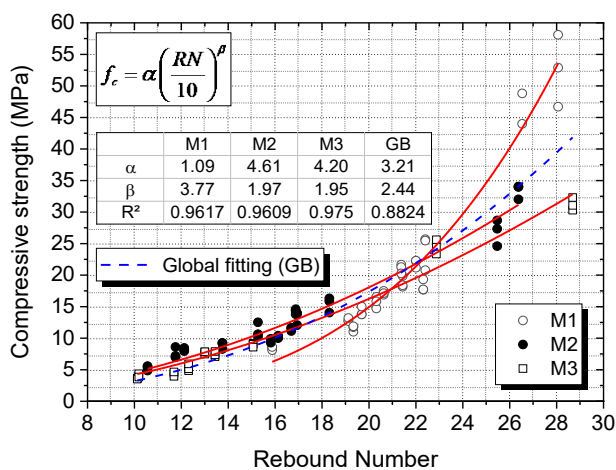
Figure 8 – Correlation between compressive strength and rebound number in phase I.

$$f_c = \alpha \left(\frac{RN}{10} \right)^{\beta} \tag{5}$$

Figure 9 shows the comparison of the phase I results with some correlation curves reported in the literature. The region formed by correlations encompasses all experimental results, which corroborates previous research. However, a high variability is observed in those relations between compressive strength and rebound number, due to the several variables cited in the introduction. This variation seems to increase for the highest values of compressive strength.

3.2 Phase II – Evaluation of a hollow-core slab

A hollow-core slab was produced with mix 1 in the laboratory. Rebound tests were performed and the results were compared with those of the first phase. Table 4 shows the results of the rebound tests and the compressive strength obtained from cylindrical specimens molded with the same concrete used in the hollow-core slab.

One of the issues evaluated was the effect of cores on the results of rebound tests. The measurements taken in hollow-core slabs were uniformly distributed over the top of the slab. Measurement points were located above the cores and over the webs, see Figure 10. The results showed the rebound number was not affected by the presence of holes in the cross-section.
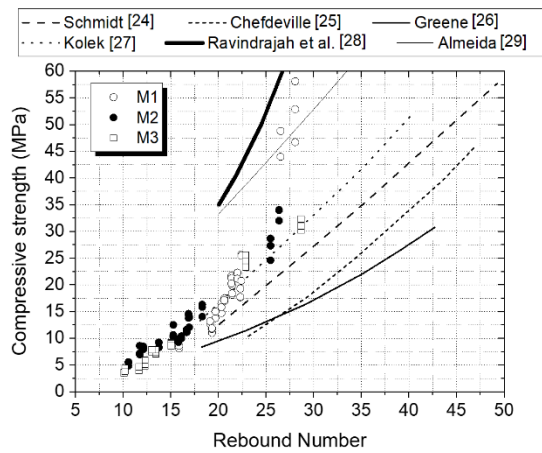
Figure 9 – Comparison between experimental data and correlation curves reported in the literature.
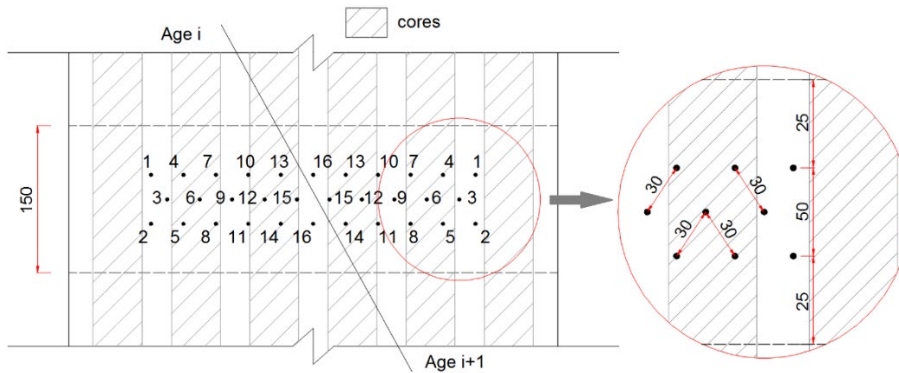
Figure 10 – Location of the measurements in the hollow-core bands (Note: units in mm).

Table 4 – Test results of the second phase of the experimental program.

ID	Age (hours)	Rebound Number[1]		Rebound Number[2]		Compressive strength	
		Mean	C.V. (%)	Mean	C.V. (%)	Mean (MPa)	C.V. (%)
M1	9.17	23.19	8.37	23.80	11.14	11.14	3.50
	10.88	23.63	9.26	27.06	12.03	18.02	5.25
	13.90	25.92	6.95	26.77	9.90	21.64	6.26
	15.88	25.93	7.50	24.88	12.62	23.58	2.74
	17.83	27.67	9.33	27.33	10.41	24.21	3.94
	19.93	26.13	9.36	26.27	7.94	26.05	3.60
	22.87	27.31	8.53	27.67	9.82	27.90	3.61
	24.97	27.06	8.58	26.88	11.44	30.14	3.04
	168	28.06	12.31	27.93	10.65	42.88	6.46
	672	31.43	7.14	32.07	6.52	50.82	4.58

[1] – Rebound Number in the region of the slab with no superior reinforcements. [2] – Rebound Number in the region of the slab with superior reinforcements.

Figure 11 displays the variation in the rebound number along the width of the hollow-core slab. No pattern related to the position of the cores and webs in regions with (BR) or without (BW) superior reinforcements was observed. Two statistical hypothesis tests, namely F-test and T-test, were applied to the rebound measurements towards improving the evaluation. F-test compares two samples for testing the hypothesis of equality of their variances, whereas T-test determines if they are significantly different. A 5% significance level was assumed in both tests.

Rev. IBRACON Estrut. Mater., vol. 13, no. 4, e13406, 2020

9/14

(a)   (b)
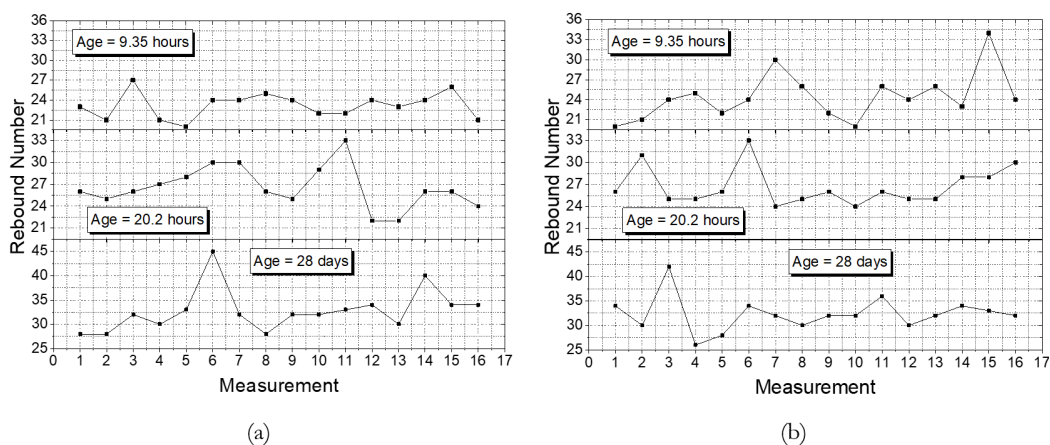
Figure 11 – Variation in the rebound number along the width of the hollow-core slab in the regions: (a) BW and (b) BR.

Rebound measurements were divided into two groups according to their position (Table 5), i.e., above the webs (1, 2, 3, 9, 10 and 16) and over the cores (4, 5, 6, 7, 8, 12, 13, 14 and 15). Readings different from the average by more than 6 units were discarded, as recommended by ASTM C805/C805M [44]. This procedure was applied to each group separately. F-test was applied to the rebound numbers followed by T-test (Table 6). The former showed the variances in the two groups were equal, whereas T-test indicated the measurements above the webs or cores were not significantly different in most cases. The results were obtained in both regions of the hollow-core slab with and without reinforcements, however, in the former, three ages exhibited probabilities for T-test lower than 5%.

Table 5 – Rebound measurements of the second phase of the experimental program divided by groups.

Age (hours)	Web[1] Mean	Web[1] C.V. (%)	Core[1] Mean	Core[1] C.V. (%)	Web[2] Mean	Web[2] C.V. (%)	Core[2] Mean	Core[2] C.V. (%)
9.17	22.86	9.26	23.44	8.01	22.43	10.25	25.00	9.80
10.88	22.86	8.90	24.22	9.18	28.57	10.07	25.13	9.38
13.90	23.50	15.86	26.00	7.45	29.25	7.58	25.67	8.03
15.88	26.50	8.52	25.56	6.81	25.57	10.31	24.33	14.53
17.83	27.83	8.63	27.56	10.28	25.86	13.10	27.67	11.57
19.93	25.83	6.67	26.33	11.07	26.86	9.72	25.75	5.78
22.87	26.57	10.39	27.89	6.81	26.33	4.60	27.88	9.08
24.97	26.86	8.97	27.22	8.77	27.00	6.05	26.78	14.79
168	26.14	10.46	29.56	11.24	25.40	6.59	29.33	8.86
672	31.29	7.54	32.63	11.22	32.67	6.32	31.00	8.83

[1] – Rebound Number in the region of the slab with no superior reinforcements. [2] – Rebound Number in the region of the slab with superior reinforcements.

Table 6 – Probabilities of F-Test and T-Test.

Age (hours)	Web x Cores[1] F-Test	Web x Cores[1] T-Test	Web x Cores [2] F-Test	Web x Cores [2] T-Test	With x Without reinforcements F-Test	With x Without reinforcements T-Test
9.17	0.7345	0.5662	0.8933	0.0572	0.2421	0.4667
10.88	0.8529	0.2273	0.6095	0.0242	0.1347	0.0015
13.90	0.0987	0.1102	0.7683	0.0163	0.1951	0.3506
15.88	0.4876	0.3762	0.4906	0.4528	0.0812	0.2721
17.83	0.7446	0.8469	0.8571	0.2925	0.7214	0.7394
19.93	0.2614	0.7131	0.1675	0.3230	0.5599	0.8735
22.87	0.3240	0.2765	0.1236	0.1962	0.5616	0.6991
24.97	0.9503	0.7669	0.0444	0.8816	0.2889	0.8470
168	0.6540	0.0454	0.4123	0.0106	0.5938	0.9109
672	0.3044	0.4232	0.5539	0.2283	0.8057	0.4401

[1] – Rebound Number in the region of the slab with no superior reinforcements. [2] – Rebound Number in the region of the slab with superior reinforcements.

The reinforcement in the superior region of the slabs exerted a very small influence on the rebound tests. The coefficients of variation of the rebound numbers in that region were slightly higher than those of the region without reinforcements. However, F-Test and T-test also indicated the rebound numbers in both regions were not significantly different.

The correlation between the rebound numbers and the compressive strength of the concrete was also little influenced by reinforcements. Fitting equations for both regions with and without reinforcements showed differences lower than 10% for previsions of the compressive strength from rebound numbers between 26 and 34 (Figure 12 and Figure 13). Compressive strength previsions from rebound number by the equation obtained in phase I for M1 were higher than the compressive strength measured in cylindrical specimens, see. On average, the experimental values of compressive strength were 63% lower than those predicted.
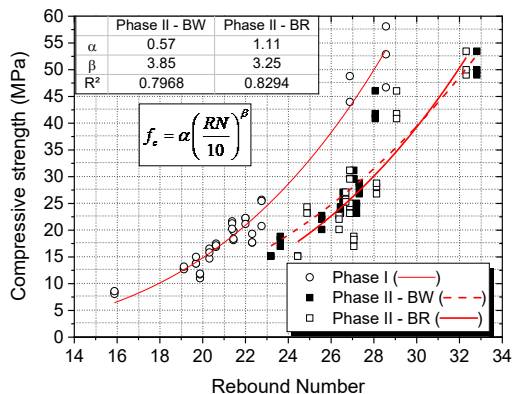
Figure 12 – Correlation between compressive strength and rebound number in phase II.
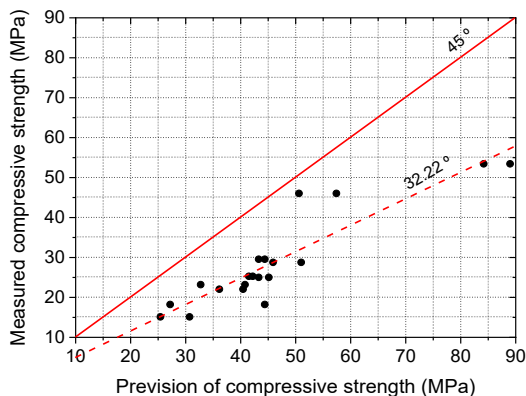
Figure 13 – Relation between prevision and measurement of compressive strength of the concrete used in hollow-core slabs.

In both phases, the compressive strength was evaluated through tests in cylindrical specimens. Differences between measurements and previsions are probably related to the influence of shape and mass of the specimens on the rebound test. In the first phase of the research, prismatic specimens were used in the rebound tests and the rebound numbers ranged from 15.88 to 28.07. In phase II, hollow-core slabs were tested and the rebound numbers were higher than those obtained in phase I, i. e., they ranged from 23.19 to 32.07. For the same concrete mixture, the hollow-core slab showed rebound numbers more than 15% higher than those of prismatic specimens. According to Malhotra and Carino [35], if a test specimen is small, any movement under the impact will decrease the rebound number. Prismatic specimens were tested inside the molds at early ages, which probably generates some movement under the impact and caused the behavior pointed out by Malhotra and Carino [35].

Despite the differences in the results of phases I and II, coefficient β of the correlation Equation 5 showed a very small variation in all cases and assumed an average value of 3.57. On the other hand, coefficient α showed the highest variation and was influenced by reinforcements, shape and mass of the specimens.

4 CONCLUSIONS AND FINAL REMARKS

This paper has addressed a possible application of rebound tests to improve the technological control of the concrete used in precast hollow-core slabs. The study was divided into two phases for the obtaining of a correlation curve between the rebound number and compressive strength in the first phase to be applied in the second phase, in which a hollow-core slab was produced in the laboratory.

Results of the first phase corroborated with previous research and showed a good correlation between the rebound number and compressive strength of the concrete. However, such a correlation was highly influenced by the concrete mixture. An evolution in the compressive strength and surface hardness gain was observed in this phase. Both properties followed an exponential curve also influenced by the concrete mixture.

Statistical analyses applied to results of tests performed in hollow-core slabs showed both reinforcements and the holes in the cross section exerted a negligible influence on the results of the rebound tests. On the other hand, the correlation curve obtained in phase I did not provide reliable previsions for the compressive strength. The differences in the shape and mass of the specimens used in phases I and II seemed to significantly influence the results.

A very good correlation between rebound number and compressive strength confirmed the possible application of the rebound test for the technological control of the concrete used in the construction of hollow-core slabs. However, the correlation curve to be used for previewing the compressive strength from the rebound number should not be obtained from small specimens, since their shape and mass strongly influence this relation.

ACKNOWLEDGMENTS

REFERENCES

[1] Prestressed Concrete Institute, *PCI Design Handbook: Precast and Prestressed Concrete*, 6th ed. Chicago: PCI, 2004.

[2] J. V. Aguado, A. Espinos, A. Hospitaler, J. Ortega, and M. L. Romero, "Influence of reinforcement arrangement in flexural fire behavior of hollow core slabs," *Fire Saf. J.*, vol. 53, pp. 72–84, 2012.

[3] A. Maazoun, J. Vantomme, and S. Matthys, "Damage assessment of hollow core reinforced and prestressed concrete slabs subjected to blast loading," *Procedia Eng.*, vol. 199, pp. 2476–2481, 2017.

[4] P. Kankeri and S. S. Prakash, "Experimental evaluation of bonded overlay and NSM GFRP bar strengthening on flexural behavior of precast prestressed hollow core slabs," *Eng. Struct.*, vol. 120, pp. 49–57, 2016.

[5] S. Foubert, K. Mahmoud, and E. El-Salakawy, "Behavior of prestressed hollow-core slabs strengthened in flexure with near-surface mounted carbon fiber-reinforced polymer reinforcement," *J. Compos. Constr.*, vol. 20, no. 6, pp. 10p, 2016.

[6] E. Baran, "Effects of cast-in-place concrete topping on flexural response of precast concrete hollow-core slabs," *Eng. Struct.*, vol. 98, pp. 109–117, 2015.

[7] I. S. Ibrahim, K. S. Elliott, R. Abdullah, A. B. H. Kueh, and N. N. Sarbini, "Experimental study on the shear behaviour of precast concrete hollow core slabs with concrete topping," *Eng. Struct.*, vol. 125, pp. 80–90, 2016.

[8] Prestressed Concrete Institute, *PCI Manual for the Design of Hollow Core Slabs*, 2nd ed. Chicago: PCI, 1998.

[9] P. K. Mehta and P. J. M. Monteiro, *Concrete: Microstructure, Properties and Materials*, 3rd ed. New York: McGraw-Hill, 2006.

[10] A. M. Lawrence, M. Tia, C. C. Ferraro, and M. Bergin, "Effect of early age strength on cracking in mass concrete containing different supplementary cementitious materials: experimental and finite-element investigation," *J. Mater. Civ. Eng.*, vol. 24, no. 4, pp. 362–372, 2012.

[11] P. R. Singh and D. C. Rai, "Effect of piped water cooling on thermal stress in mass concrete at early ages," *J. Eng. Mech.*, vol. 144, no. 3, pp. 04017183, 2018.

[12] J. Sercombe, C. Hellmich, F. J. Ulm, and H. Mang, "Modeling of early-age creep of shotcrete. I: model and model parameters," *J. Eng. Mech.*, vol. 126, no. 3, pp. 284–291, 2000.

[13] C. Hellmich, J. Sercombe, F. J. Ulm, and H. Mang, "Modeling of early-age creep of shotcrete. II: application to tunneling," *J. Eng. Mech.*, vol. 126, no. 3, pp. 292–299, 2000.

[14] A. Mohajerani et al., "Two possible new techniques for determining the early-age shear strength of shotcrete: auger penetrometer and vane shear tester," *J. Mater. Civ. Eng.*, vol. 30, no. 3, pp. 04017298, 2018.

[15] C. Li, G. Wei, F. Zhang, J. Liu, J. Ma, and T. Ge "Experimental study on high-early-strength precast concrete," in *Proc. 10th Asia Pac. Transp. Dev. Conf.*, Beijing, China, 2014.

[16] Y. H. Kim, M. B. D. Hueste, and D. Trejo, "Flexural behavior of high-early-strength self-consolidating concrete pretensioned bridge girders: experimental evaluation," *J. Bridge Eng.*, vol. 20, no. 2, pp. 04014064, 2015.

[17] J. H. Jeong, D. G. Zollinger, J. S. Lim, and J. Y. Park, "Age and moisture effects on thermal expansion of concrete pavement slabs," *J. Mater. Civ. Eng.*, vol. 24, no. 1, pp. 8–15, 2012.

[18] J. Zhang, D. Hou, and Y. Gao, "calculation of shrinkage stress in early-age concrete pavements. I: calculation of shrinkage strain," *J. Transp. Eng.*, vol. 139, no. 10, pp. 961–970, 2013.

[19] J. Zhang, D. Hou, and Y. Gao, "Calculation of shrinkage stress in early-age concrete pavements. II: calculation of shrinkage stress," *J. Transp. Eng.*, vol. 139, no. 10, pp. 971–980, 2013.

[20] British Standards Institution, *Guide to the Use of Nondestructive Methods of Test for Hardened Concrete*, BS 1881:Part201. London: BSI, 1986.

[21] M. Azenha, L. F. Ramos, R. Aguilar, and J. L. Granja, "Continuous monitoring of concrete E-modulus since casting based on modal identification: a case study," *Cement Concr. Compos.*, vol. 10, pp. 10–15, 2012.

[22] V. G. Haach and L. M. Juliani, "Possibilities of using ultrasound for the technological control of concrete of hollow-core slabs," *Constr. Build. Mater.*, vol. 133, pp. 409–415, 2017.

[23] Prestressed Concrete Institute, *PCI Manual for Quality Control for Plants and Production of Structural Precast Concrete Products*, 4th ed. Chicago: PCI, 1999.

[24] E. Schmidt, "Rebound hammer for concrete testing," *Schweiz Bauztg*, vol. 68, no. 28, pp. 378–379, 1950.

[25] J. Chefdeville, *Application of the Method Toward Estimating the Quality of Concrete* (RILEM Bulletin 15, Special issue-vibration testing of concrete: part 2). Paris: RILEM, 1953.

[26] G. W. Greene, "Test hammer provides new method of evaluating hardened concrete," *J. Am. Concr. Inst.*, vol. 26, no. 3, pp. 249–256, 1954.

[27] J. Kolek, "An appreciation of the Schmidt rebound hammer," *Mag. Concr. Res.*, vol. 10, no. 28, pp. 27–36, 1958.

[28] R. S. Ravindrajah, Y. H. Loo, and C. T. Tam, "Strength evaluation of recycled-aggregate concrete by in-situ tests," *Mater. Struct.*, vol. 21, pp. 289–295, 1988.

[29] I. R. Almeida "Emprego do esclerômetro e do ultra-som para efeito da avaliação qualitativa dos concretos de alto desempenho," Ph.D. dissertation, Univ. Fed. Fluminese, Niteroi, Brasil, 1993.

[30] G. Pascale, A. Di Leo, and V. Bonora, "Nondestructive Assessment of the Actual Compressive Strength of High-Strength Concrete," *J. Mater. Civ. Eng.*, vol. 15, no. 5, pp. 452–459, 2003.

[31] B. S. Mohammed, N. J. Azmi, and M. Abdullahi, "Evaluation of rubbercrete based on ultrasonic pulse velocity and rebound hammer tests," *Constr. Build. Mater.*, vol. 25, no. 3, pp. 1388–1397, 2011.

[32] K. Szilágyi, A. Borosnyói, and I. Zsigovics, "Rebound surface hardness of concrete: Introduction of an empirical constitutive model," *Constr. Build. Mater.*, vol. 25, pp. 2480–2487, 2011.

[33] O. Tsioulou, A. Lampropoulos, and S. Paschalis, "Combined non-destructive testing (NDT) method for the evaluation of the mechanical characteristics of ultra-high performance fibre reinforced concrete (UHPFRC)," *Constr. Build. Mater.*, vol. 131, pp. 66–77, 2017.

[34] I. Völgyi and G. Farkas, "Rebound testing of cylindrical spun-cast concrete elements," *Period. Polytechnica*, vol. 55, no. 2, pp. 129–135, 2011.

[35] V. M. Malhotra and N. J. Carino, *Handbook on Nondestructive Testing of Concrete*, 2nd ed. Boca Raton: CRC Press, 2004.

[36] M. Saleem, W. A. Al-Kutti, N. M. Al-Akhras, and H. Haider, "Nondestructive testing procedure to evaluate the load-carrying capacity of concrete anchors," *J. Constr. Eng. Manage.*, vol. 142, no. 5, pp. 04015104, 2016.

[37] T. Gupta, A. Tiwari, S. Siddique, R. K. Sharma, and S. Chaudhary, "Response assessment under dynamic loading and microstructural investigations of rubberized concrete," *J. Mater. Civ. Eng.*, vol. 29, no. 8, pp. 04017062, 2017.

[38] Associação Brasileira de Normas Técnicas. *Standard Specification for Portland Cement*, C150/C150M-11, 2011.

[39] Associação Brasileira de Normas Técnicas. *Standard Practice for Making and Curing Concrete Test Specimens in the Laboratory*, C192/C192M-06, 2006.

[40] L. A. P. Oliveira, J. P. Castro Gomes, L. F. A. Bernardo, and M. M. M. Ramos, "Evaluation of dry mortar ratio as mixture design parameter for steel fibre reinforced self compacting concrete," *Constr. Build. Mater.*, vol. 40, pp. 642–649, 2013.

[41] Associação Brasileira de Normas Técnicas. *Molding and Curing of Concrete Cylindrical or Prismatic Test*, NBR 5738, 1994.

[42] American Society for Testing and Materials. *Standard Test Method for Compressive Strength of Cylindrical Concrete Specimens*, C39/C39M-16b, 2016.

[43] American Society for Testing and Materials. *Standard Practice for Use of Unbonded Caps in Determination of Compressive Strength of Hardened Cylindrical Concrete Specimens*, C1231-15, 2015.

[44] American Society for Testing and Materials. *Standard Test Method for Rebound Number of Hardened Concrete*, C805/C805M-13a, 2013.

[45] European Standard. *Eurocode 2 – Design of Concrete Structures – General Rules and Rules for Buildings*, EN 1992-1-1, 2004.

Rev. IBRACON Estrut. Mater., vol. 13, no. 4, e13406, 2020

14/14

IBRACON Structures and Materials Journal
Revista IBRACON de Estruturas e Materiais

ORIGINAL ARTICLE

Development of Brazilian highway live load model for unlimited fatigue life

Desenvolvimento do modelo rodoviário brasileiro de carga móvel para vida útil ilimitada à fadiga

Anselmo Leal Carneiro[a,b] (iD)
Enson de Lima Portela[c] (iD)
Túlio Nogueira Bittencourt[a] (iD)

[a]Universidade de São Paulo – USP, Escola Politécnica, São Paulo, SP, Brasil
[b]Universidade Federal do Rio de Janeiro – UFRJ, Macaé, RJ, Brasil
[c]Instituto Federal do Ceará – IFCE, Departamento de Construção Civil, Fortaleza, CE, Brasil

Abstract: This work studies the fatigue live load model used in Brazil for highway bridges. Using the unlimited fatigue life approach, the current live load model is evaluated in relation to the actual traffic and a new fatigue live load model is proposed. Weigh-in-motion (WIM) stations data on two important Brazilian highways are used. The main structural analysis performed in this paper consider the bridges as box girders or multiple girders. The ratio between real traffic and the live load model load effect (bias factor) are determined for single and continuous spans in terms of bending moment and shear force. It is found that the bias factor of the current live load can vary a lot and may not ensure unlimited fatigue life. The proposed model, on the other hand, presents more uniform bias factors and is in accordance with the unlimited fatigue life approach for the WIM data.

Keywords: highway bridges, fatigue, live load, weigh-in-motion.

Resumo: Este trabalho estuda o modelo de carga móvel utilizado no Brasil para a verificação de fadiga em pontes rodoviárias. Mediante a abordagem de vida útil ilimitada à fadiga, avalia-se o trem tipo vigente em relação ao tráfego real e propõe-se um novo modelo de carga móvel de fadiga. São utilizados dados de estações de pesagem em movimento (*weigh-in-motion – WIM*) localizadas em duas importantes rodovias brasileiras. São consideradas estruturas típicas de pontes em grelha e seção celular, onde as razões entre as solicitações do tráfego e do modelo de carga móvel (fatores viés) são determinadas para vãos biapoiados e contínuos em termos de momento fletor e força cortante. Verifica-se que o trem tipo atual apresenta considerável variação nos fatores viés e pode não assegurar vida útil ilimitada à fadiga. O modelo proposto, por outro lado, apresenta fatores viés mais uniformes e condiz melhor com abordagem de vida útil ilimitada à fadiga para o tráfego obtido das estações WIM.

Palavras-chave: pontes rodoviárias, fadiga, carga móvel, pesagem em movimento.

1 INTRODUCTION

The highway bridges are susceptible to the fatigue as they are subjected to live load from the traffic. Fatigue can be described as the process by which the damage in a given material is generated by stress fluctuations. This damage may result in the structural rupture of the component, even if the highest applied stress is below the elastic limit of the material.

The live load of the ABNT (Brazilian Technical Code Association) NBR 7188 [1], comes from a retired German code that, according to Pfeil [2], used a design vehicle corresponding to the army tank, surrounded by distributed load. For the fatigue load, a weighting factor is used for the current model. This design load, nonetheless, was not proposed considering the traffic reality in Brazil. Whereas the Brazilian code presents a single model of fatigue load, the main international codes, for instance the Eurocode [3] and AASHTO LRFD [4], present a fatigue live load model for both limited and unlimited fatigue life.

In Brazil, the main studies about live load on highway bridges are focused on the Ultimate Limit State (ULS). Fatigue studies can be found in Baroni [5], Rodrigues et al. [6] and Santos and Pfeil [7]. Most studies in Brazil use data from static weighing stations to consider traffic. It is important to remark, however, that static stations can present biased data, since the measurement methodology does not provide total reliability. Moreover, the overloaded vehicles can trace alternative routes and the data is not collected 24 hours a day, in days and months in a row.

Baroni [5], through the analysis of four vehicles database on a Brazilian highway, warns about the possibility of shortening the service life of short span concrete bridges (between 10 m and 20 m). Rodrigues et al. [6] evaluate the reliability indexes of short span concrete bridges (7 m, 10 m and 13 m), considering the Ultimate Limit State and fatigue. Using 204 days of data from São Paulo weighing stations in 2005, the authors verify that safety levels, especially in relation to fatigue, fall short the desired levels. Santos and Pfeil [7], considering steel bridges submitted to the passage of vehicles registered at weighing stations, report a preliminary proposal of live load model for a limited fatigue service life and evaluate the proposed model by analyzing the fatigue service life of a connecting detail of the metallic structure.

This research studies the live load model used in Brazil to verify the fatigue in highway bridges. Through the unlimited fatigue life approach, the current live load model is evaluated in relation to actual traffic and a new fatigue live load model is proposed. To consider the actual traffic, data from weigh-in-motion (WIM) stations are used. Two stations are considered, one is located in BR-381 highway (also known as Fernão Dias, which connects the states of São Paulo and Minas Gerais) and the other one in BR- 290 (also known as Osvaldo Aranha, in the state of Rio Grande do Sul). Typical structures as box girders or multiple girders are considered. The ratios between traffic and Brazilian model load effects (bias factors) are determined for single and continuous spans, in terms of bending moment and shear force. These bias factors are also calculated for the proposed model.

2 FATIGUE IN HIGHWAY BRIDGES

Fatigue occurs due to stress fluctuations from in-service variable loads that, after a certain number of cycles, may lead to fracture of the material. Thus, it can be said that, from the point of view of the loads, fatigue has a character of Service Limit State and, from the point of view of the resistance, has a character of Ultimate Limit State. Normative codes, in general, behave towards the phenomenon in a particular way, calling it the Fatigue Limit State.

Stress ranges with high amplitudes require low number of cycles to fail the material, while stress ranges with low amplitudes require a high number of cycles for failure. These two regimes are known as low cycle fatigue (LCF) and high cycle fatigue (HCF), respectively. Low cycle fatigue is characterized by stress cycles close to the ultimate strength of the material. For bridge structures, the stress cycles from traffic are generally lower than the strength of the material, requiring a high number of cycles to cause the rupture of the structure due to fatigue. Thereby, in general, fatigue in bridges due to traffic is related to high cycle regime.

2.1 Methods of verification

In order to determine the fatigue strength, the S-N curve is used. This curve is a plot of the stress range magnitude (S) and the number of cycles to failure (N). Figure 1 shows two S-N curves for reinforcing bars embedded in concrete beams. It is important to mention that besides the stress range, there are many variables that affect the number of cycles to failure, including bar diameter, bar curvature, type of bar (ribbed or flat), etc.

In Figure 1, it is possible to notice that around one million cycles the curves tend to horizontal, indicating a fatigue limit. According to ACI 215R-74 [8], the stress range associated with the steeper or flatter part of the curves refers to the finite or "infinite" fatigue life, respectively. This limit, below which the fatigue rupture does not happen even for a large number of stress cycles, is called Constant Amplitude Fatigue Limit (CAFL).

It is important to note, however, that, unlike reinforcing bars, concrete does not present CAFL. For highway bridges, Wassef et al. [9] considered a hundred million cycles to determine the stress range corresponding to the unlimited concrete fatigue life .
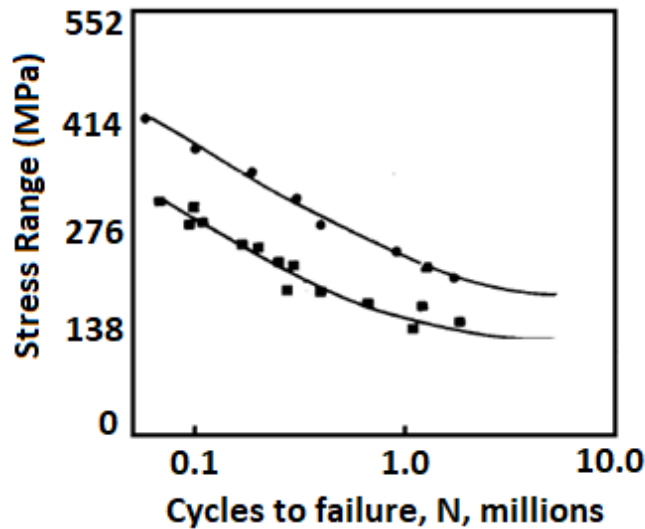
Figure 1. S-N curves for reinforcing bars (adapted from ACI 215R-74 [8]).

If the maximum stress range generated by the load is lower than the CAFL value, the fatigue verification will be guaranteed and the structure will have a fatigue life longer than that required in the design, as long as its original state of full integrity is maintained. This procedure, known as unlimited fatigue life, is used in AASHTO LRFD [4] for concrete bridges. In the calibration of this code, Wassef et al. [9] calibrated the live load model to a bending moment value of traffic that has a 0.01% probability of being exceeded. According to the authors, this moment is related to the maximum stress range that corresponds to the unlimited fatigue life.

Eurocode 1 [3] presents two live load models for unlimited fatigue life. According to the code, they are applicable only for steel structures. There is a contradiction between Eurocode 1 [3] and AASHTO LRFD [4] in this matter. Sanpaolesi and Croce [10], which discuss the Eurocode 1 [3], present two ways to estimate the maximum stress range corresponding to unlimited fatigue life. One of them considers the maximum stress range as being responsible for 99% of the total damage resulting from the entire stress range from the real load spectra below the maximum stress range. The other one considers the maximum stress range, as the one which is exceeded 50000 times in a hundred-year design service life.

The fatigue verification can also be limited to the design service life of the structure, using the equivalent damage method. Santos and Pfeil [7] explain that in this method, the design load must have the characteristic of generating, for a prefixed number of cycles, the same damage that would be generated by the load spectra during the design service life of the structure. With the appropriate weighting coefficients, the verification is performed by comparing the stress range of the live load model with the fatigue strength obtained from the S-N curves. This method, however, is not considered in this paper.

The equivalent damage method is considered in AASHTO LRFD [4] and Eurocode 1 [3] for steel bridges and concrete bridges, respectively. Wassef et al. [9] emphasize that this method should not be used to verify fatigue in concrete and reinforcement. There is a contradiction between Eurocode 1 [3] and AASHTO LRFD [4] in this matter. As reported by Eurocode 1 [3], models for limited and unlimited life are not numerically comparable. The Eurocode 1 [3] presents three models for limited fatigue life.

2.2 Brazilian live load model

The Brazilian live load model of NBR 7188 [1] is shown in Figure 2, with the concentrated and distributed loads. The TB450 values ("TB" refers to the Brazilian live load model and "450" is the total vehicle weight, in kN) must also be pondered by the vertical impact coefficient (CIV, in Portuguese) and, when it's necessary, by the number of lanes coefficient (CNF, in Portuguese) and the additional impact coefficient (CIA, in Portuguese). The live load assumes any position on the entire highway with the wheels in the most unfavorable position, considering shoulders and clearances. The distributed load must be positioned in the most unfavorable condition, regardless the road lanes.
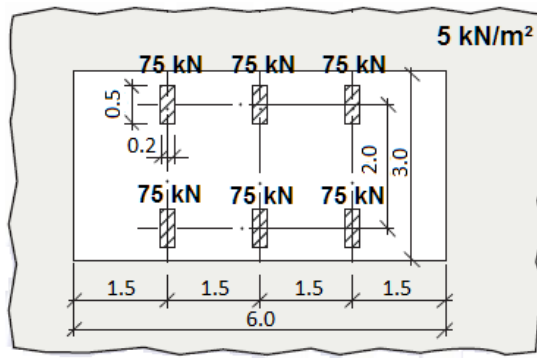
Figure 2. Brazilian live load model, dimensions in meters (adapted from NBR 7188 [1]).

NBR 6118 [11] establishes the reducing factor of 0.5 to be implemented in the model for fatigue verification in bridge girders. According to the code, the fatigue verification in reinforcement will be satisfied if the maximum calculated stress range, $\Delta\sigma_s$, satisfies Equation 1,

$$\gamma_f \Delta\sigma_s \leq \Delta f_{sd,fad} \tag{1}$$

where $\gamma_f = 1.0$; and $\Delta f_{sd,fad}$ = characteristic fatigue strength for 2×10^6 cycles.

According to Laranjeiras [12], the value of 2×10^6 cycles was also used in the German code (DIN 1045, 1989) and the American one (ACI 343R, 1986). It is worth noting that, according to Figure 1, the S-N curves tend to horizontal at around one million cycles indicating unlimited fatigue life.

For fatigue verification in steel girders with up to 100-m span, the NBR 16694 [13] also establishes the factor of 0.5. The NBR 8681 [14] also indicates the reducing factor of 0.5 for girders up to 100-m span. According to Laranjeiras [12], this value was provided in a retired German code (DIN 1075, 1988), where the live load was similar to the Brazilian one.

3 WEIGH-IN-MOTION (WIM)

3.1 Description of the system and WIM stations

Regarding the relevance of actual traffic, this work uses vehicle records obtained from high speed weigh-in-motion stations (HS-WIM), as shown in Figures 3 and 4. The system is installed on the road lanes, and vehicles are registered with no need to stop or to lower their speeds. In general, the system consists of lines of piezoelectric sensors, inductive loops, temperature sensor and a device to collect and analyze the records (Figure 5). Inductive loops detect vehicles and measure the distance between axles and speed, while piezoelectric sensors are responsible for weighting. In this work, data from the BR-381 (Fernão Dias, SP-MG) and BR-290 (Osvaldo Aranha, RS) stations are used. Figure 6 shows the final layout of the system in both highways.

In BR-381, the system is installed in two road lanes in the same direction (Minas Gerais to São Paulo) and the data are sent to the Structures and Structural Materials Laboratory of the Polytechnic School of the University of São Paulo - LEM / USP. The traffic statistics presented in this work cover the period from September 2015 to August 2017, with daily records (data from February to May 2016 are missing). The station is currently in operation.

In the BR-290 station, the system was installed between the cities of Porto Alegre and Osório, in 2013. The highway has three lanes in the same direction, however the sensors were installed only in the two lanes on the right, where most trucks circulate. The data used in this work covers the period from March to June 2014, summing 79 days (there are days without records). The station is no longer in operation.
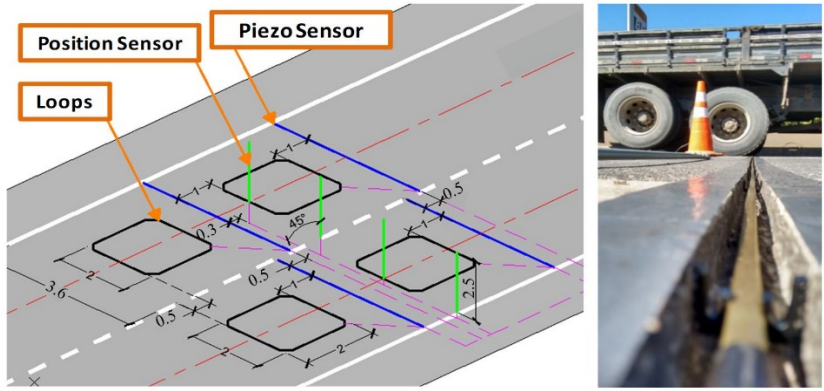
Figure 3. HS-WIM system in BR-381 (MG-SP) and weighting sensor before grout (adapted from Portela [15]).
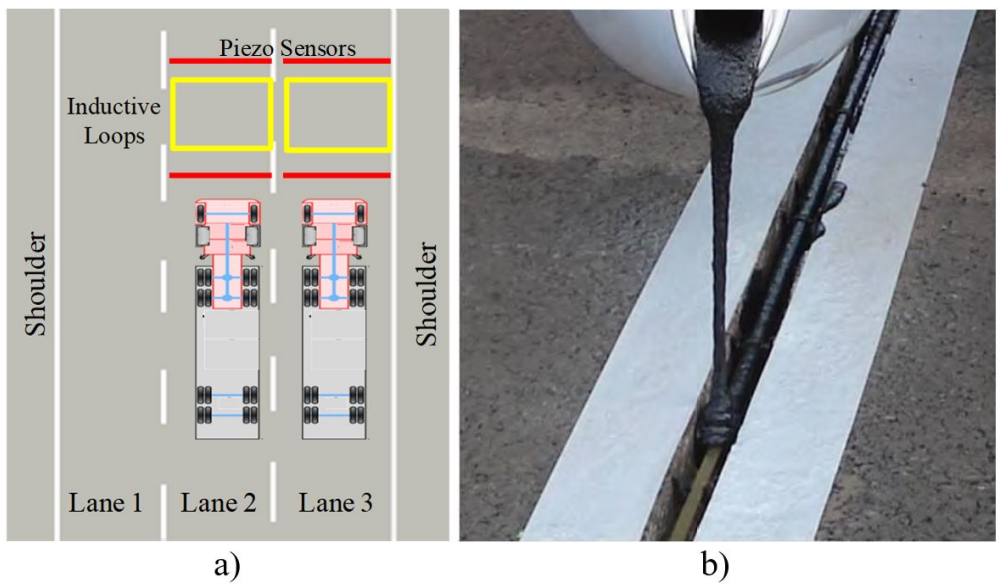
Figure 4. a) HS-WIM system in BR-290 [15]; b) weighting sensor with grout [16].

Figure 5. Sensors and data collecting system from BR-290 (adapted from Brito and Bock [16]).

a)   b)

Figure 6. Final appearance of HS-WIM system in both highways: a) BR-381 [15]; b) BR-290 [16].

For each vehicle that passes through the sensors, the system provides information, such as day, hour, lane, speed, total length, total weight, axle spacing and axle weight. In this work, the records are analyzed using Microsoft Excel spreadsheets. Table 1 shows the organization of the data, where each line corresponds to a truck. The outline of the five most frequent classes obtained from WIM are shown in Figure 7, with the respective legal weights (5% of tolerance).

Table 1. WIM data in the spreadsheets.

Day	Hour	Lane	Speed (Km/h)	DNIT	Total length (m)	Total weight (kN)	d12 (m)	d23 (m) ‥	P1 (kN)	P2 (kN)	P3 (kN) ‥
01/15/17	01:28:41	2	90.4	2C	12.86	112.8	6.94		36.9	75.8	
01/15/17	01:29:59	2	89.0	3C	10.49	157.3	5.11	1.36	36.7	65.6	54.9

*d12 e d23 are the axle spacing and P1, P2, P3 are the axle weight

Figure 7. Frequent classes with the respective legal weights.

It is worth noting that the HS-WIM system avoids evasion, as drivers do not notice it. In addition, due to the continuous process of obtaining data (24 hours a day, on consecutive days), the system allows the knowledge of the real frequency of occurrence of the vehicles, which is essential for the fatigue analysis. These particularities give the technology a great advantage over static weighing stations.

Static weighing, on the other hand, is more accurate. As WIM sensors are strongly influenced by temperature, the system must undergo periodic calibrations. In these measurements, a known weight truck passes through the sensors at varying speeds at different times of the day. From July 2015 to August 2017, the Fernão Dias station was calibrated in July 2015, October 2015, February 2016, February 2017 and May 2017. According to Portela [15], the error of the BR-381 system, in relation to the total weight of the trucks, is around 10%. The Rio Grande do Sul station was calibrated in February 2013, as shown by Brito and Bock [16]. HS-WIM is widespread in United States, where the data are widely used to calibrate bridge design codes. In Brazil, nonetheless, considering the reduced number of stations, the use of this system is not common.

3.2 Filtering process

Even with calibrations, the system might present incorrect data: weights greater than the maximum traction capacity or smaller than the self-weight are some examples. Furthermore, several data are unnecessary for the study of live load in bridges. Passenger vehicles and light trucks, for instance, can be neglected, in most analyses, due to irrelevant load effect on the bridge. Thus, WIM data needs to be filtered before it can be used. The filtering criteria need to be defined considering the particular characteristics of the Brazilian fleet and may vary according to the analysis need, in other words Ultimate Limit State, service or fatigue.

For service and fatigue analysis, which is the purpose of this work, Wassef et al. [9] explain that the frequency of occurrence of loads is essential, it means the load spectra. In this case, heavy trucks with fewer frequencies have little influence on the analysis and can even be ignored. Light trucks also make no significant contribution. Among the 14 criteria used in Wassef et al. [9], a type of filter is designed to eliminate trucks with a total weight less than 90 kN. As reported by Laranjeiras [12], trucks weighing less than 70 kN accumulate fatigue damage that is irrelevant to the safety of the structure, even if they are occur many times.

The following list presents, in order, the filters that are applied to the stations considered. The filters were set after a research in the National Department of Transportation (DNIT, in Portuguese) resolutions and truck manufacturers catalogs. Vehicles that fit any of the filters have been excluded.

1- $GVW \leq 62$ kN (GVW is the total gross vehicle weight);
2- $P_i \leq 22$ kN, where "P_i" is the axle weight;
3- $P_d > 320$ kN, where "P_d" is the weight of double tandem;
4- $d_i \leq 0.92$ m, where "d_i" is the distance between axles;
5- $C > 36$ m, where "C" is the total length of the vehicle;
6- $C > 15.4$ m and $GVW \leq 104.3$ kN;
7- $P_i > 180$ kN;
8- $GVW \geq 1.1\sum P_i$ or $GVW \leq 0.9\sum P_i$, where "$\sum P_i$" represents the sum of the weights of the axles;
9- $\sum d_i > C$, where "$\sum d_i$" this represents the sum of the wheelbase;
10- $C < 5$ m;
11- $V > 170$ Km/h, where "V" is the vehicle speed;
12- $P_1 > 100$ kN, where "P_1" is the weight of the first axle (front);
13- $GVW > 1500$ kN.

On the Fernão Dias highway, the average number of daily vehicles is 13292 before and 3632 after filtering. On the BR-290 the average number of daily vehicles recorded is 11736 before and 1963 after filtering. It shows that the Fernão Dias highway presents, after filtering, an average amount of daily vehicles 85% larger than the BR-290. In Figure 8, the filtering percentages for both stations are shown. The following sub-item presents an overview of traffic composition of the Fernão Dias and Rio Grande do Sul highways after filtering.

3.3 The current traffic composition

In terms of the average monthly values of the Fernão Dias highway, the average number of vehicles per day varies from 3043 to 4053 and the respective coefficient of variation range from 21% to 39%. Compared to the monthly average values of BR-290, the average number of daily vehicles varies from 1619 to 2190 and the respective coefficient of variation range from 30% to 53%. Tables 2 and 3 show the traffic composition statistics for the five most frequent

classes of Fernão Dias and BR-290 highways, respectively. It is worth pointing out, nevertheless, that a possible reduction of the minimum weight filter value would increase the frequency of class 2C. Although, in Tables 2 and 3, only the most frequent classes are presented, this work also considers other classes.
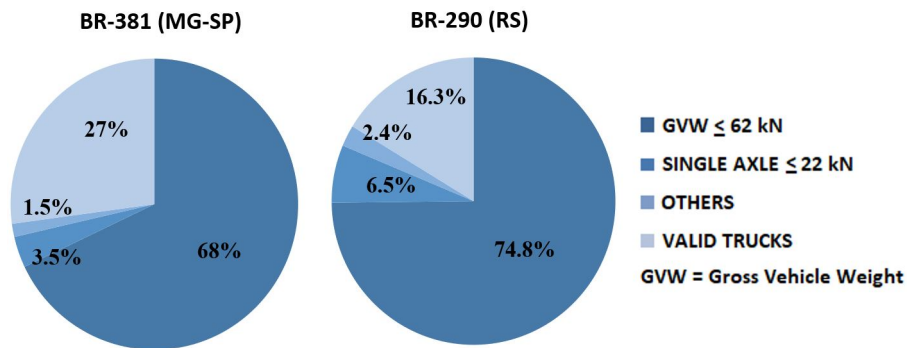
Figure 8. Statistics of filtered data (adapted from Portela [15]).

Table 2. Statistics for main classes of BR-381 (adapted from Portela [15]).

DNIT	Frequency (%)	Average GVW (kN)	Minimum GVW (kN)	Maximum GVW (kN)	Average total length (m)
2C	15.36	103.6	62.0	275.1	10.24
3C	23.40	173.2	66.8	416.5	10.95
2S2	12.96	199.1	96.7	585.0	18.45
2S3	9.46	337.6	124.2	712.2	17.53
3S3	14.75	430.2	139.9	899.4	17.21

GVW: Gross vehicle weight (total)

Table 3. Statistics for main classes of BR-290 (adapted from Portela [15]).

DNIT	Frequency (%)	Average GVW (kN)	Minimum GVW (kN)	Maximum GVW (kN)	Average total length (m)
2C	18.21	101.2	63.0	273.0	9.19
3C	23.37	166.2	67.2	423.0	9.76
2S2	7.45	192.1	100.0	547.0	16.67
2S3	10.56	318.5	121.0	660.0	17.40
3S3	15.55	400.4	154.0	807.0	16.57

GVW: Gross vehicle weight (total)

4 EVALUATED BRIDGES AND METHODS FOR DETERMINING THE LOAD EFFECTS

This work examines typical structures of bridges including box girders and multiple girders (Figure 9), which are the most common types considered in typical projects.

The multiple girders bridges were obtained from real projects in the state of Minas Gerais with dates of 2012 and 2013. The highways have two traffic lanes of 3.60 m, two 0.6-m clearances and two New Jersey barriers of 0.4 m. Six bridges with simply supported prestressed girders are considered, without intermediate crossbeams (crossbeams only in the supports), with spans of 14, 16, 18, 28, 37 and 41 meters. The 37-m span has four girders and the others have three girders, as shown in Figure 9. Bridges with spans of 18, 28 and 41 meters were also considered with intermediate crossbeams.

Regarding box girders bridges, one, two, three or four traffic lanes of 3.60 m are contemplated, where two clearances of 0.6 m each are also used, as shown in Figure 9. For each box section, spans of 10, 30, 50 and 70 meters are contemplated in simply supported and two-span continuous structures.

For the determination of the longitudinal global load effects in box bridges, it is accepted that the structure is a single beam, homogeneously distributing the forces from the loads on the deck. In this matter, due to the high torsional rigidity of the closed section, it is not necessary to assess the transversal distribution of the load effects.
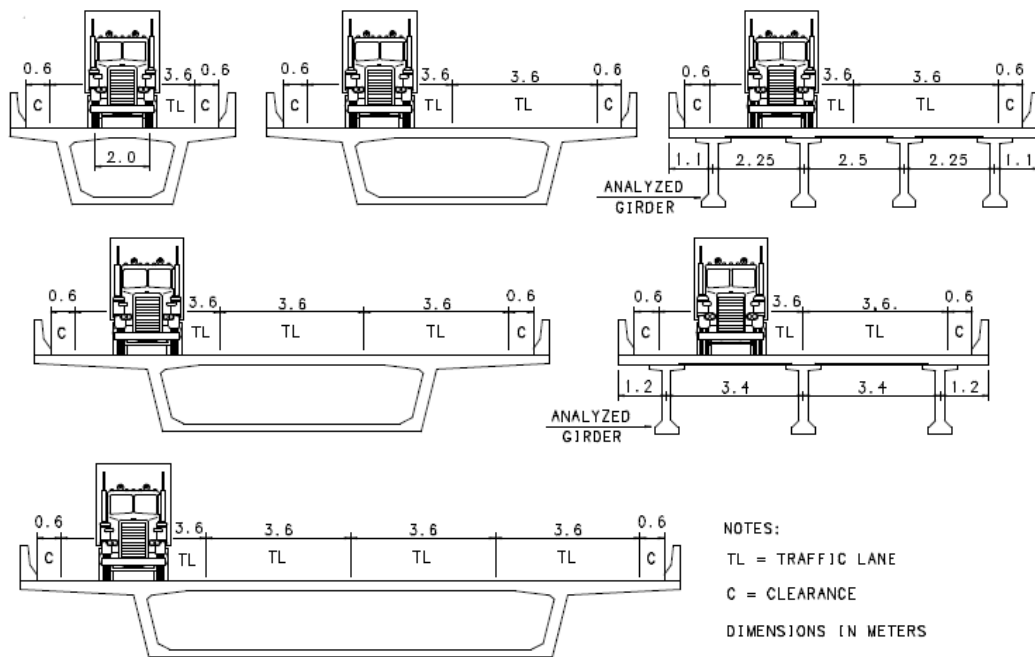
Figure 9. Cross-section of bridges.

On the multiple girders bridges, in contrast, it is necessary to study the girder distribution factors. This work uses the Engesser-Courbon and Fauchart methods for structures with and without intermediate crossbeams, respectively, as presented in Stucchi [17]. For both methods, routines were developed in Microsoft Excel and for the Fauchart method the Ftool structures analysis program [18] was also used.

Regarding to longitudinal analysis for simply supported bridges, which can be multiple girders or box girders, the bending moment at mid-span and the shear force at support are evaluated. In continuous box girder bridges, the bending moment at support is evaluated. In Figure 10, the influence lines, that were implemented in Microsoft Excel, are shown.

5 DETERMINATION OF TRAFFIC LOAD EFFECT CORRESPONDING TO UNLIMITED FATIGUE LIFE

To determine the load effects due to current traffic for unlimited fatigue life, this work considers the same approach as in Wassef et al. [9]: the individual passage of vehicles. According to Wassef et al. [9], fatigue analysis requires the frequency of occurrence of loads, in other words, the load spectra. Thus, the authors do not consider the situations of trucks in multiple presence, due to the small probability of occurrence. It must be point out, however, that the consideration of multiple presence is essential for the Ultimate Limit State. This issue, however, is not part of this paper. The multiple presences statistics for the WIM data of Fernão Dias highway are presented in Portela [15].

It is important to add that the present work does not consider the dynamic effect of trucks, that means it is a static analysis in order to evaluate the Brazilian live load model without impact. Dynamic amplification must be studied separately.

In order to compute the distribution of load effect of girder bridges, it is considered that trucks are centered in the traffic lane and the transversal distance between wheels is 2 m, as shown in Figure 9. The exterior girders (close to cantilever slabs) present the highest load effects for both live load model and traffic. Thus, the bias factor for girder bridges are analyzed for exterior girders. Considering that the trucks are centralized in the traffic lane, it appears that, based on the Engesser-Courbon and Fauchart methods, the values of the load effect for exterior girders do not change due to possible changes in the transverse distance between wheels.

The routines for computing the load effect due to the real traffic, according to the influence lines in Figure 10, were implemented in Microsoft Excel spreadsheets that contain the WIM record. The routines were validated with the Ftool program [18] by comparing load effects from different vehicles. In the routines, it is possible to include a value for the transversal load distribution factor, which is 1.0 for box girders. For girder bridges, this factor varied from 0.42 to 0.59 (exterior girders).
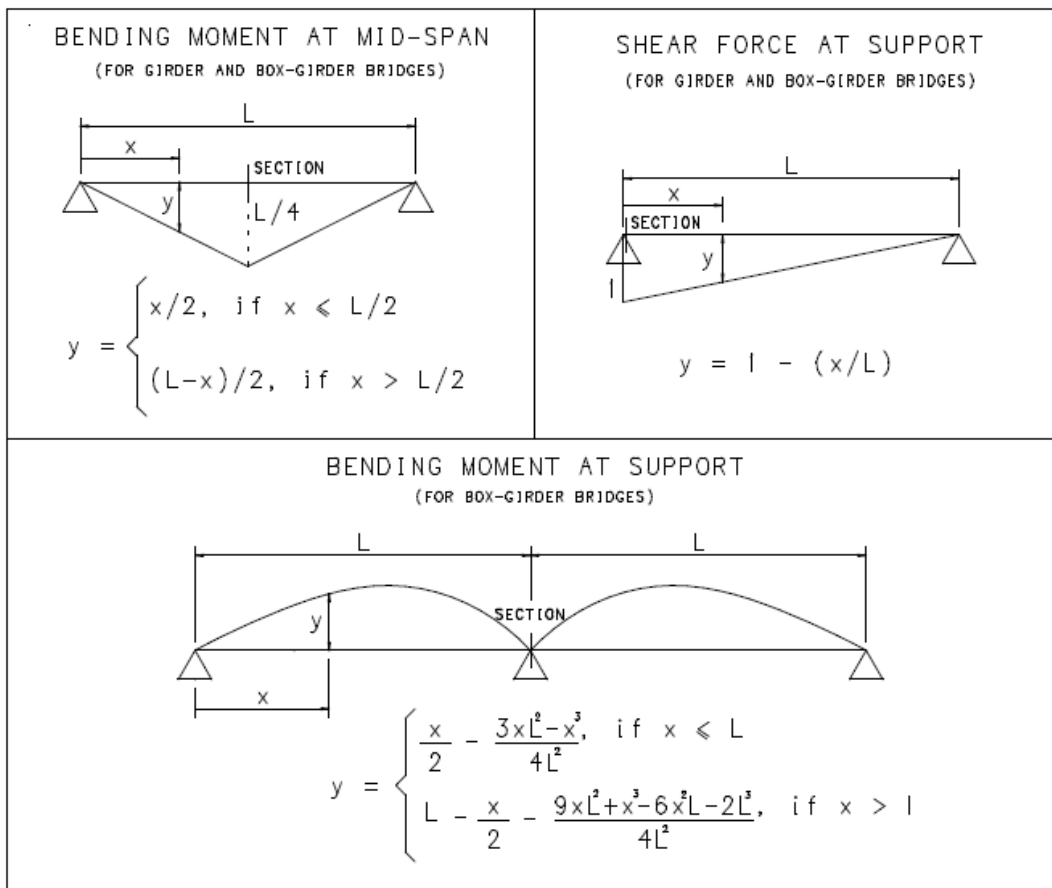
Figure 10. Influence lines.

Similarly to Wassef et al. [9], this work uses the graphical method of the normal probability paper for the statistical interpretation of the data. In this method, the horizontal axis represents the variable and the vertical axis represents the number of standard deviations from the mean value, which is also referred as "standard normal variable" or "z-score". The vertical axis can also be interpreted as the probability of being exceeded. Since "X" is the random variable and "Q" is the number of points in the sample, the graphical construction procedure, according to Nowak and Collins [19], follows the steps:

1- The values of the variable X are organized in ascending order, assigning to each value an index "i" ranging from 1 to Q. Repeated values are not discarded;

2- for each "x_i" value, the accumulated probability is associated to "$p_i = i/(Q+1)$";

3- for each "p_i" value, $z_i = \Phi^{-1}(p_i)$ is determined, which represents the inverse of the standard normal distribution;

4- ploting the coordinates (x_i, z_i).

This procedure is performed on each bridge for each database. The random variable X corresponds to the load effect (bending moment or shear force) for each truck of WIM data and "Q" represents the number of trucks, after filtering.

The most important property of the normal probability paper is that the plot of a normal random variable is represented as a straight line. Thus, the straighter the plotting of the data, the more accurate the representation as a normal distribution will be. However, even if the curve does not approximate to a normal distribution, some important statistical parameters can be obtained. The intersection of the curve with the zero value of the vertical axis ($z = 0$) gives the mean value, which corresponds to the probability $p_i = 0.5$. The slope of the curve is equal to $1/\sigma_x$, where σ_x is the standard deviation. Thus, the steeper the curve, the smaller the standard deviation.

For the calibration of the live load model for unlimited fatigue life of AASHTO LRFD [4], Wassef et al. [9] obtain bending moments regarding the 0.01% probability of being exceeded. This corresponds to the percentage of 99.99%,

which represents the vertical value z = 3.8 on the probability paper. These moments are related to the maximum stress range for unlimited fatigue life.

The approach of Sanpaolesi and Croce [10] for the unlimited fatigue life of Eurocode 1 [3], considers the maximum stress range that exceeds 50000 times in a hundred-year design service life. Therefore, this approach requires contemplating the volume of truck traffic in the future. Rodrigues et al. [6] consider the average daily truck traffic (ADTT) of 5000 vehicles for two lanes. It is worth pointing out that the ADTT for two lanes of BR-381 and BR-290 is 3632 and 1963 vehicles, respectively.

For the BR-381 and BR-290 highways, the Sanpaolesi and Croce [10] approach results in the probability of the load effect being exceeded of 0.027% for bridges with ADTT = 5000 and 0.014% for bridges with ADTT = 10000. Hence, the value of 0.01% presented in Wassef et al. [9] meets these values. These probabilities result in close load effects and bias factors. The values presented in this work, for bending moment and the shear force, are related to the probability of 0.01% of the load effect being exceeded.

In Figure 11, considering data from BR-381 (Fernão Dias Highway), the determination of bending moment at mid-span for the simply supported bridge is shown. The curve shown in Figure 11 consists of several points and each point represents a truck of the database after filtering. As the analysis consider the single trucks, the load effect for box-girder bridges does not change with more lanes. It is worth noting, however, that the respective bias factors are changed according to the number of lanes, since the factor also depends on the live load model.
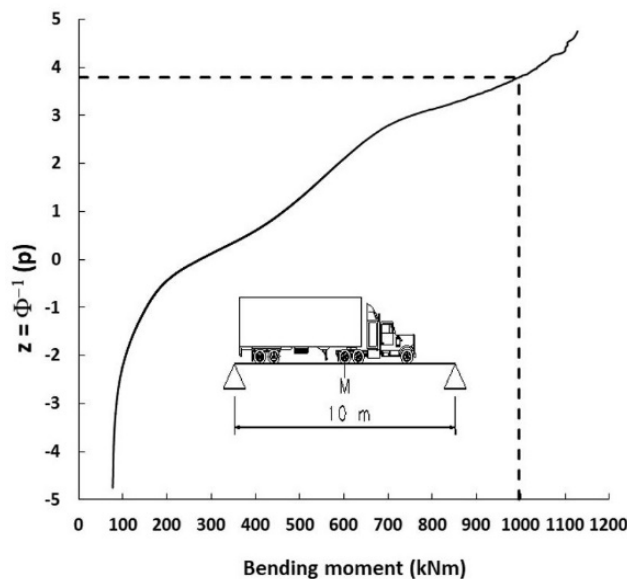
Figure 11. Determination of the load effect on the normal probability paper.

To determine the load effect from Fernão Dias highway, this work uses WIM data from September 2016 to May 2017 (273 days). It was verified that, as long as at least four months of the station are used, the results practically do not change with the increase in the number of months. For BR-290, all four available months are used (March to June 2014). It is important to comment that the possibility of changing the Filter 1 was studied, where the value of 90 kN was tested, as used in Wassef et al. [9]. This change, however, did not significantly alter the load effects related to unlimited fatigue life.

6 EVALUATION OF THE BRAZILIAN LIVE LOAD MODEL IN RELATION TO REAL TRAFFIC

To evaluate the Brazilian live load model, the ratio between load effect due to real traffic and live load model are computed. The Brazilian model is considered according to the loads on Figure 2. Impact and weighting coefficients are not contemplated. Thus, the fatigue-reducing factor of 0.5 is assessed according to the bias factors obtained. Factors larger than 0.5 indicate that the Brazilian model falls short of the actual traffic for an unlimited fatigue life. It is worth

remembering that for girder bridges, the bias factors refer to the exterior girders, since they presented the highest load effects on the structures considered.

Bias factors are presented for bending moment at mid-span of simply supported bridges, bending moment at support of continuous bridges, and shear force at support of simply supported bridges. The load effects were computed for the WIM data and the live load model using the routines developed in Microsoft Excel. To calculate load in the live load model for continuous bridges, the Ftool program [18] was used yielding curved influence lines (Figure 10).

It was considered unnecessary to carry out the analysis for continuous bridges in terms of bending moment near the mid-span or shear force at supports. After analyzing some results with the Ftool program [18], it was found that the bias factors of these load effects are very close to the respective values for simply supported bridges. In fact, it's verified, according to Figure 12, that the influence lines for the bending moment at mid-span and the shear force at supports of continuous structures are like those of simply supported structures. Thus, the bias factors of these load effects for simply supported bridges also apply to continuous bridges.
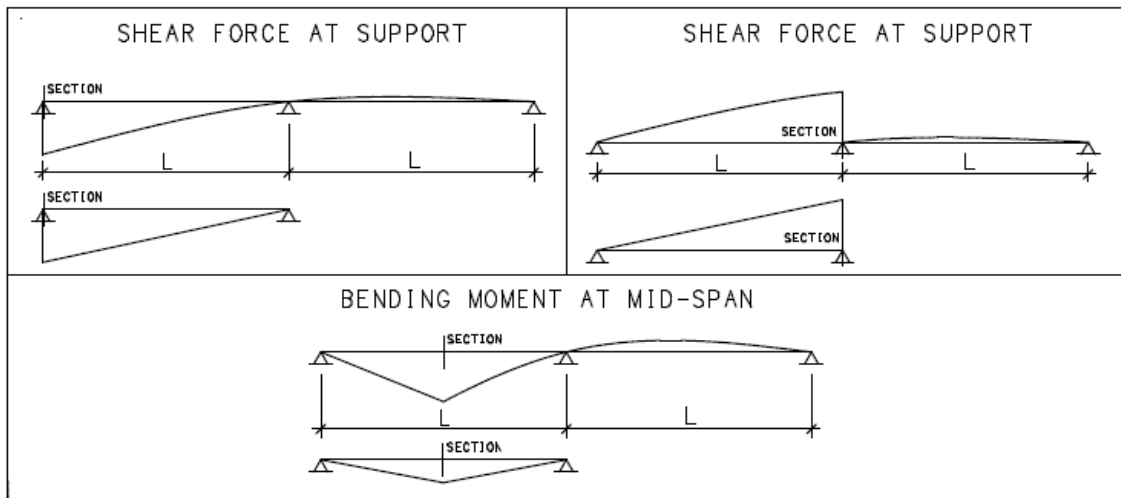
Figure 12. Similar influence lines.

Figures 13 to 20 show the bias factors for the BR-381 (Fernão Dias) and BR-290 highways. It is verified that the bias factors are not uniform, i.e., the current model can cover the real traffic load effects or fall short for it depending on the span length and width of the bridge. In general, the live load model satisfies real traffic for larger spans and multiple lanes bridges. For short span bridges, especially for bridges with one and two lanes, the Brazilian live load model does not satisfies the current truck traffic. Based on these results, it can be observed that is important to develop a Brazilian live load model for unlimited fatigue life, especially for short span bridges.

In the particular case of simply supported girder bridges with two lanes up to 40 meters, which are the most frequent structures on Brazilian highways, the bias factors vary around the mean value close to 0.8, as shown in Figures 19 and 20. Thus, for these structures, the reducing factor of 0.8 for the TB450 corresponds better to the unlimited fatigue life approach.

The fact that the live load model of NBR 7188 [1] is conservative for bridges with larger extensions and wider cross section is mainly due to the distributed load considered along the entire width of the bridge and to its longitudinal extension, in the most unfavorable way. It is worth noting that, if the coefficient of number of lanes (CNF) of NBR 7188 [1] were considered, the bias factors would undergo few changes between approximately 5% and 10%. The coefficient is 1.05 for one lane, 1.0 for two lanes, 0.95 for three lanes and 0.90 for four lanes.

7 BRAZILIAN LIVE LOAD MODEL PROPOSAL FOR UNLIMITED FATIGUE LIFE

To determine the load effect corresponding to the unlimited fatigue life, it is verified that the 3S3 six-axle truck is responsible for most of load effects getting close to the percentage of 99.99%. Hence, after the evaluation of the six-axle vehicles associated with the percentage considered, the model in Figure 21 is proposed for the Brazilian live load model for unlimited fatigue life.
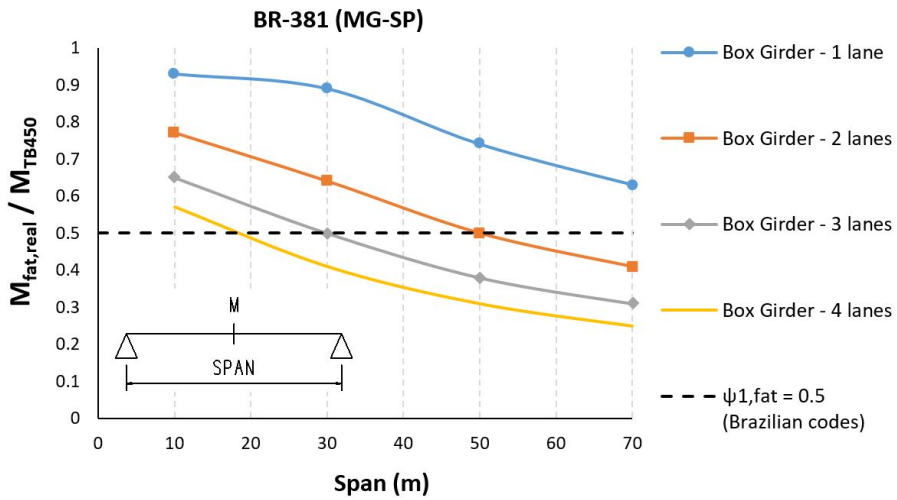
Figure 13. Bias factors for bending moment at mid-span in simply supported box-girder bridges – BR-381 (MG-SP).
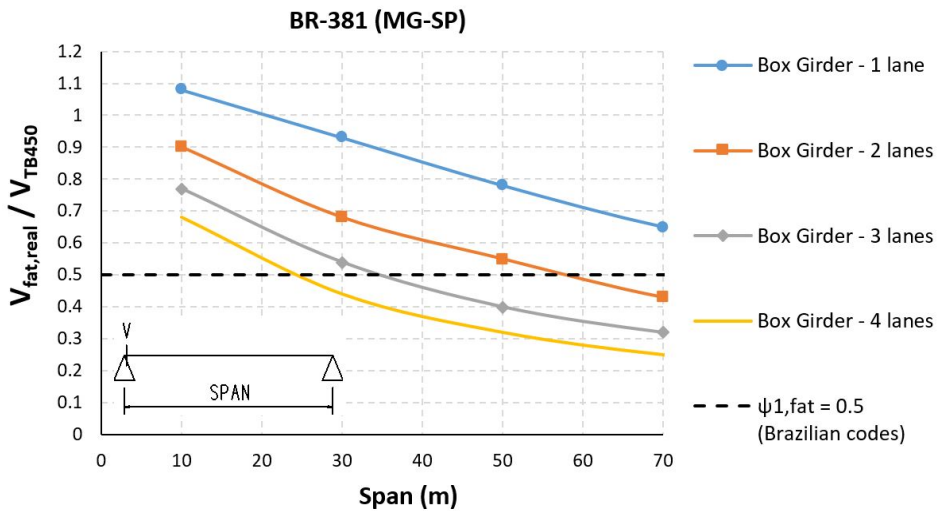
Figure 14. Bias factors for shear force at support in simply supported box-girder bridges – BR-381 (MG-SP).
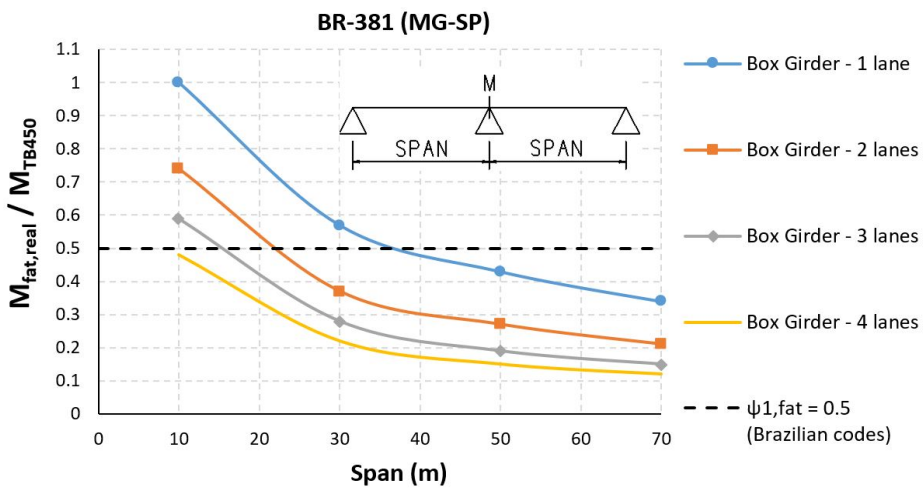
Figure 15. Bias factors for bending moment at support in continuous box-girder bridges – BR-381 (MG-SP).
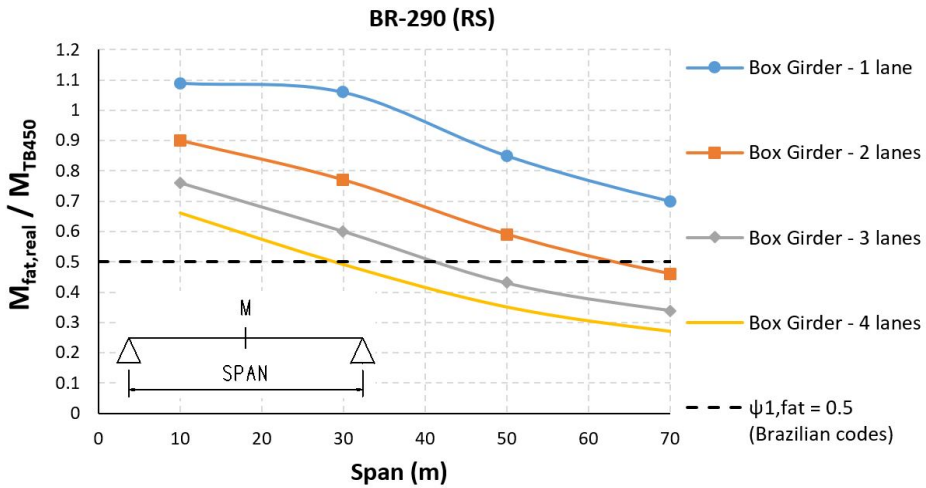
Figure 16. Bias factors for bending moment at mid-span in simply supported box-girder bridges – BR-290 (RS).
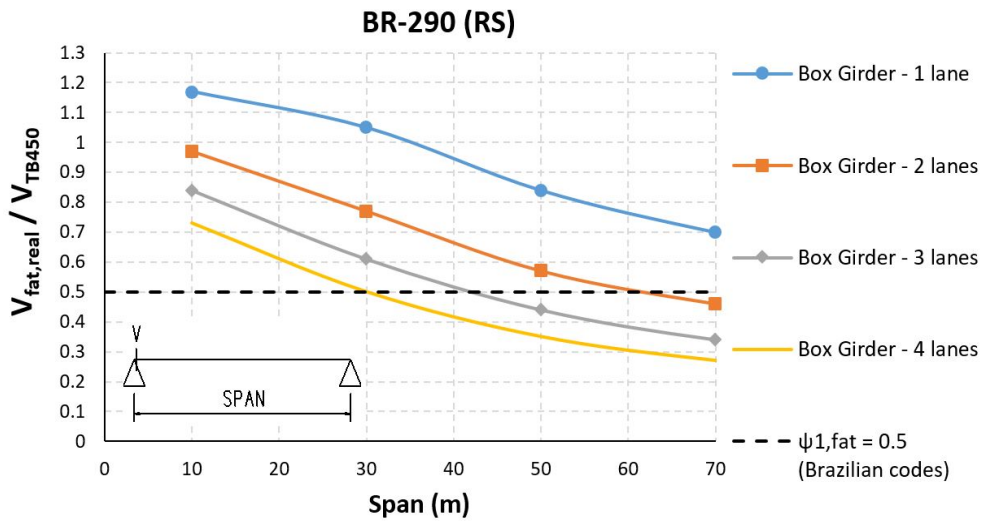
Figure 17. Bias factors for shear force at support in simply supported box-girder bridges – BR-290 (RS).
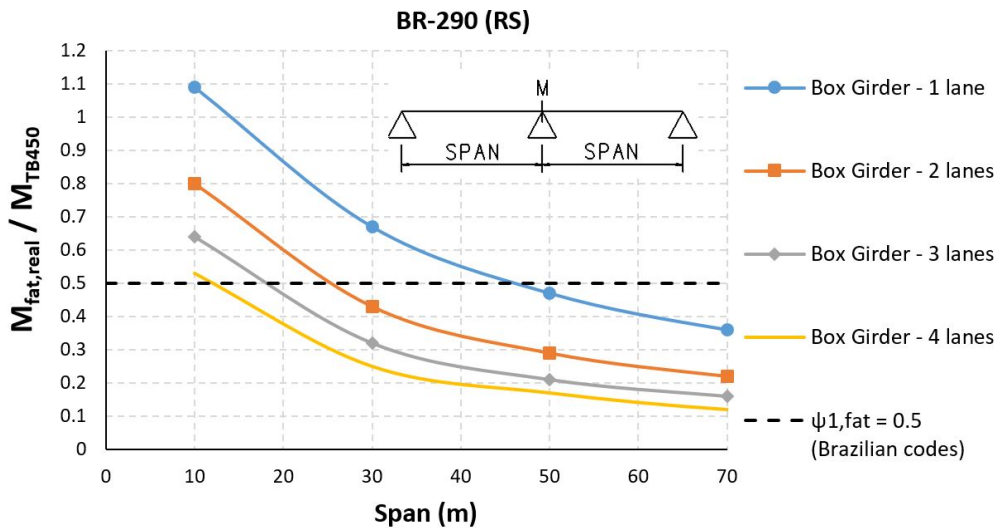
Figure 18. Bias factors for bending moment at support in continuous box-girder bridges – BR-290 (RS).

Rev. IBRACON Estrut. Mater., vol. 13, no. 4, e13407, 2020

14/20
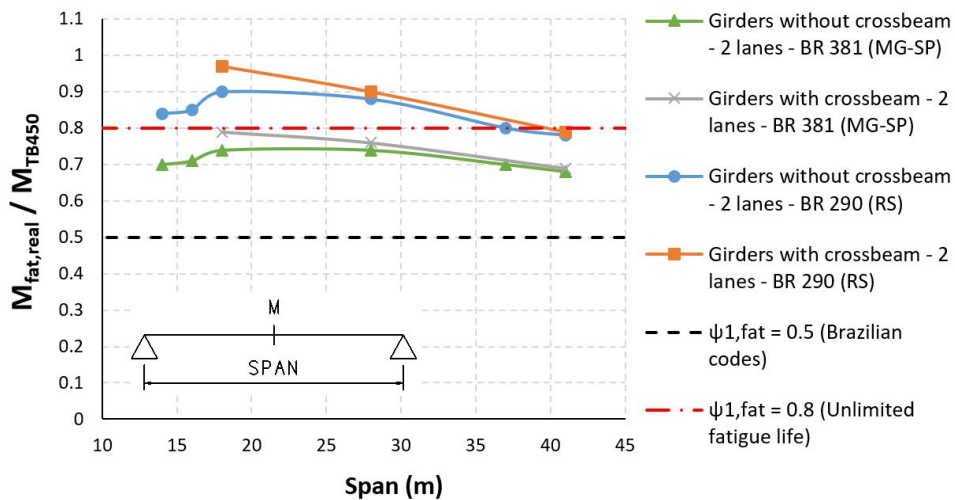
Figure 19. Bias factors for bending moment at mid-span in simply supported girder bridges.
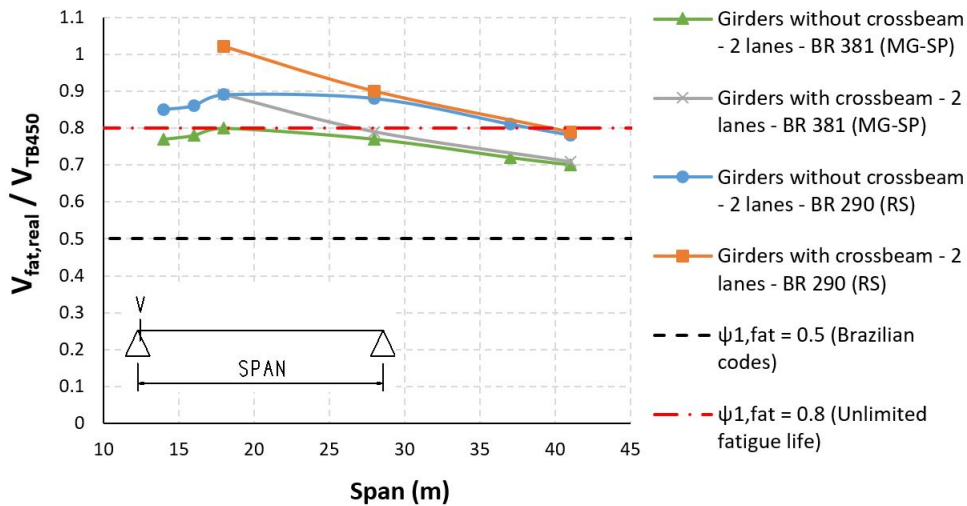
Figure 20. Bias factors for shear force at support in simply supported girder bridges.

Although the trucks associated with the 99.99% percentage exceed the legal weight, it was used the weight of 500 kN for design truck, which is in accordance with the value of the Brazilian law (509.25 kN, as shown in Figure 7). After the evaluation of the proposed model in relation to the current traffic data, a weighting coefficient is proposed for the loads according to the bias factors obtained.

The proposed model considers the design truck centralized in a 3.5 m wide design lane. This lane is independent of the road lanes and assumes any position in the entire highway, in the most unfavorable way, including shoulders and clearances. This most unfavorable cross-sectional position ensures that, for girder bridges, the model satisfies even a possible traffic lane leaning against the barrier. For girder bridges where the traffic lane does not touch the barrier, the model is conservative. For box girder bridges, the transverse positioning of the loads does not influence the longitudinal load effects of bending moment and shear force. It is interesting to point out that the load effects of the proposed model do not depend on the number of road lanes, since the distributed loading is not considered. This is consistent with the load effect from actual traffic.

Figures 22 and 23 show the bias factors for the proposed model for the Fernão Dias and BR-290 highways. It is verified that the bias factors are more uniform and vary around the mean value of 1.7. Thus, this work proposes a fatigue coefficient γ_{fad} . = 1.7 to be applied to the live load model.
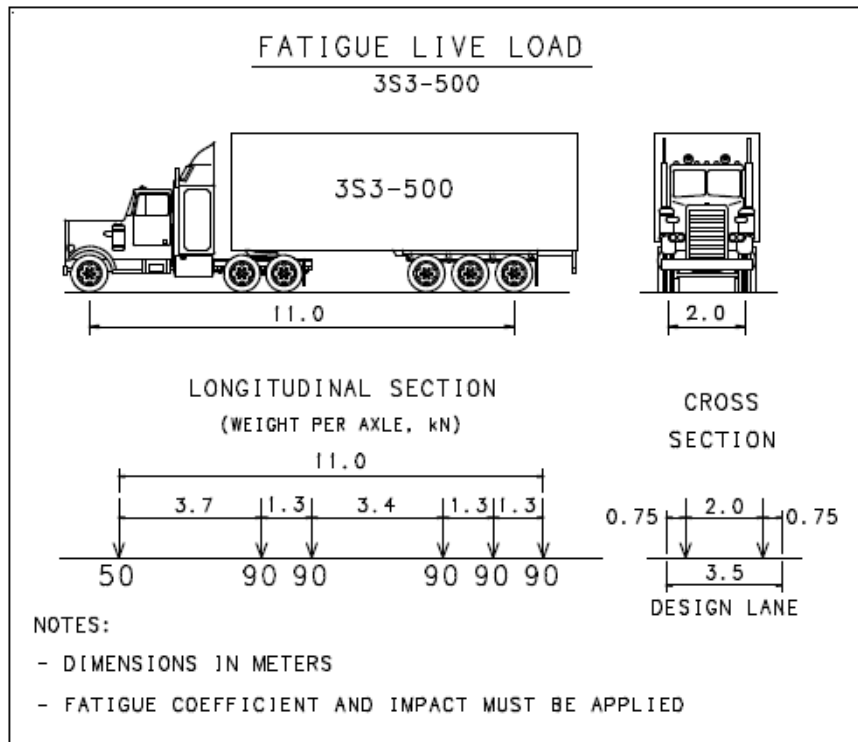
Figure 21. Brazilian live load model proposal for unlimited fatigue life.
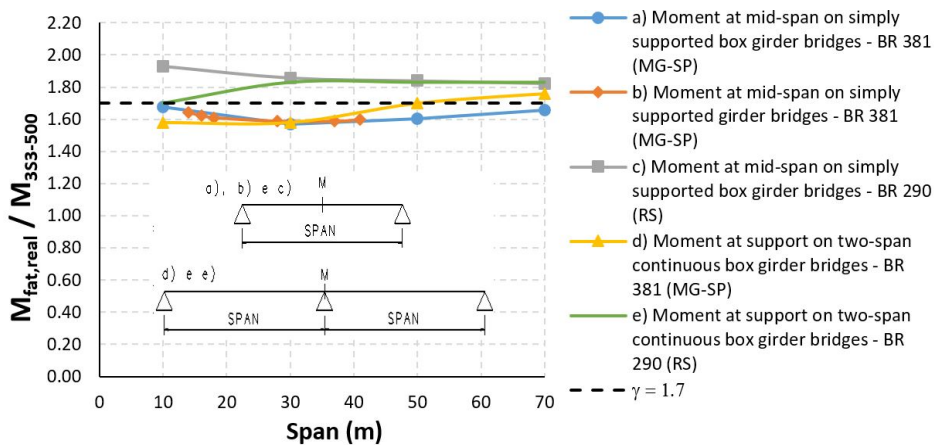
Figure 22. Bias factors for bending moment related to the proposed model.

The proposed model does not consider the impact, which must be studied separately. In the absence of dynamic analysis studies, one option is the vertical impact coefficient (CIV) of NBR 7188 [1]. The number of lanes coefficient (CNF) should not be applied, since the truck is considered in a single design lane.

It is important to point out that the proposed model was developed through the analysis of longitudinal load effects. Thus, for slabs and crossbeams, for example, additional studies are required. In addition, the model is appropriate only for new bridge designs that consider unlimited fatigue life.

It is worth remarking that the proposed live load model and the fatigue coefficient can be reassessed by analyzing more databases and with reliability studies. For the AASHTO LRFD [4] calibration, for instance, Wassef et al. [9] used 15 WIM stations, where the ADTT varied from 97 to 4590. The authors evaluated the bias factors in terms of bending moment for simply supported and continuous bridge for five span lengths (9, 18, 27, 36 and 61 meters). The average bias factors varied from 1.34 to 2.07. The average bias factor, considering all stations and spans, was 1.74. After the

statistical analysis of the bias factors, the authors recommended a fatigue coefficient equal to 2.0 to be applied to the live load model. The coefficient adopted by AAHSTO LRFD [4], however, was 1.75.
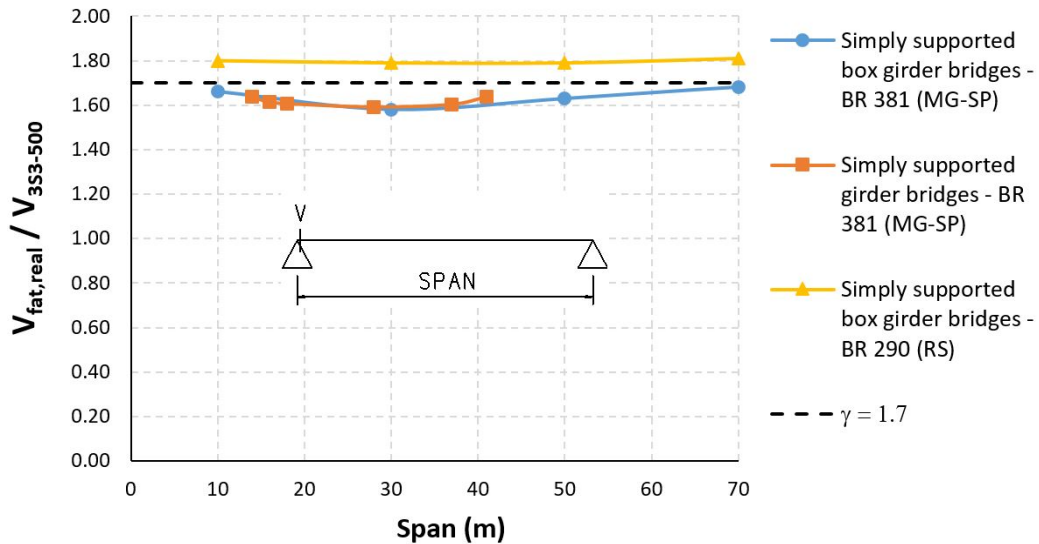
Figure 23. Bias factors for shear force related to the proposed model.

8 COMPARISON OF MODELS

In Figures 24 to 26, a comparison between the proposed model and the NBR 7188 [1] model is presented. The box girder section is considered, as shown in Figure 9, and fatigue and impact coefficients are applied. The Ftool program [18] was used for this. The impact coefficient of NBR 7188 [1], which is also applied to the proposed model, is calculated according to expression (2), where "L" is the span length. For the NBR 7188 [1] model, the number of lanes coefficient (CNF) also applies. The fatigue coefficients of the proposed model and the NBR 7188 [1] are 1.7 and 0.5, respectively.

$$CIV = 1 + 1.06 \left(\frac{20}{L + 50} \right) \leq 1.35 \tag{2}$$
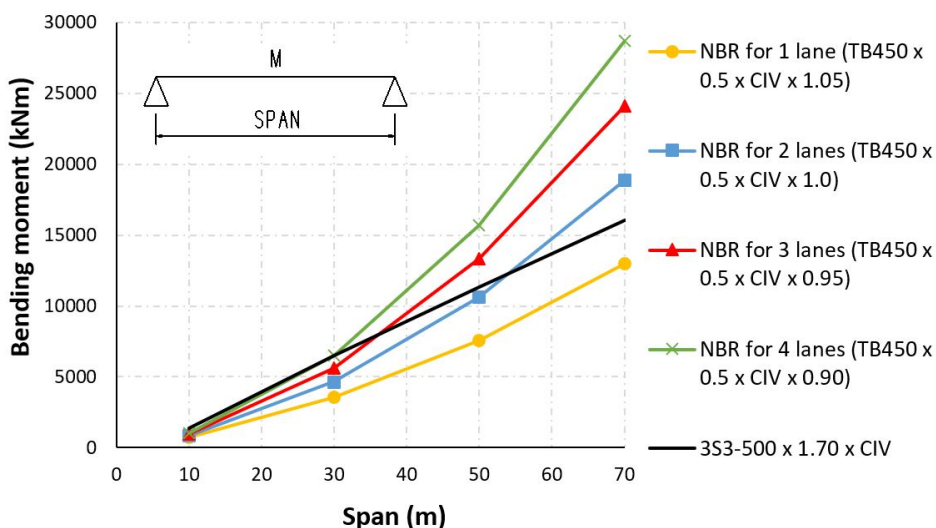
Figure 24. Comparison between models for maximum bending moment at span in simply supported bridges.
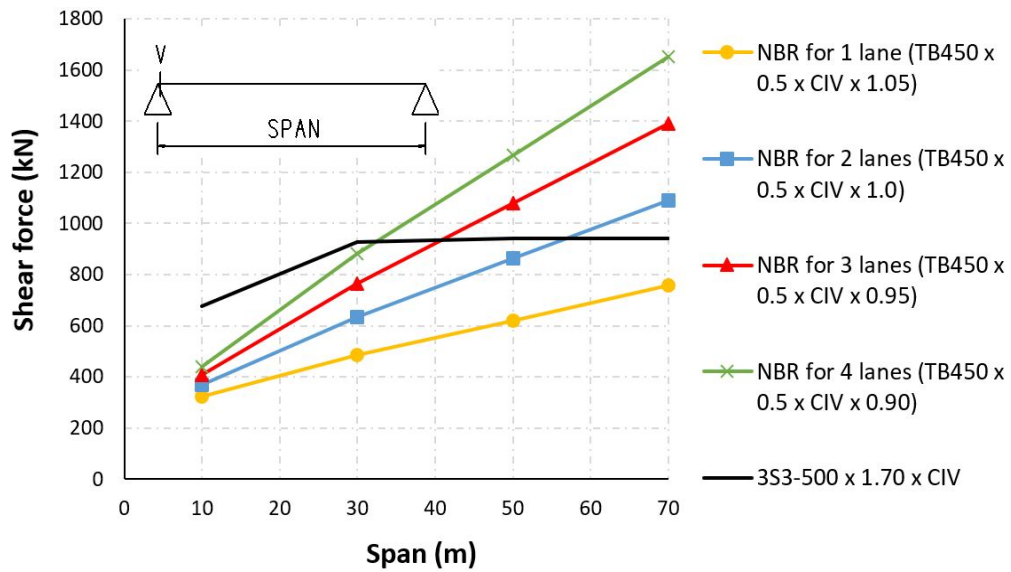
Figure 25. Comparison between models for shear force at support in simply supported bridges
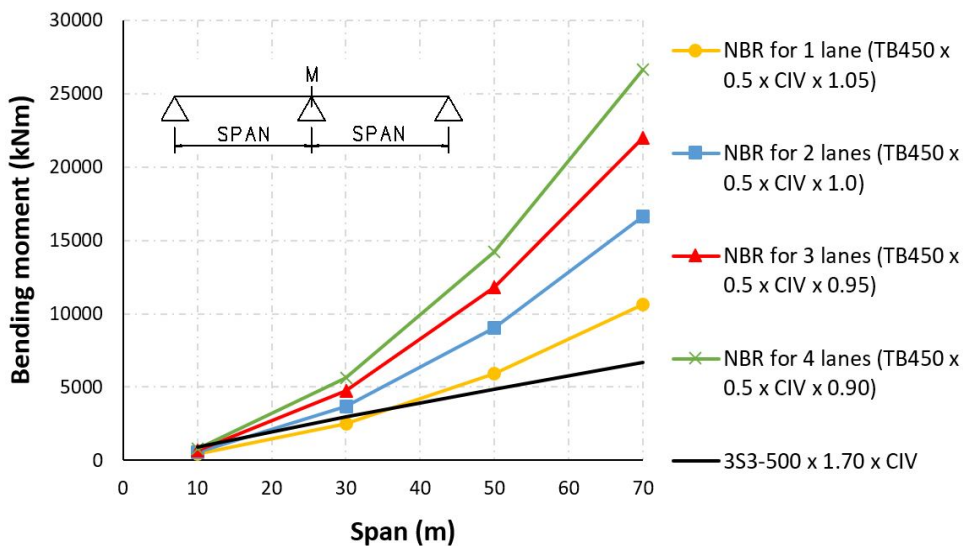
Figure 26. Comparison between models for bending moment at support in continuous bridges.

For short spans (up to 30 m), up to four traffic lanes, it is verified that, in terms of positive bending moment and shear force, the proposed model presents higher load effects. As the deck width or the span length increase, the proposed model tends to present lower load effects. For simply supported bridges with two traffic lanes, for example, the proposed model presents higher load effects up to 50-m span, approximately. For the negative moment in continuous bridges, it appears that, in general, the proposed model presents lower load effects. In this case, the proposed model presents higher load effects only for bridges up to 40-m span with one traffic lane, or for short spans (up to 10 m) up to four traffic lanes. The fact that the current Brazilian model is conservative for bridges with larger extensions and wider decks, is mainly due to the distributed load.

9 FINAL CONSIDERATIONS AND CONCLUSIONS

This work performed an assessment of the Brazilian live load model for fatigue in highway bridges. The present analysis considered real traffic data from two different HS-WIM stations located in two major highways in Brazil: BR-381 and BR-290. This paper also proposed a new fatigue live load model for Brazilian highway bridges. Under the

consideration of unlimited fatigue life approach, bias factors were estimated. A direct comparison between models was presented. Based on this work the following conclusions can be made:

- The current Brazilian live load model does not present uniform bias fators for different span lengths. For large span and multiple lanes bridges, the TB450 presents results that do guarantee unlimited fatigue life for the current truck traffic. On the other hand, for short span bridges, especially with one or two lanes, the current model can not guarantee the same.
- For simply supported girder bridges up to 40-m span, with two lanes (most Brazilian bridges), the factor of 0.8 for TB450 corresponds better to the unlimited fatigue life approach.
- The proposed model, which has a design vehicle more similar to the current Brazilian trucks, presents more uniform bias factors that are consistent with the current traffic.
- For short span bridges up to four lanes, the proposed model presents higher load effects than the ones from the current Brazilian live load model. As more lanes are add or the span length increases, the proposed model tend to present lower load effects compared to TB450.

It is important to note, however, that these findings do not conclude on the safety of the Brazilian live load model, but that it may not guarantee an unlimited fatigue life. To analyze the safety level of the current model and the proposed model, further studies are needed to assess reliability indexes and fatigue life in steel and concrete bridges. In addition, data from more Brazilian highways can be considered.

ACKNOWLEDGEMENTS

REFERENCES

[1]   Associação Brasileira de Normas Técnicas, *Carga Móvel Rodoviária e de Pedestres em Pontes, Viadutos, Passarelas e Outras Estruturas*, NBR 7188, 2013.

[2]   W. Pfeil, *Pontes em Concreto Armado*. Rio de Janeiro, RJ, Brasil: Livros Técnicos e Científicos, 1979.

[3]   European Committee for Standardization, *Eurocode 1 – Actions on Structures – Part 2: Traffic Loads on Bridges*, 2003.

[4]   American Association of State Highway and Transportation Officials, *AASHTO LRFD Bridge Design Specifications*, 2017.

[5]   H. J. M. Baroni, "Simulação da vida útil de fadiga do concreto em vigas de tabuleiro de pontes em função do fluxo de veículos pesados," Ph.D. dissertation, Esc. Eng., Univ. Federal do Rio Grande do Sul, Porto Alegre, Brasil, 2010. [Online]. Available: https://www.lume.ufrgs.br/handle/10183/26005

[6]   J. F. S. Rodrigues, J. R. Casas, and P. A. O. Almeida, "Fatigue-safety assessment of reinforced concrete (RC) bridges: application to the Brazilian highway network," *Struct. Infrastruct. Eng.*, vol. 9, no. 6, pp. 601–616, Jun 2013., http://dx.doi.org/10.1080/15732479.2011.598939.

[7]   F. L. Santos and M. S. Pfeil, "Desenvolvimento de modelo de cargas móveis para verificação de fadiga em pontes rodoviárias," in *An. VII Congr. Brasileiro Pont. Estrut.*, Rio de Janeiro, RJ, Brasil, May 21-23, 2014. [Online]. Available: http://www.abpe.org.br/trabalhos/trab_36.pdf

[8]   ACI Committee 215, *Considerations for Design of Concrete Structures Subjected to Fatigue Loading*, ACI 215R-74, 1992.

[9]   W. G. Wassef, H. Nassif, D. Mertz, and A. S. Nowak, *Calibration of AASHTO LRFD Concrete Bridge Design Specifications for Serviceability, NCHRP Project 12-83*. Washington: National Academy of Sciences, 2014. [Online]. Available: https://www.nap.edu/catalog/22407/calibration-of-aashto-lrfd-concrete-bridge-design-specifications-for-serviceability

[10] L. Sanpaolesi and P. Croce, *Handbook 4 – Design of Bridges – Guide to Basis of Bridge Design Related to Eurocodes Supplemented by Practical Examples*, Leonardo da Vinci Pilot Project CZ/02/B/F/PP-134007, 2005.

[11] Associação Brasileira de Normas Técnicas, *Projeto de Estruturas de Concreto – Procedimento*, NBR 6118, 2014.

[12] A. C. R. Laranjeiras, "Fadiga das estruturas de concreto," in *An. II Simp. EPUSP sobre Estrut. Concr.*, São Paulo, SP, Brasil, 1990.

[13] Associação Brasileira de Normas Técnicas, *Projeto de Pontes Rodoviárias de Aço e Mistas de Aço e Concreto*, NBR 16694, 2020.

[14] Associação Brasileira de Normas Técnicas, *Ações e Segurança nas Estruturas – Procedimento*, NBR 8681, 2003.

[15] E. L. Portela "Analysis and development of a live load model for Brazilian concrete bridges based on WIM data," Ph.D. dissertation, Polytech. Sch., Univ. São Paulo, Brazil, 2018. [Online]. Available: https://www.teses.usp.br/teses/disponiveis/3/3144/tde-11122018-151658/pt-br.php

[16] L. A. T. Brito and A. Bock, *Estudo do Espectro de Cargas dos Veículos Comerciais Rodantes na BR-290/RS, Freeway, Através do Uso da Técnica do Weigh-in-Motion (WIM)*. Porto Alegre, RS, Brasil, Doc. Nº 12-0020, Apr. 2013.

[17] F. R. Stucchi, *Pontes e Grandes Estruturas*. São Paulo, SP, Brasil: Esc. Politéc., Univ. São Paulo, 2006.

[18] L. F. Martha, *Ftool: Interactive-Graphics Program for Structural Analysis*, Version 4.00, 2018. [Online]. Available: https://webserver2.tecgraf.puc-rio.br/ftool

[19] A. Nowak and K. Collins, *Reliability of Structures*. New York, NY, USA: McGraw-Hill, 2013.

Rev. IBRACON Estrut. Mater., vol. 13, no. 4, e13407, 2020

20/20

IBRACON Structures and Materials Journal
Revista IBRACON de Estruturas e Materiais

ORIGINAL ARTICLE

Effects of alkali-silica reaction on mechanical behavior of four-pile caps

Efeitos da reação álcali-sílica no comportamento mecânico de blocos sobre quatro estacas

Christiane Mylena Tavares de Menezes Gameleira[a] (iD)
Valmiro Quéfren Gameleira Nunes[a] (iD)
Paulo de Araújo Régis[a] (iD)
Paulo Marcelo Vieira Ribeiro[a] (iD)
Arnaldo Manoel Pereira Carneiro[a] (iD)
Romilde Almeida de Oliveira[b] (iD)

[a]Universidade Federal de Pernambuco – UFPE, Departamento de Engenharia Civil, Recife, PE, Brasil
[b]Universidade Católica de Pernambuco – UNICAP, Departamento de Engenharia Civil, Recife, PE, Brasil

Abstract: The structural behavior resulting from alkali-aggregate reactions on four-pile caps was numerically studied using software based on the Finite Element Method. The cracking was analyzed in terms of reduction rates in the mechanical properties of the concrete (compressive strength, tensile strength and modulus of elasticity) as a consequence of the expansion induced by the alkali-aggregate reaction (AAR) referred to in the literature. One option for dealing with changes in mechanical properties, reported as influenced by the reactive aggregate type, environmental conditions and stress state, is to directly use the value of the properties of the material tested in the analysis, an approach adopted in the study and implemented in the analysis. From the results found in the analysis program the three main effects of AAR could be better understood: expansion, cracking and degradation of mechanical properties of concrete.

Keywords: concrete, alkali-aggregate reaction, pile caps, mechanical properties, numerical analysis.

Resumo: Estudou-se numericamente o comportamento estrutural resultante de reações álcali-agregado em blocos sobre quatro estacas utilizando software baseado em Método dos Elementos Finitos. Analisou-se a fissuração considerando taxas de reduções nas propriedades mecânicas do concreto (resistência à compressão, resistência à tração e módulo de elasticidade) consequentes da expansão induzida pela reação álcali-agregado (RAA), existentes na literatura. Uma opção para lidar com as mudanças nas propriedades mecânicas, relatadas como influenciadas pelo tipo de agregado reativo, pelas condições ambientais e pelo estado de tensão consiste em usar diretamente o valor das propriedades do material testado na análise, abordagem que foi adotada na pesquisa e implementada no programa de análise. A partir dos resultados encontrados foi possível compreender melhor os três principais efeitos da RAA: expansão, fissuração e degradação das propriedades mecânicas do concreto.

Palavras-chave: concreto, reação álcali-agregado, blocos sobre estacas, propriedades mecânicas, análise numérica.

C. M. T. M. Gameleira, V. Q. G. Nunes, P. A. Régis, P. M. V. Ribeiro, A. M. P. Carneiro, and R. A. Oliveira

1 INTRODUCTION

Assessment of damage to AAR-affected concrete generally depends on the measurement of the expansion, monitoring of cracks and testing the concrete properties. It is well established that sound conventional concrete has high compressive strength and modulus of elasticity, low tensile strength, poor response to uniaxial load (compressive or tensile) and increased ductility and strength (compressive and tensile) in a confined environment. This sensitivity to the confinement state is linked to the presence of minor defects, or even microcracking, which will exist in the concrete. So, even for a non-deteriorated concrete in a triaxial compression state, there will always be local zones in stress within the volume of the material due to its heterogeneous and defective nature.

The literature includes several experimental studies on the alkali-aggregate reaction, namely Gomes [1], for example, who studied experiments on the structural recovery of foundation caps; Sanchez et al. [2] addressed a new method called the accelerated Brazilian concrete prism test (ABCPT), in which the results indicated that that test had great potential to detect aggregate reactivity in current engineering projects; Sanchez et al. [3], who presented test results from the Stiffness Damage Test (SDT) and the microscopic evaluation of the Damage Rating Index (DRI) to assess the level of damage to the AAR-affected concrete. However, there are only a few numerical studies on expressions of such reactions on foundation caps. The purpose of this paper, therefore, is to numerically study the effect of the reductions on the concrete's mechanical properties (compressive strength, tensile strength and modulus of elasticity) as a result of the AAR-induced expansion in the cracking results in four-pile foundation caps and was based on Gameleira's thesis of doctorate [4]. Moreover, a numerical simulation on the AAR effect on concrete structures is a valuable tool to predict damage, specify repairs and act as support for standard modifications related to structural designs.

2 METHODOLOGY

The methodology consisted of bibliographic research in order to find a theoretical basis for the AAR. It is necessary to have a better understanding of the numerical models presented and the parameters used for each of them. Soon after, from results obtained using analytical models, a numerical analysis was undertaken using the DIANA program [5], [6] ,[7], based on the finite element method.

For a numerical analysis the behavior of the material was adopted as non-linear. The results of interest were a distribution of cracks and cracking fields of the models in order to study the influence of the variation of the mechanical properties on the materials at different expansion levels.

2.1 Alterations to the design mechanical parameters as a result of AAR

The fact that AAR has harmful impacts on the mechanical properties of the concrete structures is a problem apparent after many investigations. ASTM C1293 [8] and the Canadian CSA-A23.2-14A [9] describe aggregates that cause expansion of more than 0.04% in the concrete as a potentially harmful reaction [10].

In Marzouk and Langdon [11], normal highly resistant concretes show, under the AAR action, a drop in compressive and tensile strength and in the modulus of elasticity, with the modulus of elasticity as the most affected property, since it depends more on changes to the concrete's microstructure.

When studying concrete samples taken from the drainage gallery of Furnas hydropower plant in Rio Grande, municipality of Alpinopolis (Minas Gerais state), in a study submitted by Hasparyk [12], there was a sharp drop in the modulus of elasticity, but no major alterations to the compressive strength.

Both Hoobs [13] and Larive [14] show the fall in the modulus of elasticity in AAR presence. St. John [15] noted a reduction in the tensile strength value when studying airport runways.

Generally AAR causes a very sharp drop in terms of tensile strength and modulus of elasticity. These two properties are far more affected than compressive strength, which only begins to drop significantly with high expansion levels [16]–[19]. The classic AAR effect on the aforementioned concrete's mechanical properties suggests that microcracking caused by this harmful mechanism can be identified even before the material reaches significant expansion and macrocracking and, possibly, a significant loss of compressive strength [16]. According to ISE [20], the compressive strengths would normally increase in concrete structures exposed to the natural environmental conditions to reach figures beyond the design values (28 days); thus, the loss of compressive strength due to AAR is generally less or similar to the difference between the design and actual strength values measured at any given moment. On the other hand, a significant loss of compressive strength may be found for concrete elements undergoing major expansions (that is, 1 mm/m or 0.10%) [21]-[23]. According to these authors, for expansions of 0.10% or less, it is very likely that the

concrete element, or even the structure, efficiently withstands their active stresses. However, after a 0.30% expansion, a structural evaluation must be undertaken [21]-[23].

Furthermore, Kubo and Nakata [24] reported the results of recent studies showing losses of compressive strength for concretes with expansion levels of more than 0.30%. For expansion levels of 0.50%, the authors observed around 30% losses of compressive strength. In the same study, the authors discovered that neither the water-cement ratio of the concrete mixes nor the aggregates deployed had a significant influence on the compressive strength, at least to the expansion levels of 0.30%. On the other hand, researchers found major differences in the stress/strain behavior (especially for the modulus of elasticity) at similar expansion levels when different reactive aggregates were used. They associated these differences to different crack patterns when different reactive aggregates are used in concrete [24].

However, Naar [25] suggested that the analysis of the reductions in the mechanical properties due to AAR is complicated and many contradictory results feature in the literature. In terms of compressive strength, some authors found losses only at very high expansion levels. In contrast, others found almost no change, or even an increase, in the compressive strength with the expansion increase due to AAR. Considering the loss of the modulus of elasticity, most authors agree with a rapid loss even at low expansion levels (0.0% to 0.05%); losses were reported varying from 20% to 80% of the modulus of elasticity of non-reactive concretes, considered to be a huge variation.

Sanchez et al. [26] measured the influence of the type and nature of the aggregates, together with the sample's compressive strength, in the mechanical properties of the AAR-affected concrete. Three concrete types were used in this study (25, 35 and 45 MPa), based on which approximately 765 cylindrical test samples (100 mm × 200 mm in size) were molded and then stored in conditions that allow AAR development. When the test samples reached the four expansion levels chosen for this study (0.05%, 0.12%, 0.20% and 0.30%; ± 0.01%), they underwent the stiffness damage test (SDT). The concrete test samples were examined petrographically at the same expansion levels mentioned above, in order to determine the degree of their physical damage. The mixes were tested with the aggregates. The authors discovered that the modulus of elasticity and tensile strength are, in fact, more strongly affected than the compressive strength, but the compressive strength at higher expansion values may drop sharply (30% or less). It was discovered that the last property is related to the microscopic characteristics of AAR deterioration, which tend to start inside the aggregate particles and spread to the cement paste only at moderate and high expansion levels.

Gorga [27] measured the effect of the consequences of the AAR-induced expansion in the mechanical properties of the concrete (compressive strength, tensile strength and modulus of elasticity). These properties are reduced over time and are the direct consequence of physical degradation (that is, cracking) inside the aggregate particles and cement paste.

It is, therefore, evident that the deterioration of the concrete's mechanical properties is a very important phenomenon directly related to the expansion level, type and nature of the aggregate and compressive strength of the material. Today, however, there is very restricted information about the ratio between the development of the AAR micromechanical characteristics and the losses in the mechanical properties of the AAR-affected concrete.

2.2 Numerical analysis

The DIANA software (DIsplacement ANAlyzer) used in the study is a finite element software package based on the displacement method.

The program has been developed since 1972 by engineers from TNO Building and Construction Research Company (Netherlands) and is a powerful tool for concrete simulation, considering complex effects such as cracking, creep, shrinkage, curing, temperature effects, instability, and so on.

DIANA uses parameters of fracture mechanics to describe this behaviour of the concrete. To study concrete cracking the program provides discrete models with interface elements or distributed crack models in fixed or rotational directions.

In the study the distributed crack model was used as being the easiest. The parameters required for the model are as follows: fracture energy in Gf stress (energy required for a unit area of crack), fracture energy in Gc compression, tensile and compressive strength, shear retention factor β and length of crack band h.

Stoner [28] studied the approach of fracture energy to define the tensile behaviour of concrete in stirrup-less beams. Values were analysed provided by equations for estimating fracture energy, in the absence of the test, supplied by: Model Code 1990; Trunk and Wittmann [29], fib Bulletin 42 [30] and Model Code 2010 [31], and the conclusion was reached that the fracture energy calculated according to Model Code 1990 gave more accurate consistent results for all beams studied.

So, in this study the CEB Model Code 1990 [32] was used to estimate the fracture energy, and the Gf value was calculated using Equation 1.

$$G_f = G_{F0} \cdot \left(\frac{f_{ck}}{f_{cmo}}\right)^{0.7} \left[N.mm / mm^2\right] \tag{1}$$

where:

f_{cmo} = 10 MPa

G_{F0} = basic value of fracture energy, depends on the diameter of the aggregate (Table 1)

f_{ck} = characteristic compressive strength of concrete, in N/mm^2

Table 1. G_{F0} in function of the maximum diameter of the aggregate.

$d_{max}(mm)$	$G_{FO}(N.mm / mm^2)$
8	0.025
16	0.030
32	0.058

Equation 2 calculated the crack band length, where f_t is the tensile strength of the concrete and ε_u the ultimate tensile strain of the concrete adopted at 0.238% (strain at yield level of a CA-50 steel bar)

$$\frac{G_f}{h} = \frac{\varepsilon_u \cdot f_t}{2}$$

$$h = \frac{2 \cdot G_f}{\varepsilon_u \cdot f_t} \tag{2}$$

The value of the compressive fracture energy G_c, is between 10 and 25 N.mm/mm^2 that corresponds to a value between 50 and 100 times G_f, as recommended by Feenstra and Borst [33].

The characteristics compressive strength of the concrete f_{ck} was considered and the concrete's average tensile strength was calculated from the Equation 3 in NBR 6118 [34].

$$f_{ct,m} = 0.3 \cdot f_{ck}^{\frac{2}{3}} \text{, for concretes in classes of C50 or less.} \tag{3}$$

The program provides two Total Strain models that are able to describe the concrete behavior under compressive and tensile stresses based on the stress-strain ratio: the Total Strain Rotating Crack Model and Total Strain Fixed Crack Model. These models satisfactorily represent the ultimate and service limit states of reinforced concrete structures.

The Total Strain Fixed Crack Model was used for the study, which stays in the crack direction as it spreads through the concrete.

The input data of this model are: longitudinal modulus of elasticity of the material, Poisson's ratio, tensile and compressive strength and the concrete compressive and tensile behavior curves.

For the study, the exponential curve for the concrete's tensile behavior and the parabolic curve for the concrete's compressive behavior were used.

The concrete numerical simulation adopted a 20-node isoparametric solid element with quadratic interpolation for displacement, HE20 CHX60. Each node represents three degrees of freedom, which are the displacements in x, y and z directions.

For reinforcement a resource of the program called embedded reinforcement was used, designed to stiffen the fine elements of the model. By fitting this resource into the mesh of finite elements representing the concrete, the software simulates the presence of reinforcement in that specific region. This method does not have its own degrees of freedom and, as a standard, its strains are counted from the strain field of the elements where it is inserted. This is why it cannot be considered a finite element.

Rev. IBRACON Estrut. Mater., vol. 13, no. 4, e13408, 2020

4/11

C. M. T. M. Gameleira, V. Q. G. Nunes, P. A. Régis, P. M. V. Ribeiro, A. M. P. Carneiro, and R. A. Oliveira

The reinforcement requires perfect adhesion between reinforcement and concrete, and only with the inclusion of interface elements is it possible to consider that the adhesion between reinforcement and concrete is not perfect. By means of "embedded reinforcements" non-linearity can be included in the reinforcement behavior, such as steel hardening and plasticization. The embedded reinforcements help in fast and simplified creation of the finite element mesh, attributing practicality to the model's creation.

This study involved the use of: $Gc = 100Gf$, $\beta = 0.99$ while the Regular Newton-Raphson method was used to solve non-linear equation systems, with an energy convergence criterion and tolerance of 0.1.

The analysis adopted the following steps: definition of the properties of materials, type of finite element to be used, mesh, actions and contour conditions.

For the numerical simulation of the foundation caps complete models were used; that is, without taking into account the benefits introduced by symmetry.

The pile models were defined as rectangular to facilitate the construction of the numerical mesh. The piles and pillars were modeled with the height of the block, a procedure normally adopted in experimental tests.

A four-pile cap was used, undergoing the centered force action, with a square 40 cm x 40 cm pillar and square piles with section 40 cm × 40 cm and a failure load of 472 tf.

For the finite element mesh, a mapped mesh was chosen, to enable obtaining good results without needing a larger degree of discretization, which would not be possible when automatically using a mesh division. Every analysis was made with the size of the line divisions, that is, 50 mm distance between the nodes. For this division, 17545 nodes, 3984 elements and an average processing time of 5 h 30 min were created. Figure 1 shows the modeled caps with the mapped mesh and Figure 2 shows the cap reinforcements.
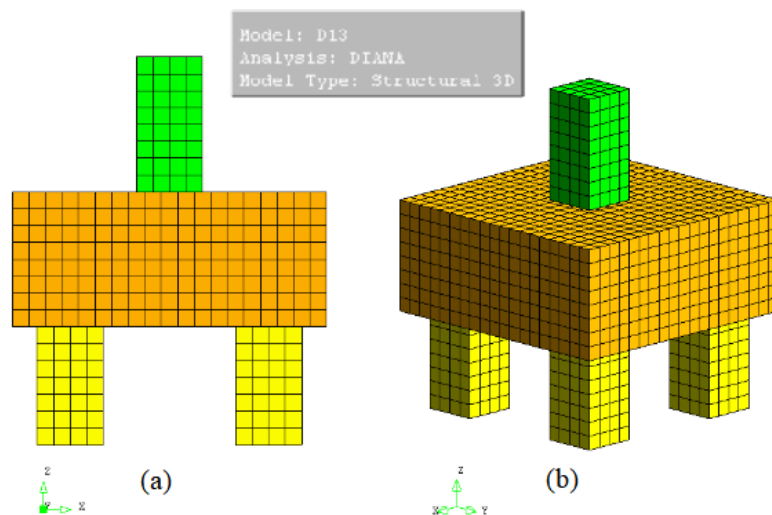
Figure 1. Finite element mesh. (a) front view and (b) perspective.
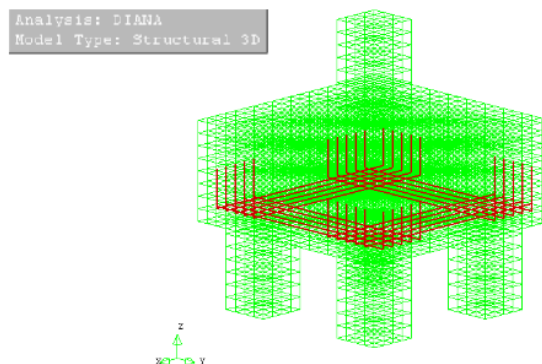
Figure 2. Reinforcement of four-pile caps.

For the foundation caps, contour conditions were defined (Figure 3a) that restricted all nodes on the surface of the caps on plane xz, in the two directions and in the normal direction to this plane; that is, the three directions were restricted. The intention of preventing model rotation is due to the idea of studying the cap behavior, keeping conditions coherent with those of an experimental test. For the loading condition (Figure 3b), applying an action in form of distributed pressure on the top cross-section area of the pillar was considered, in a negative direction of z.
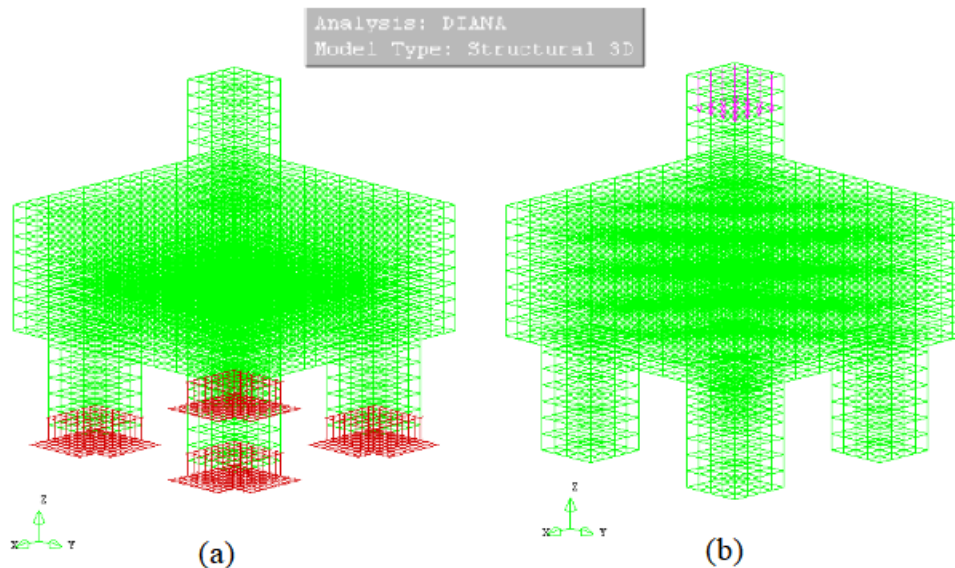
Figure 3. (a) Contour conditions in piles. (b) Action applied as pressure on the pillar.

The piles and pillar were modeled considering C50 concrete and the cap with C20 concrete, since the purpose of the study is to analyze the cap. Table 2 describes the concrete physical properties of the caps, piles and pillars.

Table 2. Physical properties of concretes.

	Compressive strength f_{cm} (MPa)	Tensile strength $f_{ct,m}$ (MPa)	Modulus of elasticity E_{cs} (MPa)	Poisson's ratio v	Energy of fracture G_f (N.mm/mm^2)
Cap	20	2.21	21287.37	0.2	0.048735
Pillar	50	-	33658.28	0.2	-
Pile	50	-	33658.28	0.2	-

The reinforcement steel considered a modulus of elasticity of 210 GPa, Poisson's ratio of 0.3 and characteristic yield strength of 500 MPa.

A pressure of 1 MPa was applied to the top of the pillar. Consequently, the program makes an increase to the same pressure value, while permitted, and the actual program corrects the increased value if necessary. For the distributed cracking model used a maximum number of 50 interactions was permitted.

3 RESULTS AND DISCUSSIONS

First, in the literature experimental data show that there is the drop in AAR-affected concrete mechanical properties compared to healthy concrete. There are two options to address the changes in the mechanical properties, reported as influenced by the type of reactive aggregate, environmental conditions and stress state. One alternative consists of directly using the value of the properties of the material tested in the analysis. The other option evaluates the compressive and tensile stresses, and the modulus of elasticity as a result of the free expansion based on constitutive equations. Both options disregarded the directional nature of the degradation in the mechanical properties caused by the stress level. The first approach was adopted in the study and implemented in the analysis program.

The reductions established in the study by Sanchez et al. [3], described in Table 3, were applied in order to study the distribution of cracking in the cracking fields along these reductions.

Table 3. Reduction rates in the mechanical properties of concrete submitted to AAR according to the expansion level.

Expansion level benchmark (%)	Minimum values			Average values			Maximum values		
	Reduction by AAR			Reduction by AAR			Reduction by AAR		
	Modulus of elasticity (%)	Compressive strength (%)	Tensile strength (%)	Modulus of elasticity (%)	Compressive strength (%)	Tensile strength (%)	Modulus of elasticity (%)	Compressive strength (%)	Tensile strength (%)
0	0	0	0	0	0	0	0	0	0
0.05	5	0	15	21	8	38	37	15	60
0.12	20	5	40	35	13	53	50	20	65
0.2	35	13	45	48	19	58	60	25	70
0.3	40	20	50	54	28	63	67	35	75

Source: Adapted from Sanchez et al. [3].

Although the analysis of the reductions in the mechanical properties as a result of the expansion due to the AAR is complicated, and there are many contradictory results in the literature, the choice of parameters studied by Sanchez et al. [3] was due, from among the authors that related the degradation of concrete mechanical properties to the expansion due to the AAR, described herein, and is experimental study that provided the most complete parameters on the subject.

The first model was called a benchmark model in which reduction rates were not applied to the mechanical properties due to the AAR. Then there are the models numbers 1 to 4, 5 to 8 and 9 to 12, to which the minimum, average and maximum reduction rates of the mechanical properties were applied according to the expansion level. Table 4 shows the input data in the program for these models.

Table 4. Input data of models.

Models (four-pile caps)	Modulus of elasticity (MPa)	Compressive strength (MPa)	Tensile strength (MPa)	Expansion level (%)	Length of crack band h (mm)
Benchmark	21287.37	20	2.21	0	18.52764
Minimum values of reduction in mechanical properties due to AAR					
1	20223.00	20	1.88	0.05	21.79772
2	16598.69	19	1.28	0.12	30.82667
3	12906.09	17,4	1.11	0.2	33.53064
4	11424.00	16	0.95	0.3	36.78072
Average values of reduction in mechanical properties due to AAR					
5	16130.32	18.4	1.29	0.05	29.80036
6	12906.09	17.4	0.95	0.12	39.23798
7	9962.49	16.2	0.81	0.2	43.80475
8	8308.95	14.4	0.66	0.3	49.52947
Maximum values of reduction in mechanical properties due to AAR					
9	12364.37	17	0.79	0.05	46.06882
10	9520.00	16	0.67	0.12	52.54389
11	7374.16	15	0.55	0.2	61.16945
12	5663.60	13	0.41	0.3	73.05412

Table 5 and Figure 4 provide the results relating a maximum crack opening (mm) and expansion level (%) of the models studied for the ultimate force of each model. It is found that the maximum opening of cracks increases with the expansion level. This crack opening behavior can be explained through the damage model used in the numerical simulation.

The Smeared Crack Model treats concrete as a heterogeneous material, which when accompanied by reinforcement, is able to form multiple small cracks, which in high load stages will combine and form one major crack or more [35].
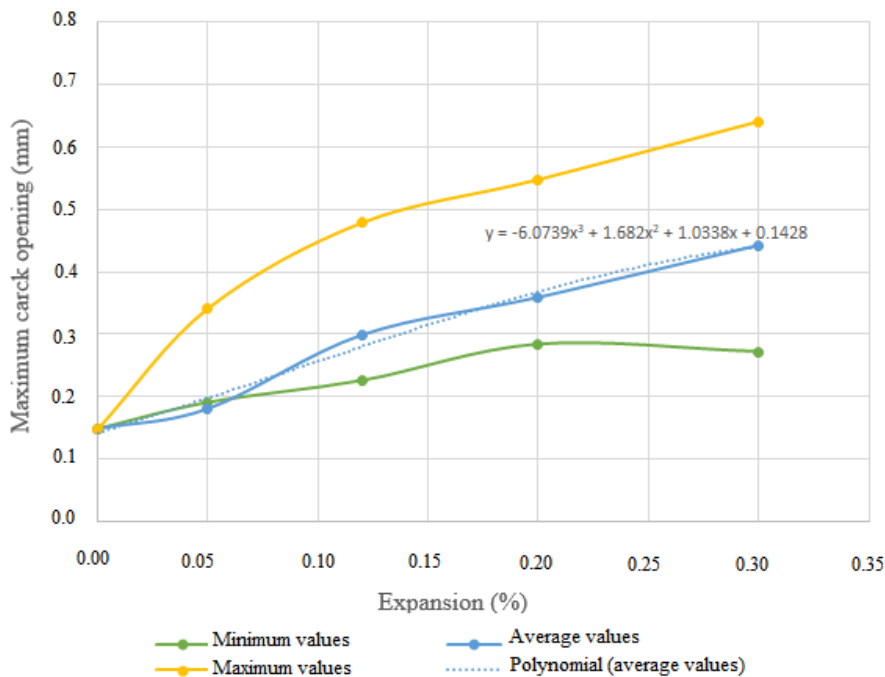
Figure 4. Maximum crack opening versus expansion level.

Table 5. Maximum crack opening versus expansion level.

Models (four-pile caps)	Expansion level (%)	Maximum crack opening (mm)
Benchmark	0	0.149
Minimum values of reduction in mechanical properties due to AAR		
1	0.05	0.191
2	0.12	0.226
3	0.2	0.284
4	0.3	0.272
Average values of reduction in mechanical properties due to AAR		
5	0.05	0.181
6	0.12	0.299
7	0.2	0.359
8	0.3	0.442
Maximum values of reduction in mechanical properties due to AAR		
9	0.05	0.342
10	0.12	0.479
11	0.2	0.548
12	0.3	0.641

The crack opening for foundation caps must have a restricted value since they are structures in direct contact with the ground. Standard NBR 6118 [34] makes reference to openings of less than 0.3 mm in elements of environmental aggressiveness class II and III. So, the benchmark model (without AAR) is within that set out by the standard. For models with reductions due to the AAR, the models had crack openings of more than 0.3 mm based on the average reductions in the 0.2% expansion level.

Figures 5 and 6 show cracking fields in the failure for the non-AAR model and for the model with maximum reduction rate of AAR-affected mechanical properties, respectively. The cracking fields show crack openings wider than 0.1 mm. For the AAR-affected foundation caps the main visual inspection points to check the cracking are the top part of the cap and side surfaces.
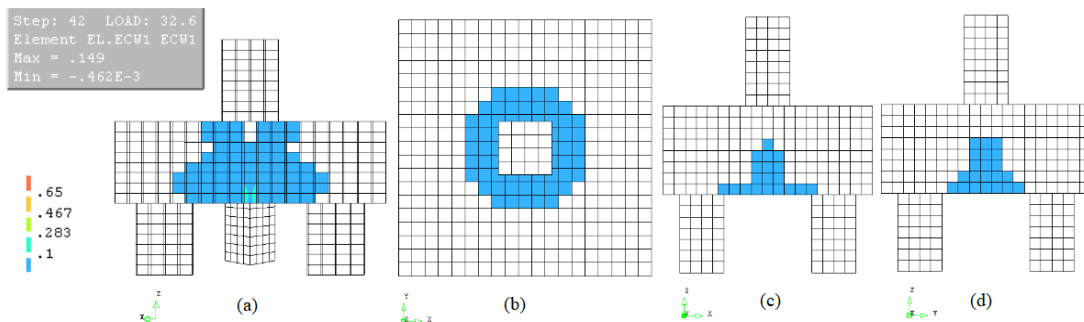
Figure 5. Cracking fields in failure for the benchmark model (without AAR), with indication of openings wider than 0.1 mm. (a) diagonal section of cap; (b) top view; (c) and (d) side views.
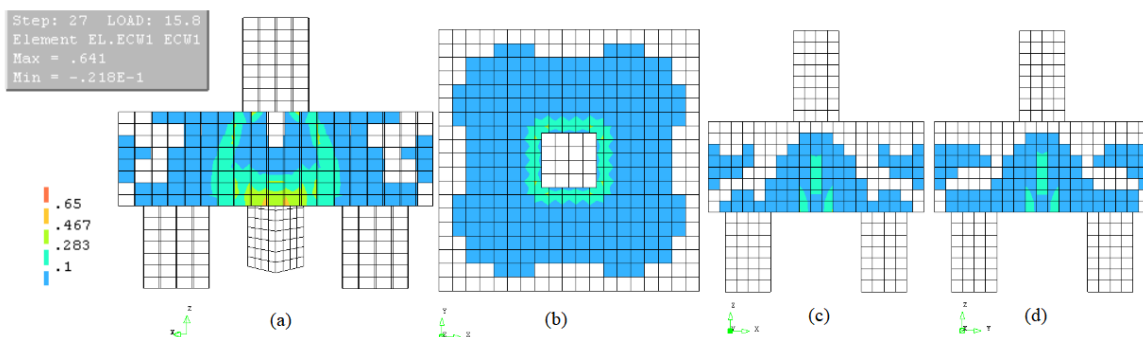
Figure 6. Cracking fields in failure for model 12 (Maximum values of reduction in mechanical properties due to AAR - expansion rate 0.3%), with indication of openings wider than 0.1 mm. (a) diagonal section of cap; (b) top view; (c) e (d) side views.

In general, the cracking fields clearly showed an increase in AAR due to the expansion rate, since the crack opening tended to widen. And this is in accordance with distributed cracking model adopted in the simulation, where the cracks spread along the element after the load was applied.

It may also be found that the wider cracks occurred at the cap bases, close to the cap centers (directly below the pillars' position), confirming the places where the major strains of the structure occur.

According to Meléndez et al. [36], one of the main failure modes in four-pile foundation caps is shearing in the rod due to cracks caused by the concrete's compressive softening. It was, therefore, found that the AAR models had more cracks in the rod region, thereby further impairing the cap's capacity. Probably the cause is the perpendicular tensile stress on the rod.

4 CONCLUSIONS

The reduction in mechanical properties impacted the crack opening. It is found that the cracks widen in size and quantity according to the increase in the expansion level (from 0.05% to 0.30%).

The distributed crack model used by the program is able to form multiple small cracks per unit of length, distributed over a certain area. These cracks may spread as unit cracks after loading, providing higher values than reported in the article, which is consistent with results in AAR-impacted structures.

AAR models were found to have more cracks in the region of the rods, further impairing the cap capacity. It is likely that the cause is the perpendicular tensile stress on the rod.

As the expansion level increases the load from the start of cracking was less consistent with the structure's state of degradation due to AAR action.

In general, the cracking fields clearly portray the expected result for AAR-affected concretes. The crack openings were relatively wider in models with reductions in the mechanical properties due to the AAR than for the non-AAR model.

After the different simulations performed it may be said that the non-linear analysis for the AAR problem can accurately capture the behaviors referring to the cracking of the analyzed cap.

C. M. T. M. Gameleira, V. Q. G. Nunes, P. A. Régis, P. M. V. Ribeiro, A. M. P. Carneiro, and R. A. Oliveira

Lastly, this study includes the understanding of the three main AAR impacts: expansion, cracking and degradation of the concrete's mechanical properties. And it is evident that the deterioration of the mechanical properties is related to AAR-induced expansion.

ACKNOWLEDGEMENTS

REFERENCES

[1] E. A. O. Gomes, "Recuperação estrutural de blocos de fundações afetados pela Reação Álcali-Agregado – a experiência do Recife," M.S. thesis, Univ. Cat. Pernambuco, Recife, PE, 2008

[2] L. Sanchez, S. C. Kuperman, and P. Helene, "Using the accelerated Brazilian concrete prism test (ABCPT) to evaluate alkali aggregate reaction (AAR)," *Rev. IBRACON Estrut. Mater.*, vol. 4, no. 4, pp. 575–581, 2011.

[3] L. Sanchez, B. Fournier, M. Jolin, J. Bastien, and D. Mitchell, "Tools for assessing damage in concrete affected by AAR coming from fine and coarse aggregates," *Rev. IBRACON Estrut. Mater.*, vol. 10, no. 1, pp. 84–91, 2017.

[4] C. M. T. M. Gameleira, "Reduções das propriedades mecânicas do concreto devido à RAA na simulação de blocos sobre quatro estacas," Ph.D. dissertation, Univ. Fed. Pernambuco, Recife, PE, 2019.

[5] DIANA, *Finite Element Analysis – Users Manual Release 9 – Analysis Procedures*, 2005.

[6] DIANA, *Finite Element Analysis – Users Manual release 9 – Material Library*, 2005.

[7] DIANA, *Finite Element Analysis – Users Manual Release 9 – Element Library*, 2005.

[8] American Society for Testing and Materials, *Standard Test Method for Determination of Length Change of Concrete due to Alkali-Silica Reaction*, ASTM C-1293/08, 2008.

[9] Canadian Standards Association, *Potential Expansivity of Aggregates – Procedure for Length Change due to Alkali-aggregate Reaction in Concrete Prisms – Methods of Test for Concrete*, CSA A23.2-14A, 2014.

[10] I. Hafçi, "Effect of alkali-silica reaction expansion on mechanical properties of concrete," M.S. thesis, Middle East Tech. Univ., Turkey, 2013.

[11] H. Marzouk and S. Langdon, "The effect of alkali-aggregate reactivity on the mechanical properties of high and normal strength concrete," *Cement Concr. Compos.*, vol. 25, no. 4-5, pp. 549–556, Jun 2003.

[12] N. P. Hasparyk, "Investigação de concretos afetados pela reação álcali-agregado e caracterização avançada do gel exsudado," Ph.D. dissertation, Progr. Pós-grad. Eng. Civ., Univ. Fed. Rio Grande do Sul, Porto Alegre, 2005.

[13] D. W. Hobbs, *Alkali-silica Reaction in Concrete*. London: Thomas Telford, 1988.

[14] C. Larive, "Apport combinés de l'expérimentation et de la modélisation à la compréhension de l'alcali-réaction et ses effets mécaniques," Ph.D. dissertation, Éc. Natl. Ponts Chaussées, Paris, France, 1997.

[15] D. A. St. John, "Alkali-aggregate reaction: New Zealand experience," in *The Alkali-Silica Reaction in Concrete*, R. N. Swamy, Ed., New York: Van Nostrand Reinhold, 1992.

[16] P. J. Nixon and R. Bollinghaus, "The effect of alkali aggregate reaction on the tensile strength of concrete," *Durab. Build. Mater.*, vol. 2, pp. 243–248, 1985.

[17] N. Smaoui, M. A. Bérubé, B. Fournier, and B. Bissonnette, "Influence of specimen geometry, orientation of casting plane, and mode of concrete consolidation on expansion due to ASR," *Cem. Concr. Aggreg.*, vol. 26, no. 2, pp. 58–70, 2004.

[18] N. Smaoui, M.-A. Bérubé, B. Fournier, B. Bissonnette, and B. Durand, "Evaluation of the expansion attained to date by concrete affected by ASR – Part I: experimental study," *Can. J. Civ. Eng.*, vol. 31, no. 5, pp. 826–845, 2004.

[19] R. Pleau, M. A. Bérubé, M. Pigeon, B. Fournier, and S. Raphael, "Mechanical behavior of concrete affected by AAR," in Proc. 8th Int. Conf. Alkali-Aggregate Reaction Concr., 1989.

[20] Institution of Structural Engineers, *Structural Effects of Alkali-Silica Reaction*. London: SETO, 1992.

[21] G. M. Wood and R. A. Johnson, "An engineer's perspective on UK – experience with alkali-aggregate reaction," in Proc. 8th Int. Conf. Alkali-Aggregate Reaction Concr., 1989.

[22] G. M. Wood, P. Norris, and D. Leek, "Physical behavior of AAR damaged concrete in structures and in test conditions," in Proc. 8th Int. Conf. Alkali-Aggregate Reaction Concr.,´1989.

[23] G. M. Wood and R. A. Johnson, *The Appraisal and Maintenance of Structures with Alkali-silica Reaction*. London: Institution of Structural Engineers, 1993.

[24] Y. Kubo and M. Nakata, "Effect of reactive aggregate on mechanical properties of concrete affected by alkali-silica reaction," in Proc. 14th Int. Conf. Alkali-Aggregate Reaction Concr., 2012.

Rev. IBRACON Estrut. Mater., vol. 13, no. 4, e13408, 2020

10/11

[25] R. Naar, "Modélisation du comportement mécanique du béton par approche multi-physique (couplage chimie-mécanique) – application à la réaction alcali-silice," Ph.D. dissertation, Éc. Natl. Supér. Min. Paris, Paris, France, 2010.

[26] L. F. M. Sanchez, B. Fournier, M. Jolin, D. Mitchell, and J. Bastien, "Overall assessment of Alkali-Aggregate Reaction (AAR) in concretes presenting different strengths and incorporating a wide range of reactive aggregate types and natures," *Cement Concr. Res.*, vol. 93, pp. 17–31, 2017.

[27] R. V. Gorga, "Engineering-based FE approach to appraise slender structures affected by Alkali-Aggregate Reaction (AAR)," M.S. thesis, Dep. Civ. Eng., Univ. Ottawa, Ottawa, Ontario, Canada, 2018.

[28] J. G. Stoner, "*Finite element modelling of GFRP reinforced concrete beams*," Ph.D. dissertation, Univ. Waterloo, Ontario, Canada, 2015.

[29] B. Trunk and F. Wittmann, "Experimental investigation into the size dependence of fracture mechanics parameters," in Proc. 3rd Int. Conf. Fract. Mech. Concr. Struct., vol. 3, pp. 1937-1948, 1998.

[30] International Federation for Structural Concrete, *Constitutive Modelling of High Strength/High Performance Concrete* (Bulletin 42). Lausanne, Switzerland, 2008.

[31] Comite Euro-Internacional Du Béton, *Model Code 2010 – First Complete Draft*. Lausanne, Switzerland, 2010.

[32] Comite Euro-Internacional Du Béton, *CEB-FIP: Model Code 1990* (Bulletin d'Information, 203-205). Paris: CEB-FIP, 1993.

[33] P. H. Feenstra and R. Borst, "Aspects of robust computational modeling for plain and reinforced concrete," *Heron*, vol. 38, no. 4, pp. 3–76, 1993.

[34] Associação Brasileira de Normas Técnicas, *Concrete Structures Design*, NBR 6118:2014, 2014.

[35] Borst, J. J. C. Remmers, A. Needleman, and M.-A. Abellan, "Discrete vs smeared crack models for concrete fracture: bridging the gap," *Int. J. Numer. Anal. Methods Geomech.*, vol. 28, no. 78, pp. 583–607, 2004.

[36] C. Meléndez, J. Sagaseta, P. F. M. Sosa, and L. P. Rubio, "Refined three-dimensional strut-and-tie model for analysis and design of four-pile caps," *ACI Struct. J.*, vol. 116, no. 4, pp. 15–29, Jul 2019.

ORIGINAL ARTICLE

Probabilistic corrosion time initiation modelling in reinforced concrete structures using the BEM

Modelagem probabilística do tempo de início da corrosão em estruturas de concreto armado usando o MEC

Giovanni Pais Pellizzer[a] ID
Edson Denner Leonel[b] ID

[a]Universidade Federal de Mato Grosso do Sul – UFMS, Faculdade de Engenharia, Arquitetura e Geografia, Campo Grande, MS, Brasil
[b]Universidade de São Paulo – USP, Escola de Engenharia de São Carlos, Departamento de Estruturas, São Carlos, SP, Brasil

Abstract: The reinforcement's depassivation in reinforced concrete structures occurs when the chloride concentration at the reinforcement's interface reaches the threshold content. The depassivation phenomenon starts the propagation period, in which huge mechanical degradation processes are triggered. Moreover, it is well established that the propagation period is considerably shorter than the initiation period. Therefore, the accurate prediction of the corrosion time initiation is a major issue in structural durability domain. This study presents a transient formulation based on the Boundary Element Method (BEM) for the corrosion time initiation assessment. The diffusion fields evaluated by the BEM are utilized into a probabilistic framework, which enables the assessment of probabilistic values for corrosion time initiation. Therefore, the formulation handles properly the uncertainties in this problem, which is largely subjected to randomness. Three applications are presented. The robustness and accuracy of the proposed approach over classical analytical models are highlighted.

Keywords: chloride ingress, boundary element method, probabilistic modelling, diffusion-like transport.

Resumo: A despassivação das armaduras em estruturas de concreto armado ocorre quando a concentração de cloretos na interface das armaduras atinge a concentração limite. O fenômeno da despassivação inicia o período de propagação, no qual enormes processos de degradação mecânica são desencadeados. Além disso, é largamente conhecido que o período de propagação é consideravelmente curto se comparado com o período de iniciação. Portanto, a precisa previsão do tempo de início da corrosão é um tema de importância maior no domínio da durabilidade estrutural. Este estudo apresenta uma formulação transiente baseada no Método dos Elementos de Contorno (MEC) para a avaliação do tempo de início da corrosão. Os campos transientes avaliados pelo MEC são utilizados em uma modelagem probabilística, a qual possibilita a avaliação de valores probabilísticos para o tempo de início da corrosão. Portanto, a formulação representa adequadamente as incertezas deste problema, o qual é largamente sujeito aos efeitos das aleatoriedades. Três exemplos são apresentados. A robustez e a precisão da abordagem proposta sobre modelos analíticos clássicos é destacada.

Palavras-chave: ingresso de cloreto, método dos elementos de contorno, modelagem probabilística, transporte tipo difusão.

1 INTRODUCTION

The reinforced concrete (RC) structures have been widely utilized worldwide. The success of this structural system, particularly in civil engineering applications, may be attributed to some of its characteristics such as the adequate mechanical strength, affordability, versatility, chemical and thermal protection of steel, durability in addition to the financial aspects. Nevertheless, pathological problems reduce the service life of such structures. Among these problems,

sulphate expansion, alkali-aggregate reaction, leaching and reinforcements' corrosion are mentioned [1]–[3]. Moreover, it is worth highlighting that the reinforcements' corrosion have caused enormous economic loss worldwide. It is estimated that the costs with inspection, maintenance and repair caused by reinforcements' corrosion reach 4% of the Gross Domestic Product (GDP) in industrialized countries and exceeds US$ 1.8 trillion worldwide [4], [5].

The reinforcements' corrosion occurs through chemical and/or electrochemical reactions. In RC structures, the reinforcements are protected against such reactions by the passivating layer. This thin layer surrounding the reinforcements is chemically stable because of the alkalinity of the aqueous solutions at the concrete pores. Nevertheless, the chemical effects of Cl$^-$ ions into the concrete pores disturb the chemical stability of this layer [6]–[8]. Particularly, the corrosion process triggers when the Cl$^-$ concentration at the passivating layer reaches the threshold content. In this case, the depassivation phenomenon occurs.

The classic approach for RC durability assessment divides the structural service life into two periods: initiation period and propagation period [9], [10]. The initiation period concerns the time span from the construction until the reinforcements' depassivation. This period is governed by diffusion-like transport mechanisms such as the Cl$^-$ into the concrete pores. On the other hand, the propagation period refers to the reinforcements' mass loss and the mechanical degradation properties along time. It is well-established that the propagation period is shorter than the initiation period [11], [12]. Because the corrosion products occupy larger volume than the initial configuration, internal stresses lead to the cracking and spalling, as observed in Figure 1. Then, the accurate prediction and modelling of the initiation period have major importance for structural engineering applications in order to avoid and to prevent complex and faster mechanical degradation phenomena.

Figure 1 – Reinforcements' corrosion in a reinforced concrete column.

The Cl$^-$ ions ingress into the concrete pores involves dynamic and nonlinear processes, which include several transport mechanisms such as ionic diffusion, capillarity absorption, advection, chemical activity, permeation and dispersion [13]–[15]. In spite of the large complexity of this phenomenon, it is often modelled exclusively through the diffusion-like transport mechanism [16]–[18]. The pure diffusion assumptions are properly applied when saturated conditions are observed in concrete pores. It is worth mentioning that when tidal zones are accounted, the Cl$^-$ ingress has significant influence of capillarity absorption in addition to advection.

The chloride diffusion process is commonly modelled through analytical or empirical approaches available in the literature [19]–[21]. Among them, it is worth citing the Fick's approach [22]–[25]. The first Fick's law is applicable for steady-state processes. The second Fick' law, which represents the transient condition, is written as a function of time. The latter law of diffusion assumes the material as homogeneous, isotropic and inert. Moreover, the material properties during the diffusion phenomenon are assumed as equal along all directions and remain constant along time [26], [27]. In addition, the Fick's law solution is obtained from semi-infinite domains, in which the boundary conditions are assumed as constant along time and the flux occurs in one-directional form. It is worth

stressing that, in spite of been largely utilized in the literature, the Fick's approach incorporates inherent strong simplifications, which make it non-robust and inaccurate for a large amount of applications.

To handle properly the Cl⁻ diffusion into concrete pores, numerical methods have been successfully applied along the last years. Among them, it is worth citing the Finite Element Method (FEM), which was largely utilized for this purpose [28]–[32]. In addition, improved FEM approaches, such as the eXtended FEM (XFEM) has been also utilized for solving this problem [33], [34]. In the latter case, improved shape functions enable the accurate representation of the diffusion fields. In both cases, domain meshes are required, i.e. domain approximation, in spite of the boundary conditions are applied at the bodies boundaries. Moreover, both approaches require much finer discretisation in both the spatial and temporal domains, which results in large amount of unknowns and large computational time consuming.

Alternatively, the Boundary Element Method (BEM) handles accurately the diffusion modelling. In this numerical method, the governing differential equations are written into integral form at the body's boundary. Then, the BEM enables the mesh dimensionality reduction by one order. Moreover, the BEM does not require a domain mesh for solving the boundary value problem. Therefore, the internal diffusion fields are accurately determined since the boundary values are properly assessed [35]. This characteristic has major importance for assessing the corrosion time initiation because the Cl⁻ concentration along time and along the material domain is accurately determined by the BEM. Thus, this characteristic makes the BEM accurate for solving the corrosion time initiation problem. In addition, the diffusion problem is solved by small algebraic system of equations (in comparison with domain methods) because the mesh is positioned solely at the boundary [35], [36]. In spite of the above-mentioned advantages, the BEM has been marginally utilized for handling the corrosion time initiation problem. Particularly [37], [38], utilized the diffusion BEM formulation for assessing the chloride distribution along the concrete cover. The propagation period is modelled through commercial BEM and FEM software by Warkus et al. [39], in which the BEM advantages are highlighted. Chen and Leung [40] studied the durability of RC structures subjected to reinforcements' corrosion using the BEM approach. Thus, the present research contributes with this scientific domain by utilizing the transient BEM approach for the solution of time-dependent chloride diffusion into the concrete pores.

In spite of the large efforts dedicated towards the development of robust and general approaches for diffusion modelling, most of the models available in the literature utilize deterministic approaches for this purpose [11]. Moreover, it is well-known that the diffusion phenomenon is subjected to large randomness. Among the observed randomness aspects, it is worth citing: chloride binding capacity [41], [42], time and space effects on the coefficient of diffusion [43], [44], external variation of chloride concentration along time [45], [46], chemical composition of concrete [47]–[49], concrete curing process [21], [50], [51], critical chloride content [52], among others. Therefore, this complex engineering problem is solely analysed properly in the context of accurate numerical formulations coupled to probabilistic approaches. Then, the present study contributes with this scientific domain by coupling an accurate approach for diffusion with a probabilistic framework.

It is worth mentioning that the concepts of probabilistic modelling and life cycle are not included explicitly in several RC design codes. However, these concepts have evolved considerably in the last years. Significant advances were achieved concerning the design, monitoring, maintenance and repair phases [53], [54]. Nevertheless, these studies do not account for robust numerical approaches for representing the diffusion problem, which highlight the importance of the model proposed in the present study.

In this context, the present study proposes a diffusion-probabilistic framework for the robust and accurate modelling of Cl⁻ diffusion into concrete pores. The proposed model handles the corrosion time initiation taking into account the inherent problem randomness. The diffusion process is modelled by the BEM, in which transient conditions are accounted. Therefore, time dependent boundary conditions are properly represented by the BEM. Moreover, the BEM model is capable of simulating multi-directional domain flux caused by external Cl⁻. It is worth mentioning that these aspects make the proposed model superior to the empirical approaches utilized in the literature. High-order boundary elements are available for spatial integration. The temporal integration is performed by the constant approach. The randomness's are quantified by the Monte Carlo simulation method. This approach has been utilized because of the adequate computational performance of the BEM model. Moreover, because domain mesh (domain approximation) is not required by BEM, accurate values for Cl⁻ concentration at the material domain are assessed.

The proposed approach is applied in the analysis of three applications. The first application handles the comparative analysis against the Fick's modelling, in which the robustness of the BEM is demonstrated. The limitations of the analytical approach are also emphasized. The second and third applications concern the analyses of complex RC cross-sections, in which complex boundary conditions are applied along time. In both cases, accurate responses are obtained.

2 THE BOUNDARY ELEMENT FORMULATION

2.1 Governing Equations and Boundary Integral Equation

Classical potential problems are properly represented by the Poisson's equation. This equation enables the representation of thermal conductivity, torsion, conduction of fluids, among others, accounting for time independent conditions. The Poisson's equation is written as follows:

$$\nabla^2 u + b = 0 \tag{1}$$

where u is the potential and b represents the domain term. When the domain term is nil, a particular case is obtained, which is named as Laplace.

Equation 1 is solved by enforcing boundary conditions as follows:

- Essential: $u = \bar{u}$ in Γ_1

- Natural: $q = \bar{q} = \dfrac{du}{d\eta}$ in Γ_2

in which $\bar{u}$ indicates the prescribed potential value, $\bar{q}$ represents the prescribed flux value, Γ_1 and Γ_2 are the boundaries where potential or flux are prescribed, respectively. The flux is defined as $q = \dfrac{du}{d\eta}$, which is the directional derivative of u in relation to the outward normal vector η, as illustrated in Figure 2.
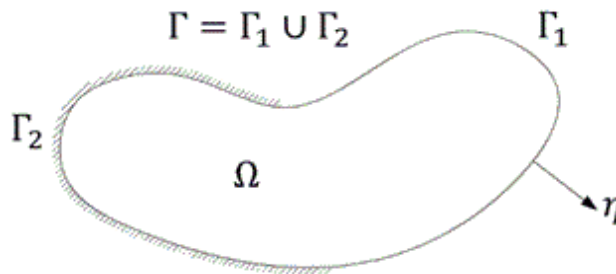
Figure 2 – Domain, boundaries and outward vector

Equation 1 represents properly the values of potential and flux for time independent conditions. Therefore, this approach is not accurate for representing the evolution of these diffusion fields during transient analyses. To incorporate time dependent boundary conditions or even for analysing the evolution of the diffusion fields along time, the transient approach must be accounted. The differential equation that governs the transient potential problem is the following:

$$\nabla^2 u - \frac{1}{\kappa} \frac{\partial u}{\partial t} = 0 \tag{2}$$

where κ is the domain-related parameter, such as thermal diffusivity or diffusion coefficient and t is time. The last equation is solved by enforcing the boundary conditions, similarly as described for Equation 1. Then, the potential and flux values at the boundary must be prescribed at each time step. It is worth mentioning that the diffusion problems

Rev. IBRACON Estrut. Mater., vol. 13, no. 4, e13409, 2020

4/26

analysed in the present study apply Equation 2. In such case, the potential values represent the chloride concentration along time whereas the flux represents the chloride flux along the time.

The differential equation Equation 2 can be transformed into a boundary integral representation by utilizing either the Laplace transform, the finite differences technique or the fundamental time dependent solutions [35], [55]–[57]. The latter approach is utilized in the present study. The boundary integral representation for the transient problem is achieved by applying the Green's second identity at the Equation 2. Afterwards, the integration by parts is applied. Finally, the usual limit process, necessary to evaluate the integral equation at the boundary, is performed. The above-mentioned procedures lead to the following integral representation, in which spatial and temporal integrations are required:

$$c(\underline{\xi})u(\underline{\xi},t_F) = \kappa \int_{t_0}^{t_F}\int_{\Gamma} q(\underline{x},t)u^*(\underline{\xi},\underline{x},t_F,t)d\Gamma(\underline{x})dt - \kappa \int_{t_0}^{t_F}\int_{\Gamma} u(\underline{x},t)q^*(\underline{\xi},\underline{x},t_F,t)d\Gamma(\underline{x})dt$$

(3)

where $\underline{\xi}$ refers to the source points, $\underline{x}$ represents the field points, t_0 indicates the initial time, t_F is the observation time, u^* and q^* are the fundamental time-dependent solutions for potential and flux, respectively, and c is the free term. The parameter c is equal to 1 for source points positioned at the domain. Otherwise, this parameter is equal to 0.5 for source points positioned at smooth boundary geometries. In two-dimensional case, the fundamental solutions are the following [35], [58]:

$$u^*(\underline{\xi},\underline{x},t_F,t) = \frac{1}{4\pi\kappa\tau}\exp\left(-\frac{r^2}{4\kappa\tau}\right)$$

(4)

$$q^*(\underline{\xi},\underline{x},t_F,t) = \frac{r\frac{\partial r}{\partial \eta}}{8\pi\kappa^2\tau^2}\exp\left(-\frac{r^2}{4\kappa\tau}\right)$$

(5)

in which $\tau = t_F - t$, r indicates the distance between the source $\underline{\xi}$ and the field $\underline{x}$ points and $\frac{\partial r}{\partial \eta} = r_{,k}\,\eta_k$.

2.2 Algebraic Equations

The potential and flux values at the boundary for a given time step are evaluated by Equation 3. Thus, spatial and temporal integrations must be performed to solve this equation. The spatial integration is performed by dividing the boundary geometry into boundary elements over which geometry and diffusion fields are approximated by shape functions. In the present study, polynomial functions are utilized for this purpose. The temporal integration is performed accounting for constant approximation. In the latter case, the time dependent kernels required by the BEM are integrated analytically.

Therefore, the discretisation of the body's boundaries Γ into Ne boundary elements, the discretisation of the time interval $t_F - t_0$ into Nt time steps and inverting the integration order lead to the following:

$$c_i u_i^{Nt} = \kappa \sum_{j=1}^{Ne}\sum_{k=1}^{Nt}\int_{\Gamma_j}\int_{t_0^k}^{t_f^k} q^k u^* dt\, d\Gamma_j - \kappa \sum_{j=1}^{Ne}\sum_{k=1}^{Nt}\int_{\Gamma_j}\int_{t_0^k}^{t_f^k} u^k q^* dt\, d\Gamma_j$$

(6)

in which u_i^{Nt} indicates the potential value at the time t^{Nt} for a given source point i. The last equation is rewritten bearing in mind that functions u^* and q^* are constantly integrated along time during each time step. In addition, it is assumed that source points are positioned at smooth boundaries. Thus:

$$0.5u_i^{Nt} = \kappa \sum_{j=1}^{Ne} \int_{\Gamma_j} \sum_{k=1}^{Nt} q^k \int_{t_0^k}^{t_f^k} u^* dt \, d\Gamma_j - \kappa \sum_{j=1}^{Ne} \int_{\Gamma_j} \sum_{k=1}^{Nt} u^k \int_{t_0^k}^{t_f^k} q^* dt \, d\Gamma_j \qquad (7)$$

Because the temporal integration is constantly performed, the last equation is rewritten as follows [35]:

$$0.5u_i^{Nt} = \kappa \sum_{k=1}^{Nt} \left(\sum_{j=1}^{Ne} q_j^k \int_{\Gamma_j} U_k^* \, d\Gamma_j - \sum_{j=1}^{Ne} u_j^k \int_{\Gamma_j} Q_k^* \, d\Gamma_j \right) \qquad (8)$$

in which the analytical evaluation of the fundamental solutions along time lead to the following [35]:

$$U_k^* = \int_{t_0^k}^{t_f^k} u^* dt = \frac{1}{4\pi\kappa} \left\{ E_I \left[\frac{r^2}{4\kappa \left(t_F - t_0^k \right)} \right] - E_I \left[\frac{r^2}{4\kappa \left(t_F - t_f^k \right)} \right] \right\} \qquad (9)$$

$$Q_k^* = \int_{t_0^k}^{t_f^k} q^* dt = \frac{1}{2\pi r\kappa} \frac{\partial r}{\partial \eta} \left\{ \exp \left[-\frac{r^2}{4\kappa \left(t_F - t_0^k \right)} \right] - \exp \left[-\frac{r^2}{4\kappa \left(t_F - t_f^k \right)} \right] \right\} \qquad (10)$$

where E_I represents the exponential-integral function.

As usual in BEM, Equation 8 is rewritten in terms of the influence matrices H and G. Thus:

$$0.5u_i^{Nt} = \sum_{k=1}^{Nt} \left(\sum_{j=1}^{Ne} G_{ij}^k q_j^k - \sum_{j=1}^{Ne} \widehat{H_{ij}^k} u_j^k \right) \qquad (11)$$

where H and G are the influence matrices containing the integral kernels as follows:

$$G_{ij}^k = \int_{\Gamma_j} U_k^* \, d\Gamma_j \qquad (12)$$

$$\widehat{H_{ij}^k} = \int_{\Gamma_j} Q_k^* \, d\Gamma_j \qquad (13)$$

$$H_{ij}^k = \begin{cases} \widehat{H_{ij}^k} + 0.5 & \text{if } k = 1 \text{ and } i = j \\ \widehat{H_{ij}^k} & \text{otherwise} \end{cases} \qquad (14)$$

Thus, the classical BEM system of equations is obtained as follows:

$$HU = GQ \qquad (15)$$

where H and G are NxN matrices containing the influence coefficients obtained from Equation 13 and Equation 14. N indicates the amount of collocation points into the boundary mesh.

The final system of equations is obtained by imposing the boundary conditions of the analysed problem into Equation 15. Then, the unknown values at the boundary are moved to the left side of the equation whereas the known

values are moved to the right side. This process is accompanied by the columns exchange between H and G matrices, which leads to the following:

$$AX = F \tag{16}$$

where A is a matrix composed of the coefficients from H and G associated with the unknown values, X is a vector containing the unknown values at the boundary and F is a vector obtained from the multiplication of the known values and their respective coefficients. The solution of Equation 16 provides the unknown values at the body's boundary.

Because transient analysis is performed, the diffusion fields at the present time are functions of the time history field values. Therefore, a time marching process is required. The constant approach is applied in the present model. Thus, the marching process is as follows [35]:

$$H_{t_f} U_{t_f} = G_{t_f} Q_{t_f} + S_f \tag{17}$$

in which S_f is evaluated as follows:

$$S_f = -\sum_{j=1}^{f-1} H_j U_j + \sum_{j=1}^{f-1} G_j Q_j \tag{18}$$

Then, the S_f vector is added to the F vector contained in Equation 16 to account for the time history effects.

The integration of the above-presented kernels is performed numerically. Nevertheless, the singular nature of the fundamental solutions requires special attention. The standard Gauss-Legendre quadrature is utilized when the integrated boundary element does not contain the source point. In this case, the kernels are regular. The kernels are improper for singular elements, i.e., when the integrated boundary element contains the source point. For such case, the singularity-subtraction method is utilized. By this approach, an auxiliary kernel with the same singularity order is subtracted and added to the original singular kernel. The procedure leads to a regular integral and to a new singular kernel, in which the latter has analytical solution. Then, the regular part is evaluated by the standard Gauss-Legendre quadrature whereas the analytical solution is achieved by the Cauchy principal value. This procedure enables the diffusion analyses accounting for high-order boundary elements. In addition, curved geometries are properly analysed. The analytical solution provided by the Cauchy principal value is demonstrated in Appendix A.

It is worth mentioning that Equation 6 enables the assessment of internal potential fields, in addition to the boundary values as previously mentioned. In such case, the free term c equals 1 because the source point is positioned in the domain. Because the kernels are regular for such case, all integrals are evaluated using the standard Gauss-Legendre quadrature.

3 UNCERTAINTY QUANTIFICATION MODELLING

The probabilistic approaches enable the assessment of the probability of failure, P_f, accounting for specific failure scenarios, which are formally named as limit states. In such analysis type, the set of random variables $X = [x_1, x_2, ..., x_n]^T$ must be initially identified. Then, individual probability distributions are attributed to such variables for modelling the individual randomness.

Afterwards, the failure modes must be defined/identified. The limit state function, $G(X)$, for each failure mode is defined, which separates the random space into two parts: the safe domain, $G(X) > 0$, and the failure domain, $G(X) < 0$. The $G(X) = 0$ indicates the interface between the domains, which is named as the limit state itself. Therefore, the probability of failure indicates the probability of the structural system does not accomplish one or more than one design requirements.

It is worth mentioning that explicit expressions for limit states are not usually available in complex engineering problems. Particularly, when numerical models represent the phenomenon behaviour, solely the limit state values are known at an informed amount of points. The probability of failure is assessed by the integration of the joint density function along the failure domain [59]. Therefore, the probability of failure is evaluated as follows:

$$p_f = P\big[G(\boldsymbol{X}) < 0\big] = \int \ldots \int_{G(\boldsymbol{X})<0} f_X(\boldsymbol{x}) d\boldsymbol{x} \tag{19}$$

in which: $f_X(\boldsymbol{x})$ is the joint density function of the random variables $\boldsymbol{X}$.

The explicit assessment of Equation 19 for complex engineering problems is impossible because the limit state function and consequently the failure and safe domains descriptions are implicit. Therefore, for such particular case, this integral is evaluated by simulation techniques. The most important simulation technique is the Monte Carlo simulation method (MCSM). In a brief overview, the MCSM assesses the probability of failure from a sampling of random variables, which simulates the limit state function. Then, the structural failure is observed when the sampling points leads to the failure domain. Otherwise, safe condition is observed. The probability of failure is assessed by the simulation technique through the ratio between the sampling points at the failure domain and the total amount of simulations. Thus:

$$p_f = \int_{\Omega} I[\boldsymbol{x}] f_X(\boldsymbol{x}) d\boldsymbol{x} = \frac{1}{n_t} \sum_{j=1}^{n_t} I\big[\boldsymbol{x}_j\big] = \frac{n_f}{n_t} \tag{20}$$

in which n_t is the sampling range and n_f the amount of observed failures. $I[x]$ is 1 for failure condition and nil for safe condition.

This simulation technique requires wide range of sampling for describing properly the failure and safe domains and, consequently, for achieving accurate results. Consequently, non-efficient numerical models lead to the unreliable coupling approaches. Nevertheless, the MCSM is utilized in the present study because the BEM formulation is efficient in terms of computational cost. It is worth citing that convergence analyses are recommended to verify the accuracy of the results obtained throughout the simulations. Convergence rate and its stability are directly influenced by the amount of random simulations.

It is worth mentioning that gradient-based techniques, such as First Order Reliability Method (FORM) or Second Order Reliability Method (SORM) could be applied for solving Equation 19. However, these methods require derivatives of the limit state functions, which, in such case, are assessed numerically. In addition to the numerical errors associated to the derivatives evaluation, the gradient-based techniques may lead to the local minima solutions. Therefore, in spite of the computational cost associated to the MCSM, it is certainly more robust than the gradient-based approaches.

In the present study, the limit state function depends on the time as follows:

$$G(\boldsymbol{X}) = R(\boldsymbol{X}) - S(\boldsymbol{X}, t) \tag{21}$$

in which R indicates the chloride threshold content value, which is a function of the concrete composition. Then, R indicates the material resistance against depassivation. S represents the chloride concentration at the analysed point. In the present study, the BEM model determines the chloride concentration value along time for the analysed point. Therefore, the S is assessed by the BEM whereas R is informed during the analysis. Then, the S value is a function of the material properties, structural geometry and chloride concentration at the exterior boundary. It is worth stressing that S is accurately evaluated by the BEM because of the method characteristics mentioned in section 2.

4 SUMMARY OF THE PROPOSED NUMERICAL MODEL

The diffusion-probabilistic model proposed in the present study runs as summarized in Figure 3. Then, the MCSM is initialized, in which a sample for the random variables is generated. It is worth stressing that these samples are generated as a function of the statistical distribution type, mean and coefficient of variation assigned for each random variable. These information enable the input for the BEM diffusion model.

The potential, i.e., the chloride concentration, at the material domain along time is determined by the BEM accounting for the sample values. As illustrated in Equation 21, failure occurs at a given time step k when the chloride concentration at the analysed point is higher than the chloride threshold content. Otherwise, safe condition is observed.
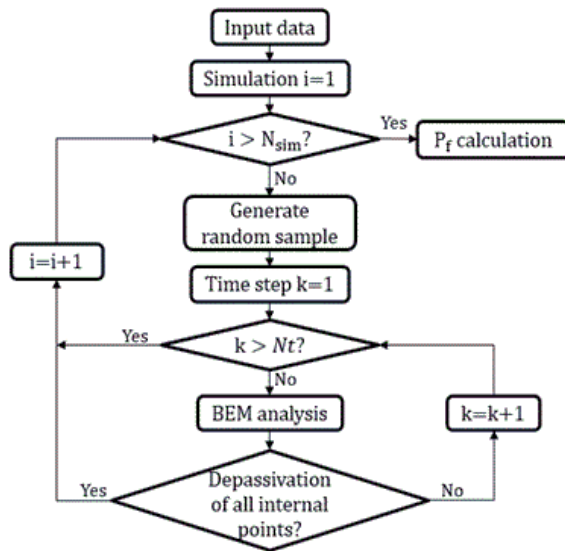
Figure 3 – Flowchart of the proposed numerical approach

5 APPLICATIONS

The diffusion-probabilistic framework proposed in the present study is utilized in the analysis of three applications. The first application concerns the deterministic comparison among the responses of the BEM and the Fick's law. This application illustrates the limitations of the Fick' law in general diffusion problems. The probabilistic modelling is included in the second and third applications. The second application handles the probabilistic diffusion modelling accounting for a rectangular cross-section. Similar analysis is performed in the third application, in which a T-shape cross-section is accounted. The statistical distribution assigned for each random variable is based on the literature references, especially [20], [60].

5.1 Application 1

The chloride diffusion transport in a rectangular 180 x 90 mm domain composed of concrete is analysed in the present application. A reinforcement of 10 mm diameter is assumed as a part of the specimen, as illustrated in Figure 4. Thus, the chloride concentration along time at the reinforcement position is evaluated in this application.
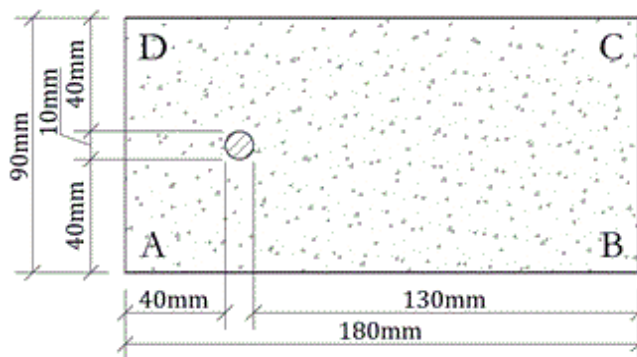
Figure 4 – Application 1. Specimen geometry dimensions

The diffusion responses achieved by the BEM are compared against the Fick's results. The chloride concentration by the Fick's approach is evaluated along time as follows [9]:

$$C(x,t) = C_s erfc\left[\frac{x}{2\sqrt{\kappa_0 t}}\right] \tag{22}$$

in which C_s indicates the chloride concentration at the body's surface, $C(x,t)$ is the chloride concentration at the desired point along time, t represents the time, x is the distance of the analysed point until the structural surface, κ_0 is the coefficient of diffusion and erfc is the complementary error function.

The coefficient of diffusion can be calculated by following the procedures proposed by [61]. Then:

$$\kappa_0 = 10^{-10+4.66w/c} \tag{23}$$

where w/c is the water/cement ratio and κ_0 is the coefficient of diffusion in square centimetres per second. The water/cement ratio is assumed as 0.5 in the present analysis. Therefore, the coefficient of diffusion is equal to $2.1379\,10^{-8}\,cm^2/s = 67.4228mm^2/year$, which is assumed as constant along time.

In the present application, the rectangular domain illustrated in Figure 4 is analysed accounting for four different boundary conditions, which compose the four cases shown in Figure 5.
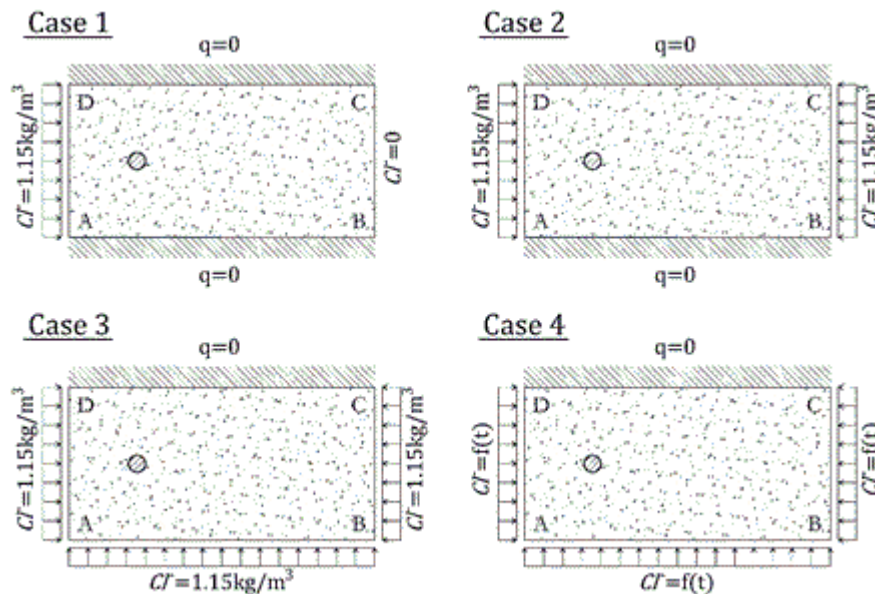
Figure 5 – Boundary conditions

The case 1 represents the pure one-directional flux, in which the chloride flux goes from the left to the right faces. The case 2 handles the mixed one-dimensional flux. In this case, the chloride flux occurs simultaneously from the left to the right faces and from the right to the left faces. The two-directional chloride flux is observed in case 3. It is worth citing that the boundary conditions illustrated for cases 1, 2 and 3 are assumed as constant along time. Then, the case 4 is added to account for time dependent boundary conditions. In the latter case, the two-directional flux is simulated, in which the chloride concentration along time varies following the systematic behaviour illustrated in Figure 6.
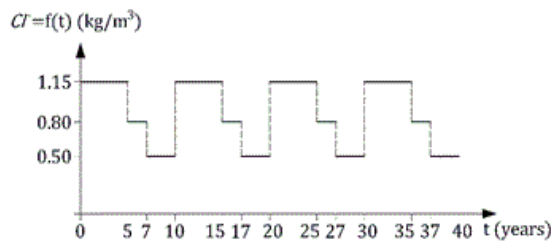
Figure 6 – Time dependent boundary conditions for case 4

It is worth emphasizing that the analytical approach incorporates inherent simplifications, as previously mentioned. Because of them, solely the boundary conditions of case 1 comply with the model requirements. Thus, this application illustrates the limitations of Fick's model and the necessity of robust approaches for solving properly this problem.

The mesh utilized by the BEM simulations is composed of 54 linear isoparametric discontinuous boundary elements, which lead to the 108 collocation points. In addition, 40 time steps were utilized for the temporal integration. Moreover, it is assumed that $u = q = 0$ in $t = 0$. The space and time discretisations have been determined accounting for standard convergence procedure. Then, further refined discretisation do not introduce significant changes into the mechanical modelling.

Internal points were added to determine the chloride concentration behaviour along time into the concrete specimen. Such points are spaced from 2 mm each other. Moreover, they were positioned at a virtual line connecting the midpoints of the boundaries AD and BC. Therefore, the internal points intercept the reinforcement's position, as illustrated in Figure 4. The chloride concentration profiles determined by the BEM and via Fick's approach are illustrated in Figure 7. In this figure, the four different boundary conditions are illustrated.
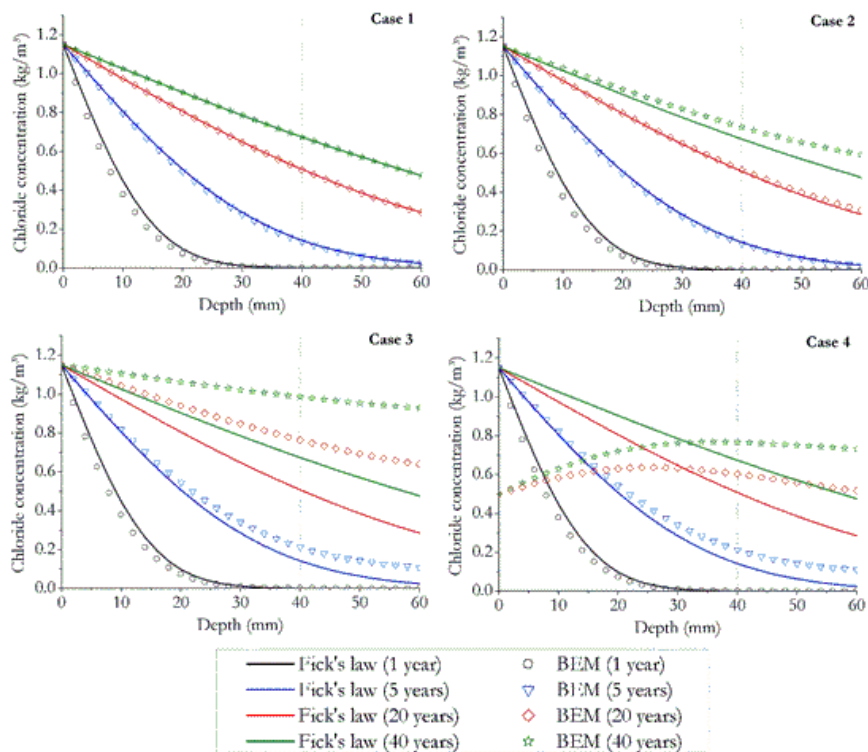
Figure 7 – Chloride profiles evolution along time for the four different boundary conditions

Moreover, the evolution of the chloride concentration along time for the fixed reinforcement position, i.e. depth of 40 mm, is illustrated in Figure 8.
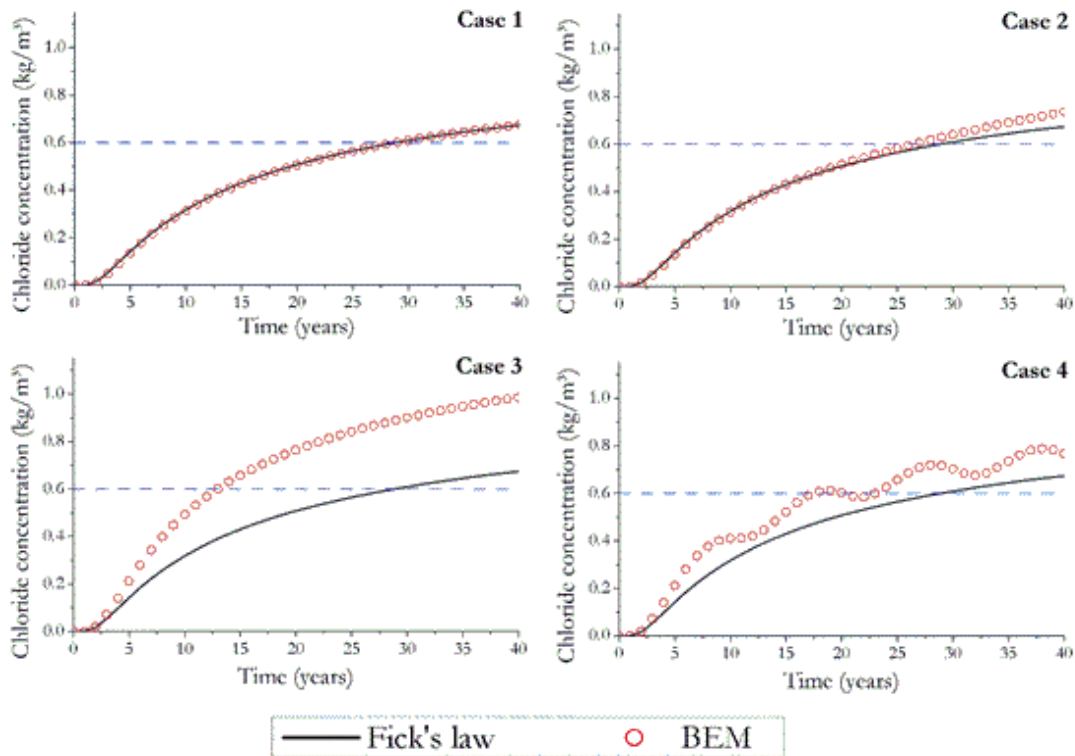
Figure 8 – Chloride concentration evolution along time for the fixed depth

Excellent agreement is observed among the numerical and analytical responses for case 1. This behaviour was expected because the Fick's hypotheses are well satisfied in the case. The responses differences for the years 5, 20 and 40 are 5.31%, 0.32% and 0.07%, respectively. Moreover, assuming the threshold chloride content as 0.6 kg/m^3, for instance, both approaches lead to the same time for corrosion initiation, 29 years.

The case 2 presents similar behaviour when early ages are analysed. Then, good agreement is observed until 5 years. Nevertheless, important differences occur after 20 years, in spite of essentially one-dimensional diffusion transport is simulated. These differences appear due to the bidirectional chloride diffusion simulated in this case, which is not properly represented by the analytical approach. It is worth emphasizing that the influence of the bidirectional chloride diffusion is evident in case 3, in which essentially two-dimensional chloride diffusion is accounted. In the latter case, large differences are observed even in early ages. Moreover, the chloride concentration evolves faster along time, in this case, in comparison with one-directional cases. The corrosion time initiation is 26 years and 13 years for cases 2 and 3, respectively. Then, in comparison with case 1, reductions of 10% and 55% are observed.

Finally, large behaviour differences among numerical and analytical responses are observed in case 4. In this case, the chloride concentration at the specimen surface is a function of time. As expected, the numerical responses are capable to represent the time dependent behaviour. Nevertheless, such behaviour is not represented properly by the analytical approach. Actually, Fick's solution assumes time independent boundary conditions, which is not observed in practical engineering problems. The time for corrosion initiation determined by the BEM is 18 years, which is 38% shorter than in case 1.

The present application illustrates some limitations of the Fick's law in simulating the chloride diffusion transport mechanism. Particularly, the limitations associated to the time dependent boundary conditions and multi-directional fluxes must be emphasized. In such cases, the hypotheses of Fick's approach are violated and this analytical approach does not represent properly the physical phenomenon. It is worth stressing that the

cases 2, 3 and 4 concern practical diffusion problems, in which multi-directional fluxes are observed and time dependent chloride concentration at the surface occurs. In such cases, major differences of chloride concentration behaviour along time are observed. Thus, based on the present results, one emphasizes that Fick's law must be criteriously utilized. Moreover, its limitations must be accounted for the proper diffusion modelling.

5.2 Application 2

In this application, the diffusion-probabilistic modelling of the specimen illustrated in Figure 4 is presented. Thus, the geometry and boundary conditions discussed in the previous application are accounted. However, the randomness on problem variables is included and the uncertainties are quantified taking into account the corrosion time initiation. The limit state function utilized in the present analysis is as follows:

$$G = t_c(X) - t_{SL}$$

(24)

in which t_c indicates the corrosion time initiation, which is a function of the random variables, X. t_{SL} is the expected structural life time. Thus, positive values in Equation 24 indicate safe condition.

In this application, t_c is calculated either by the BEM model or the Fick's approach. Moreover, the probability of failure is assessed by the MCSM. In this application, one verifies if the large differences behaviour observed in the last application lead to the similar differences behaviour on the values of probabilities of failure.

In this analysis, three random variables are considered. The statistical distributions assigned for each random variable as well as its statistical properties are described in Table 1. It is worth mentioning that the mean values for the chloride concentration at the surface for case 4 are presented in the previous application, Figure 6.

Table 1 – Statistical data for application 2

Parameter	Distribution type	Mean	C.O.V.
Chloride threshold content C_{lim}	Uniform	0.60 kg/m³	0.1443
Coefficient of Diffusion κ_0	Lognormal	67.7228 mm²/year	0.50
Chloride concentration at the Surface C_S	Lognormal	1.15 kg/m³ (moderate aggressiveness)	0.50

The BEM simulations required a mesh composed of 54 linear isoparametric discontinuous boundary elements, which lead to the 108 collocation points. In addition, 40 time steps were utilized for the temporal integration. Moreover, it is assumed that $u = q = 0$ in $t = 0$. The space and time discretisation have been determined accounting for standard convergence procedure. Then, further refined discretisation do not introduce significant changes into the mechanical modelling. The probability of failure was assessed at the internal points positioned following the pattern mentioned in the previous application. At each of these internal points, 10,000 Monte Carlo simulations were performed. It is worth mentioning that the range sample utilized in this application was sufficient for achieving the convergence during the probabilistic modelling.

The evolutions of the probability of failure along time for different depth values are illustrated in Figure 9. In this figure, the four different boundary conditions presented in the previous application are utilized. In addition, the evolution of the probability of failure along time for fixed depth values is presented in Figure 10.

Rev. IBRACON Estrut. Mater., vol. 13, no. 4, e13409, 2020

13/26
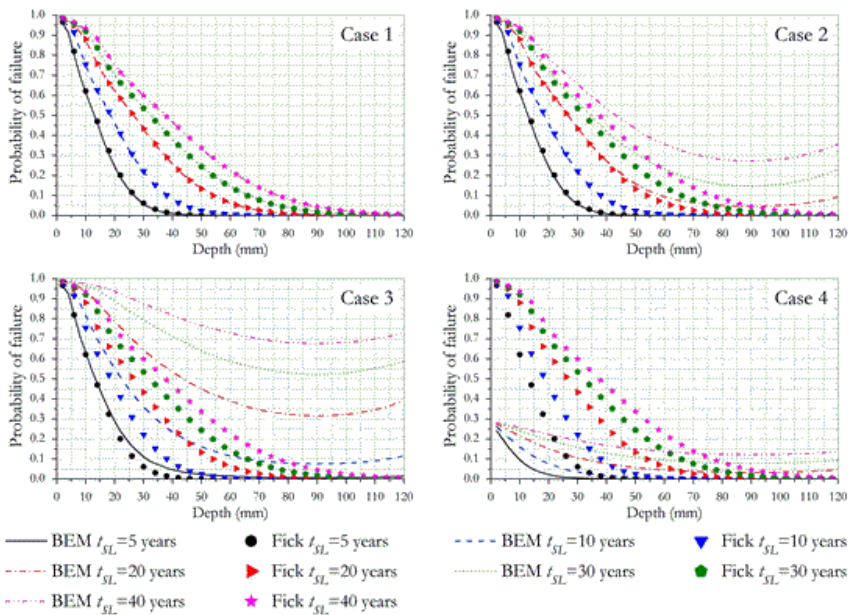
Figure 9 – Evolution of the probability of failure along time.
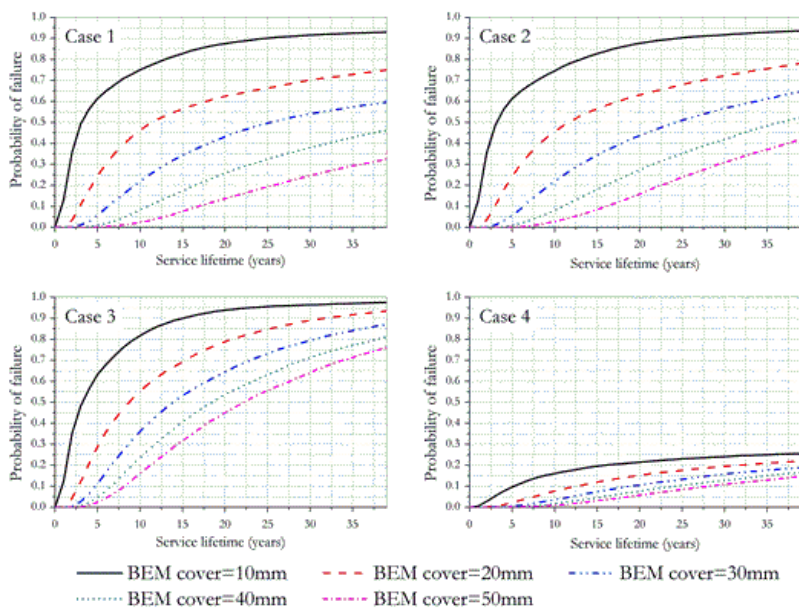
Figure 10 – Evolution of the probability of failure along time

Excellent agreement is observed among the probabilistic responses achieved by the BEM and the Fick's approach for case 1. This behaviour was expected because the chloride flux is essentially one-directional in this case. Nevertheless, major differences are observed for the other cases. Therefore, the probability of failure is largely dependent of the multi-directional flux condition in addition to the time dependent boundary conditions. This observation illustrates the weakness of the Fick's approach in simulating complex chloride ingress cases. Moreover, it demonstrates that numerical approaches are necessary to simulate properly this complex engineering problem.

It is worth mentioning that, in all cases, the probability of failure grows faster at small depths, as expected. The chloride concentration grows faster at those positions because of the near presence of chlorides at the surface. Therefore, fair cover depth values must be prescribed in structural design to assure adequate structural durability.

5.3 Application 3

This application handles the diffusion-probabilistic modelling in the cross-section illustrated in Figure 11. This problem concerns a typical reinforced concrete beam connected to a concrete slab, which is largely utilized in bridge decks systems. The beam has rectangular cross-section of 20 x 50 cm whereas the slab has 15 cm thickness. The resulting T-cross-section shape is subjected to chloride ingress along six of its boundaries. The upper boundary is subjected to external chloride concentration Cs_1 and the lower boundaries are exposed to external chloride concentration Cs_2. The cross-section dimensions and the boundary conditions are illustrated in Figure 11.
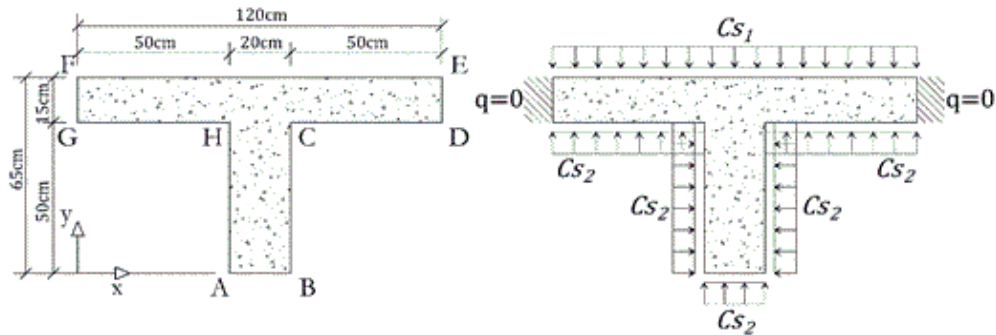
Figure 11 – Geometry and boundary conditions

The probabilistic modelling aims the determination of isoprobability of failure maps, which describe the evolution of the probability of failure along time for points that compose the cross-section domain. Thus, the limit state function considered in the present analysis is the illustrated in Equation 24. Such maps enable the accurate choice of the cover thickness by the analyst based on a given probability of failure target.

The diffusion analysis along time is performed by the BEM. The mesh utilized by the numerical model is composed of 74 quadratic isoparametric discontinuous boundary elements, which lead to the 222 collocation points. In addition, 33 time steps were utilized for the temporal integration, which cover the time span from 0 until 99 years. Moreover, it is assumed that $u = q = 0$ in $t = 0$. The space and time discretisation have been determined accounting for standard convergence procedure. Then, further refined discretisation does not introduce significant changes into the mechanical modelling.

The probabilistic modelling is performed accounting for the random variables described in Table 2. It is worth mentioning that three different environment aggressiveness were considered in the present analysis.

Table 2 – Statistical data for application 3

Environment aggressiveness level	Parameter	Distribution type	Mean	C.O.V.
All	Chloride threshold content C_{lim}	Uniform	0.90 kg/m^3	0.19
All	Coefficient of Diffusion κ_0	Lognormal	0. 2305720 cm^2/year	0.50
Moderate/Normal	Cl$^-$ concentration at the surface Cs_1	Lognormal	1.15 kg/m^3	0.50
	Cl$^-$ concentration at the surface Cs_2		0.92 kg/m^3	
High	Cl$^-$ concentration at the surface Cs_1	Lognormal	2.95 kg/m^3	0.75
	Cl$^-$ concentration at the surface Cs_2		2.36 kg/m^3	
Extreme	Cl$^-$ concentration at the surface Cs_1	Lognormal	7.35 kg/m^3	0.75
	Cl$^-$ concentration at the surface Cs_2		5.88 kg/m^3	

The probability of failure was assessed by the MCSM. For each environment aggressiveness, 10,000 simulations were performed to assess the probability of failure. It is worth mentioning that the sample range was sufficient for achieving the probabilistic convergence, as illustrated in Appendix B. Such method simulated the limit state function into 386 internal points,

which were distributed into an uniform grid at the cross-section domain. Therefore, the probability of failure is assessed for each internal point. Based on these responses, a map of isoprobability of failure is obtained.

The isoprobability of failure maps for normal, high and extreme environment aggressiveness are shown in Figure 12, Figure 13 and Figure 14, respectively. The expected structural life time of 25 years and 50 years are considered.
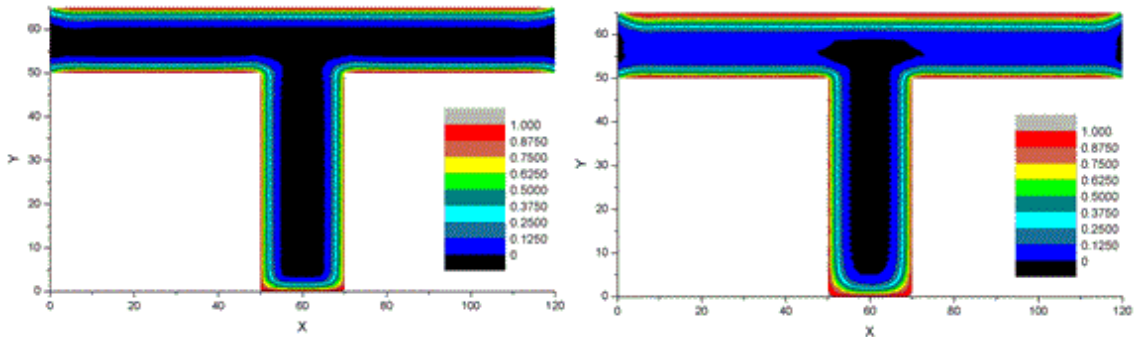
Figure 12 – Isoprobability maps for 25 years and 50 years. Normal environment aggressiveness.
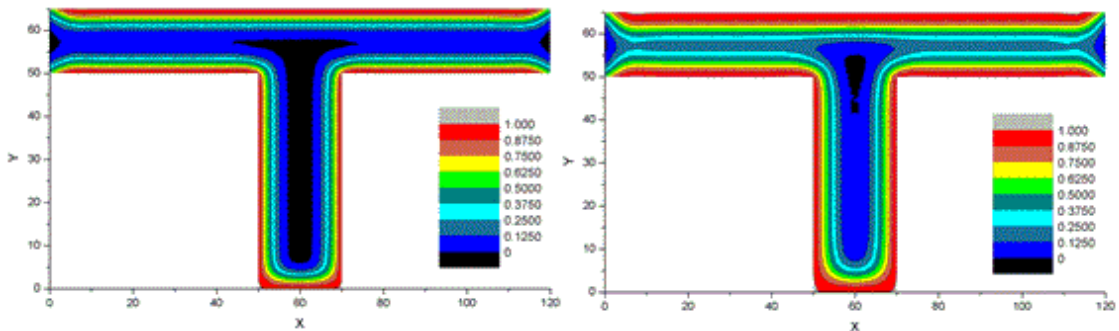
Figure 13 – Isoprobability maps for 25 years and 50 years. High environment aggressiveness.
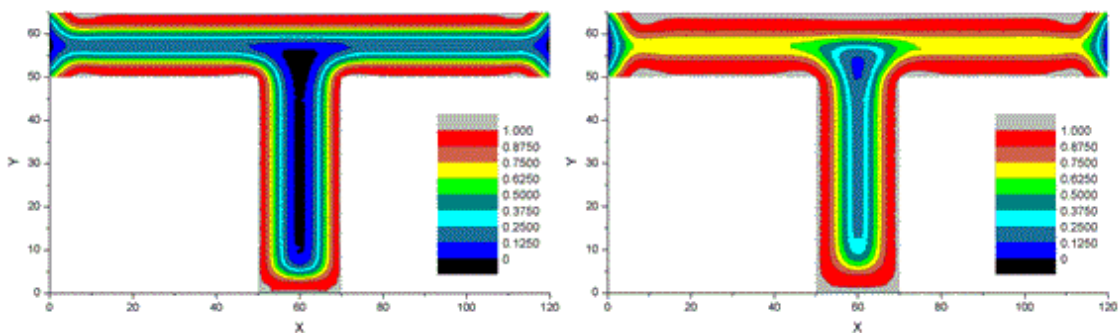
Figure 14 – Isoprobability maps for 25 years and 50 years. Extreme environment aggressiveness.

As expected, high values for the probability of failure are observed for points positioned near the external boundaries. In addition, the probability of failure values decrease faster as these points move from the boundary to the cross-section kernel. It is worth mentioning the huge influence of the environment aggressiveness level on the probability of failure values. Thus, higher probability of failure values are observed as higher is the environment aggressiveness. The probabilities of failure evolve faster at the upper cross-section boundary because at this position the chloride concentration at the surface is higher than at the other boundaries. In addition, the probabilities of failure values decrease near the boundaries in which the flux is assumed as nil, as expected. The results presented in the three last figures show the major importance of designing properly the cover thickness

taking into account the environment aggressiveness. Moreover, the corrosion time initiation may be improved by utilizing proper schemes that make nil the flux at specific structural boundaries.

Additional analyses were performed to determine, in a detailed mode, the evolution of the probability of failure in particular regions of the T-cross-section shape. Then, internal points were concentrated at specific regions, in spite of the boundary conditions are applied along the entire cross-section boundaries. Three regions were utilized for this purpose: the corner A, the corner H and the left portion of the slab. 196 internal points were utilized for achieving the map of isoprobability of failure at the corner A. The same map was obtained by 192 internal points in corner H. Finally, the slab region was analysed accounting for 196 internal points. Such points were uniformly distributed along each particular analysed region. The regions dimensions are illustrated in Figure 15, Figure 16 and Figure 17. It is worth mentioning that the additional analyses were performed taking into account solely the normal environment aggressiveness. Moreover, for each region, the probability of failure was assessed considering as structural service life of 25 years, 50 years and 75 years.
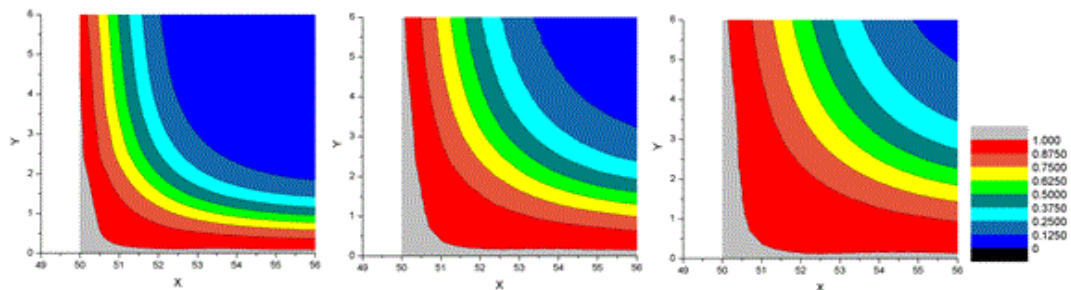
Figure 15 – Isoprobability of failure curves for corner A. Probability of failure values for 25 years, 50 years and 75 years. Dimensions in cm.
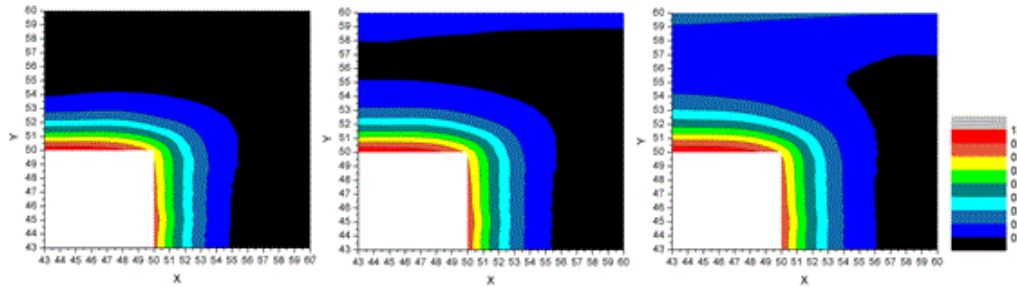
Figure 16 – Isoprobability of failure curves for corner H. Probability of failure values for 25 years, 50 years and 75 years. Dimensions in cm.
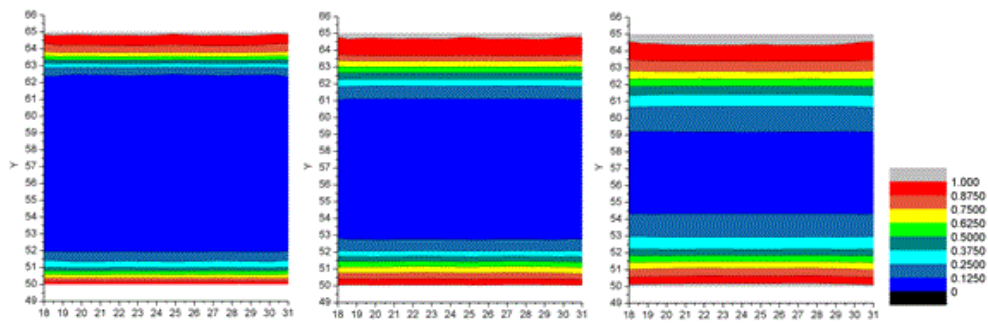
Figure 17 – Isoprobability of failure curves for slab region. Probability of failure values for 25 years, 50 years and 75 years. Dimensions in cm.

Rev. IBRACON Estrut. Mater., vol. 13, no. 4, e13409, 2020

17/26

The last three figures illustrate different evolutions of the probability of failure, although each particular region belong to the same cross-section. Such differences are explained by the boundary conditions and the cross-section geometry, which have major importance into the chloride diffusion evolution inside the material. In addition, these results demonstrate that Fick's approach is not robust in the solution of problems with multidirectional flux condition.

The probabilities of failure grow faster along time for the corner A, Figure 15. Nevertheless, the probabilities of failure values decay faster as the analysed point is far from the boundaries. For the cover thickness from 1.0 to 5.0 cm, the probabilities of failure decay from 0.9737 to 0.0745 at 50 years. This behaviour emphasizes the major importance of adopting fair values for cover thickness, which lead to the adequate durability. Similar behaviour is observed for the corner H, Figure 16. However, in this corner, the growth of the probability of failure is smooth in comparison with corner A. Such behaviour is explained by the slab presence, which smooths the chloride flux distribution at that position. Finally, the probability of failure values grow faster and uniformly at the slab thickness, Figure 17. This behaviour is explained by the bidirectional chloride flux ingress, which occur at upper and lower slab boundaries.

The results presented in this application demonstrate the large influence of the bidirectional chloride flux into the chloride concentration at the material domain. Moreover, the results illustrate the major importance of adopting proper cover thickness values because the probability of failure decay faster along the cover thickness.

6 CONCLUSIONS

This study presented a diffusion-probabilistic framework to analyse the corrosion time initiation in concrete structures. The diffusion phenomenon is modelled by the BEM, in which transient potential and flux conditions are accounted. Two-dimensional conditions are assumed. Then, the chloride concentration evolution along time for particular cross-sections are handled. The MCSM was utilized to quantify the uncertainties. The BEM has been marginally utilized in the literature for modelling the chloride ingress. Moreover, the coupling of accurate and robust numerical models for diffusion to probabilistic approaches has been also marginally explored in the literature. Then, these aspects are original in the present study.

The first application demonstrates the robustness of the diffusion BEM model over classical analytical approaches, such as the Fick's law. This application demonstrates that complex diffusion problems are not properly handled by the analytical approach, in spite of the Fick's law is largely utilized for this purpose.

The second and third applications demonstrate the uncertainty quantification process in complex diffusion problems. The evolution of the probability of failure along the cross-section domain is demonstrated. In addition, the results show the importance of designing properly the cover thickness, which enables the adequate structural durability. The cover depth value may be achieved by coupling the proposed framework to optimisation approaches. In this case, the cover depth value may be achieved accounting for a desired safety level, i.e, a probability of failure target.

7 ACKNOWLEDGEMENTS

8 REFERENCES

[1] L. Courard, A. Gillard, A. Darimont, J. M. Bleus, and P. Paquet, "Pathologies of concrete in Saint-Vincent Neo-Byzantine Church and Pauchot reinforced artificial stone," *Constr. Build. Mater.*, vol. 34, pp. 201–210, 2012., http://dx.doi.org/10.1016/j.conbuildmat.2012.02.070.

[2] D. Bru, A. González, F. J. Baeza, and S. Ivorra, "Seismic behavior of 1960's RC buildings exposed to marine environment," *Eng. Fail. Anal.*, vol. 90, pp. 324–340, 2018., http://dx.doi.org/10.1016/j.engfailanal.2018.02.011.

[3] J. R. A. Goncalves, Y. Boluk, and V. Bindiganavile, "Crack growth resistance in fibre reinforced alkali-activated fly ash concrete exposed to extreme temperatures," *Mater. Struct.*, vol. 51, no. 42, pp. 42, 2018., http://dx.doi.org/10.1617/s11527-018-1163-6.

[4] T. Ueda and K. Takewaka, "Performance-based standard specifications for maintenance and repair of concrete structures in Japan," *Struct. Eng. Int.*, vol. 4, no. 4, pp. 359–366, 2007, http://dx.doi.org/10.2749/101686607782359119.

[5] E. A. P. Liberati, C. G. Nogueira, E. D. Leonel, and A. Chateauneuf, "Failure analysis of reinforced concrete structures subjected to chloride penetration and reinforcements corrosion," in *Handbook of Materials Failure Analysis with Case Studies from the Chemicals, Concrete and Power Industries*, A. S. H. Makhlouf and M. Aliofkhazrae, Eds., Oxford: Butterworth-Heinemann, 2016.

[6] F. Shaikh, "Effect of cracking on corrosion of steel in concrete," *Int. J. Concr. Struct. Mater.*, vol. 12, no. 1, pp. 1–12, 2018, http://dx.doi.org/10.1186/s40069-018-0234-y.

[7]   A. Silva, R. Neves, and J. Brito, "Statistical modelling of carbonation in reinforced concrete," *Cement Concr. Compos.*, vol. 50, pp. 73–81, 2014, http://dx.doi.org/10.1016/j.cemconcomp.2013.12.001.

[8]   Y. Zhou, B. Gencturk, K. Willam, and A. Attar, "Carbonation-induced and chloride-induced corrosion in reinforced concrete structures," *J. Mater. Civ. Eng.*, vol. 27, no. 9, pp. 1–17, 2015, http://dx.doi.org/10.1061/(ASCE)MT.1943-5533.0001209.

[9]   K. Tuuti, *Corrosion of Steel in Concrete Swedish*. Stockholm: Cement and Concrete Research Institute, 1982.

[10] X. Shi, N. Xie, K. Fortune, and J. Gong, "Durability of steel reinforced concrete in chloride environments: An overview," *Constr. Build. Mater.*, vol. 30, pp. 125–138, 2012, http://dx.doi.org/10.1016/j.conbuildmat.2011.12.038.

[11] E. A. Liberati, C. G. Nogueira, E. D. Leonel, and A. Chateauneuf, "Nonlinear formulation based on FEM, Mazars damage criterion and Fick's law applied to failure assessment of reinforced concrete structures subjected to chloride ingress and reinforcements corrosion," *Eng. Fail. Anal.*, vol. 46, pp. 247–268, 2014, http://dx.doi.org/10.1016/j.engfailanal.2014.09.006.

[12] D. Chen and S. Mahadevan, "Chloride-induced reinforcement corrosion and concrete cracking simulation," *Cement Concr. Compos.*, vol. 30, no. 3, pp. 227–238, 2008, http://dx.doi.org/10.1016/j.cemconcomp.2006.10.007.

[13] L. Saad, A. Aissani, A. Chateauneuf, and W. Raphael, "Reliability-based optimization of direct and indirect LCC of RC bridge elements under coupled fatigue-corrosion deterioration processes," *Eng. Fail. Anal.*, vol. 59, pp. 570–587, 2016, http://dx.doi.org/10.1016/j.engfailanal.2015.11.006.

[14] T.-B. Tran, E. Bastidas-Arteaga, F. Schoefs, and S. Bonnet, "A Bayesian network framework for statistical characterisation of model parameters from accelerated tests: application to chloride ingress into concrete," *Struct. Infrastruct. Eng.*, vol. 14, no. 5, pp. 580–593, 2018, http://dx.doi.org/10.1080/15732479.2017.1377737.

[15] P. Faustino, C. Chastre, Â. Nunes, and A. Brás, "Lifetime modelling of chloride-induced corrosion in concrete structures with Portland and blended cements," *Struct. Infrastruct. Eng.*, vol. 12, no. 9, pp. 1013–1023, 2016, http://dx.doi.org/10.1080/15732479.2015.1076487.

[16] E. Bastidas-Arteaga and F. Schoefs, "Stochastic improvement of inspection and maintenance of corroding reinforced concrete structures placed in unsaturated environments," *Eng. Struct.*, vol. 41, pp. 50–62, 2012, http://dx.doi.org/10.1016/j.engstruct.2012.03.011.

[17] A. Ben-Fraj, S. Bonnet, and A. Khelidj, "New approach for coupled chloride/moisture transport in non-saturated concrete with and without slag," *Constr. Build. Mater.*, vol. 35, pp. 761–771, 2012, http://dx.doi.org/10.1016/j.conbuildmat.2012.04.106.

[18] P.-T. Nguyen, E. Bastidas-Arteaga, O. Amiri, and C.-P. El Soueidy, "An efficient chloride ingress model for long-term lifetime assessment of reinforced concrete structures under realistic climate and exposure conditions," *Int. J. Concr. Struct. Mater.*, vol. 11, no. 2, pp. 199–213, 2017, http://dx.doi.org/10.1007/s40069-017-0185-8.

[19] M. B. Otieno, H. D. Beushausen, and M. G. Alexander, "Modelling corrosion propagation in reinforced concrete structures - A critical review," *Cement Concr. Compos.*, vol. 33, no. 2, pp. 240–245, 2010, http://dx.doi.org/10.1016/j.cemconcomp.2010.11.002.

[20] D. V. Val, L. Chernin, and M. G. Stewart, "Experimental and numerical investigation of corrosion-induced cover cracking in reinforced concrete structures," *J. Struct. Eng.*, vol. 135, no. 4, pp. 376–385, 2009, http://dx.doi.org/10.1061/(ASCE)0733-9445(2009)135:4(376).

[21] A. A. Abouhussien and A. A. A. Hassan, "Experimental and empirical time to corrosion of reinforced concrete structures under different curing conditions," *Adv. Civ. Eng.*, vol. 2014, pp. 1–9, 2014., http://dx.doi.org/10.1155/2014/595743.

[22] S. Guzman, J. C. Galvez, and J. M. Sancho, "Cover cracking of reinforced concrete due to rebar corrosion induced by chloride penetration," *Cement Concr. Res.*, vol. 41, no. 8, pp. 893–902, 2011, http://dx.doi.org/10.1016/j.cemconres.2011.04.008.

[23] K. Audenaert, Q. Yuan, and G. De Schutter, "On the time dependency of the chloride migration coefficient in concrete," *Constr. Build. Mater.*, vol. 24, no. 3, pp. 396–402, 2010, http://dx.doi.org/10.1016/j.conbuildmat.2009.07.003.

[24] M. G. Stewart, X. Wang, and M. N. Nguyen, "Climate change impact and risks of concrete infrastructure deterioration," *Eng. Struct.*, vol. 33, no. 4, pp. 1326–1337, 2011, http://dx.doi.org/10.1016/j.engstruct.2011.01.010.

[25] K. A. T. Vu and M. G. Stewart, "Structural reliability of concrete bridges including improved chloride-induced corrosion models," *Struct. Saf.*, vol. 22, no. 4, pp. 313–333, 2000, http://dx.doi.org/10.1016/S0167-4730(00)00018-7.

[26] J. Crank, *The Mathematics of Diffusion*, 2nd ed. London: Clarendon Press, 1975.

[27] L. Y. Li, J. Xia, and S. S. Lin, "A multi-phase model for predicting the effective diffusion coefficient of chlorides in concrete," *Constr. Build. Mater.*, vol. 26, no. 1, pp. 295–301, 2012, http://dx.doi.org/10.1016/j.conbuildmat.2011.06.024.

[28] Y. Wu and J. Xiao, "The Multiscale Spectral Stochastic Finite Element Method for Chloride Diffusion in Recycled Aggregate Concrete," *Int. J. Comput. Methods*, vol. 15, no. 1, pp. 1750078, 2018, http://dx.doi.org/10.1142/S0219876217500785.

[29] J. Xiao, J. Ying, and L. Shen, "FEM simulation of chloride diffusion in modeled recycled aggregate concrete," *Constr. Build. Mater.*, vol. 29, pp. 12–23, 2012, http://dx.doi.org/10.1016/j.conbuildmat.2011.08.073.

[30] Y. Zeng, "Modeling of chloride diffusion in hetero-structured concretes by finite element method," *Cement Concr. Compos.*, vol. 29, no. 7, pp. 559–565, 2007, http://dx.doi.org/10.1016/j.cemconcomp.2007.04.003.

[31] C. Frier and J. D. Sorensen, "Finite element reliability analysis of chloride ingress into reinforced concrete structures," *Struct. Infrastruct. Eng.*, vol. 3, no. 4, pp. 355–366, 2007, http://dx.doi.org/10.1080/15732470600557688.

[32] O. Na, X.-C. Cai, and Y. Xi, "Corrosion prediction with parallel finite element modeling for coupled hygro-chemo transport into concrete under chloride-rich environment," *Materials*, vol. 10, no. 350, pp. 350, 2017, http://dx.doi.org/10.3390/ma10040350.

[33] H. S. Al-Alaily, A. A. A. Hassan, and A. A. Hussein, "Use of extended finite element method and statistical analysis for modelling the corrosion-induced cracking in reinforced concrete containing metakaolin," *Can. J. Civ. Eng.*, vol. 45, no. 3, pp. 167–178, 2018, http://dx.doi.org/10.1139/cjce-2017-0298.

[34] R. Duddu, "Numerical modeling of corrosion pit propagation using the combined extended finite element and level set method," *Comput. Mech.*, vol. 54, no. 3, pp. 613–627, 2014, http://dx.doi.org/10.1007/s00466-014-1010-8.

[35] L. C. Wrobel, *The Boundary Element Method: Applications in Thermos-fluids and Acoustics, vol. 1*. New York: John Wiley & Sons, 2002.

[36] E. D. Leonel and W. S. Venturini, "Non-linear boundary element formulation applied to contact analysis using tangent operator," *Eng. Anal. Bound. Elem.*, vol. 35, no. 12, pp. 1237–1247, 2011, http://dx.doi.org/10.1016/j.enganabound.2011.06.005.

[37] L. F. Yang, Z. Chen, Q. Gao, and J. W. Ju, "Compensation length of two-dimensional chloride diffusion in concrete using a boundary element model," *Acta Mech.*, vol. 224, no. 1, pp. 123–137, 2013, http://dx.doi.org/10.1007/s00707-012-0721-1.

[38] L. Guo, T. Chen, and X.-W. Gao, "Transient meshless boundary element method for prediction of chloride diffusion in concrete with time dependent nonlinear coefficients," *Eng. Anal. Bound. Elem.*, vol. 36, no. 2, pp. 104–111, 2012, http://dx.doi.org/10.1016/j.enganabound.2011.08.005.

[39] J. Warkus, M. Brem, and M. Raupach, "BEM-models for the propagation period of chloride induced reinforcement corrosion," *Mater. Corros.*, vol. 57, no. 8, pp. 636–641, 2006, http://dx.doi.org/10.1002/maco.200603995.

[40] E. Chen and C. K. Y. Leung, "A coupled diffusion-mechanical model with boundary element method to predict concrete cover cracking due to steel corrosion," *Corros. Sci.*, vol. 126, pp. 180–196, 2017, http://dx.doi.org/10.1016/j.corsci.2017.07.001.

[41] V. V. Val and P. A. Trapper, "Probabilistic evaluation of initiation time of chloride-induced corrosion," *Reliab. Eng. Syst. Saf.*, vol. 93, no. 3, pp. 364–372, 2008, http://dx.doi.org/10.1016/j.ress.2006.12.010.

[42] Q. Zhu, L. Jiang, Y. Chen, J. Xu, and L. Mo, "Effect of chloride salt type on chloride binding behavior of concrete," *Constr. Build. Mater.*, vol. 37, pp. 512–527, 2012, http://dx.doi.org/10.1016/j.conbuildmat.2012.07.079.

[43] M.-T. Liang, R. Huang, and H.-Y. Jheng, "Revisited to the relationship between the free and total chloride diffusivity in concrete," *J. Mar. Sci. Technol.*, vol. 18, pp. 442–448, 2010.

[44] Y.-M. Sun, M.-T. Liang, and T.-P. Chang, "Time/depth dependent diffusion and chemical reaction model of chloride transportation in concrete," *Appl. Math. Model.*, vol. 36, no. 3, pp. 1114–1122, 2012, http://dx.doi.org/10.1016/j.apm.2011.07.053.

[45] K. Y. Ann, J. H. Ahn, and J. S. Ryou, "The importance of chloride content at the concrete surface in assessing the time to corrosion of steel in concrete structures," *Constr. Build. Mater.*, vol. 23, no. 1, pp. 239–245, 2009, http://dx.doi.org/10.1016/j.conbuildmat.2007.12.014.

[46] S. Zhou, "Analytical model for square root increase of surface chloride concentration and decrease of chloride diffusivity," *J. Mater. Civ. Eng.*, vol. 28, no. 4, pp. 04015181, 2016, http://dx.doi.org/10.1061/(ASCE)MT.1943-5533.0001483.

[47] C. Alonso, M. Castellote, and C. Andrade, "Chloride threshold dependence of pitting potential of reinforcements," *Electrochim. Acta*, vol. 47, no. 21, pp. 3469–3481, 2002, http://dx.doi.org/10.1016/S0013-4686(02)00283-9.

[48] M. Shekarchi, A. Bonakdar, M. Bakhshi, A. Mirdamadi, and B. Mobasher, "Transport properties in metakaolin blended concrete," *Constr. Build. Mater.*, vol. 24, no. 11, pp. 2217–2223, 2010, http://dx.doi.org/10.1016/j.conbuildmat.2010.04.035.

[49] F. Farmani, B. Bonakdarpour, and A. A. Ramezanianpour, "pH reduction through amendment of cement mortar with silica fume enhances its biological treatment using bacterial carbonate precipitation," *Mater. Struct.*, vol. 48, no. 10, pp. 3205–3215, 2015, http://dx.doi.org/10.1617/s11527-014-0391-7.

[50] F. Han and Z. Zhang, "Hydration, mechanical properties and durability of high-strength concrete under different curing conditions," *J. Therm. Anal. Calorim.*, vol. 132, no. 2, pp. 823–834, 2018, http://dx.doi.org/10.1007/s10973-018-7007-3.

[51] A. Hajibabaee, M. K. Moradllo, A. Behravan, and M. T. Ley, "Quantitative measurements of curing methods for concrete bridge decks," *Constr. Build. Mater.*, vol. 162, pp. 306–313, 2018, http://dx.doi.org/10.1016/j.conbuildmat.2017.12.020.

[52] M. Shakouri, D. Trejo, and P. Gardoni, "A probabilistic framework to justify allowable admixed chloride limits in concrete," *Constr. Build. Mater.*, vol. 139, pp. 490–500, 2017, http://dx.doi.org/10.1016/j.conbuildmat.2017.02.053.

[53] F. Biondini and D. M. Frangopol, "Probabilistic limit analysis and lifetime prediction of concrete structures," *Struct. Infrastruct. Eng.*, vol. 4, no. 5, pp. 399–412, 2008, http://dx.doi.org/10.1080/15732470701270157.

[54] A. Alipour, B. Shafei, and M. S. Shinozuka, "Capacity loss evaluation of reinforced concrete bridges located in extreme chloride-laden environments," *Struct. Infrastruct. Eng.*, vol. 9, pp. 8–27, 2013, http://dx.doi.org/10.1080/15732479.2010.525243.

[55] D. Curran, M. Cross, and B. A. Lewis, "A preliminary analysis of boundary element methods applied to parabolic partial differential equations," in *New Developments in Boundary Element Methods*, C. A. Brebbia, Ed., Southampton: Comput. Mech. Publ., 1980.

[56] L. C. Wrobel and C. A. Brebbia, "A formulation of the boundary element method for axisymmetric transient heat conduction," *Int. J. Heat Mass Transfer*, vol. 24, no. 5, pp. 843–850, 1981, http://dx.doi.org/10.1016/S0017-9310(81)80007-5.

[57] L. C. Wrobel and C. A. Brebbia, "The dual reciprocity boundary element formulation for nonlinear diffusion problems," *Comput. Methods Appl. Mech. Eng.*, vol. 65, no. 2, pp. 147–164, 1987, http://dx.doi.org/10.1016/0045-7825(87)90010-7.

[58] H. S. Carslaw and J. C. Jaeger, *Conduction of Heat in Solids*, 2nd ed. Oxford: Clarendon Press, 1959.

[59] P. T. Cristensen and M. J. Baker, *Structural Reliability Theory and its Applications*. Berlin: Springer Science & Business Media, 2012.

[60] R. McGee, "Modelling of durability performance of tasmanian bridges," in *ICASP8 Applications of Statistics and Probability in Civil Engineering, vol. 1*, R. E. Melchers and M. G. Stewart, Eds., Rotterdam: Balkema, 1999, pp. 297-306.

[61] D. P. Bentz, J. R. Clifton, and K. A. Snyder, "Predicting service life of chloride-exposed reinforced concrete," *Concr. Int.*, vol. 18, no. 12, pp. 42–47, 1996.

Rev. IBRACON Estrut. Mater., vol. 13, no. 4, e13409, 2020

21/26

APPENDIX A: SINGULARITY SUBTRACTION TECHNIQUE EXPRESSIONS

The singularity subtraction technique is utilized to regularize the kernel u^*. Then, the integration by parts of kernel u^* as a function of time results in:

$$U_I^*\left(\underline{\xi},\underline{x}\right)=\int_{t_0^k}^{t_f^k}u^*\left(\underline{\xi},\underline{x},t_F,t\right)dt=\frac{1}{4\pi\kappa}\left\{E_I\left[\frac{r^2}{4\kappa\left(t_F-t_0^k\right)}\right]-E_I\left[\frac{r^2}{4\kappa\left(t_F-t_f^k\right)}\right]\right\}=\frac{1}{4\pi\kappa}\left\{E_I\left(a_0^k\right)-E_I\left(a_f^k\right)\right\} \tag{A.1}$$

where E_I is the exponential-integral function $E_I(z)=\int_z^\infty\frac{e^{-t}}{t}dt$ and a_f^k and a_0^k are as follows:

$$a_f^k=\frac{r^2}{4\kappa\left(t_F-t_f^k\right)} \tag{A.2}$$

$$a_0^k=\frac{r^2}{4\kappa\left(t_F-t_0^k\right)} \tag{A.3}$$

The singularity is observed in U_k^* when k = 1, i.e., in the first time step. Moreover, singularity is also observed when the source point approaches to the field point, i.e., when r → 0. Thus, when k = 1, Equation A.1 becomes:

$$U_I^*\left(\underline{\xi},\underline{x}\right)=\frac{1}{4\pi\kappa}\left[E_I\left(a_0^I\right)-E_I\left(a_f^I\right)\right] \tag{A.4}$$

The variables a_f^k and a_0^k always assume non-negative values because $\kappa>0$, $r\geq0$ and $t_F\geq t_f^k>t_0^k$. In Equation A.2, when r is nil and $t_f^I\to t_F$, $a_f^I\to+\infty$. Thus, the exponential-integral function is evaluated at + ∞, which results in a nil value. In Equation A.3 when r is nil, $a_0^I\to0$, because the denominator $(t_F-t_0^I)$ is always greater than zero ($t_F\geq t_f^I>t_0^I$). Thus, the exponential-integral function has nil, which results in a singularity as follows:

$$U_I^*\left(\underline{\xi},\underline{x}\right)=\frac{1}{4\pi\kappa}\left[E_I(0)-E_I(+\infty)\right]=\frac{1}{4\pi\kappa}\left[E_I(0)\right] \tag{A.5}$$

The singularity that arises in this equation is logarithmic for distinct intervals of the exponential-integral function argument, $0\leq z\leq1$ and $1<z<\infty$. Thus, the kernel containing u^* can be regularized by the following equation:

$$\int_{\Gamma_j}U_I^*\left(\underline{\xi},\underline{x}\right)d\Gamma_j=\frac{1}{4\pi\kappa}\int_{\Gamma_j}\left[E_I\left(a_0^I\right)-ln\left(a_0^{I*}\right)\right]d\Gamma_j+\frac{1}{4\pi\kappa}\int_{\Gamma_j}ln\left(a_0^{I*}\right)d\Gamma_j \tag{A.6}$$

Let ξ_0 be the dimensionless coordinate of the source point, ξ the dimensionless coordinate of the field point, x_i the real coordinate of a given point, ϕ the shape function, $\phi_{,i}$ the shape function derivative and being the Jacobian given by $J=\sqrt{\left[\phi_{,i}(\xi_0)\,x_i\right]^2}$, the real distance r between the source and the field points is calculated as follows:

$$r=r^*=|J|\varepsilon=|J|\left|\xi-\xi_0\right| \tag{A.7}$$

Rev. IBRACON Estrut. Mater., vol. 13, no. 4, e13409, 2020

22/26

where $\varepsilon = |\xi - \xi_0|$ is the dimensionless distance between the source and field points. Substituting $d\Gamma = Jd\xi$ in Equation A.6 gives:

$$\int_{\Gamma_j} U_I^* (\underline{\xi}, \underline{x}) d\Gamma_j = \frac{1}{4\pi\kappa} \int_{-1}^{1} E_I\left(a_0^I\right)\phi(\xi)J(\xi)d\xi - \frac{1}{4\pi\kappa}\int_{-1}^{1} \ln\left(a_0^{I*}\right)\phi(\xi_0)J(\xi_0)d\xi + \frac{1}{4\pi\kappa}\int_{-1}^{1} \ln\left(a_0^{I*}\right)\phi(\xi_0)J(\xi_0)d\xi \tag{A.8}$$

where:

$$a_0^{I*} = \frac{\left(r^*\right)^2}{4\kappa\left(t_F - t_0^I\right)} = \frac{\left(|J(\xi_0)||\varepsilon|\right)^2}{4\kappa\left(t_F - t_0^I\right)} \tag{A.9}$$

In Equation A.8, the first two integrals on the right side are bounded and no longer singular. Then, they are numerically evaluated by the Gauss-Legendre quadrature. The last integral is evaluated analytically, being called integral I:

$$I = \frac{1}{4\pi\kappa}\int_{-1}^{1} \ln\left(a_0^{I*}\right)\phi(\xi_0)J(\xi_0)d\xi \tag{A.10}$$

The change of the integration domain from $d\xi$ to $d\varepsilon$ and consequently the integration intervals, gives:

$$I = \frac{1}{4\pi\kappa}\int_{-1-\xi_0}^{1-\xi_0} \ln\left[\frac{\left(|J(\xi_0)||\varepsilon|\right)^2}{4\kappa\left(t_F - t_0^I\right)}\right]\phi(\xi_0)J(\xi_0)d\varepsilon \tag{A.11}$$

For simplicity, considering $t_0^I = 0$, one obtains:

$$I = \frac{1}{4\pi\kappa}\int_{-1-\xi_0}^{1-\xi_0} 2\ln\left(|J(\xi_0)||\varepsilon|\right)\phi(\xi_0)J(\xi_0)d\varepsilon - \frac{1}{4\pi\kappa}\int_{-1-\xi_0}^{1-\xi_0} \ln\left(4\kappa t_F\right)\phi(\xi_0)J(\xi_0)d\varepsilon \tag{A.12}$$

Because of the singular kernel present in Equation A.12, the integral must be evaluated in the Cauchy principal (CPV) sense. Then:

$$CPV = \lim_{\varepsilon \to 0}\left\{\frac{1}{4\pi\kappa} + \frac{1}{4\pi\kappa}\int_{+\varepsilon}^{1-\xi_0} 2\ln\left(|J(\xi_0)||\varepsilon|\right)\phi(\xi_0)J(\xi_0)d\varepsilon - \frac{1}{4\pi\kappa}\int_{-1-\xi_0}^{-\varepsilon} \ln\left(4\kappa t_F\right)\phi(\xi_0)J(\xi_0)d\varepsilon - \frac{1}{4\pi\kappa}\int_{+\varepsilon}^{1-\xi_0} \ln\left(4\kappa t_F\right)\phi(\xi_0)J(\xi_0)d\varepsilon\right\} \to$$

$$CPV = \lim_{\varepsilon \to 0}\left\{\frac{1}{4\pi\kappa}\phi(\xi_0)J(\xi_0)\left[\int_{-1-\xi_0}^{-\varepsilon} 2\ln\left(|J(\xi_0)||\varepsilon|\right)d\varepsilon + \int_{+\varepsilon}^{1-\xi_0} 2\ln\left(|J(\xi_0)||\varepsilon|\right)d\varepsilon - \int_{-1-\xi_0}^{-\varepsilon} \ln\left(4\kappa t_F\right)\phi(\xi_0)J(\xi_0)d\varepsilon - \int_{+\varepsilon}^{1-\xi_0} \ln\left(4\kappa t_F\right)d\varepsilon\right]\right\} \tag{A.13}$$

To evaluate the terms of Equation A.13 properly, they are written in separated form, from I_1 to I_4 as follows:

$$CPV = \lim_{\varepsilon \to 0}\left\{\frac{1}{4\pi\kappa}\phi(\xi_0)J(\xi_0)\left[I_1 + I_2 - (I_3 + I_4)\right]\right\} \tag{A.14}$$

Thus, evaluating I_1 one has:

$$I_1 = 2\Big[\varepsilon\ln\big(\big|J(\xi_0)\varepsilon\big|\big)\Big]_{-1-\xi_0}^{-\varepsilon} = 2\Big\{-\varepsilon\ln\big(\big|J(\xi_0)\varepsilon\big|\big)+\varepsilon-\Big[(-1-\xi_0)\ln\big(\big|J(\xi_0)(-1-\xi_0)\big|\big)+1+\xi_0\Big]\Big\} \tag{A.15}$$

Thus, evaluating I_2 one has:

$$I_2 = 2\Big[\varepsilon\ln\big(\big|J(\xi_0)\varepsilon\big|\big)\Big]_{\varepsilon}^{1-\xi_0} = 2\Big\{(1-\xi_0)\ln\big(\big|J(\xi_0)(1-\xi_0)\big|\big)-1+\xi_0-\Big[\varepsilon\ln\big(\big|J(\xi_0)\varepsilon\big|\big)-\varepsilon\Big]\Big\} \tag{A.16}$$

Then, evaluating I_3 one has:

$$I_3 = \ln\big(4\kappa t_F\big)\big[-\varepsilon+1+\xi_0\big] \tag{A.17}$$

Then, evaluating I_4 one has:

$$I_4 = \ln\big(4\kappa t_F\big)\big[1-\xi_0-\varepsilon\big] \tag{A.18}$$

Adding I_1 and I_2 one obtains:

$$I_1+I_2 = 2\Big\{-\varepsilon\ln\big(\big|J(\xi_0)\varepsilon\big|\big)+\varepsilon+(1+\xi_0)\ln\big(\big|J(\xi_0)(-1-\xi_0)\big|\big)-1-\xi_0+(1-\xi_0)\ln\big(\big|J(\xi_0)(1-\xi_0)\big|\big)-1+\xi_0-\varepsilon\ln\big(\big|J(\xi_0)\varepsilon\big|\big)+\varepsilon\Big\}\rightarrow$$

$$I_1+I_2 = 2\Big\{-2\varepsilon\ln\big(\big|J(\xi_0)\varepsilon\big|\big)+2\varepsilon-2+(1+\xi_0)\ln\big(\big|J(\xi_0)(-1-\xi_0)\big|\big)+(1-\xi_0)\ln\big(\big|J(\xi_0)(1-\xi_0)\big|\big)\Big\} \tag{A.19}$$

Adding I_3 and I_4 one obtains:

$$I_3+I_4 = \ln\big(4\kappa t_F\big)\big[-\varepsilon+1+\xi_0+1-\xi_0-\varepsilon\big]=\ln\big(4\kappa t_F\big)\big[-2\varepsilon+2\big] \tag{A.20}$$

By applying the L'Hôpital's theorem one obtains:

$$\lim_{\varepsilon\to 0}\big\{\varepsilon\ln\big(J(\xi_0)\varepsilon\big)\big\}=0 \tag{A.21}$$

Therefore, the limit of Equation A.14 is achieved as follows:

$$CPV = \frac{1}{4\pi\kappa}\phi(\xi_0)J(\xi_0)\Big\{-4+2(1+\xi_0)\ln\big(\big|J(\xi_0)(-1-\xi_0)\big|\big)+2(1-\xi_0)\ln\big(\big|J(\xi_0)(1-\xi_0)\big|\big)-2\ln\big(4\kappa t_F\big)\Big\} \tag{A.22}$$

Consequently:

$$CPV = \frac{1}{2\pi\kappa}\phi(\xi_0)J(\xi_0)\Big\{-2+(1+\xi_0)\ln\big(\big|J(\xi_0)(-1-\xi_0)\big|\big)+(1-\xi_0)\ln\big(\big|J(\xi_0)(1-\xi_0)\big|\big)-\ln\big(4\kappa t_F\big)\Big\} \tag{A.23}$$

Rev. IBRACON Estrut. Mater., vol. 13, no. 4, e13409, 2020

24/26

It is worth mentioning that Equation A.23 is valid for discontinuous elements, i.e., when the source points are not positioned at the element ends $\xi_0 = \pm 1$. When continuous elements are utilized, the finite part of Equation A.23) is evaluated, leading to the following:

$$CPV = \frac{1}{2\pi\kappa}\phi(\xi_0)J(\xi_0)\left\{-2 + 2\ln\left(\left|2J(\xi_0)\right|\right) - \ln\left(4\kappa t_F\right)\right\}$$

(A.24)

APPENDIX B: CONVERGENCE ANALYSIS FOR MONTE CARLO SIMULATIONS

This appendix presents the convergence analysis for the probabilistic modelling. Particularly, the application 3 is accounted, which is the complex case handled in this study. Figures 18, 19 and 20 illustrate the convergence analysis. These figures demonstrate that the range sampling of 10,000 is sufficient for describing the assessment space.

Because the application 3 is complex than application 2, the same range of sampling is sufficient for describing the assessment space of the latter application.
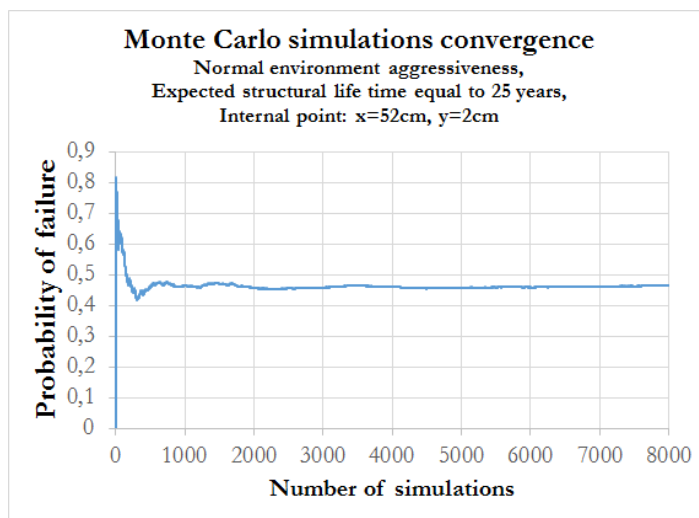
Figure 18 – Convergence analysis for x = 52 cm, y = 2 cm and t = 25 years.
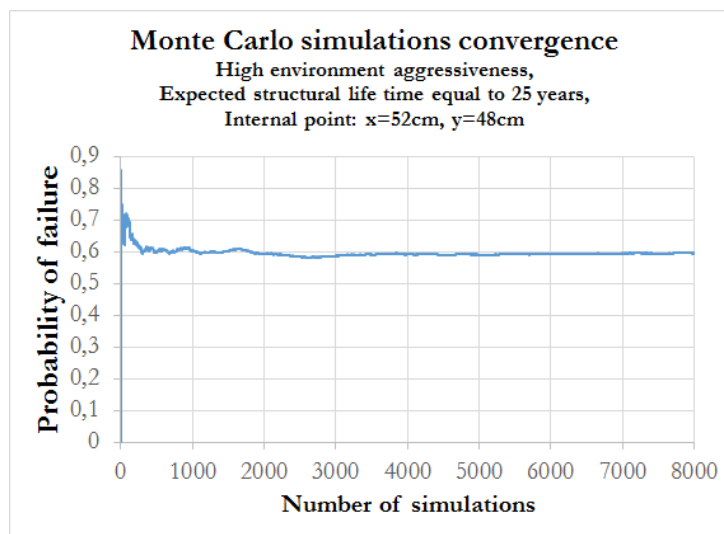
Figure 19 – Convergence analysis for x = 52 cm, y = 48 cm and t = 25 years.

Rev. IBRACON Estrut. Mater., vol. 13, no. 4, e13409, 2020

25/26
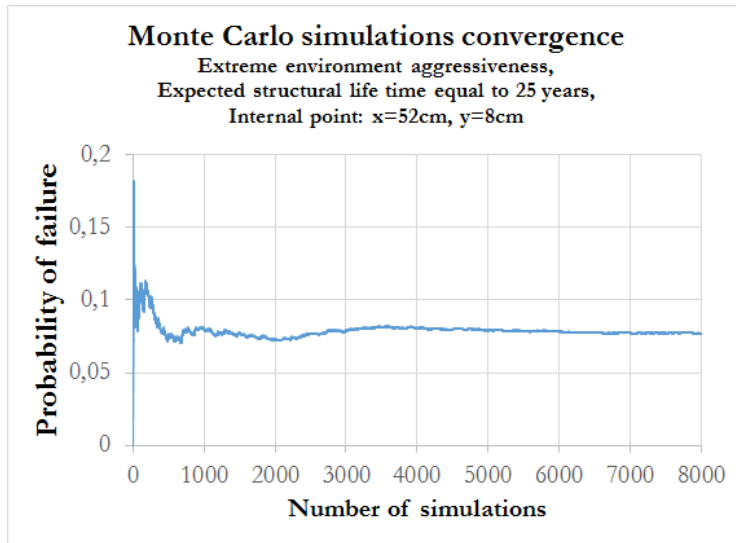
Figure 20 – Convergence analysis for x = 52 cm, y = 8 cm and t = 25 years.

Rev. IBRACON Estrut. Mater., vol. 13, no. 4, e13409, 2020

26/26

IBRACON Structures and Materials Journal
Revista IBRACON de Estruturas e Materiais

ORIGINAL ARTICLE

Predicting the mechanical properties of lightweight aggregate concrete using finite element method

Determinação de propriedades mecânicas de concreto com agregado leve via método dos elementos finitos

Aldemon Lage Bonifácio[a]
Julia Castro Mendes[b]
Michèle Cristina Resende Farage[a]
Flávio de Souza Barbosa[a]
Anne-Lise Beaucour[c]

[a]Universidade Federal de Juiz de Fora – UFJF, Departamento de Mecânica Aplicada e Computacional, Juiz de Fora, MG, Brasil
[b]Universidade Federal de Ouro Preto – UFOP, Departamento de Engenharia Civil, Ouro Preto, MG, Brasil
[c]Université de Cergy-Pontoise, Département de Génie Civil, Cergy-Pontoise, France

Abstract: The compressive strength (f_c) and Young's modulus (E_c) of concretes are properties of great importance in civil engineering problems. To this day, despite the relevance of the subject, concretes are still designed based on charts and empirical formulae. This scenario is even more imprecise for lightweight aggregate concretes (LWAC), which contain less design methodologies and case studies available in the literature. In this sense, the present work presents a numerical simulation for predicting the properties of LWAC's specimens using the Finite Element Method. The material was considered as biphasic, comprising lightweight aggregates and the enveloping mortar. Each phase was modelled with its own compressive strength, tensile strength and Young's modulus. The achieved numerical results for f_c and E_c were compared with their experimental counterparts, obtained from the literature. In total, 48 concrete formulations were assessed. Numerical results showed fair agreement with the experimental data. In general, the Mean Absolute Percentage Error (MAPE) was lower for the shale aggregates for both Young's modulus (1.75% versus 4.21% of expanded clay) and compressive strength (4.19% versus 9.89% of expanded clay). No clear trend of error was identified in relation to the aggregate proportion or to the mortar types, in which the MAPE varied from 2.36% to 8.13%. In conclusion, the simplification to spherical aggregates has shown satisfactory results, as has the adoption of a 2D model, which require less computational resources. Results encourage further applications with more complex geometrical aspects to improve the mix design and safety of LWAC.

Keywords: lightweight aggregate concrete, finite element method, prediction of compressive strength, prediction of elastic modulus.

Resumo: A resistência à compressão (fc) e o módulo de elasticidade (Ec) de concretos são propriedades de grande importância em problemas de engenharia civil. Até o presente momento, apesar da relevância do tema, o traço de concretos ainda é projetado com base em métodos gráficos e fórmulas empíricas. Esse cenário é ainda mais impreciso para concretos leves estruturais de agregados leves (LWAC), que possuem ainda menos metodologias de traço e estudos de caso disponíveis na literatura. Dessa forma, este trabalho apresenta uma simulação numérica para prever as propriedades de corpos de prova de LWAC usando o Método dos Elementos Finitos. O material foi considerado bifásico, incluindo os agregados leves e a argamassa envolvente. Cada fase foi modelada com sua própria resistência à compressão, resistência à tração e módulo de elasticidade. Os resultados numéricos obtidos para fc e Ec foram comparados com seus equivalentes experimentais, obtidos da literatura. No total 48 traços de concreto foram investigados. Os resultados numéricos mostraram uma correlação satisfatória com os dados experimentais. Em geral, o erro médio percentual absoluto (MAPE) foi menor nos agregados de xisto para o módulo de elasticidade (1,75% contra

4,21% da argila expandida) e resistência à compressão (4,19% contra 9,89% da argila expandida). Não foi identificada uma tendência clara de erro em relação à proporção de agregado ou aos tipos de argamassa, nos quais o MAPE variou de 2,36% a 8,13%. Concluindo, a simplificação para agregados esféricos mostrou resultados satisfatórios, assim como a adoção de um modelo 2D, que requer menos recursos computacionais. Os resultados encorajam outras aplicações com aspectos geométricos mais complexos para melhorar o design e a segurança de estruturas de LWAC.

Keywords: concreto com agregado leve, método dos elementos finitos, previsão de resistência a compressão, previsão de módulo de elasticidade.

1 INTRODUCTION

The concrete's compressive strength and Young's modulus are the main mechanical properties that will influence the design, cost, and safety of concrete structures. However, the proportion of materials (or mix design) of concrete is nowadays still performed through charts and empirical formulae [1] [2].

This scenario is even more imprecise for structural lightweight aggregate concretes (LWAC), which uses lightweight aggregates (LWA) in their composition. Common LWAs include pumice and expanded clay, shale or slate, usually manufactured in rotary kilns. This fabrication method generates a material more porous than conventional rock-mined aggregates. Due to their high porosity, they have bulk density lower than 1120 kg/m^3 [3], what reduces the specific weight of LWAC to below 2000 kg/m^3 [4]. Nowadays LWAC is used on a large scale to reduce the self-weight of structures [5]. It also presents transport advantages, allows longer spans and promotes thermoacoustic insulation [6] [7].

Several properties of the aggregates affect the mechanical behavior of concrete – e.g., bulk and specific density, particle shape and texture, particle size distribution, porosity, friability, compressive strength, Young's modulus, chemical composition, among others [8] [2]. Regarding LWA specifically, their absorbent structure allows the use of saturated LWA as an internal reservoir to release water as the concrete cures. This phenomenon promotes to the LWAC a reduced autogenous shrinkage; an increased mechanical interlocking between the matrix and the LWA; and, thus, a negligible interfacial transition zone due to internal curing [9] [10] [11].

In conventional concretes, the aggregate has a higher compressive strength than the mortar and the interfacial transition zone is the weak spot of the composite. Conversely, in LWAC, the aggregate's relatively low strength is the main factor controlling the concrete's fracture [12] [13]. But just like conventional concretes, the mix design of LWAC is based on limited empirical charts and formulae; and its mechanical properties are generally obtained by cost-demanding testing of specimens after a standard curing period of 28 days.

1.1 Justification

Since mechanical tests usually demand a significant amount of material and personnel for preparing the specimens and the results are only known after several weeks, several researchers have been studying numerical solutions to evaluate the concrete's properties prior to its mixing [14] [15] [16]. These initiatives have the potential to avoid structural issues in the construction, to reduce labor costs, and to decrease material waste in the laboratory.

To this purpose, some works applied Artificial Intelligence to predict the mechanical properties of LWAC. These are the cases of Altun et al. [17], Alshihri et al. [18], and a previous work by the authors [19], who used neural networks. Although a fast and reliable technique [19], neural networks provide only one single final result based on multiple variables. They do not evaluate the behavior of the concrete during the compressive test, as does the Finite Element Method (FEM), for example. Furthermore, the application of algorithms of Artificial Intelligence normally demands a robust database with a large number of experimental results relating the studied property to its respective mix design formulation.

The same limitations hold for analytical models and regression equations, as the ones developed by Bogas and Gomes [11], Cui et al. [20], and Barbosa et al. [21]. Additionally, the vast majority of prediction studies only focus on compressive strength, neglecting the modulus of elasticity, an imperative property in the design of lightweight structures.

In this sense, seeking to improve the comprehension of LWAC's mechanical properties, the present work presents a numerical simulation of the compressive behavior of LWAC's samples using FEM. It assumes the LWAC as a biphasic composite, composed of mortar and sphere-shaped lightweight aggregates (LWA). An assessment of this methodology is carried out by comparing the achieved numerical results for Young's modulus and compressive strength with their experimental counterparts obtained from the literature. The generalization capacity of the presented method

is evaluated through the simulation of 48 concrete formulations, including all possible combinations of three types of mortars, four types of aggregates and four different aggregate proportions.

2 MATERIALS AND EXPERIMENTAL PROGRAM

2.1 Materials

The experimental data used as input and for validation were obtained from an experimental study with cylindrical samples of LWAC. The tests were performed by Ke et al. [22] [23], who analyzed the compressive strength and modulus of elasticity of LWAC samples at 28 days.

In this experimental program, three types of mortars were used: normal (40 MPa), high performance (64 MPa), and very high performance (86 MPa). Regarding the aggregates, four types were used: 4/10-550-A, 4/10-430-A, 4/10-520-S and 4/8-750-S; in which each name matches the characteristic diameters (d/D, in mm), the bulk density (kg/m^3), and the type of aggregate (A - expanded clay, S - expanded shale), respectively. The combination of these materials in proportions of 12.5%, 25.0%, 37.5% and 45.0% of LWA in volume generated 48 different formulations, and over 144 specimens were tested.

The expanded clay LWA 4/10-550-A and 4/10-430-A are nodular aggregates of quasi-spherical shape. On the other hand, the shale aggregates 4/10-520-S and 4/8-750-S are more irregulars and constituted of various types of grains corresponding to different degrees of expansion. Some typical images are shown in Figure 1.
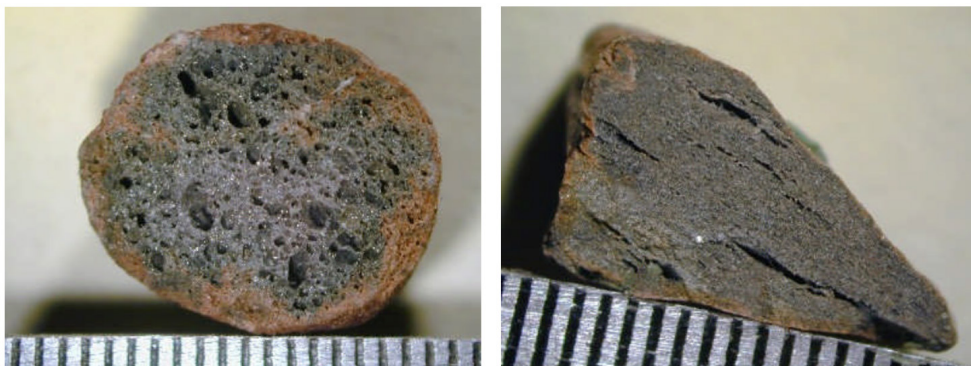
Figure 1. Typical sections of LWA [24]: a) Rounded and porous LWA, typical of expanded clay aggregates (4/10-550-A and 4/10-430-A) b) Angled and less porous LWA, corresponding to over 50% of the expanded shale aggregates (4/10-520-S and 4/8-750-S)

Table 1 presents the mass of broken/crushed grains, which are calculated based on a manual separation; and the shape index of the LWA, corresponding to the ratio between the aggregate's larger and smaller dimensions. The amount of broken/crushed grains varies significantly among the aggregate types, being on average more marked for expanded shale ones. Regarding the shape, the closer the Length/Thickness (L/T) ratio is to 1, more equidimensional and less flat will be the LWA. In this sense, the shape results confirm the visual observation (Figure 1), showing that clay aggregates usually have lower L/T values than shale ones. Within each particle size range, the larger the grain diameter is, the less spherical is its form.

Table 1 Physical and geometrical properties of aggregates [22]

	4/10-550-A	4/10-430-A	4/10-520-S	4/8-750-S
Mass of broken grains (%)	7.38	1.85	19.21	6.68
Mean ratio Length/Thickness (L/T)	1.33	1.57	1.92	2.20
Bulk Density (kg/m^3)	560.3	454.7	493.4	877.7

Table 1 also presents the LWA's bulk densities. This is one of the most important properties of this material, since it influences the dead weight of LWAC structures, and it is used to estimate the aggregate's elastic modulus and

mechanical strength by empirical relations. The studied aggregates have bulk densities ranging from 455 kg/m³ to 878 kg/m³. In average, expanded clay aggregates have lower densities than expanded shale aggregates, possibly due to their shape and pore system, which will influence other physical parameters.

Concerning the particle size distributions of the LWA, a narrow granular size distribution is observed. For 4/10-550-A, this theoretical sieve size through which 50% of the particles pass is 8.4 mm; for 4/10-430-A, 7.2 mm; for 4/10-520-S, 7.0 mm; and for 4/8-750-S, 5.4 mm. According to Ke et al. [22], the occurrence of powdery grains smaller than 2.5 mm is probably due to crushed coarser grains.

2.2 Numerical simulation

The FEM model simulated the LWAC in two phases: the mortar (m) and the LWA (a). From the aggregate's and the mortar's properties, the behavior of LWAC samples at 28 days was simulated when subjected to compressive load. The free processing software CAST3M was used, which includes built-in pre-processing and post-processing tools. CAST3M is an open source code developed by the French Atomic Energy Agency (CEA). It solves partial differential equations through the finite element method, allowing the incorporation and adaptation of models by the user. It employs a language based on object-oriented programming, named GIBIANE, and the objects are created using pre-defined operators, written in the language ESOPE [25].

The parameters used in the FEM simulation were:

- Compressive strength (f_m) and Young's modulus (E_m) of the mortar matrix (experimentally obtained by Ke et al. [23]);
- Tensile strength (t_m) of the mortar, based on empirical correlations with its compressive strength proposed by Chust and Figueiredo [26];
- Volume fraction of lightweight aggregate adopted in the concrete's mixture (12.5%, 25.0%, 37.5% and 45.0%);
- Particle size distribution of the aggregates [24];
- Young's modulus of the LWA (E_a), obtained empirically, based on its dry density [23];
- Compressive strength of the LWA (f_a), obtained in an analytical inverse method by Ke et al. [23].
- Tensile strength (t_a) of the LWA, from [22];
- For comparison purposes, compressive strength ($f_{c,exp}$) and Young's modulus ($E_{c,exp}$) measured on hardened LWAC samples [23];

The FEM model considers a longitudinal cross-section of a standard cylindrical sample with 16 cm of diameter and 32 cm high (Figure 2). For computational efficiency, 1/4 of the section was used in this work, considering the boundary conditions of geometric symmetry of the sample. In this specimen, the LWA were modeled as perfect spheres randomly distributed within the homogeneous mortar matrix (Figure 3), with the same particle size distribution as the experimental program. The procedure to create 2D models from 3D spheres with the proper particle size distribution adopts image processing techniques described in references [27] and [28].
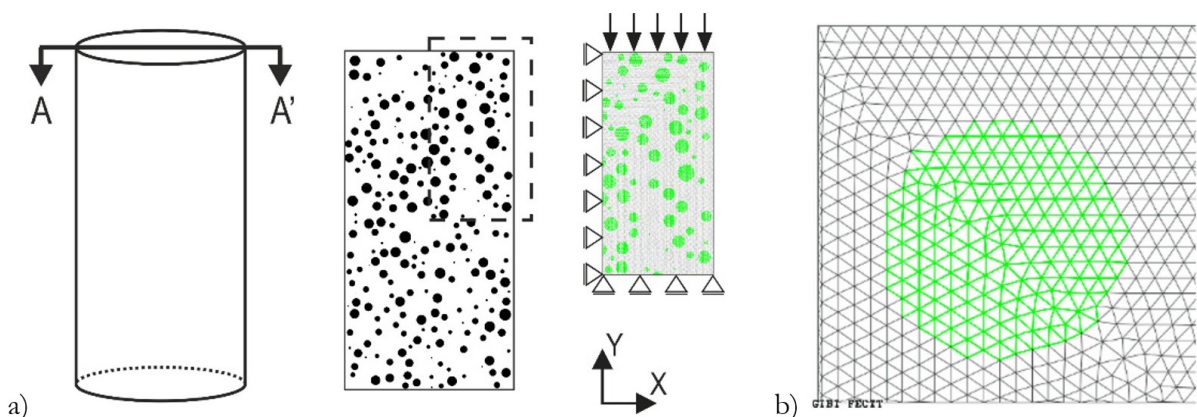
Figure 2 Numerical representation of one LWAC sample: (a) The geometry of the modeled LWAC sample (16-cm diameter and 32-cm height), from which a middle cross section was used; (b) Typical FE triangle mesh used; the round green circle representing the aggregate, surrounded by the mortar, in grey
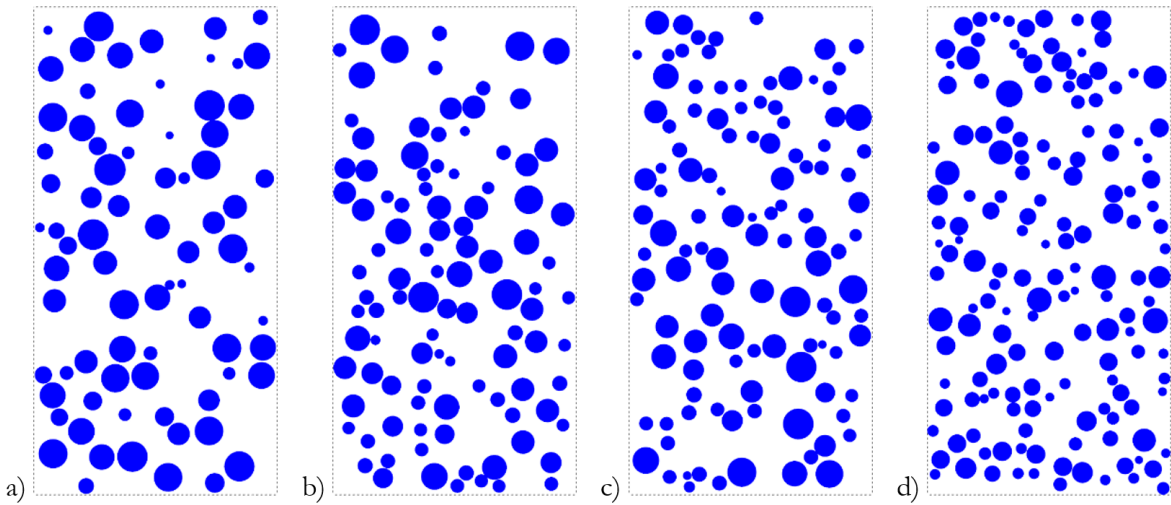
Figure 3 Examples of the longitudinal section of samples containing 25% of aggregates and following the particle size distribution of each type: (a) 4/10-550-A (b) 4/10-430-A (c) 4/10-520-S (d) 4/8-750-S

The authors highlight that an actual plane stress case would require prismatic samples. By using cylindrical samples, errors arising from this approach are reduced in the central region, marked with a hatch in Figure 4. The present work considers this area in the computational modeling. This geometric simplification was necessary due to the high level of processing cost demanded by a 3D model. This sensitivity analysis was performed by the authors [29], who observed similar results between the 2D and 3D simulations, with the latter taking 98 times longer.
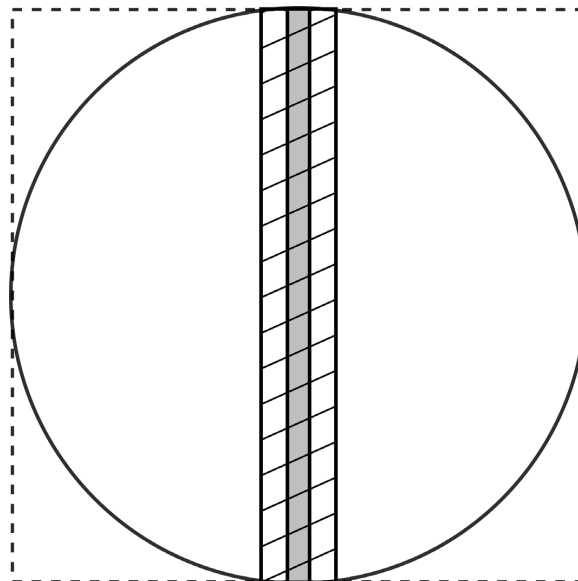
Figure 4 Top view of the cylindrical specimen. The hatched area representing where a plane stress simplification would incur in less distortions. The grey area corresponds in scale to the thickness adopted by the model.

Additionally, even in a 2D domain, the processor traditionally adopts a unit thickness to the modelled plane. However, the extrusion of circles from the 2D domain to 3D is a cylinder, and not a sphere. To reduce this imprecision, instead of a unit thickness, we adopted a value (t) that would keep constant the volume of the maximum aggregate diameter (1cm). By relating the spherical volume of the maximum aggregate diameter with the thickness of its respective cylindrical extrusion (Equation 1), a model thickness of 0.667 cm was adopted (Figure 4).

A. L. Bonifácio, J. C. Mendes, M. C. R. Farage, F. S. Barbosa, and A. L. Beaucour

$$\frac{4}{3}\pi\left(\frac{1}{2}\right)^3 = \pi\left(\frac{1}{2}\right)^2 t \tag{1}$$

For both expanded clay and shale aggregates, the same strategy was applied, which considers the LWA's geometry as perfect spheres. The effectiveness of this choice will be discussed further on. To account for the dispersion of results, three models with random aggregate scattering (within the real particle size distribution) were generated from each synthetic sample.

An elastoplastic material behavior was adopted for the FEM simulations, with Drucker-Prager yield criterion [25]. Limits for compressive and tensile strength for each material were assumed according to the input parameters, and a perfect plastic yield was considered. The materials properties of aggregates and mortar adopted for the simulation and validation of these models are shown in Table 2 and Table 3, respectively.

Table 2 Properties of the aggregates used in the numerical simulation

Aggregates	4/10-550-A		4/10-430-A		4/10-520-S		4/8-750-S	
Parameter	Mean	Std.Dv.	Mean	Std.Dv.	Mean	Std.Dv.	Mean	Std.Dv.
E_a (GPa)	9.88	1.99	8.26	1.05	11.30	1.20	25.11	4.72
f_a (MPa)	23.40	5.93	19.90	4.26	28.33	6.74	53.43	17.68
t_a (MPa)	3.08	0.78	2.04	0.44	2.59	0.62	6.67	2.21
$E_{c,exp}$ (GPa)	23.58	4.53	22.42	4.15	24.24	4.22	29.97	3.35
$f_{c,exp}$ (MPa)	39.70	10.36	37.35	10.00	44.92	12.07	58.47	14.71

Where E_a - LWA's Young's modulus; E_m - Mortar's Young's modulus; f_a - LWA's compressive strength; f_m - Mortar's compressive strength; t_a - LWA's tensile strength; t_m - Mortar's tensile strength; $E_{c,exp}$ - LWAC's Young's modulus; $f_{c,exp}$ - LWAC's compressive strength.

Table 3 Properties of the mortars used in the numerical simulation

Mortars	Normal		High Performance		Very High Performance	
Parameter	Mean	Std. Dev.	Mean	Std. Dev.	Mean	Std. Dev.
E_m (GPa)	28.59	1.16	33.18	0.68	35.40	0.46
f_m (MPa)	40.18	1.17	64.18	0.83	85.96	2.42
t_m (MPa)	3.52	0.33	4.42	0.19	4.98	0.50
$E_{c,exp}$ (GPa)	21.34	3.84	31.93	4.57	27.30	4.86
$f_{c,exp}$ (MPa)	33.72	5.98	43.85	9.87	55.89	14.92

Where E_m - Mortar's Young's modulus; f_m - Mortar's compressive strength; t_m - Mortar's tensile strength; $E_{c,exp}$ - LWAC's Young's modulus; $f_{c,exp}$ - LWAC's compressive strength.

To simulate the compressive strength test, a downward linear displacement of 0.5 mm was incrementally imposed on the upper surface up to 3.0‰ strain, which relates to the maximum stress value in a typical stress-strain curve obtained from a concrete sample. The compressive stress values were evaluated from the support conditions at the base of the sample.

In addition, to evaluate the performance results, the statistical parameter Mean Absolute Percentage Error (MAPE) was employed according to the mathematical definition given by Equation 2, where n is the number of samples, y_i is the experimental value and p_i is the numerical value.

$$MAPE = \frac{1}{n}\sum_{i=1}^{n}\left(\left|\frac{y_i - p_i}{y_i}\right|\right) \tag{2}$$

The MAPE statistical metric is dimensionless and provides an effective means of residual error compared to each observed value with their respective numerical value. The lower the MAPE values, the better the performance of the numerical model.

Another statistical parameter used in this work is the Pearson correlation coefficient (r), defined by Equation 3, which measures the power of association between two variables. It is dependent on the linear relationships between the numerical and experimental values. The closer the r value is to 1, the better the association between the experimental and numerical values.

$$r = \left(\frac{\sum_{i=1}^{n} \left[(y_i - \overline{y})(p_i - \overline{p}) \right]}{\sqrt{\sum_{i=1}^{n} (y_i - \overline{y})^2 \sum_{i=1}^{n} (p_i - \overline{p})^2}} \right) \tag{3}$$

where n is the number of samples, y_i is the experimental value, $\overline{y}$ is the mean of experimental values, p_i is the numerical value and $\overline{p}$ is the mean of numerical values.

3 RESULTS AND DISCUSSIONS

Table 4 presents the mean results, standard deviations and MAPE of the numerical simulations of LWAC for each type of aggregate for the studied mechanical properties: Young's modulus (E_c) and compressive strength (f_c). When evaluating the MAPE, it is observed that the smallest error was obtained for the aggregate 4/8-750-S (0.24% for E_c and 3.62% for f_c), and the most substantial error was obtained by aggregate 4/10-430-A (4.57% for E_c and 11.19% for f_c). The r values for the four aggregates and both mechanical properties were higher than 0.9677, which indicates that there is a robust correlation between the experimental and numerical results.

Table 4 Numerical results of the mechanical properties (Young's modulus, E_c; and compressive strength, f_c) for each aggregate type; including MAPE and Pearson correlation coefficient (r) statistical parameters.

Parameter	E_c (GPa)				f_c (MPa)			
Aggregates	Mean	Std. Dev	MAPE	r	Mean	Std. Dev	MAPE	r
4/10-550-A	22.69	4.44	3.84%	0.9970	40.23	12.69	8.58%	0.9699
4/10-430-A	21.50	4.44	4.57%	0.9973	39.39	12.78	11.19%	0.9677
4/10-520-S	23.44	4.02	3.26%	0.9964	45.04	13.13	4.76%	0.9860
4/8-750-S	29.98	3.41	0.24%	0.9995	60.16	16.17	3.62%	0.9974

Figure 5 shows the numerical and experimental results of the LWAC properties represented in boxplot graphs. These graphs allow the visualization and evaluation of the position, dispersion, symmetry, and outliers of the data sets for each type of LWA. None of the properties presented significantly different results between the numerical and experimental values. On the left, Figure 5 shows that the quartiles of E_c are positioned slightly below the quartiles of the experimental results, except for the 4/8-750-S aggregate, although all have similar dispersions. Whereas on Figure 5 right, the quartiles of the numerical results for f_c are slightly more dispersed than the quartiles of the experimental results, without a clear tendency of underestimation or overestimation.
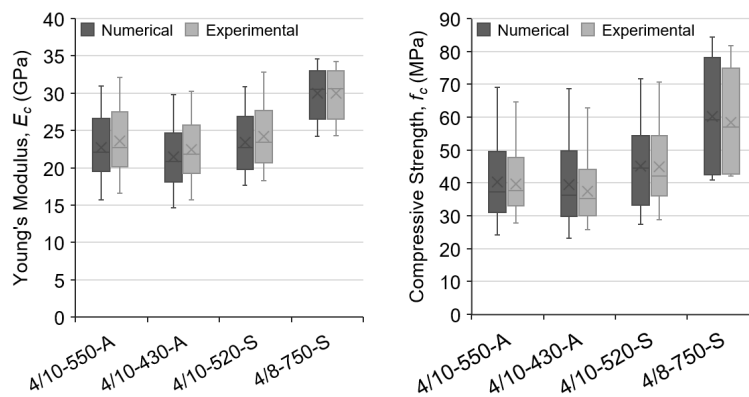
Figure 5 Numerical (dark grey) and experimental (light grey) results of the mechanical properties of LWAC for each type of LWA: left - Young's modulus; right - compressive strength.

Table 5 presents the statistical parameters MAPE and Pearson correlation coefficient (r) for Young's modulus and compressive strength properties according to the aggregate material, expanded clay (A) and expanded shale (S). The r values for the two types of aggregates in both mechanical properties were higher than 0.96, which indicates that there

is a robust correlation between the experimental and numerical results. Concerning MAPE values, results for expanded shale (S) were slightly better than those achieved for expanded clay (A). These last results indicate that, for the proposed model, the actual geometry of the LWA is not a crucial parameter. Initially, it could be expected that the rounded expanded clay aggregates (A) would incur in lower errors since the developed FE mesh considers LWA as spheres. However, uncertainties concerning the input parameters presented in Table 2, as well as imperfections in the adopted elastoplastic model, probably have an essential role in the prediction of the mechanical properties through the presented method.

Table 5 Statistical parameters of the correlation between the numerical and experimental data of each type of aggregate for Young's modulus (E_c) and compressive strength (f_c).

Parameter	E_c		f_c	
Aggregate type	r	MAPE	r	MAPE
Expanded clay (A)	0.9963	4.21%	0.9654	9.89%
Expanded shale (S)	0.9955	1.75%	0.9943	4.19%

In turn, Figure 6 shows the linear regression from the experimental and numerical data of expanded clay (A) and expanded shale (S) for Young's modulus (Figure 6 left) and compressive strength (Figure 6 right). Those graphs confirm a reliable correlation between numerical and experimental data.
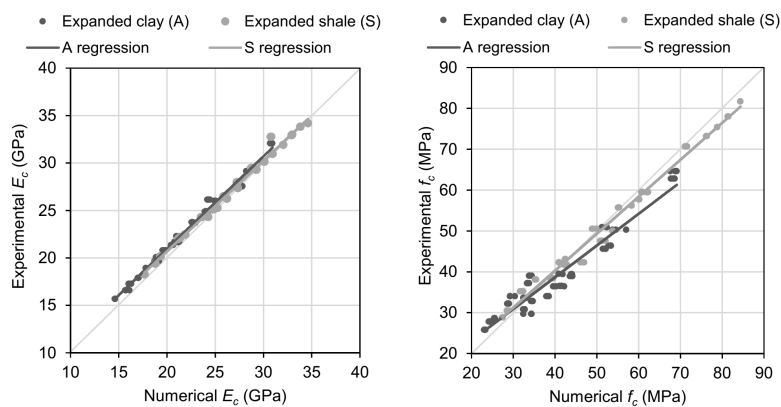
Figure 6 Comparison of the linear regression models for expanded clay (A) and expanded shale (S) aggregates and each mechanical property: left - Young's modulus; right - compressive strength.

When evaluating the numerical results according to the relative volume of the aggregates, it is observed in Table 6 that the highest MAPE value for Young's modulus (E_c) was 3.58% for 45.0% of LWA and the lowest MAPE was 2.36% for 25.0% LWA. For compressive strength (f_c), the highest MAPE value was 8.13% to 25.0% LWA, and the lowest MAPE was 6.11% to 12.5% LWA. Thus, there was no clear trend in relation to the volume of aggregates.

Table 6 Numerical results of the mechanical properties (Young's modulus, E_c; and compressive strength, f_c) for each aggregate volume; including MAPE and Pearson correlation coefficient (r) statistical parameters.

Parameter	E_c (GPa)				f_c (MPa)			
Volume	Mean	Std. Dev.	MAPE	r	Mean	Std. Dev	MAPE	r
12.5%	29.25	3.00	2.60%	0.9698	54.00	13.87	6.11%	0.9846
25.0%	26.16	3.62	2.36%	0.9973	46.56	13.18	8.13%	0.9738
37.5%	23.14	4.51	3.39%	0.9986	40.98	13.43	7.46%	0.9851
45.0%	21.66	4.92	3.58%	0.9988	38.90	12.56	6.45%	0.9886

Additionally, the standard deviations for the numerical results grouped by volume (Table 6) are very close to those grouped by aggregates (Table 2). The highest standard deviation value for Young's modulus was 4.53 GPa for the

aggregate 0/10-550-A and 4.92 GPa for 45.0% LWA; and the lowest standard deviation was 3.35 GPa for 4/8-750-S and 3.00 GPa for 12.5% LWA. On the other hand, the highest standard deviation value for compressive strength was 14.71 GPa for 4/8-750-S and 13.87 GPa for 12.5% LWA; and the lowest one was 10.00 GPa for 4/10-430-A and 12.56 GPa for 45.0% LWA. Therefore, these values indicate that the dispersion of the numerical results grouped by volume and by aggregates are very close. Thus, we conclude that our modeling has no bias concerning these parameters.

Finally, a similar analysis was performed with the numerical data grouped by mortar type (Table 7 and Figure 7). The highest MAPE value for the modulus of elasticity was 3.23%, for normal mortar (M8), and the lowest MAPE was 2.80%, for high-performance mortar (M9). For compressive strength, the highest MAPE value was 7.80% for normal mortar (M8), and the lowest MAPE was 5.96% to high-performance mortar (M9). Figure 7 shows in boxplots the experimental and numerical data of the mechanical properties grouped by mortar type, which allows the visualization of the proximity of the results predicted by the numerical models. Therefore, the assortment by mortar types also did not present a clear tendency of underestimation or overestimation; but similar mean values and dispersion.

Table 7 Numerical results of the mechanical properties (Young's modulus, E_c; and compressive strength, f_c) grouped under mortar type; including MAPE and Pearson correlation coefficient (r) statistical parameters.

Parameter	E_c (GPa)				f_c (MPa)			
Mortar Type	Mean	Std Dev	MAPE	r	Mean	Std Dev	MAPE	r
Normal (M8)	21.89	3.81	3.23%	0.9938	34.69	5.93	7.80%	0.9818
High Performance (M9)	25.44	4.38	2.80%	0.9979	44.12	10.11	5.96%	0.9780
Very High Performance (M10)	27.83	4.88	2.91%	0.9946	56.42	15.71	7.36%	0.9954
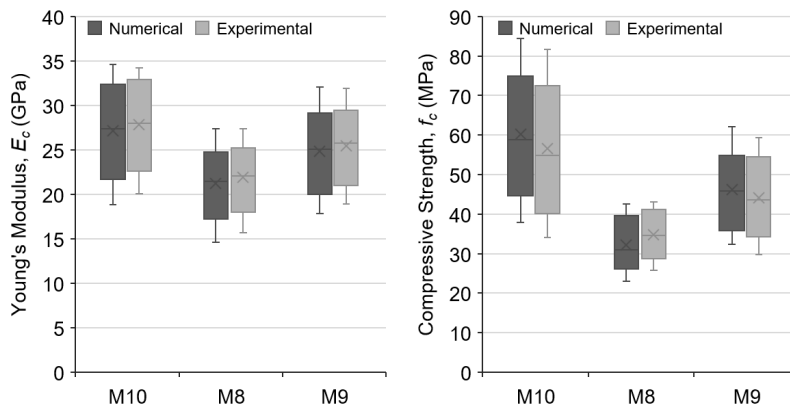
Figure 7 Numerical (dark grey) and experimental (light grey) results of the mechanical properties of LWAC grouped under mortar type (M8 - normal, M9 - high performance and M10 - very high performance): left - Young's modulus; right - compressive strength.

4 CONCLUSIONS

The present work evaluates the accuracy of a numerical FEM simulation in predicting the compressive strength and Young's modulus of LWAC. The capacity of generalization of the presented method was also investigated. To this purpose, the compressive behavior of 48 LWAC formulations was simulated, and the achieved numerical results were compared with their experimental counterparts.

Overall, a reasonable agreement was found for both analyzed mechanical properties. The larger errors for compressive strength and Young's modulus predictions were 11.19% and 4.57%, respectively, which is considered a satisfactory result. Not only the mean results but also the dispersion of the values were very similar between the numerical and experimental data. The results of the linear regression and the Pearson correlation coefficient (r) also indicate that there is a strong correlation between the experimental values and the numerical values, since the r value was greater than 0.96 for all types of aggregates and mechanical properties.

In general, the MAPE error values were lower for the irregular-shaped shale aggregates (S) for both Young's modulus (4.21% for expanded clay versus 1.75% for expanded shale) and compressive strength (9.89% for expanded

clay versus 4.19% for expanded shale). No clear trend of error was identified in relation to the volume of aggregates in the LWAC or to the mortar types.

In conclusion, the simplification to spherical aggregates (circles in the 2D model) has shown satisfactory results, despite some of the aggregates being roughly irregular. In addition, the efficacy of the 2D model, which require less computational resources and shorter simulation time, was demonstrated. This result indicates that the 2D model ensures that the aggregate volume and particle size distribution are very close to the actual percentage of the experimental specimens, and that the distortions caused by the cylindrical shape of the real specimens are negligible in the central area adopted for the simulations.

These results encourage further applications with more complex geometrical aspects to improve the mix design and safety of LWAC structures. In conclusion, the prediction of the mechanical properties by the FEM models developed here is a feasible contribution to the mixture design of LWAC.

ACKNOWLEDGEMENTS

REFERENCES

[1] K. W. Day, J. Aldred, and B. Hudson, *Concrete Mix Design, Quality Control and Specification*. Boca Raton: CRC Press, 2013.

[2] A. M. Neville and J. J. Brooks, *Concrete Technology*. Philadelphia: Trans-Atlantic Publications, 2010.

[3] American Society for Testing and Materials, *Standard Terminology Relating to Concrete and Concrete Aggregates*, ASTM C125, 2018.

[4] Associação Brasileira de Normas Técnicas, *Concrete for Structural Use – Density, Strength and Consistence Classification*, NBR 8953, 2015.

[5] W. G. Moravia, A. G. Gumieri, and W. L. Vasconcelos, "Fator de eficiência e modulo de elasticidade do concreto leve produzido com argila expandida," *Rev. IBRACON Estrut. Mater.*, vol. 3, no. 2, pp. 195-204, 2010.

[6] B. C. D. Santis and J. A. Rossignolo, "Influência dos agregados leves de argila calcinada nas propriedades mecânicas de concretos estruturais," *Materia*, vol. 20, no. 2, pp. 399–406, 2015.

[7] B. C. de Santis and J. A. Rossignolo, "Avaliação da influência de agregados leves de argila calcinada no desempenho de concretos estruturais," *Ambient. Constr.*, vol. 14, no. 4, pp. 21–32, 2014.

[8] P. Mehta and P. J. M. Monteiro, *Concrete: Microstructure, Properties, and Materials*, 2nd ed. São Paulo: IBRACON, 2014.

[9] A. Bentur, S. I. Igarashi, and K. Kovler, "Prevention of autogenous shrinkage in high-strength concrete by internal curing using wet lightweight aggregates," *Cement Concr. Res.*, vol. 31, no. 11, pp. 1587–1591, 2001.

[10] D. P. Bentz and K. A. Snyder, "Protected paste volume in concrete: Extension to internal curing using saturated lightweight fine aggregate," *Cement Concr. Res.*, vol. 29, no. 11, pp. 1863–1867, 1999.

[11] J. A. Bogas and A. Gomes, "Compressive behavior and failure modes of structural lightweight aggregate concrete–Characterization and strength prediction," *Mater. Des.*, vol. 46, pp. 832–841, 2013.

[12] M. H. Zhang and O. E. Gjvorv, "Mechanical properties of high-strength lightweight concrete," *ACI Mater. J.*, vol. 88, no. 3, pp. 240–247, 1991.

[13] C. C. Yang and R. Huang, "Approximate strength of lightweight aggregate using micromechanics method," *Adv. Cement Base. Mater.*, vol. 7, no. 3-4, pp. 133–138, 1998.

[14] I. B. Topcu and M. Sarıdemir, "Prediction of compressive strength of concrete containing fly ash using artificial neural networks and fuzzy logic," *Comput. Mater. Sci.*, vol. 41, no. 3, pp. 305–311, 2008.

[15] R. Le Roy, E. Parant, and C. Boulay, "Taking into account the inclusions' size in lightweight concrete compressive strength prediction," *Cement Concr. Res.*, vol. 35, no. 4, pp. 770–775, 2005.

[16] I. C. Yeh, "Modeling of strength of high-performance concrete using artificial neural networks," *Cement Concr. Res.*, vol. 28, no. 12, pp. 1797–1808, 1998.

[17] F. Altun, Ö. Kişi, and K. Aydin, "Predicting the compressive strength of steel fiber added lightweight concrete using neural network," *Comput. Mater. Sci.*, vol. 42, no. 2, pp. 259–265, 2008.

[18] M. M. Alshihri, A. M. Azmy, and M. S. El-Bisy, "Neural networks for predicting compressive strength of structural light weight concrete," *Constr. Build. Mater.*, vol. 23, no. 6, pp. 2214–2219, 2009.

[19] A. Bonifácio, J. Mendes, M. Farage, F. Barbosa, C. Barbosa, and A. Beaucour, "Application of Support Vector Machine and Finite Element Method to predict the mechanical properties of concrete," *Lat. Am. J. Solids Struct.*, vol. 16, no. 7, e205, 2019.

[20] H. Z. Cui, T. Y. Lo, S. A. Memon, F. Xing, and X. Shi, "Analytical model for compressive strength, elastic modulus and peak strain of structural lightweight aggregate concrete," *Constr. Build. Mater.*, vol. 36, pp. 1036–1043, 2012.

[21] F. S. Barbosa, M. C. R. Farage, A. L. Beaucour, and S. Ortola, "A Methodology to Evaluate Elastic Modulus of Lightweight-Aggregate Concrete," *ACI Mater. J.*, vol. 113, no. 1, 2016.

[22] Y. Ke, A. L. Beaucour, S. Ortola, H. Dumontet, and R. Cabrillac, "Influence of volume fraction and characteristics of lightweight aggregates on the mechanical properties of concrete," *Constr. Build. Mater.*, vol. 23, no. 8, pp. 2821–2828, 2009.

[23] Y. Ke, S. Ortola, A. L. Beaucour, and H. Dumontet, "Micro-stress analysis and identification of lightweight aggregate's failure strength by micromechanical modeling," *Mech. Mater.*, vol. 68, pp. 176–192, 2014.

[24] Y. Ke, *Caractérisation du Comportement Mécanique des Bétons de Granulats Légers: Expérience*. Cergy: Univ. Cergy-Pontoise, 2008.

[25] Commissariat a l'Energie Atomic, "Notices | cast3m - mode." 2003. http://www-cast3m.cea.fr/index.php?page=notices&notice=MODE (accessed Aug. 15, 2016).

[26] C. R. Chust and J. R. Figueiredo Fo., *Cálculo e Detalhamento de Estruturas Usuais de Concreto Armado*. São Carlos: EdUFSCar, 2004.

[27] F. S. Barbosa, M. C. R. Farage, A. L. Beaucour, and S. Ortola, "Evaluation of aggregate gradation in lightweight concrete via image processing," *Constr. Build. Mater.*, vol. 29, pp. 7–11, 2012.

[28] F. S. Barbosa, A. L. Beaucour, M. C. R. Farage, and S. Ortola, "Image processing applied to the analysis of segregation in lightweight aggregate concretes," *Constr. Build. Mater.*, vol. 25, no. 11, pp. 3375–3381, 2011.

[29] A. Bonifácio, "Estratégia computacional para avaliação de propriedades mecânicas de concreto de agregado leve," Ph.D. dissertation, Univ. Fed. Juiz de For a, Juiz de Fora, 2017.

IBRACON Structures and Materials Journal
Revista IBRACON de Estruturas e Materiais

ORIGINAL ARTICLE

Evaluation of concrete resistances: an alternative to the criteria of Brazilian standard NBR 12655 based on a Bayesian approach

Avaliação das resistências do concreto: uma alternativa aos critérios da norma brasileira NBR 12655 baseada em uma abordagem Bayesiana

Claudia Interlandi[a]
Fernando Rebouças Stucchi[b]
Luiz Fernando Campos Ramos Martha[c]
Sergio Hampshire de Carvalho Santos[d]

[a]Pontifícia Universidade Católica do Rio de Janeiro – PUC-Rio, Rio de Janeiro, RJ, Brasil
[b]Universidade de São Paulo, São Paulo, SP, Brasil
[c]Pontifícia Universidade Católica do Rio de Janeiro – PUC-Rio, Departamento de Engenharia Civil, Rio de Janeiro, RJ, Brasil
[d]Universidade Federal do Rio de Janeiro, Escola Politécnica, Departamento de Estruturas, Rio de Janeiro, RJ, Brasil

Abstract: Frequently the required concrete resistance is not attained in Brazilian constructions. Partially to circumvent this problem, a new revision of Brazilian Standard ABNT NBR 12655 was issued in 2015. This revision maintains the insufficiently stringent criteria for evaluation of the concrete compression strength in existent and under construction structures of the revision of 1996. This evaluation can be based on very few test specimens, even in the result of a single test. It is shown herein that these criteria are clearly unsafe. Alternative criteria are proposed, based in a Bayesian approach. The proposed criteria are checked against some hundred tests done on actual structures of different characteristics, bridges and buildings.

Keywords: concrete resistance, Brazilian standard, Bayesian approach.

Resumo: Frequentemente, a resistência requerida do concreto não é atingida nas construções brasileiras. Parcialmente para solucionar este problema, uma nova revisão da Norma Brasileira ABNT NBR 12655 foi emitida em 2015. Esta revisão mantém os critérios insuficientemente rigorosos definidos na revisão anterior de 1996, para a avaliação das resistências à compressão de concreto em estruturas existentes e em construção. Essa avaliação pode ser baseada em muito poucas amostras de teste, até mesmo no resultado de um único teste. É mostrado aqui que esses critérios são claramente inseguros. Critérios alternativos são propostos, baseados em uma abordagem Bayesiana. Os critérios propostos são verificados contra resultados de algumas centenas de ensaios realizados em estruturas reais de diferentes características, pontes e edifícios.

Palavras-chave: resistência do concreto, norma brasileira, abordagem Bayesiana.

1 INTRODUCTION

High resistance concretes are nowadays frequently used in the structural design in Brazil. This poses new technological problems for our construction industry, still in an adaptation process to this new technology. Therefore, the concrete compressive strength required in the design is frequently not attained in the construction.

The Brazilian standard related to this issue, the ABNT NBR 12655 [1], maintained in its 2015 revision the same criteria defined in its 1996 previous version [2] for the evaluation of the concrete compression strength, in existent and under construction structures. This evaluation in based on a very disputable probabilistic basis and the standard allows that it should be based on very few specimens, even in the result of a single specimen. It is shown in this paper that the criteria defined in ABNT NBR 12655 [2] are clearly unsafe.

Considering the necessity of the evaluation of the resistance of the concrete in the construction, with a more solid probabilistic basis, alternative criteria are herein proposed, based on a Bayesian approach.

As exposed, for instance in Ang and Tang [3], Melchers and Beck [4] and Nowak and Collins [5], the Bayesian approach allows for the updating of previously known data, combining them with new data obtained, for instance, in new tests in a structure. It also allows for a better consideration of data, insufficient on the statistical point of view, through the combination of these data with a subjective interpretation of them (in a "engineering judgment"), done by an experimented professional.

The information and examples found in these references have a predominantly theoretical character. A practical application of the Bayesian approach can be found in Jacinto [6], that express the theory in a practical formulation and applies it in the safety evaluation of an existent bridge, analyzing the resistance of prestressed cables of this bridge, combining previously known data with results of actual tests performed in some of the cables.

The criteria herein proposed are checked against the results of some hundreds of tests done in real structures with different characteristics, as bridges and buildings.

This paper extends, summarizes and better interpret results previously presented by the authors Stucchi and Santos [7], Interlandi et al. [8] and Chaves [9]. The relevance of the presented issue recommends that it should be put for discussion among the Brazilian technical community of structural concrete and eventually could lead to revisions in the criteria presently defined in the standards.

2 EVALUATION OF CONCRETE STRENGTH – PRESENT STANDARD CRITERIA

2.1 Characteristic strength

For the design of a structure, the criteria of the modern design standards are based on probabilistic concepts, in which resistances and actions are treated as aleatory variables and, from probabilistic analyses, partial safety factors are defined, for increase loads and reduce resistances, in order to attain the required reliability level.

Regarding the concrete compression strength, subject of the study in this paper, its definition as an aleatory variable is justifiable, considering uncertainties such as imprecision in the concrete mixing, non-homogeneity of concrete and variability of its component materials. This reflects in different results obtained in tests in cylinders poured in the same concrete mix. The concrete strength shall therefore be represented by probabilistic functions.

In a probabilistic point of view, considering the existence of a sufficient number of specimens for characterizing this probability distribution, the use of the Normal Distribution for modelling the concrete strength is justifiable. This will be also discussed later on in the paper.

Considering these uncertainties, it is necessary to define a reference value for the concrete strength, for permitting the usual design calculations still done in a deterministic basis.

Then, the concept of characteristic concrete strength is defined, as the strength value, for which it is expected that only 5% of the test results should be below of. Its value, considering the Normal Distribution is given by:

$$f_{ck} = f_{cm} - 1.65 * \sigma$$
(Equation 1)

Where:

f_{ck} = characteristic concrete strength

f_{cm} = average strength of concrete specimens

σ = standard deviation of strength of concrete specimens

In this way, the strength f_{ck} shall be defined in the structural design and attained in the construction. The verification whether the design strength was attained shall be demonstrated in tests that shall follow the methodologies defined by ABNT for pouring the cylinders, for the execution of the tests and for acceptance of the concrete strengths.

2.2 Technological concrete control

In order that the results obtained in tests could permit to decide for the acceptance or not of a given concrete volume, it is necessary to apply a process of technological concrete control.

In Brazil, the standards ABNT NBR 5738 [10], ABNT NBR 5739 [11] and ABNT NBR 12655 [1] define, respectively, how to perform the stage of molding and curing, the tests of specimens and the technological control of the concrete batches.

ABNT NBR 12655 also regulates the acceptance concrete control [1]. According it, each specimen shall be composed by two cylinders of the same mix, for each test age and being simultaneously poured. The specimen strength shall be taken as the higher value obtained in the compression tests, to be done according ABNT NBR 5739 [11].

In order to facilitate the concrete resistance control of a structure as a whole, the ABNT NBR 12655 [1] allows for the definition of "lots", which shall obey to the conditions stablished in Table 1. From each lot, a sampling shall be extracted, with a number of specimens defined according the control type (these types are defined in the next items).

Two basic types of control are defined in ABNT NBR 12655 [1]: statistical control for "total" sampling and control for "partial" sampling.

Table 1: Maximum values for the formation of concrete lots[a] (NBR 12655)

Identification (the more demanding in each case)	Main solicitations in the structural elements	
	Compression or compression and flexure	**Pure flexure [b]**
Concrete volume	50 m^3	100 m^3
Number of floors	1	1
Time of pouring	Three days of pouring [c]	

[a]In case of total sampling control, each mix shall be considered as a lot, according 6.2.3.1. [b]In the case of the complement of a column, the concrete belongs to the volume of slabs and beams. [c]This period shall be within the total maximum period of seven days, including eventual interruption for the treatment of joints

The idea of the total sampling is that the characteristic strength value f_{ck} can be evaluated with tests performed in a single specimen of a mix. However, all the concrete mixes shall be tested.

In the partial sampling, the tests are performed is some of the concrete mixes and the characteristic strength value f_{ck} of the lot is evaluated from the results of these tests.

2.3 Concrete control with partial sampling

In the concrete control with partial sampling, at least six specimens for concretes of Group I (Classes up to C50) and 12 specimens for concretes of Group II (Classes above to C50), shall be extracted for testing, for each lot.

a) If the number of specimens (n) is between 6 and 20, the expected value for the characteristic strength (denoted by $f_{ck,est}$) will be given by the highest value found with Equations 2 and 3:

$$f_{ck,est} = 2 \times \frac{f_1 + f_2 + ... + f_{m-1}}{m-1} - f_m \qquad \text{(Equation 2)}$$

Where:

$m = n/2$ (If n is odd, the higher f_i is discarded)

$f_1, f_2, ..., f_m = $ values of the specimens strength, in crescent order

$$f_{ck,est} = \Psi_6 \times f_1 \qquad \text{(Equation 3)}$$

Where:

$\Psi_6 = $ coefficient given in Table 2, to be defined according the concrete preparation condition and of the number of specimens of the sampling, linear interpolation being admitted. The preparation conditions are defined as follows:

Condition A (applicable to all the concrete classes): cement and aggregates are measured in mass, water measured in mass or volume, corrected in function of the aggregate humidity;

Table 2: Values of Ψ_6 (NBR 12655)

Preparation condition	Number of specimens (n)										
	2	3	4	5	6	7	8	10	12	14	≥ 16
A	0.82	0.86	0.89	0.91	0.92	0.94	0.95	0.97	0.99	1.00	1.02
B or C	0.75	0.80	0.84	0.87	0.89	0.91	0.93	0.96	0.98	1.00	1.02

NOTE Values of n between 2 and 5 are used in exceptional cases

Condition B (appliable to classes C10 to C20): cement is measured in mass, water is measured in volume and aggregates are measured in mass combined with volume;

Condition C (appliable only to classes C10 and C15): cement is measured in mass, aggregates are measured in volume and water is measured in volume and corrected in function of the estimative of the humidity of the aggregates.

b) If the number of specimens (n) is superior to 20, the expected value for the characteristic strength ($f_{ck,est}$) is given considering a Normal Distribution:

$$f_{ck,est} = f_{cm} - 1.65 . s_d \qquad \text{(Equation 4)}$$

$$s_d = \sqrt{\frac{1}{n-1} \sum_{i-1}^{n} (f_i - f_{cm})^2} \qquad \text{(Equation 5)}$$

Where:

f_{cm} is the average strength of the specimens of the lot;

s_d is the standard deviation of the strength of these n specimens

2.4 Concrete control with total sampling

The control for total sampling consists in the sampling of all the mixes, in order that each of them forms a lot (from what it is called 100% sampling). Then, the characteristic compressive strength is given by:

$$f_{ck,est} = f_{c, betonada} \qquad \text{(Equation 6)}$$

This type of control was modified in the 2015 last revision of ABNT NBR 12644 [1]. In the 1996 version [2], the control with total sampling was defined for two situations:

a) Number of samplings (n) smaller than 20:

$$f_{ck,est} = f_1 \qquad \text{(Equation 7)}$$

Where:

$f_1 = $ smaller strength found in the tested samplings;

b) Number of samplings (n) greater than que 20:

$$f_{ck,est} = f_i \qquad \text{(Equation 8)}$$

Where:

$i = 0,05 \, n$ (whether i is fractionary, the immediately superior number should be adopted)

3 STRENGTH EVALUATION – PROPOSAL OF ALTERNATIVE CRITERIA

3.1 The proposed Bayesian approach

Herein, the proposed Bayesian approach is briefly described. The used mathematical expressions are the ones already described by Jacinto [6].

Initially, it is shown how would be an analysis without any previous knowledge of the problem. It is first shown that the adequate probabilistic distribution in the case of a small number of specimens is the T-Student distribution. It is shown that the direct consideration of this distribution, in a sampling with a small number of specimens, would lead to very small, unacceptable values for the characteristic concrete strength.

Then, it is shown how is considered the previous knowledge that the contractor possess in the concrete production. Let us suppose initially two sets of concrete cylinders. The first set (called "Tests") includes the n elements corresponding to the cylinders effectively tested, with their respective strengths obtained in the tests. The second set (called "Previous") contains n_0 virtual elements, possessing the set average and standard deviation corresponding to the value of f_{ck} defined by the designer for the concrete production. The value of n_0, that express with relation to n, the confidence that the analyst possess in the quality of the concrete production and in the experience of the contractor, will be qualitatively defined by an "engineering judgement". The combination of the two sets is done and the combined updated values of the concrete average and standard deviation values are obtained (called "A Posteriori").

3.2 Probabilistic analysis without previous knowledge

In the analysis of a finite (small) number of specimens, it should be considered that the Normal Distribution shall be replaced by a T-Student distribution (see Jacinto [6]). The two distribution are similar, possessing the T-Student the same parameters of the Normal, plus the parameter v (degree of freedom, related to the number of specimens); its definition is given by Equation 9.

$$f_x\left(x|a,b,v\right)=\frac{c}{b}\left(1+\frac{1}{v}\left(\frac{x-a}{b}\right)^2\right)^{\frac{v-1}{2}} \qquad c=\frac{\Gamma\left(\frac{v+1}{2}\right)}{\sqrt{\pi v}\ \Gamma\left(v/2\right)} \qquad \text{(Equation 9)}$$

Where:

Number of specimens $= n$; $v = n - 1$; average: $\mu = a$; variance: $\sigma = b^2.v/(v-2)$

The T-Student distribution presents a more sparse shape compared with the Normal distribution, being the more representative one in the case of a small number of specimens. As long as the number of degrees of freedom v increases, that is to say, when $v \to \infty$, the T-Student distribution tends to be closer to the Normal distribution.

Applying the already presented equations to the determination of the concrete characteristic strength, for a limited number of specimens, the consideration of the T-Student distribution would lead to a reduction in the evaluated characteristic values. For this, Equation 10 can be applied:

$$\rho=\frac{1+V.\sqrt{1+\frac{1}{n}}.t(0.05\ ,\ v)}{1-1.645.V} \qquad \text{(Equation 10)}$$

Where:

ρ – relationship between characteristic values determined with T-Student and Normal distributions;

t $(0.05, v)$ - inverse T-Student distribution for a 5% quantile e v, degree of freedom;

V – variation coefficient $=\sqrt{\dfrac{\sigma}{\mu}}$

Figure 1 shows the variation of ρ against n (number of specimens), considering an usual value for $V = 0.10$. Clearly, using a very limited number of specimens, the characteristic value is drastically reduced, preventing its direct application and leading to the proposition of another approach, such as the Bayesian one, using "previous knowledge", as present next.

Rev. IBRACON Estrut. Mater., vol. 13, no. 4, e13411, 2020

5/15
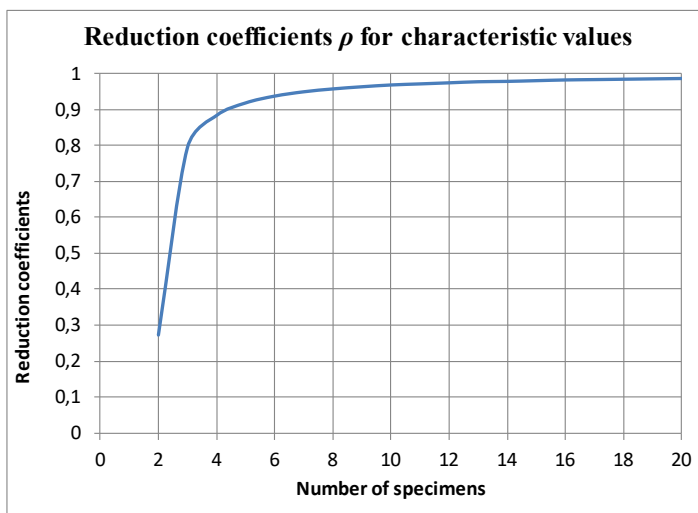
Figure 1: Relationship between characteristic values, using T-Student and Normal probabilistic distributions

3.3 Probabilistic analysis with previous knowledge

The probabilistic analysis with previous knowledge considers that the contractors possess a great previous knowledge on the production of concrete, in order to obtain the strength required by the designer, The Bayesian approach is linked to the importance that will be given to this previous knowledge.

The required formulation for the combination of the previous knowledge with the sampling data was developed by Jacinto [6]. The sampling data, modeled with a T-Student distribution, possess the parameters: $\bar{x}$ (average), s (standard deviation) e n (number of specimens).

The previous knowledge, represented by a T-Student distribution, possess average μ_0 and standard deviation s_0. The variable n_0 represents the relative weight of the contractor's previous knowledge. The value of the variable n_0 shall be defined by the analyst, based on his "engineering judgement". Auxiliary parameters α_0 and β_0 are also defined (Equations 11).

Finally, the *a posteriori* distribution combines the sampling information with the previous knowledge using a T-Student distribution.

A parametric analysis with the variable n_0 is advisable, for evaluating how the variation of n_0 values could affect the final results.

The expressions presented by Jacinto [6] are reproduced in the sequel.

a) Previous knowledge:
- number of specimens: n_0 (arbitrary in Bayesian sense); average: μ_0 ; standard deviation: s_0
- auxiliary parameters: $\alpha_0 = ((n_0 - 1))/2;\ \beta_0 = (n_0/2)s_0^2$ (Equations 11)

b) From actual tests:
- number of specimens: n ; average: $\bar{x}$; standard deviation: s

c) "A posteriori" distribution:
- number of specimens: $n_n = n_0 + n$

- average: $\mu_n = \dfrac{n_0\mu_0 + n\mu}{n_0 + n}$; $\alpha_n = \alpha_0 + \dfrac{n}{2}$; $\beta_n = \beta_0 + \dfrac{n-1}{2}s^2 + \dfrac{n_0 n(\mu_0 - \bar{x})}{2(n_0 + n)}$ (Equation 12)

d) T-Student (St) distribution:

$$f_x(x) = St(x \mid \mu_n \ , \sqrt{\left(1 + \frac{1}{n_n}\right)\frac{\beta_n}{\alpha_n}}, 2.\,\alpha_n)$$
     (Equation 13)

3.4 Analysis with corrected total sampling

The total sampling criteria could be enhanced according to the approach proposed by Stucchi [12]. This approach considers a Monte Carlo simulation for generating virtual values for the concrete strength (using a "virtual concrete mixer"), using probabilistic parameters for the strength compatible with the concrete produced in Brazil.

From these analyses, a correction criterion is proposed, that corresponds to consider in the corrected total sampling, the value of $f_{ck} = 0.93 * f_{cm}$. It is to be observed that the value obtained in the test is considered as the f_{cm} and that in the mix the variation coefficient is 4.5%, encompassing both the variability of concrete and also measurement errors. Then:

$$f_{ck} = f_{cm} * (1 - 1.645 * 0.045) \cong 0.93 * f_{cm}$$ (Equation 14)

4 APPLICATION – STRENGTH EVALUATION IN A BRIDGE

4.1 Analysis according the NBR 12655

Table 3 shows a part of a report with the results of tests performed in four columns in a bridge built in Brazil. Each column was executed in four different days, leading to the consideration of four different concrete lots. Each lot corresponds to six mixes with their respective set of tests, each one including the rupture of two or three cylinders. According to NBR 12655 [1], between these two or three results, the higher strength is considered as the representative one. The nominal characteristic strength is $f_{ck} = 35$ MPa.

Table 3 shows the results of the analyzed tests. Table 4 shows a summary of the results of the tests in each lot and the characteristic strength values f_{ck} of each lot, with the application of Equations 2 and 3 or 4 (although this one formally cannot be applied for $n < 20$). It can be observed that the results are equivalent.

Table 3 – Results of tests in the bridge

RMCP	SÉRIE	Data Conc.	Tipo	Local Aplicação	Itens Concretados	Vol (m³)	f_{ck}	Data Rompimento	Idade (dias)	CP1 Kgf	CP1 f_{ck}	CP2 Kgf	CP2 f_{ck}	CP3 Kgf	CP3 f_{ck}
008	035	08/06/16	Convencional	Rio Guaraí	Apoio 02	8,0	35,0	06/07/16	28	0,00	36,00	0,00	36,40	0,00	0,00
008	036	08/06/16	Convencional	Rio Guaraí	Apoio 03	8,0	35,0	06/07/16	28	0,00	32,40	0,00	32,70	0,00	0,00
008	038	08/06/16	Convencional	Rio Guaraí	Apoio 04	8,0	35,0	06/07/16	28	0,00	34,30	0,00	34,90	0,00	0,00
008	040	08/06/16	Convencional	Rio Guaraí	Apoio 05	8,0	35,0	06/07/16	28	0,00	35,40	0,00	36,20	0,00	0,00
008	041	08/06/16	Convencional	Rio Guaraí	Apoio 06	8,0	35,0	06/07/16	28	0,00	36,20	0,00	36,50	0,00	0,00
008	042	08/06/16	Convencional	Rio Guaraí	Apoio 07	3,0	35,0	06/07/16	28	0,00	34,50	0,00	34,70	0,00	0,00
010	045	20/06/16	Convencional	Rio Guaraí	Apoio 05	8,0	35,0	18/07/16	28	0,00	44,10	0,00	44,90	0,00	45,20
010	046	20/06/16	Convencional	Rio Guaraí	Apoio 05	8,0	35,0	18/07/16	28	0,00	41,30	0,00	41,60	0,00	42,60
010	047	20/06/16	Convencional	Rio Guaraí	Apoio 05	8,0	35,0	18/07/16	28	0,00	41,20	0,00	42,70	0,00	44,00
010	048	20/06/16	Convencional	Rio Guaraí	Apoio 05	8,0	35,0	18/07/16	28	0,00	41,60	0,00	41,80	0,00	42,40
010	049	20/06/16	Convencional	Rio Guaraí	Apoio 05	8,0	35,0	18/07/16	28	0,00	47,10	0,00	47,40	0,00	47,70
010	050	20/06/16	Convencional	Rio Guaraí	Apoio 05	8,0	35,0	18/07/16	28	0,00	41,20	0,00	41,90	0,00	43,30
013	061	24/06/16	Convencional	Rio Guaraí	Apoio 03	8,0	35,0	22/07/16	28	36,04	45,08	36,95	46,22	35,96	44,98
013	062	24/06/16	Convencional	Rio Guaraí	Apoio 03	8,0	35,0	22/07/16	28	33,41	41,79	32,96	41,23	35,03	43,82
013	063	24/06/16	Convencional	Rio Guaraí	Apoio 03	8,0	35,0	22/07/16	28	35,93	44,94	34,82	43,56	36,13	45,19
013	064	24/06/16	Convencional	Rio Guaraí	Apoio 03	8,0	35,0	22/07/16	28	33,90	42,41	34,20	42,78	32,97	41,24
013	065	24/06/16	Convencional	Rio Guaraí	Apoio 03	8,0	35,0	22/07/16	28	34,96	43,73	37,59	47,02	37,14	46,46
013	066	24/06/16	Convencional	Rio Guaraí	Apoio 03 C	8,0	35,0	22/07/16	28	33,26	41,60	35,33	44,19	38,08	47,63
016	074	30/06/16	Convencional	Rio Guaraí	Apoio 04	8,0	35,0	28/07/16	28	38,18	47,76	39,25	49,10	38,86	48,61
016	075	30/06/16	Convencional	Rio Guaraí	Apoio 04	8,0	35,0	28/07/16	28	34,13	42,69	37,45	46,85	33,66	42,11
016	076	30/06/16	Convencional	Rio Guaraí	Apoio 04	8,0	35,0	28/07/16	28	33,95	42,47	33,55	41,97	35,20	44,03
016	077	30/06/16	Convencional	Rio Guaraí	Apoio 04	8,0	35,0	28/07/16	28	37,07	46,37	35,71	44,67	34,59	43,27
016	078	30/06/16	Convencional	Rio Guaraí	Apoio 04	8,0	35,0	28/07/16	28	35,22	44,06	34,11	42,67	34,58	43,26
016	079	30/06/16	Convencional	Rio Guaraí	Apoio 04	3,0	35,0	28/07/16	28	35,43	44,32	35,17	43,99	36,36	45,48

Table 4: Summary of test results and characteristic strengths of the lots

Concrete lot	Column	Results of tests (MPa)						f_{ck}	
								Equations 2 and 3	Equation 4
8	2	36.4	32.7	34.9	36.2	36.5	34.7	32.50	32.82
10	5	44.9	42.6	44.0	42.4	47.7	43.3	41.70	40.91
13	3	46.2	43.8	45.2	42.8	47.0	47.6	41.41	42.35
16	4	49.1	46.9	44.0	46.4	44.1	45.5	42.61	42.81

On the other hand, it seems evident that the total sampling criterion (directly from the results of the tests) is clearly unsafe. Therefore, for the most critical situation, the concrete lot 008 (column 02), a Bayesian updating was done.

4.2 Bayesian updating

The following data were considered, with relation to the previous knowledge:

- Considered number of specimens: $n_0 = 10$
- Strength average: $\mu_0 = 43.3$ MPa; standard deviation: $s_0 = 4.33$ MPa

(selected values for corresponding to $f_{ck} = 35$ MPa in the T-Student distribution).
Figures 2 and 3 show, respectively, the probability distribution and accumulated probability distributions corresponding to Test no. 40 (with average of 35.8 MPa and V, coefficient of variation = 4.5%).

- Blue lines (dashed): previous knowledge;
- Red lines (continuous): test results;
- Green lines (dashed): "a posteriori" probabilities.
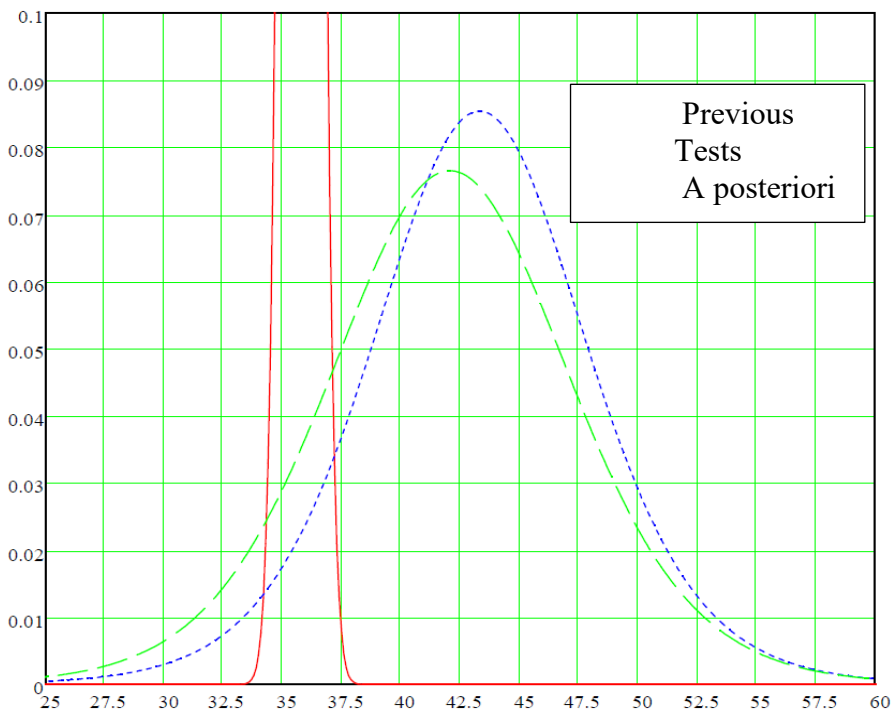
Figure 2: Density Probability Functions – Test 40

Rev. IBRACON Estrut. Mater., vol. 13, no. 4, e13411, 2020

8/15
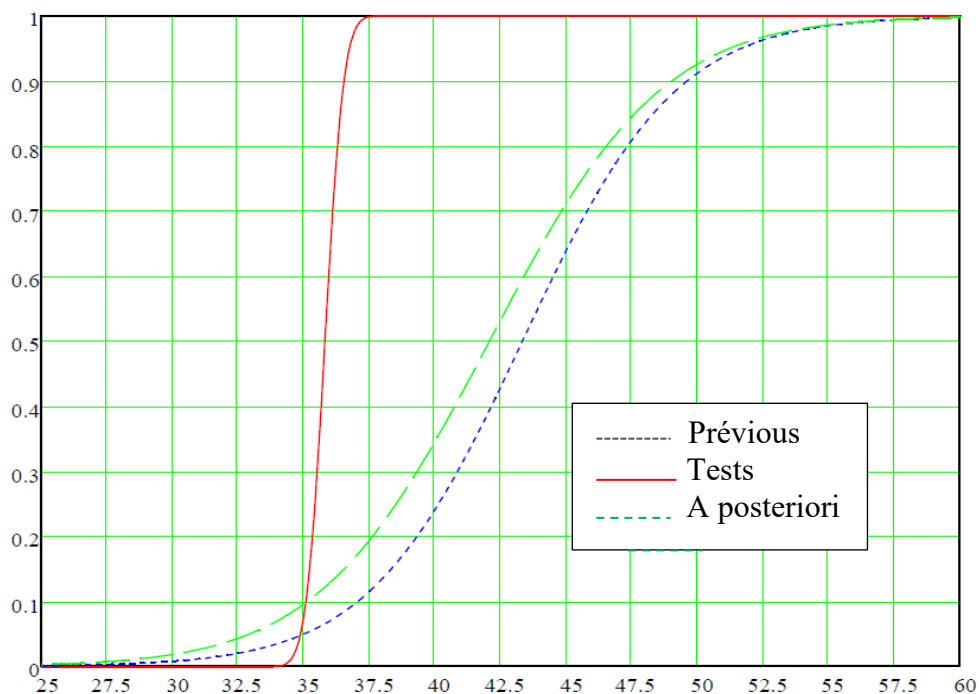
Figure 3: Accumulated Probability Functions – Test 40

Table 5 show the Bayesian updating for the test results performed for the Lot 008 (Column 02). Also in the table, the results obtained with the approach proposed by Stucchi [12] are presented. The deviation between results obtained with the two criteria are shown, indicating that the two proposed approaches lead practically to the same results. It is also evident that total sampling criteria of NBR 12655 are not safe.

Table 5: Results of the Bayesian updating for Lot 008 (column 02)

Test	NBR 12655	Bayesian approach	$f_{ck} = 0.93 f_{cm}$	Deviation
35	36.4	33.2	33.7	1.5%
36	32.7	30.8	30.3	1.6%
38	34.9	32.2	32.2	-
40	36.2	32.9	33.3	1.2%
41	36.5	33.3	33.8	1.5%
42	34.7	32.3	32.2	-

It is to be pointed out the simplicity of the proposed approaches, which lead to acceptable and also more consistent results, in a probabilistic point of view, that the ones defined in the present standard criteria.

5 APPLICATION – STRENGTH EVALUATION IN A BUILDING

5.1 Analysis with partial sampling

Data obtained from the construction of a building in the city São Paulo are used. These data, which can be found in a more detailed form in Chaves [9], encompass: date of the production of the test cylinders; design value of f_{ck}; volume that each pair of cylinders represent; concreted structural element and compression strength, obtained in tests performed in 28 days.

For the evaluation of the strength of each lot, according to the partial sampling control defined by NBR 12655 [1], Equation 2 and 3 were used, since all the lots possess the number of specimens between 6 and 20.

In Table 6, the values found with the two equations are presented, as well as the f_{ck} of each lot, according to NBR 12655 [1] (are considered as accepted the lots which estimated f_{ck} is higher than the defined in the design).

Table 6: Results of partial sampling

Concrete lot	f_{ck} (MPa) Equation 2	f_{ck} (MPa) Equation 3	f_{ck} (MPa) Estimated	f_{ck} Design	ACCEPTED?	f_{ck} Normal	f_{ck} T-Student
1	29.7	28.8	29.7	30	NO	29.60	30
2	28.4	27.2	28.4	30	NO	27.58	30
3	38.6	38.6	38.6	40	NO	39.40	40
4	39.9	38.9	39.9	40	NO	40.56	40
5	44.3	41.0	44.3	35	YES	44.19	35
6	41.1	40.2	41.1	40	YES	40.52	40
7	29.6	30.5	30.5	35	NO	32.45	35
8	40.6	41.3	41.3	40	YES	41.54	40
9	32.3	34.4	34.4	35	NO	35.32	35
10	34.1	32.8	34.1	30	YES	33.80	30
11	28.9	25.8	28.9	30	NO	29.14	30
12	28.1	28.6	28.6	30	NO	29.52	30
13	34.6	34.1	34.6	30	YES	34.47	30
14	39.6	38.6	39.6	45	NO	42.01	45
15	43.9	41.5	43.9	45	NO	42.56	45
16	36.3	37.6	37.6	40	NO	39.13	40
17	41.7	40.2	41.7	40	YES	42.22	40
18	41.2	39.2	41.2	45	NO	39.94	45
19	48.0	47.2	48.0	45	YES	48.18	45
20	42.6	44.7	44.7	45	NO	44.29	45
21	42.9	40.9	42.9	45	NO	43.54	45
22	48.8	46.9	48.8	45	YES	49.49	45
23	32.4	29.9	32.4	35	NO	31.32	35
24	44.3	44.9	44.9	45	NO	44.78	45
25	40.2	38.2	40.2	40	YES	39.25	40

5.2 Analysis with probability distributions

In Table 6, the evaluation of the characteristic strengths using the Normal e T-Student distributions are also presented. Figures 4 and 5 show, respectively, the probability density functions and accumulated probability density functions for the lot 14, taken as an example. The blue color lines represent the T-Student distribution (dashed) and the red color lines represent the Normal distribution (continuous). In this way, the strength values corresponding to the accumulated probability of 5% are obtained.

Only 6 of 50 obtained results differ more than 5% in relation to the ones obtained according NBR 12655 and in no case the difference is greater than 10%. This shows that the partial sampling criterion for samplings between 6 and 20 specimens is satisfactory in a statistical point of view. In two cases, results obtained with the Normal distribution present a difference greater than 5% in relation to the obtained with NBR 12655. But in both cases the Standard criterion is the more conservative one.

However, in four results, obtained with the more correct T-Student distribution, the values found with NBR 12655 [1] are greater than the ones of the T-Student distribution, indicating that in these four cases the results obtained with the Standard are slightly nonconservative.
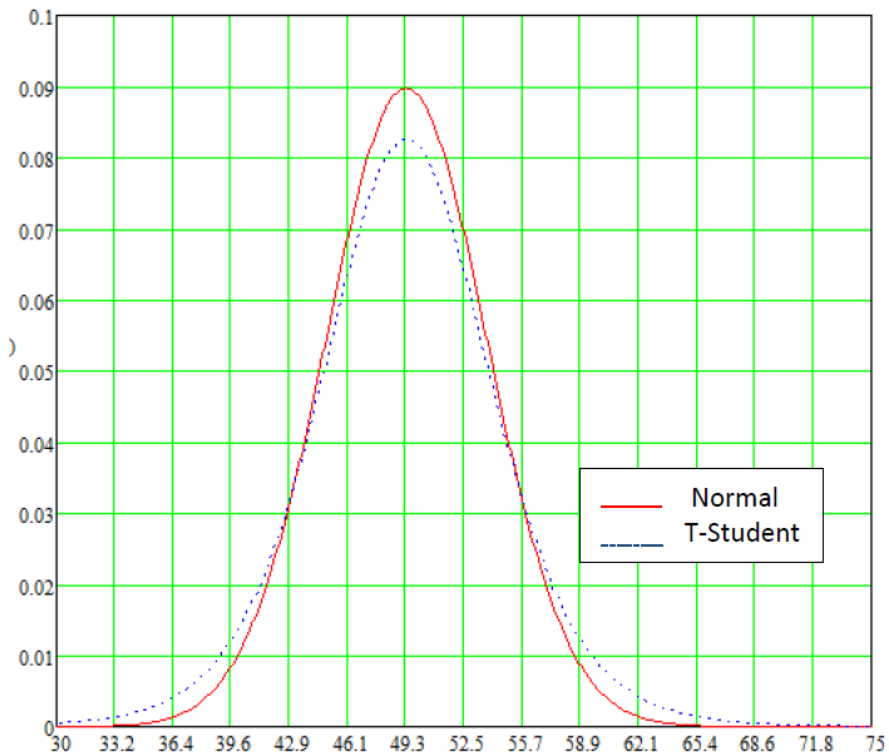
Figure 4: Density Probability Functions, Normal e T-Student – Lot 14
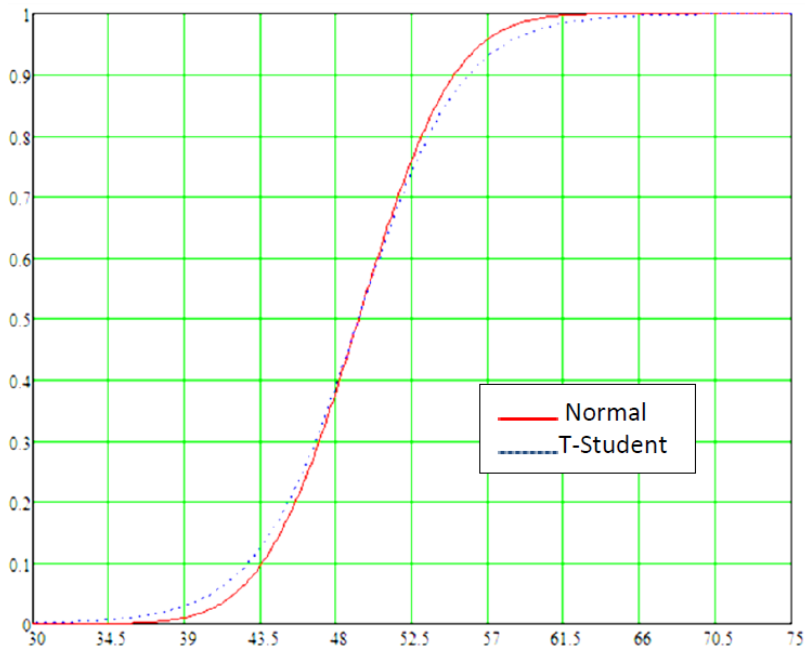
Figure 5: Accumulated Probability Functions, Normal and T-Student – Lot 14

5.3 Analysis with total sampling

Considering the total sampling criteria for the 231 specimens (each one composed by two cylinders) distributed in the 25 lots, 23 deles were rejected (marked in yellow and bold in Table 7).

5.4 Comparison between partial and global analyses

In lots 1, 4, 9, 20 e 24, all the specimens of the respective lots present strengths superior to the ones defined in the design and therefore would be approved in case they were analyzed with the total sampling criterion. However, if they would be considered as part of a lot analyzed with the partial sampling criterion, they would be rejected, since their evaluated characteristic strengths are inferior to their respective design strengths.

These situations show that the total sampling criteria, although involves 100% of the mixes, is not totally safe. Allowing for the acceptation of specimens that would be rejected in the partial sampling, this kind of control shows its incompatibility with the concept of characteristic compression strength (where the strength shall be attained in 95% of the concrete volume).

Table 7: Analysis with total sampling

Lot	n_e	f_{ck} (MPa)	1	2	3	4	5	6	7	8	9	10	11	12	13
1	9	30	30.8	30.9	30.4	30.0	30.3	30.8	32.8	31.1	31.3				
2	12	30	37.5	37.0	31.4	34.5	31.3	31.5	31.2	34.2	35.0	32.5	**28.4**	**27.5**	
3	10	40	42.2	45.1	**39.8**	49.4	44.0	44.1	42.8	44.0	47.8	47.7			
4	8	40	43.9	41.2	40.9	43.0	43.4	43.4	45.2	42.2					
5	6	35	44.7	45.0	45.6	45.9	46.4	44.6							
6	11	40	41.7	44.8	43.4	44.8	46.6	44.1	43.5	41.0	42.3	41.7	42.3		
7	6	35	38.5	37.6	27.6	**34.0**	**33.2**	40.0							
8	12	40	47.4	49.6	44.1	50.8	47.1	52.3	50.8	46.5	43.5	48.6	41.7	43.4	
9	8	35	41.2	42.9	43.0	36.4	37.5	36.2	41.1	41.8					
10	8	30	36.5	36.8	39.3	34.5	35.4	40.8	41.1	38.1					
11	12	30	36.0	34.0	38.9	35.4	34.8	39.2	36.7	36.1	37.3	**26.1**	31.3	40.3	
12	9	30	35.5	38.1	34.8	34.7	33.5	**29.8**	**29.8**	50.4	44.7	51.0	47.7		
13	11	30	35.4	39.2	42.3	37.5	37.7	34.8	40.1	40.1	38.0	37.3	36.6		
14	9	45	51.8	50.2	52.8	54.7	51.2	**40.2**	**44.5**	49.5	49.0				
15	7	45	47.1	**44.5**	**44.2**	49.5	48.4	**44.8**	51.4						
16	9	40	48.8	52.8	58.0	**39.2**	49.0	47.5	50.0	53.9	41.0				
17	11	40	52.8	47.9	45.8	54.6	41.0	48.8	48.6	50.4	44.7	51.0	47.7		
18	7	45	52.8	**41.7**	46.2	47.9	46.6	**43.2**	**43.7**						
19	13	45	50.4	53.4	52.5	52.6	50.4	52.0	47.4	52.3	48.9	51.4	50.0	54.2	50.8
20	10	45	56.8	57.0	46.2	54.8	47.8	51.1	52.0	53.1	46.1	47.3			
21	7	45	45.5	46.2	**43.5**	45.1	45.4	**44.9**	**44.3**						
22	12	45	57.1	60.8	52.8	59.5	55.9	47.4	54.7	55.8	54.8	57.0	59.5	51.9	
23	6	35	**34.1**	**32.5**	39.0	38.9	**34.2**	39.2							
24	11	45	46.6	51.1	48.8	46.9	49.5	45.8	48.9	46.9	55.0	51.1	51.1		
25	7	40	42.2	40.6	43.7	41.8	48.3	47.2	47.9						

5.5 Updated results

For each one of the specimens of lots 1, 4, 9, 20 e 24 the updating methodologies described in item 3 were used.

For the results of the tests, average values $\bar{x}$ and standard deviations s were determined from the results obtained in the two cylinders that compose each specimen, being then the number n of samplings taken as two.

For the previous knowledge, the values μ_0 and s_0 were taken in the way that the characteristic strength in a T-Student distribution corresponds to the design strength in this specimen, considering a variation coefficient of 0.10. The n_0 used values were 3, 10, 20 e 50, in the way that it would be possible to analyze in a parametric way the influence of the weight given to the previous knowledge.

Then, using the *a posteriori* T-Student distribution, the updated strength value for each specimen is obtained using the respective accumulated distribution functions. The results for different n_0 values are summarized in Tables 8 to 12.

A first glance in the Tables 8 to 12 permits to discard the values $n_0 = 3$ and $n_0 = 50$ as references for the weight to be given to the previous knowledge. In the case of $n_0 = 3$, it seems clear that the Bayesian update leads to excessively low values for f_{ck}, and for $n_0 = 50$, the f_{ck} values are excessively close to the design values, with a very small influence of the test data. These two values are then not adequate.

Table 8: Bayesian updating in specimens of lot 1

Lot	n_i	f_{ck} (Design)	f_{ck} (Total)	$n_0 = 3$	$n_0 = 10$	$n_0 = 20$	$n_0 = 50$	0.93*f_{cm}	% $(n_0 = 10)$
1	1	30.0	30.8	20.2	28.1	29.1	29.6	28.4	1.11
	2	30.0	30.9	20.3	28.2	29.1	29.6	28.5	0.91
	3	30.0	30.4	19.8	27.9	29.0	29.6	28.1	0.67
	4	30.0	30.0	19.4	27.7	28.9	29.6	27.8	0.39
	5	30.0	30.3	19.7	27.9	29.0	29.6	28.0	0.50
	6	30.0	30.8	20.3	28.2	29.1	29.6	28.5	0.91
	7	30.0	32.8	22.5	29.1	29.6	29.8	30.0	3.23
	8	30.0	31.1	20.7	28.3	29.2	29.7	28.7	1.54
	9	30.0	31.3	21.0	28.5	29.3	29.7	29.0	1.65

Table 9: Bayesian updating in specimens of lot 4

Lot	n_i	f_{ck}(Design)	f_{ck} (Total)	$n_0 = 3$	$n_0 = 10$	$n_0 = 20$	$n_0 = 50$	0.93*f_{cm}	% $(n_0 = 10)$
4	1	40.0	43.9	30.7	39.1	39.6	39.9	40.50	3.58
	2	40.0	41.2	27.3	37.7	38.9	39.5	38.08	1.02
	3	40.0	40.9	26.6	37.3	38.7	39.5	37.57	0.73
	4	40.0	43.0	29.4	38.6	39.4	39.8	39.62	2.64
	5	40.0	43.4	29.7	38.7	39.4	39.8	39.80	2.85
	6	40.0	43.4	29.8	38.7	39.4	39.8	39.9	3.09
	7	40.0	45.2	32.6	39.7	39.9	40.0	41.76	5.18
	8	40.0	42.2	28.4	38.1	39.1	39.7	38.87	2.03

Table 10: Bayesian updating in specimens of lot 9

Lot	n_i	f_{ck}(Design)	f_{ck} (Total)	$n_0 = 3$	$n_0 = 10$	$n_0 = 20$	$n_0 = 50$	0.93*f_{cm}	% $(n_0 = 10)$
9	1	35.0	41.2	30.4	35.3	35.2	35.1	37.8	6.96
	2	35.0	42.9	33.3	35.9	35.4	35.2	39.7	10.62
	3	35.0	43.0	33.4	35.9	35.4	35.2	39.8	10.75
	4	35.0	36.4	24.4	33.2	34.1	34.7	33.7	1.54
	5	35.0	37.5	25.8	33.8	34.4	34.8	34.7	2.63
	6	35.0	36.2	23.8	32.9	34.0	34.6	33.3	1.06
	7	35.0	41.1	30.7	35.4	35.2	35.1	38.0	7.32
	8	35.0	41.8	31.6	35.6	35.3	35.1	38.6	8.28

Table 11: Bayesian updating in specimens of lot 20

Lot	n_i	f_{ck} (Design)	f_{ck} (Total)	$n_0 = 3$	$n_0 = 10$	$n_0 = 20$	$n_0 = 50$	0.93*f_{cm}	% $(n_0 = 10)$
20	1	45	56.8	45.2	46.4	45.7	45.2	52.6	13.34
	2	45	57.0	45.6	46.4	45.7	45.3	52.9	14.05
	3	45	46.2	30.3	42.2	43.6	44.5	42.6	0.93
	4	45	54.8	42.3	46.0	45.5	45.2	50.7	10.18
	5	45	47.8	32.6	43.2	44.2	44.7	44.2	2.26
	6	45	51.1	37.2	44.9	45.0	45.0	47.3	5.43
	7	45	52.0	38.4	45.2	45.1	45.1	48.1	6.48
	8	45	53.1	39.9	45.6	45.3	45.1	49.1	7.68
	9	45	46.1	30.5	42.3	43.7	44.5	42.7	1.02
	10	45	47.3	32.0	42.9	44.0	44.6	43.8	2.00

Table 12: Bayesian updating in specimens of lot 24

Lot	n_i	f_{ck} (Design)	f_{ck} (Total)	$n_0 = 3$	$n_0 = 10$	$n_0 = 20$	$n_0 = 50$	0.93*f_{cm}	% ($n_0 = 10$)
	1	45.0	46.6	31.2	42.6	43.8	44.5	43.2	1.4
	2	45.0	51.1	37.3	44.9	45.0	45.0	47.4	5.53
	3	45.0	48.8	33.8	43.7	44.4	44.8	45.1	3.11
	4	45.0	46.9	31.3	42.6	43.9	44.6	43.3	1.62
	5	45.0	49.5	35.2	44.2	44.7	44.9	46.0	4.05
24	6	45.0	45.8	30.1	42.1	43.6	44.4	42.4	0.73
	7	45.0	48.9	33.8	43.7	44.4	44.8	45.0	3.00
	8	45.0	46.9	31.0	42.5	43.8	44.5	43.1	1.42
	9	45.0	55.0	42.9	46.1	45.6	45.2	51.1	10.75
	10	45.0	51.1	37.2	44.8	45.0	45.0	47.3	5.56
	11	45.0	51.1	37.2	44.8	45.0	45.0	47.3	5.56

For $n_0 = 10$ and $n_0 = 20$, it can be verified that the updated values presents a significant influence of the test data, with a more natural correction of the previous knowledge. This shows that, for the engineering judgement to be done, values of n_0 within this range are recommended. In this way, the selected n_0 value shall be proportional to the confidence of the analyst in the concrete batcher. An important "confidence estimator" in the concrete batcher is the batcher standard deviation, calculated from results of the concrete test results of the batcher during a predetermined time period.

The NBR 7212 [13] divides the batchers in four categories, according this standard deviation, as shown in Table 13.

Table 13: Levels of concrete batchers according their standard deviations

Site of concrete production	Standard deviation			
	MPa			
	Level 1	Level 2	Level 3	Level 4
Concrete batcher	Sn < 3.0	3.0< Sn < 4.0	4.0 < Sn < 5.0	Sn > 5.0

Tables 8 to 12 furnish the deviation between the two herein recommended criteria, the one from Stucchi [12] and the Bayesian updating with $n_0 = 10$.

6 CONCLUSIONS

With an average deviation of only 3.06% with relation to the values of the Bayesian updating with $n_0 = 10$, the consideration of the f_{ck} of each specimen as $f_{ck} = 0,93 * f_{cm}$, is an interesting alternative to the present criteria of total sampling defined by NBR 12655 [1].

With the updating of the individual results through the formula $f_{ck} = 0,93 * f_{cm}$, it could be observed that only 21 of the results of lots 1, 4, 9, 20 e 24 would be accepted by the "updated" total sampling criterion, that considers both aspects of the partial sampling, but also considers the value of each sampling.

On the other hand, regarding the total sampling control, it is clear that the criterion defined in NBR 12655 [1] ignore the probabilistic definition of characteristic strength, as well as presents incompatibility with the partial sampling control. In defining the characteristic strength of a mix has the higher value found in the test of two cylinders, there is no evidence that this value could be the one below which is the resistance of no more than 5% of the mix volume.

Two criteria are finally proposed in this paper, which are the one of Stucchi [12], proposing $f_{ck} = 0,93 * f_{cm}$ and the Bayesian updating, with $n_0 = 10$. Regarding the last one, it would be interesting the development of future studies relating the classification levels of the concrete batchers according NBR 7212 [13], with the weight to be given to the previous knowledge in the Bayesian approach. This approach will permit that concrete batchers with a small standard deviation (in other words, with better control of the productive process), could count on a greater level of confidence, according to the Bayesian approach.

It is evident that for the implementation of changes in the present standards, more studies would be necessary, considering moreover the concretes produced in different Brazilian areas. This is the proposition in the conclusion of this paper.

REFERENCES

[1] Associação Brasileira de Normas Técnicas. *Concreto de Cimento Portland – Preparo, Controle, Recebimento e Aceitação – Procedimento*, NBR 12655, 2015.

[2] Associação Brasileira de Normas Técnicas. *Concreto de Cimento Portland – Preparo, Controle e Recebimento – Procedimento*, NBR 12655, 1996.

[3] A. H.-S. Ang and W. H. Tang, *Probability Concepts in Engineering*, Hoboken, USA: John Wiley & Sons, 2007.

[4] R. E. Melchers and A. T. Beck, *Structural Reliability Analysis and Prediction*, 3rd ed. Hoboken, USA: John Wiley & Sons, 2018.

[5] A. S. Nowak and K. R. Collins, *Reliability of Structures*, 2nd ed. Boca Raton, USA: CRC Press, 2013.

[6] L. A. C. Jacinto, "Avaliação da segurança de pontes existentes: abordagem probabilística Bayesiana," M.S. thesis, Fac. Ciên. Tecnol., Univ. Nova de Lisboa, Lisboa, 2011.

[7] F. R. Stucchi and S. H. C. Santos, "Updating of concrete resistances: proposal of an alternative to the Brazilian standard NBR 12655 criteria based on a Bayesian approach," in *Proc. 12th Int. Conf. Struct. Saf. Rel.*, Aug. 2017.

[8] C. Interlandi, A. Pereira, L. F. C. R. Martha, and S. H. C. Santos, "Confiabilidade em estruturas de concreto armado: abordagem Bayesiana da reavaliação da resistência do concreto: um estudo de caso," in *An. 59° Cong. Bras. Concr.*, 2017.

[9] P. A. J. Chaves, *Controle de Aceitação do Concreto Segundo a NBR 12655*. Rio de Janeiro: Dep. Estrut., Esc. Politéc., Univ. Fed. Rio de Janeiro, Project, 2017.

[10] Associação Brasileira de Normas Técnicas. *Concreto – Procedimento para Moldagem e Cura de Corpos de Prova*, NBR 5738, 2015.

[11] Associação Brasileira de Normas Técnicas. *Concreto – Ensaio de Compressão de Corpos-de-Prova Cilíndricos*, NBR 5739, 2007.

[12] F. R. Stucchi, *Controle da Resistência do Concreto, Estruturas Existentes e a Teoria da Confiabilidade* (Palestra). São Paulo: ABECE, 2015.

[13] Associação Brasileira de Normas Técnicas. *Execução de Concreto Dosado em Central – Procedimento*, NBR 7212, 2012.

IBRACON Structures and Materials Journal
Revista IBRACON de Estruturas e Materiais

ORIGINAL ARTICLE

Increasing structuration rate of 3D printable concretes: the effect of viscosity enhancing admixtures

Elevação da taxa de estruturação de concretos para impressão 3D: o efeito de aditivos modificadores de viscosidade

Jessica Amanda Hasse[a]
Ariane Prevedello Rubin[a]
Lucas Carvalho Quintanilha[a]
Wellington Longuini Repette[a]

[a]Universidade Federal de Santa Catarina – UFSC, Departamento de Engenharia Civil, Florianópolis, SC, Brasil

Abstract: In the last decades, 3D printing has emerged as a promising new paradigm for manufacturing. Even in the civil construction industry, it has gained attention from companies and researchers around the world. Despite of that, the properties of materials applied in the additive manufacturing process are still understudied. One of the challenges is the need to conciliate both high bearing capacity, sparing the need of any confining measures, and the ability of keeping fluidity for enough time, in order to avoid cold joints between the layers. In that scenario, viscosity enhancing admixtures (VEAs) can be a solution, because they are able of promoting flocculation, viscosity gain and yield strength increase, reducing the deposition time in between the layers, which may decrease the formation of cold joints. This research evaluated rheological parameters of four different VEAs and found out that they show potential for increasing the cohesion and buildability of concretes for 3D-printing. The results showed that this effect varies with the type and amount of the admixture adopted and bentonite clay, as a mineral powder material, performed best in comparison to other polymeric VEAs, presenting structuration rates of up to 62% higher than the reference mixture.

Keywords: 3D printing, additive manufacturing, extrudable concrete, viscosity-enhancing admixtures, bentonite clay.

Resumo: Nas últimas décadas, a impressão 3D emergiu como um novo e promissor paradigma de fabricação. Mesmo na indústria da construção civil, ela tem ganhado atenção de empresas e pesquisadores de todo o mundo. Apesar disso, as propriedades dos materiais aplicados no processo de manufatura aditiva ainda são pouco estudadas. Um dos desafios está na necessidade de conciliar alta capacidade portante, poupando a necessidade de quaisquer medidas restritivas, com a capacidade de manter a fluidez por tempo suficiente, a fim de evitar juntas frias entre as camadas. Nesse sentido, os aditivos Modificadores de viscosidade (VMAs) podem ser uma solução, pois são capazes de promover floculação, ganho de viscosidade e aumento da tensão de escoamento, reduzindo o tempo de deposição entre as camadas, o que pode diminuir a formação de juntas frias. Esta pesquisa avaliou parâmetros reológicos de quatro VMAs diferentes e descobriu que eles apresentam potencial para aumentar a coesão e a construtibilidade de concretos para impressão 3D. Os resultados mostraram que esse efeito varia com o tipo e a quantidade de aditivo adotado. Particularmente, a argila bentonita, como aditivo mineral em pó, apresentou melhor desempenho em comparação com os VMAs poliméricos, produzindo taxas de estruturação até 62% superiores à mistura de referência.

Palavras-chave: impressão 3D, manufatura aditiva, concretos extrudáveis, aditivos modificadores de viscosidade, argila bentonita

J. A. Hasse, A. P. Rubin, L. C. Quintanilha, and W. L. Repette

1 INTRODUCTION

The additive manufacturing technology, or simply 3D printing, dates back to the 1980s and it was initially developed in the scope of prototyping [1]. In the last two decades, however, there has been a growing interest around the additive fabrication processing of large-scale components for civil construction. The technique can be used to optimize time, reduce costs, flexibilize projects, reduce waste generation, and fabricate structures without formwork and falsework [2]–[5].

However, in the additive manufacturing process with concrete, the challenge of stacking layers tightly attached to one another still persists. If the layers overlaps occur too quickly, they won't have sufficient strength to avoid deformations caused by their own weight. On the other hand, if optimal waiting time between depositions is exceeded, there will be loss of interlayer adhesion and formation of cold joints, which compromises the final mechanical performance of the structure [3], [6].

The stability of the printed structure depends on two distinct factors: (a) the vertical stress acting on the prior deposited layers and (b) the material's yield strength. Both are time dependent, being the former related to the construction rate, i.e. the speed at which each new layer is deposited after the previous layer, while the latter relates to the structuring at rest of the concrete [3], [6].

1.1 Extrudable concretes

In recent years, 3D printing systems have been successfully applied to the construction of structural elements and architectural components, adopting a variety of cementitious compositions. However, there is still no domain or consensus in the technical-scientific community regarding the preparation of cementitious mixtures suitable for additive manufacturing [1], [4], [7]. Among the main objects of study in this matter are the topics related to the properties at the fresh state of the material, mainly extrudability and buildability.

Extrudability refers to the ability of the material to continuously flow through the tubes and nozzles in the print head, and it is measured based on the distance by which the concrete can be printed without blocking the nozzle, free from cracks and separations. Buildability refers to the ability of the material to maintain the extruded shape under its own weight and the stresses from the upper layers and it can be measured by the maximum number of printed layers without collapse [2], [4], [6]. The maintenance of desirable properties can be obtained by using chemical admixtures capable of adjusting the mixture's desired workability. Note that the material must be sufficiently fluid for extrusion purposes, but sufficiently firm for mechanical stability of the structure. For this reason, the influence of several admixtures on such material is the subject of lots of recent studies [4], [8].

1.2 Structuration rate

The resting time between the casting of two successive layers is directly related to the development of the microstructure of the cementitious material. This process depends basically on: (a) a reversible physical phenomenon, due to the flocculation processes of the colloidal particles, and (b) an irreversible chemical phenomenon, due to the hydration processes in the cement paste [9]–[11], promoting an increase on the materials yield strength, but also diminishing its workability throughout the resting time [12]–[15].

In this context, the yield strength can be defined as the ability of the cementitious material to withstand the stresses, resulting from the attractive interparticular forces between cement and the other particles that constitute the mixture. Therefore, to ensure the stability of the printed structure, fresh concrete yield strength, over resting time, must increase and be greater than the imposed stresses [9].

The materials yield strength evolution over resting time, during the flocculation period of cementitious matrices, follows a linear regimen, previously denominated as structuration rate (*Athix*) and may be estimated be estimated by the following equation from [13]:

$$Athix = \left(\tau 0(t) - \tau 00 \right) / t$$

Where: Athix is the structuration rate (Pa/s); τ0(t) is the yield strength after some time (Pa); τ00 is the initial yield strength (Pa); and t is the elapsed time (s).

1.3 Viscosity enhancing admixtures

One way to control the rheological behavior of cementitious matrices is by the use of viscosity enhancing admixtures (VEAs), which are generally applied to concretes in order to reduce the risk of segregation and exudation [16]-[18]. Since their action increases the viscosity and yield strength of the mixtures, their use may be extended to printable concretes [7].

There are many types of VEAs, which can be mineral compounds in the form of extremely fine powders (such as silica fumes and nanoclays), natural polymers (xanthan gum and agar) and synthetic or semi-synthetic polymers (polyacrylates, polyvinyls, ether derivatives) [16], [17]. Similarly, the actuation mechanism of such additives may also vary [7]. It is evident that the extent of viscosity increase will depend on the type and concentration of the admixture, its adsorption capacity by the cement particles, anionicity and molecular weight [19], as well as the shear rate applied to the concrete. The modes of action of the main polymeric VEAs, according to [17], are:

- Adsorption: Long-chain polymer molecules adhere to water molecules, fixating it in part and expanding so that the viscosity of the liquid medium in the mixture is increased.
- Association: Polymer molecules develop attractive forces with each other so that, when connected, they block the free passage of water from the mixture. This promotes gel formation with consequent increase in viscosity.
- Intertwining: At higher concentrations, polymeric molecules can intertwine and entangle, increasing the viscosity of the assembly in which they fit. This effect can disappear at sufficiently high shear rates by aligning the polymer chains in the flow direction, generating a behavior known as pseudoplasticity.

Since these admixtures have a potential increase in the yield strength of concrete, their insertion may be able to improve the structuring rate of mixtures intended for 3D printing. However, because of the variability of types and modes of operation, especially with regard to polymeric VEAs, it is important to evaluate the various commercially available products.

1.4 Bentonites

Mineral compounds in the form of fine powders are among the most used viscosity enhancing admixtures for concrete. Among them, but not so disseminated, nanoclays and, particularly, bentonite clays arouse special interest because of their unique properties, such as the capacity of producing thixotropic gels, expanding up to 20 times its original volume when put in contact to water [20], [21].

Due to the high concentration of adsorbed cations over the clay particle surface, when the particles are dispersed in a liquid, the diffusion phenomenon happens so to equalize the concentration all over the fluid. However, the ease to which this should happen depends on the electromagnetic field originated around the particle' surface, and also on the ion-surface interactions that are unique to every type of exchangeable cation. The phenomenon caused by the combination of these two opposite events is called diffuse double layer [22], [23].

It is known that the montmorillonite particles are extremely small, flats and floc shaped, with 1nm of thickness by 220nm of length, and have two different charges on its surfaces. On the face of the particle a negatively charged surface occurs, resulted from the isomorphic replacements that occur internally with the cations on the crystal lattice. On the other hand, on the borders of the particles a pH dependent surface is formed, resulted from the protonation and deprotonation of the OH^- groups, varying from positive to negative as the solution pH is altered [24], [25].

Figure 1 shows the behavior of the clays when dispersed in a fluid. When submitted to a forced flow, particles tend to orientate according to the flow. When the flow is discontinued, particles are rearranged by the attraction of the negatively charged faces to the positively charged extremities, forming a tridimensional structure inside the fluid [26].
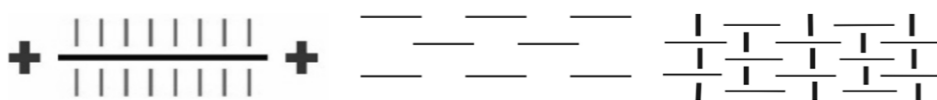
Figure 1. Bentonite clays behavior: charged particle, under forced flow and at rest [Zhang et al., 2018].

The unique thixotropic gels formation in these materials is then produced by this combination of effects, where the electro-viscous effect under low ionic forces, caused by the well-developed diffuse double layer, is later kept by

the particle immobilization on the tridimensional formed net. Besides that, particles that have opposite charged to the clay-minerals, i.e. the oxides from the iron and aluminum hydroxides, also favor the thixotropic tendency of the solutions through the formation of connection points between them [21], [25].

When interacting, bentonite clays and cement may alter the mixes properties by three different reasons: the significant increase in the pH solution (around 12 ~ 13 caused by the cement), would promote the thixotropic gels formation from the alteration of the charges on the bentonite particles ends, the supersaturation of Ca^{2+} ions, which may favor or prejudice the cation exchange, depending on the bentonite nature, as well as promote a higher water retention between the particle's layers, compressing the double diffuse layer for the high ion concentration that will result in higher flocculation, and a somewhat meaningful presence of K^+ ions. All of these effects would promote the retention of water, significantly increasing the viscosity of the mixture [27].

2 MATERIALS AND EXPERIMENTAL PROGRAM

In this context, the present work analyzes the effect of different viscosity enhancing admixtures in extrudable concretes and their influence in the materials' yield strength over time, in order to favor its structuration rate (Athix), required to improve buildability of printable mixtures.

2.1 Materials and mixture proportions

For this research, nine different mixtures were produced as stated in Table 1: one reference mixture (without any VEA content), and eight other mixtures with four different types of VEA in two amounts (three polymeric commercial VEAs and one type of bentonite clay). All of them were made with Portland cement with pozzolanic addition, classified as CP-IV, according to ABNT NBR 5736/1991 [28]. Table 2 presents the chemical composition of the adopted powder materials. The granulometric composition measured with a Microtrac S3500 laser granulometer of the dry materials is shown in Figure 2.

Table 1 Mixes proportioning.

Mix	Portland cement (Kg/m³)	Fine sand (Kg/m³)	Water (Kg/m³)	Silica fume (Kg/m³)	HRWR (%*)	VEA1 (%*)	VEA2 (%*)	VEA3 (%*)	Bent (%*)
REF	706	1178	290	79	1.5	-	-	-	-
VEA1 0.6	706	1178	290	79	1.5	0.6	-	-	-
VEA1 1.2	706	1178	290	79	1.5	1.2	-	-	-
VEA2 0.6	706	1178	290	79	1.5	-	0.6	-	-
VEA2 1.2	706	1178	290	79	1.5	-	1.2	-	-
VEA3 0.6	706	1178	290	79	1.5	-	-	0.6	-
VEA3 1.2	706	1178	290	79	1.5	-	-	1.2	-
BENT 0.3	706	1178	290	79	1.5	-	-	-	0.3
BENT 0.6	706	1178	290	79	1.5	-	-	-	0.6
	*to the cement weight								

Table 2 Chemical composition of the powder materials.

Determination	Cement (%)	Silica Fume (%)	Bentonite (%)
SO_3	3.18	0.80	-
Al_2O_3	4.3	< 0.04	18.77
SiO_2	18.96	84.87	61.22
Fe_2O_3	2.95	2.17	4.94
MgO	3.26	1.98	3.69
CaO	60.76	1.24	0.71
K_2O	-	2.49	0.50
Na_2O	-	1.18	1.41
TiO_2	-	0.36	-
Mn_2O	-	1.98	-
P_2O_5	-	<0.01	-
Insoluble residue	0.72	-	-
Heat loss	3.45	4.00	5.9
Free CaO	0.75	-	-
Alkali equiv.	0.68	-	-

J. A. Hasse, A. P. Rubin, L. C. Quintanilha, and W. L. Repette
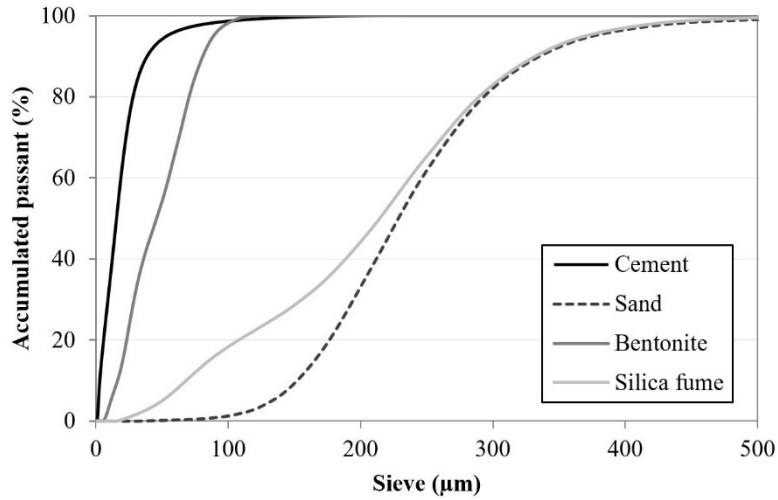
Figure 2. Gradation of the powder materials.

All mixtures were made using a polycarboxylate based high range water reducer admixture (HRWR). Also, besides bentonite clay, three commercial viscosity enhancing admixtures (denominated VEA1, VEA2 and VEA3) were investigated. Table 3 shows their main characteristics.

Table 3 Physical chemical characteristics for the admixtures.

Characteristic	HRWR	VEA1	VEA2	VEA3
Specific weight (g/cm³)	1.05 – 1.10	1.00	1.02	1.01
pH	3 - 6	6	6	8
Aspect	Liquid	Liquid	Gel	Liquid
Solid content (%)	-	9.53	10.00	9.60

In order to obtain a reference mix that would meet the extrudability requirements, a few different batches were tested according to the method proposed by [29], in which concrete filaments with 1 to 2cm width are extruded for a minimum of 30cm length. The material should keep its cohesion and shape to be considered extrudable, as shown in Figure 3a. Figure 3b shows the printing process of one sample.
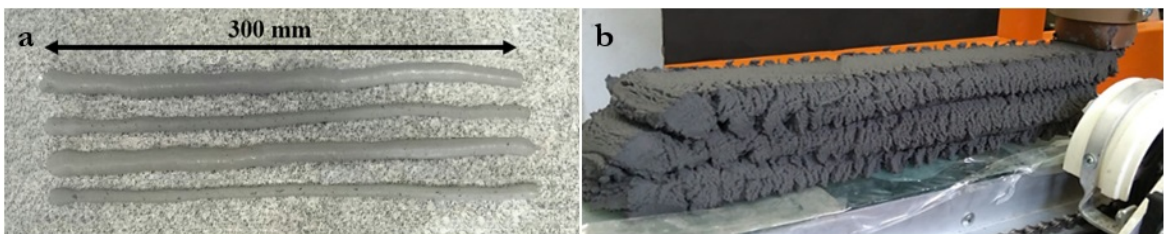
Figure 3. a) Extrudability test. b) Printed layers.

The established mixing procedure was the same for all mixes: dry materials were manually mixed prior to mechanical mixing was started and, thereafter, on the course of the first minute of mixing, they were gradually added to the mixing water, where the HRWR was already diluted. After that, the materials were mixed for 5 more minutes,

put at rest for 1min for the addition of the viscosity promoters, when the case, and proceeded to mix for 2 final minutes. The mixture velocity was fixed in 25rpm, in a Tedemix ML-03 mixer, equipped with a Ø80mm cowls disc.

After the sample preparation, mixes were submitted to rheological tests, in order to evaluate the effect of the viscosity enhancing admixtures on the materials' yield strength over time, as well as to the materials' structuration rate.

2.2 Rheological and complementary tests procedures

Yield strength measurements were taken for all mixes at 10, 45 and 90min after the addition of the cement to the water. For the rheological measurements, a Thermo Scientific HAAKE MARS III rheometer with Vane geometry was used.

The rotor was immersed into the mixes right after the mixture procedure was ended and kept at rest until the defined measurement times were reached. A new batch was made for each measurement that was taken. The tests were carried out maintaining a constant shear rate with angular velocity of 0,25rpm. Results were obtained from the medium value of a pair of data, at each established resting time, and plotted as a function of the yield strength over time.

After the rheological tests, the consistency index was measured according to ABNT NBR 13276/2016 [30], at the same resting times established for the rheological measurements (10, 45 and 90min), in order to evaluate the materials' fluidity loss over time. The test was carried out placing the material into the test recipient, and then left at rest until the established times were reached for testing.

The reaction kinetics of the mixtures were measured by isothermal calorimeter model TAM AIR (TA Instruments) of eight channels with controlled temperature of 23ºC for 60 hours. Also, measurements for the fresh state specific weight, as well as the 28 days compressive strength, according to ABNT NBR 13278/2005 [31] and ABNT NBR 7215/1997 [32], respectively, were made.

3 RESULTS AND DISCUSSIONS

3.1 Yield strength

Figure 4 shows the yield strength obtained for all of the mixtures with 10, 45 and 90 minutes of rest. The increasing values over time observed is the result mostly of the flocculation processes that come from the interaction of colloidal particles inside the mixes, which can be also inferred from the calorimetry tests (see section 3.3), and also from the calcium silicate hydrates on the contact points between the cement particles that usually occur on cementitious materials [9], [14].
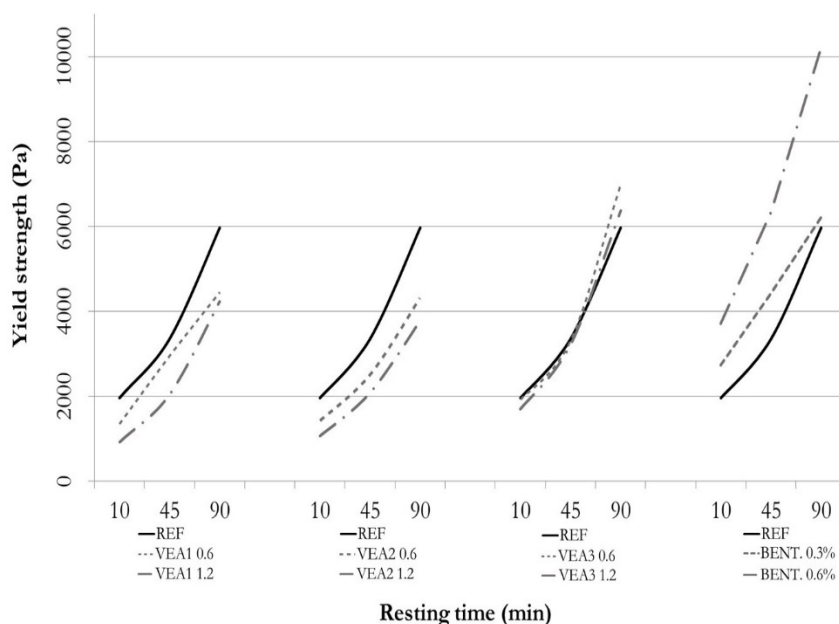
Figure 4. Yield strength evolution over time

Regarding the mixtures with the polymeric VEAs, it can be said that:

1) VEA 1 and VEA2 were not able to increase, comparing to the reference mixture, the yield strength in any of the measured resting times.
2) For the mixture with VEA3, there was no significant variation from the reference mixture after up to 45 minutes, with a slightly increase at the 90 minutes measure.

This behavior may seem to go in opposition to what was expected, since the addition of the viscosity enhancing admixtures should increase the mixtures' viscosity and its yield strength. However, the mechanism in which each of this admixtures work can be affected both by the shear rate applied and the w/c ratio. About the former, since the incorporation of the polymeric VEAs was made without discounting the water content of the solution, and their solid content was only approximately 10%, the mixtures with VEA1, VEA2 and VEA3 had a slightly higher w/c ratio than the reference mixture, which can lead to viscosity reduction and yield strength decrease. This means that the three-dimensional polymeric structure expected to be formed due to the presence of such VEAs was not enough to produce an increase in the yield strength under this particular shear rate and in face of the w/c difference.

It should be noted, nevertheless, that this does not mean that polymeric VEAs are always not suited for increasing the yield strength of printable concretes, because different applications subject the material to different shear rates. Besides, the water content of the polymeric solution can be subtracted from the mixture, if it is shown that to be the case. Regards to the chemical composition, there are many different commercially available polymeric VEAs, with different acting mechanisms – as discussed early on in this paper (see section 1.3) – which means that some of them may be better suited for some specific applications than others.

In contraposition to the mixes using the VEAs, the mixes that used bentonite on its composition, for both the lower (0.3%) and the higher (0.6%) percentages, showed an increase to the yield strength when compared to the reference mixture, for all measured resting times. The registered increase was up to 70% higher for the longer periods (90min rest). It must be considered the fact that the incorporation of bentonite clay elevates the solid/liquid rate of the mixture, which alone can improve its viscosity and yield strength. But this behavior is not only due to the fact that the bentonite clay is a very fine material with high surface area, but also tend to form a thixotropic gel when dispersed in a liquid phase, which alters the rheological response of the mixture, as noted by previous works [33]. The results obtained here confirmed that the three-dimensional network was indeed formed by the bentonite presence, even with the dispersion happening on a cement-based matrix. This is of great value concerning 3D printing with concrete, because of the great gain in buildability.

3.2 Structuration rate

Table 4 shows the structuration rate values (Athix) of the investigated mixes. It is clear that the presence of VEA1 and VEA2 did not benefit the Athix value, lowering its measure of up to 32,6% of the original value (REF). On the other hand, the mixes with VEA 3 and bentonite clay presented structuration rates of up to 61,23% higher than the REF mix. In a previous study [34] involving the use of VEA in cement pastes, three different dosages of the admixture were tested, and as a result it was obtained that higher amounts of VEA would improve both the materials yield strength as well as the structuration rate. In that case, the obtained values for the Athix were slightly lower than the ones found here, firstly because said study wasn't carried for printability purposes, and secondly because the presence of the aggregates should improve the robustness of the material, resulting in higher yield strength. The increase on the structuration rates is an important asset for 3D printing applications because there is not only a need for high yield strength, but for a rapid increase to such values after the layer casting. The speed in which the structuration of the mixture under rest increases must be as higher as it is possible to print the next layers (to avoid cold joints), what varies with the available printer. That's why there is not a target value per se, but, in general, higher Athix values are preferable [6], [8]. In another recent work [35], it was also confirmed the effectiveness of clays in increasing the structuration rates of the mixes, there referred as the robustness of the material, when compared to mixes containing silica fume and viscosity modifying admixtures. In this case, superplasticizer was used to compensate the extremely higher yield strength in the mixes containing clays, in order to reach the same properties for printability purposes. However, according to [12], all produced mixes could be considered highly thixotropic. The BENT 0.6% mix produced the highest result for such a behavior, while VEA 1.2%, the lowest.

Table 4 Structuration rate, mass density and entrained air of the mixes.

Property	REF	VEA1 0.6	VEA1 1.2	VEA2 0.6	VEA2 1.2	VEA3 0.6	VEA3 1.2	BENT 0.3	BENT 0.6
A_{thix} (Pa/s)	0.841	0.644	0.694	0.605	0.567	1.066	0.982	0.723	1.356
Mass density (kg/m³)	2040.4	1917.2	1899.6	2047.3	2038.3	2036.1	2022.4	2044.5	2065.1
Entrained air (%)	8.88	14.38	15.17	8.57	8.97	9.07	9.68	8.70	7.78

3.3 Isothermal calorimetry

Figure 5 shows the heat flow released by the mixtures over time. It is possible to conclude that the induction periods (measured by the slope of the curves during the acceleration period) and the maximum heat release peaks have reached similar behaviors for all mixtures. It is evident that the different types and amounts of viscosity modifiers used have not produced significant alterations on the heat flow for the first hour, that is, they did not accelerate nor retard the hydration process of the mixtures in that period, meaning that potential modifications on the structuration rates, measured through the rheometry tests, were not due by an alteration on the cement hydration process.
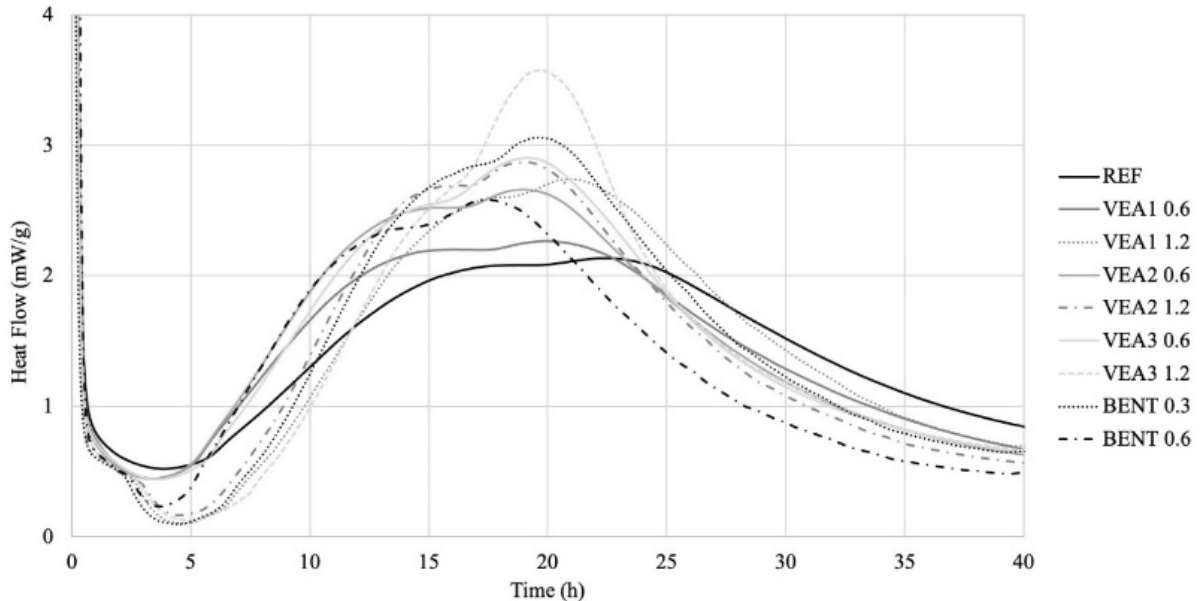
Figure 5. Heat flow over time.

3.4 Consistency index

Figure 6 shows that all mixes presented a decrease on the consistency index over time (10min, 45min and 90min resting times), as it was expected, being it a result of (a) the particle rearrangement; (b) the viscosity modifiers effect, or (c) as a result of the hydration products of the cement, even minimally. Through the results, it is possible to observe that VEA mixes have initially performed an increase on the flowability of the mixes, possibly caused by the change on the water/cement ratio due to the water content present on the VEAs. Such an increase was ceased for the longer waiting periods (90min resting time), where all mixes showed an increase on the consistency when compared to the REF mix. Previous studies with printable concretes have reported that using VEAs should result on the diminishing of the fluidity of the material on fresh state [36], [37], and that the consistency keeps increasing over time [36], as observed here. REF mix showed a 14% reduction on the consistency index during the 10 to 90min interval, while VEAs produced a decrease of up to 38%, and bentonites 40%. When looking at the percentages between the same materials, it was not observed significant changes in any of the mixes. This result show that the incorporation of the different VEAs made the mixtures less susceptible to deformation over time, which is very useful to additive manufacturing applications.

3.5 Mass density and entrained air

The mass density and the entrained air values were measured for the fresh state of mixes. Table 4 shows these results. As it may be noted, most values were found to be similar to the REF mix, in exception of mixes VEA1 on both levels, which have shown a significant decrease in the mass density, as a result of a great air entrapment percentile. For mixes with VEA1 the entrained air values were up to 40% larger than the ones obtained by the REF mix, whereas mixes BENT showed the same amount or even slightly smaller values than REF. Usually, when looking into the VEAs action, it is not always expected for them to increase the air entrained content on cementitious mixtures [17], [38], although it might sometimes come as a secondary effect depending on the family of VEA that is used [17], like methylcellulose viscosity

modifiers, for example [39]. In this case, the air entrainment would justify the lower performance of the VEA1 mixes when compared to the REF for the yield strength, structuration rate and even compressive strength obtained. For 3D printing, the incorporation of some air can be a good asset regards to the flowability of the mixture, but it is important that it does not negatively affect its mechanical performance. In this particular case, mixtures with higher amounts of entrained air (VEA1 0.6 and VEA1 1.2) performed among the worse results in the yield strength evaluation.
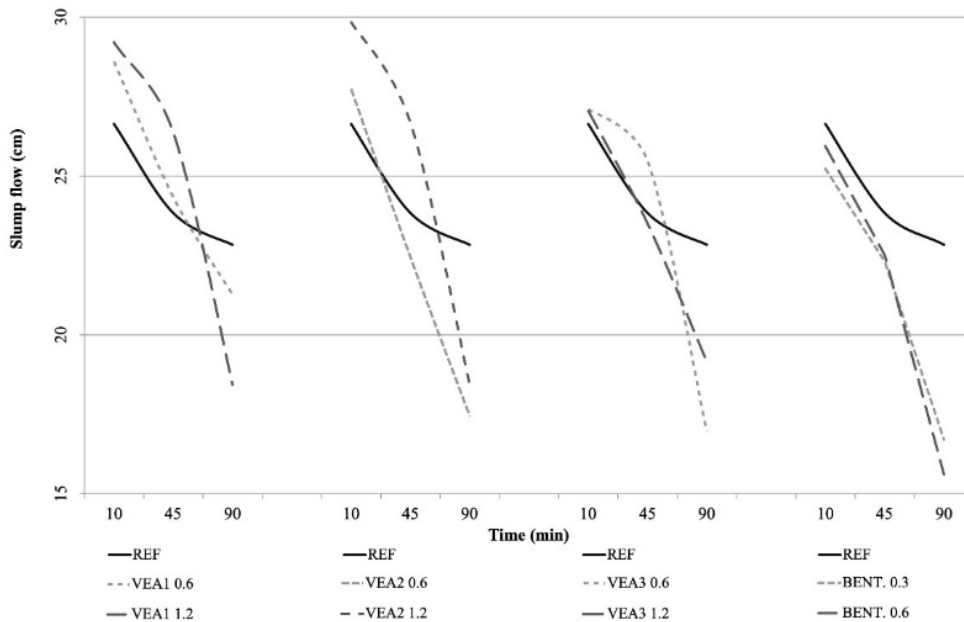
Figure 6. Consistency index.

3.6 Compressive strength

Figure 7 shows the compressive strength results on 28 days test. The results were statistically analyzed using variation analysis test (ANOVA), and the Fisher variation test. All mixes, except mixes VEA1, reached statistically the same value as the REF mix, which was 37.7MPa. Mix VEA1 1.2 had the worst result, 21% smaller than the REF mix, with only 29,6MPa. This may be due to the higher air incorporation. The compressive strength of a concrete mixture for 3D printing varies with its application, therefore there isn't a specific range of compressive strength that should be aimed for. In this particular work, the aim was to see if the incorporation of VEAs would harm mechanical performance, which was not the case for the majority of the mixtures.

3.7 Overall discussion

For this study, viscosity-enhancing admixtures were used in order to benefit the structuration rate of the materials and to improve buildability by increasing the yield strength of the mixes. The consistency index test indicates that the modifiers did perform their job of promoting an increase in the cohesion of the mixture. However, the magnitude to which bentonite produced such effects, in both trials, was shown to be more expressive than that produced by polymeric VEAs.

It is important to state that the results make it evident that there is no direct numerical correlation between the consistency index and rheometry results, since the same range of consistency values may encompass distinct flow voltages.

The increased cohesion and yield strength, mainly presented by BENT mixtures, could be justified as an acceleration of the formation of cement hydration products. However, the calorimetry test proves that all the measurements performed occurred during the mixes dormant period, implying that the main effect was due to the physical flocculation phenomenon by internal arrangement of particles, regardless of the modifier used. When Bentonite clays were incorporated to the mixtures, the thixotropic effect can also be pointed as responsible for the structuration response.
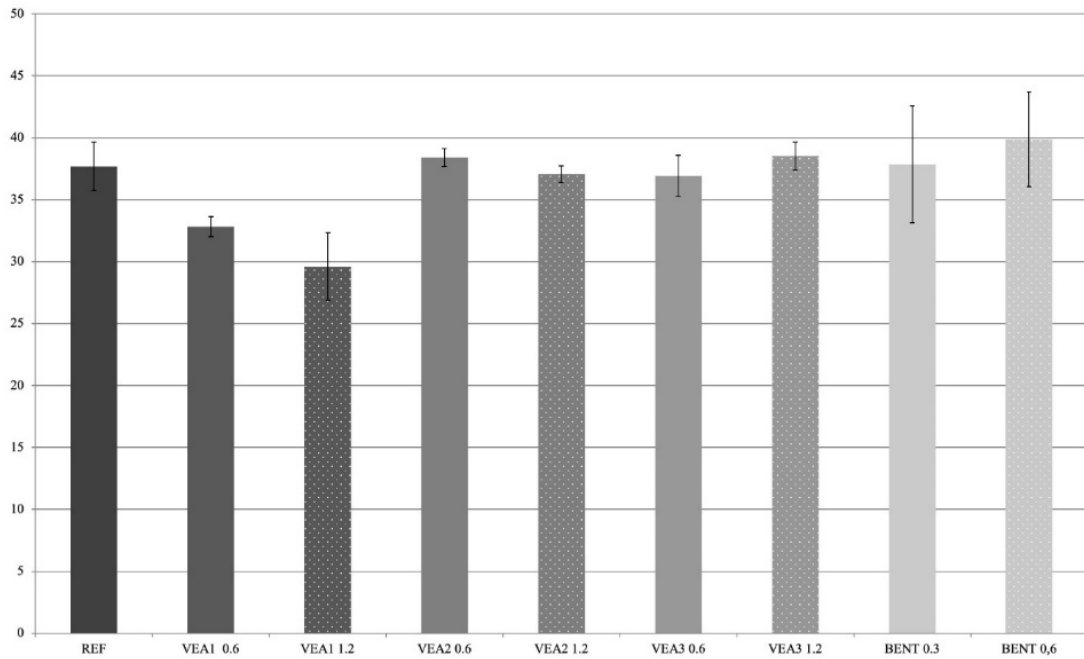
Figure 7. Compressive strength of all mixtures at age of 28 days.

Regarding the amounts of tested VEAs, the higher availability of the product in the mixture did not increase the cohesion and gain of the yield strength, except for the bentonites, where the higher content resulted in improved buildability. This could be due to (a) saturation of the VEAs into the mixture, (b) the adsorption difference with the cement particles, (c) its anionicity, (d) its molecular weight, (e) to an increase in the water/cement ratio (since the liquid admixtures were added without withdrawing the equivalent water amount of the mixture) and (f) due to an increase of the entrained air into the mixture (as it was the case with VEA1 0.6 an VEA1 1.2).

Furthermore, the presence of viscosity modifiers did not change the compressive strength values of the mixtures, except for mixtures VEA1. In this case, the higher content of incorporated air, confirmed by the fresh mass density test, justifies both the reduction in the compressive strength and also the lower performance of the product when compared to VEA2 and VEA3 in every other test.

The values of yield strength and structuration rate were higher for bentonite mixtures than those obtained by the other mixtures analyzed. The calorimetry test also proves that the improvement in the stiffness of the cementitious matrix by the presence of clay is not due to the increase of the formation of cement hydration products. Therefore, the structuration phenomenon is attributed to the internal arrangement, and especially to the formation of thixotropic gel, the formation of a three-dimensional network, free water retention and ionic attraction of the particles' effects caused by this type of material.

The results point to the technical feasibility of the use of viscosity modifiers in favor of the load bearing capacity of concrete suitable for 3D-printing, due to the increased cohesion. It should be noted, however, that not all types of VEAs would be capable of delivering the same effect, while bentonites would be the best of the options, showing a better behavior than any other modifier.

4 CONCLUSIONS

The study set to investigate the effect of three commercial viscosity enhancing admixtures and bentonite clay over the structuration rate of 3D printable concretes allows to conclude that:

- VEAs show potential for increasing the cohesion and buildability of concretes for 3D-printing;
- It was not possible to determine a direct relationship between the structuration rate, cohesion of the mixture and its buildability;

- With due control in the content, the presence of bentonite clay in concrete for 3D printing does not influence negatively the values of compressive strength;
- The use of bentonite clays in concrete mixes for 3D printing proved to be very effective in promoting cohesion and increasing buildability, being a field of research with imminent potential.

ACKNOWLEDGEMENTS

REFERENCES

[1] P. Wu, J. Wang, and X. Wang, "A critical review of the use of 3-D printing in the construction industry," *Autom. Construct.*, vol. 68, pp. 21–31, Aug. 2016.

[2] Z. Malaeb, H. Hachem, A. Tourbah, T. Maalouf, N. E. Zarwi, and F. Hamzeh, "3D concrete printing: Machine and mix design," *Int. J. Civ. Eng.*, vol. 6, no. 6, pp. 14–22, June 2015.

[3] T. Wangler et al., "Digital concrete: Opportunities and challenges," *RILEM Tech. Lett.*, vol. 1, pp. 67–75, Oct. 2016.

[4] G. Ma and L. Wang, "A critical review of preparation design and workability measurement of concrete material for largescale 3D printing," *Front. Struct. Civ. Eng.*, vol. 12, no. 3, pp. 1–19, Aug. 2017.

[5] J. Buchli et al., "Digital in situ fabrication-Challenges and opportunities for robotic in situ fabrication in architecture, construction, and beyond," *Cement Concr. Res.*, vol. 112, pp. 66–75, Oct. 2018.

[6] N. Roussel, "Rheological requirements for printable concretes," *Cement Concr. Res.*, vol. 112, pp. 76–85, Oct. 2018.

[7] D. Marchon et al., "Hydration and rheology control of concrete for digital fabrication: Potential admixtures and cement chemistry," *Cement Concr. Res.*, vol. 112, pp. 96–110, Oct. 2018.

[8] A. Perrot, D. Rangerard, and A. Pierre, "Structural built-up of cement-based materials used for 3D printing extrusion techniques," *Mater. Struct.*, vol. 49, pp. 1213–1220, Apr. 2016.

[9] N. Roussel, G. Ovarlez, S. Garrault, and C. Brumaud, "The origins of thixotropy of fresh cement pastes," *Cement Concr. Res.*, vol. 42, pp. 148–157, Jan. 2012.

[10] A. Yahia, S. Mantellato, and R. J. Flatt "Concrete rheology: A basis for understanding chemical admixtures," in *Science and Technology of Concrete Admixtures* (Series in Civil and Structural Engineering 59), P. C. Aïtcin, R. J. Flatt, Orgs., United Kingdom: Woodhead Publishing, 2015, pp. 97-127.

[11] L. Reiter et al., "The role of early age structural build-up in digital fabrication with concrete," *Cement Concr. Res.*, vol. 112, pp. 86–95, June 2018.

[12] N. Roussel and F. Cussigh, "Distinct-layer casting of SCC: The mechanical consequences of thixotropy," *Cement Concr. Res.*, vol. 38, pp. 624–632, May 2008.

[13] N. Roussel, "A thixotropy model for fresh fluid concretes: Theory, validation and applications," *Cement Concr. Res.*, vol. 36, pp. 1797–1806, Sept 2006.

[14] P. C. Aïtcin, "The importance of the water-cement and water-binder ratios," in *Science and Technology of Concrete Admixtures* (Woodhead Publishing Series in Civil and Structural Engineering, 59). P. C. Aïtcin, and R. J. Flatt, Orgs., United Kingdom: Woodhead Publishing, 2015, pp. 03-14.

[15] S. G. Gauffinet, "The rheology of cement during setting," in *Understanding the Rheology of Concrete*, N. Roussel, Org., Cambridge, UK: Elsevier, 2012.

[16] Experts for Specialized Construction and Concrete Systems. *Guidelines for Viscosity Modifying Admixtures for Concrete*. Belin, Germany: EFCA, 2006.

[17] K. H. Khayat, "Viscosity-enhancing admixtures for cement-based materials — An overview," *Cement Concr. Compos.*, vol. 20, pp. 171–188, 1998.

[18] A. Leemann and F. Winefeld, "The effect of viscosity modifying agents on mortar and concrete," *Cement Concr. Compos.*, vol. 29, pp. 341–349, 2007.

[19] H. Bessaies-Bey, "Polymères et propriétés rhéologiques d'une pâte de ciment: une approche physique générique," Ph.D. dissertation, Univ. Paris Est, France, 2015. [Online]. Available: http://www.theses.fr/2015PEST1042.

[20] R. E. Grim, *Applied Clay Mineralogy*. New York: Mcgraw-hill Book Company, Inc., 1962.

[21] P. S. Santos, *Tecnologia de Argilas Aplicada às Argilas Brasileiras*, Vol. 1 e 2, São Paulo: Editora Edgard Blucher Ltda., 1975.

[22] H. Van Olphen, *Clay Colloid Chemistry: For Clay Technologists, Geologists, and Soil Scientists*, 2. ed. Malabar, FL: Krieger Publishing Company, 1991.

[23] J. K. Mitchell and K. Soga, *Fundamentals of Soil Behavior*, 3rd ed. Hoboken, NJ: John Wiley & Sons, 2005.

[24] F. Galindo-Rosales and F. Rubio-Hernandez, "Structural breakdown and build-up in bentonite dispersions," *Appl. Clay Sci.*, vol. 33, no. 2, pp. 109–115, July 2006. http://dx.doi.org/10.1016/j.clay.2006.03.011.

[25] M. Wu and Y. Adachi, "Effects of electrolyte concentration and pH on the sedimentation rate of coagulated suspension of sodium montmorillonite," *Colloids and Surf. A: Physicochem. Eng. Asp.*, vol. 506, pp. 686–693, Oct. 2016. http://dx.doi.org/10.1016/j.colsurfa.2016.07.027

[26] Y. Zhang, Y. Zhang, G. Liu, Y. Yang, M. Wu and B. Pang, "Fresh properties of a novel 3D printing concrete ink," *Constr. Build. Mater.*, vol. 174, pp. 263–271, June 2018. http://dx.doi.org/10.1016/j.conbuildmat.2018.04.115.

[27] D. Plee et al., "Microstructure, permeability and rheology of bentonite-cement slurries," *Cement Concr. Res.*, vol. 20, no. 1, pp. 45–61, Jan. 1990.

[28] Associação Brasileira de Normas Técnicas, *NBR 5736: Cimento Portland Pozolânico*. Rio de Janeiro: ABNT, 1991.

[29] T. T. Le, Austin S. A., Lim S., Buswell R. A., Gibb A. G. F., and Thorpe T., "Mix design and fresh properties for high-performance printing concrete," *Materials and Structures*, vol. 45, no. 8, pp. 1221-1232, Jan. 2012. http://dx.doi.org/10.1617/s11527-012-9828-z.

[30] Associação Brasileira de Normas Técnicas. *NBR 13276: Argamassa para Assentamento e Revestimento de Paredes e Tetos - Preparo da Mistura e Determinação do Índice de Consistência*, 2005.

[31] Associação Brasileira de Normas Técnicas. *NBR 13278: Argamassa para Assentamento e Revestimento de Paredes e Tetos - Determinação da Densidade de Massa e do Teor de Ar Incorporado*, 2005.

[32] Associação Brasileira de Normas Técnicas. *NBR 7215: Cimento Portland: Determinação da Resistência à Compressão*, 1996.

[33] Abu-Jdayi, B., "Rheology of sodium and calcium bentonite-water dispersions: Effect of electrolytes and aging time," *International Journal of Mineral Processing*, vol. 98, no. 3-4, pp. 208-213, Mar. 2011. http://dx.doi.org/10.1016/j.minpro.2011.01.001.

[34] M. Thiedeitz, T. Kränkel, and C. Gehlen, "Thixotropy-Dependent Form Filling Ability of Cement Paste. in *Rheology and Processing of Construction Materials*. Cham: Springer, 2019. pp. 273–280.

[35] A. V. Rahul, M. Santhanam, H. Meena, and Z. Ghani, "3D printable concrete: Mixture design and test methods," *Cement Concr. Res.*, vol. 97, pp. 13–23, Mar. 2019. http://dx.doi.org/10.1016/j.cemconcomp.2018.12.014.

[36] Z. Li, L. Wang, and G. Ma, "Method for the enhancement of buildability and bending resistance of three-dimensional-printable tailing mortar," in *3D Concrete Printing Technology*, 1st ed., J.G. Sanjayan, A. Nazari, and B. Nematollahi, Eds., Amsterdam, The Netherlands: Elsevier, 2019. pp. 161–180.

[37] M. Rubio, M. Sonebi, and S. Amziane, "Fresh and rheological properties of 3d printing bio-cement-based materials," 2nd Int. Conf. Bio-based Build Mater., June 2017.

[38] M. Lachemi, K. M. A. Hossain, V. Lambros, P. C. Nkinamubanzi, and N. Bouzoubâa, "Self-consolidating concrete incorporating new viscosity modifying admixtures," *Cement Concr. Res.*, vol. 34, no. 6, pp. 917–926, June 2004.

[39] B. Łaźniwska-Piekarczyk, "The type of air-entraining and viscosity modifying admixtures and porosity and frost durability of high performance self-compacting concrete," *Constr. Build. Mater.*, vol. 40, pp. 659–671, Mar 2013.

Rev. IBRACON Estrut. Mater., vol. 13, no. 4, e13412, 2020

12/12

IBRACON Structures and Materials Journal
Revista IBRACON de Estruturas e Materiais

ORIGINAL ARTICLE

Compression resistance of repaired structural concrete elements after core extraction

Resistência à compressão de elementos estruturais de concreto reparados após extração de testemunhos

Tauana Bartikoski[a]
Vanessa Oerle Kautzmann[a]
Vinicius de Kayser Ortolan[a]
Bernardo Fonseca Tutikian[b]
Regina Modolo[b]

[a]Universidade do Vale do Rio dos Sinos – UNISINOS, São Leopoldo, RS, Brasil
[b]Universidade do Vale do Rio dos Sinos – UNISINOS, Programa de Pós-graduação em Engenharia Civil – PPGEC, São Leopoldo, RS, Brasil

Abstract: Core sampling for testing is considered a reliable method to provide information on structural materials and is one of the most implemented techniques in the evaluation of concrete elements. However, core drilling results in a decrease in cross section that can compromise structural mechanical strength even if the extracted section is repaired. Norm NBR 7680-1 recommends dry pack as a repair method but also allows the use of other techniques as long as its effectiveness is proven. This work evaluated the resistance of repaired structural prototypes after core drilling sampling. Concrete blocks with 20 MPa resistance were produced from which cores of 100 mm, 75 mm and 50 mm in diameter were extracted. The blocks were repaired with 20 MPa concrete, grout and dry pack techniques. The reconstitution with concrete showed poorest performance, while dry pack led to strengths even higher when compared to reference values.

Keywords: core sampling, dry pack, grout, compression strength.

Resumo: A extração de testemunhos para ensaios é considerada um método confiável no fornecimento de dados do material que compõe uma estrutura, sendo um dos mais utilizados na avaliação de elementos de concreto. Porém, a retirada de volume de material representa a diminuição da seção transversal, podendo comprometer a resistência mecânica da estrutura, mesmo com recomposição da seção. Apesar de indicar o *dry pack* como técnica de preenchimento, a NBR 7680-1 permite o uso de outros meios de reconstituição, desde que comprovada sua eficácia. Este artigo avaliou a resistência à compressão de protótipos estruturais submetidos à extração de testemunhos reconstituídos. Foram preparados blocos de concreto C20 dos quais extraiu-se testemunhos nos diâmetros de 100, 75 e 50 mm. Os blocos foram preenchidos com concreto C20, *graute* e *dry pack*. O reparo com concreto demonstrou o pior desempenho, enquanto o *dry pack* resultou em resistências superiores aos blocos de referência.

Palavras-chave: extração de testemunhos, *dry pack*, graute, resistência à compressão.

1 INTRODUCTION

On-site evaluation methods are used to evaluate the compression resistance of reinforced concrete. This is necessary due to uncertainties in the properties of concrete or to better assess the loading capacity of the structural element [1]–[3]. Among *in situ* methods, core extraction is considered the most reliable since it replicates closely the real properties of the material [4]–[7]. Core

extraction results are considered superior to mold casting since core samples are subjected to the same environmental and load conditions as the source material during curing and aging [8].

Core extraction is recognized as a semi-destructive technique [9], [10] since part of the volume of the structure is lost in sampling and small fissures may appear from the extraction process. This may result in a decrease in mechanical strength of the structure and compromise either performance or safety. In order to prevent these, the missing section of the element must be reconstituted with material capable of, at least, restoration to its initial condition [11], [12].

There are several reference works indicating techniques and materials for repairing concrete and specific norms which recommend suitable techniques for a variety of situations [13]–[16]. In Brazil, norm ABNT NBR 7680-1:2015 [17] recommends different techniques depending on the sample extracted. Compacted mortar with a dry consistency, commonly known as dry pack, is recommended for reconstitution of holes drilled horizontally, as in pillars and beams. Structural grout or pourable concrete is recommended for holes drilled vertically, as in slabs. However, ABNT NBR 7680-1:2015 allows the use of other techniques and materials as long as their efficiency is proven. In specific cases, besides grout and dry pack, concrete itself may be used as a repair material [18]–[23]

Compatibility between the original structure and repair material is another important aspect in reconstitution. To this end, several properties are considered relevant but Morgan [18] denotes the modulus of elasticity and volumetric variance of the repair material. In the case of using concrete itself as the repair material, special attention must be given to the filling process since adhesiveness between new and old concrete might be hard to achieve and the use of additional bonding agents might be necessary [24], [25]. This concern is not limited only to concrete as a repair material. Several works stress the need to promote adhesiveness to the drilled structure regardless of the repair material, be it through bonding agents or mechanical methods [19], [20], [26]–[30]

The use of grout is advantageous because it reaches elevated resistances early on and is a material with a high degree of fluidity, compactness and uniformity. Because of its fluidity, grout usually requires molds [31]–[33]. On the other hand, there is a resistance to adhesiveness since fluid materials are more affected by shearing motions between the concrete surface and repairing material [34].

The use of dry pack is more suitable for situations in which molding is not possible since it lacks fluidity. Dry pack can be used for repairs in either horizontal or vertical directions and is less susceptible to shrinkage due to its low water/cement ratio. This also results in less fissures and more of adhesiveness to the drilled structure [28], [33]. This technique is also recommended to fill deep cavities with limited accessibility [35].

Concrete itself can also be used as a repair material in situations in which a large volume must be filled back in. Compared to grout or plaster, it is a more economical alternative and tends to have thermal dilation properties similar to the structure to be repaired while also allowing a more uniform finish [26], [28].

Core sample dimensions are relevant to testing, especially with regards to diameter-to-height ratio. Some studies have noted that there is no difference in compression resistance values with regards to the dimensions of core samples [36]–[39]. However, other studies report that samples with smaller diameters present lower compression resistance values [40], [41]. Overall, a recommended height-to-diameter ratio of 2 was considered necessary to avoid the use of correction factors in the results [17], [36]–[39], [42], [43].

Core sample extraction has the potential to create micro-fissures in concrete. This not only reduces the mechanical resistance of the material but also can induce lower resistance in samples with smaller diameters since they have a higher surface-to-volume ratio [36], [44]. The minimum sample diameter recommended by ASTM is of 100 mm [16] while British Standards EN 12504 allows compression testing on samples as small as 50 mm in diameter without the need for correction factors [45]. Norm ABNT NBR 7680:2015 recommends a minimum diameter of 100 mm for core samples but allows diameters of 75 mm and 50 mm in specific situations [17]. Another factor to be considered is the concrete class which causes further effects in compression tests of samples of varying diameter. The volume of the sample may or may not be important depending on the mechanical resistance of the concrete. Concretes with higher resistance are less likely to develop fissures during the extraction process when compared to concretes with lower resistance. Higher resistance concretes also present a more robust transition zone with higher adhesiveness surface with less flaking [44].

The objective of this study is to further contribute to the analysis of different repair methods in finished structures from which core samples have been extracted. In particular, structural grout and dry pack techniques were analyzed and compared. Also, since there were divergences with respect to the effect of sample diameters, comparative mechanical tests were conducted on blocks with different repair sizes.

2 METHODOLOGY

2.1 Materials

A total of 24 concrete blocks of class C20 were produced in a batch plant and divided in 3 groups, each containing 8 blocks. Group 1 contained clocks measuring 500 mm × 300 mm × 230 mm, group 2 contained clocks measuring 375 mm × 225 mm × 180 mm and group 3 contained clocks measuring 250 mm × 250 mm × 150 mm. Concrete dosing followed the methodologies of Tutikian and Helene [46] and Gil et al. [47]. This procedure was adopted so the extracted core samples had a constant volume ratio with respect to the original concrete blocks.

Following core extraction, three different recovery methods were used. The fist method made use of concrete with the same characteristics as the original block. The concrete mixture was prepared in a vertical axis mixer. The second method utilized industrial-grade structural grout made from Portland cement, quartz sand and special additives. Grout was prepared with a water/solid material ratio of 0.12 and aging compression tests measured a resistance of 42 MPa after 7 days and 50 MPa after 28 days. The third method utilized dry pack made from a thixotropic and single component industrial plaster specific for structural repairs. Preparation used a water/solid material ratio of 0.13 and aging compression tests measured a resistance of 30 MPa after 7 days and 40 MPa after 28 days. Coarse basalt aggregate with a maximum granulometry of 9.5 mm was incorporated between layers as proposed by norm ABNT NBR 7680-1, Anex A [17].

2.2 Curing of concrete blocks

Concrete blocks were demolded and conditioned in a climate-controlled chamber kept at 23 ± 2 °C and relative air humidity of 97% for 28 days. Following this period, core samples were extracted.

2.2.1 Core sample extraction

Cylindrical core samples were extracted from the cured blocks. Procedures followed ABNT NBR 7680-1 [17] recommendations with a height/diameter ratio (h/d) of 2. Three distinct sample diameters were chosen: Ø100 mm, Ø75 mm e Ø50 mm with the last 2 reserved for concrete blocks with higher reinforcement.

Table 1 displays the characteristics of the concrete, source concrete block dimensions, sample dimensions, number of samples extracted, % volume of the sample relative to the block and the type of material used in the repair. From the blocks measuring 500 mm × 300 mm × 230 mm and 375 mm × 225 mm × 180 mm, 2 samples with diameters of 100 mm and 75 mm were extracted, respectively. From the blocks measuring 250 mm × 250 mm × 150 mm, 4 samples 50 mm in diameter were extracted. The position of each hole of extraction kept at distance of at least one sample-diameter from each other, and one sample-diameter with respect to the edges of the block as seen in Figure 1. Two blocks from each dimension were kept intact as reference. The drilled blocks had samples extracted horizontally in a direction perpendicular to the pouring of concrete. The drill was diamond-crowned and water-cooled.
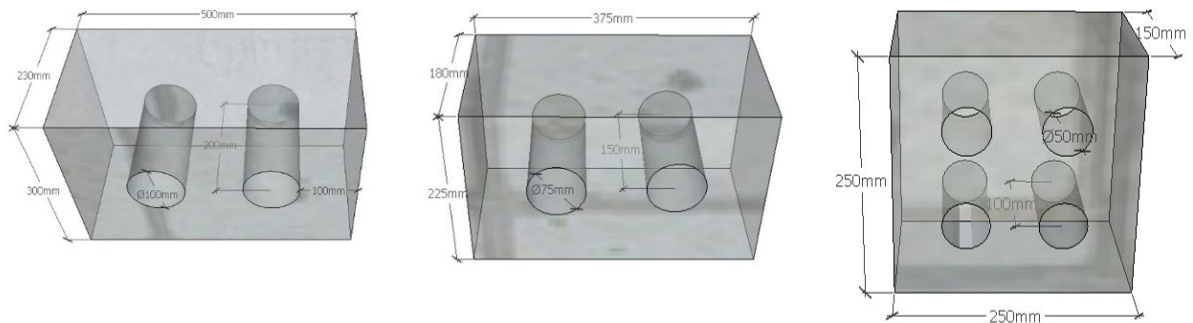
Figure 1 – Drilling hole placement according to block dimension

IBRACON Struct. Mater. J., vol. 13, no. 4, e13413, 2020

3/9

Table 1 – Concrete block and core sample identifications

Block Resistance Class	Block Dimensions			Sample Size		Number of Samples	% Extracted Volume	Type of Repair
	L (mm)	H (mm)	W (mm)	D (mm)	H (mm)			
C20	500	300	230	-	-	0	0	Reference
C20	500	300	230	-	-	0	0	Reference
C20	500	300	230	100	200	2	9	C20
C20	500	300	230	100	200	2	9	C20
C20	500	300	230	100	200	2	9	*Grout*
C20	500	300	230	100	200	2	9	*Grout*
C20	500	300	230	100	200	2	9	*Dry Pack*
C20	500	300	230	100	200	2	9	*Dry Pack*
C20	375	225	180	-	-	0	0	Reference
C20	375	225	180	-	-	0	0	Reference
C20	375	225	180	75	150	2	9	C20
C20	375	225	180	75	150	2	9	C20
C20	375	225	180	75	150	2	9	*Grout*
C20	375	225	180	75	150	2	9	*Grout*
C20	375	225	180	75	150	2	9	*Dry Pack*
C20	375	225	180	75	150	2	9	*Dry Pack*
C20	250	250	150	-	-	0	0	Reference
C20	250	250	150	-	-	0	0	Reference
C20	250	250	150	50	100	4	8	C20
C20	250	250	150	50	100	4	8	C20
C20	250	250	150	50	100	4	8	*Grout*
C20	250	250	150	50	100	4	8	*Grout*
C20	250	250	150	50	100	4	8	*Dry Pack*
C20	250	250	150	50	100	4	8	*Dry Pack*

2.2.2 Block repair

Block repair was conducted utilizing C20 concrete, grout and dry pack. Each block was prepared according to NBR 7680-1 [17], with the internal surface of each hole cleaned and saturated with moisture. This procedure was realized in order to ensure a better adhesiveness between the concrete block and the repair material [34], [48], [49]. Concrete repair was conducted by inserting fresh C20 material in molds and extruding it into the hole. After hardening, excess concrete was shaved off. Grout repair followed the same procedure as concrete as seen in Figure 2. Dry pack repair was conducted according to NBR 7680-1, Annex A [17]. The drilled hole was filled with alternating layers of mortar of thickness of less than 5 cm and coarse gravel of thickness between 9.5 mm and 25 mm. A cylindrical pestle 25 mm in diameter was used to push in and compact each layer as seen in Figure 3. Once filled, the external surface of the repair was smoothed out with a metallic trowel and curing allowed to happen. Figure 4 shows the finished repaired blocks with concrete, grout and dry pack.

Figure 2 – Molds for concrete and grout repair
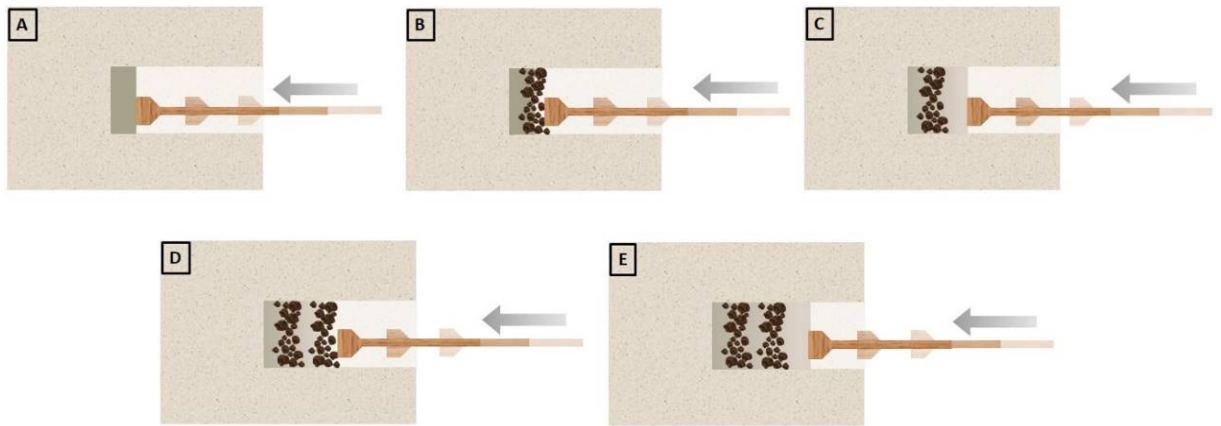
Figure 3 – Dry pack filling procedure

Figure 4 – Finalized repaired blocks with concrete, grout and dry pack (left to right)

2.2.3 Curing of repair material and testing

Repair material applied to the blocks was cured for 7 days with water spraying. After curing, the repaired block was allowed to age for a total of 28 days from the date of reconstitution. Compressions tests were performed in a universal press and neoprene slabs were used to distribute the load along the contact surface as seen in Figure 5.

Figure 5 – Compression test in universal press

3 RESULTS AND DISCUSSION

Results are presented in Table 2 and Table 3. Table 2 displays the compression resistance of cylinders measuring Ø 10 cm × 20 cm of C20 and grout after 28 days of aging. Table 3 displays the compression resistance of the concrete blocks with respect to each repair material and core sample size. The potential tension values are in accordance with norm ABNT NBR 12655:2015 [50]. Table 3 shows that, of the repaired concrete blocks, the ones with dry pack repair had the best performance. In particular, the repair with 100 mm diameter had a compression resistance 8.2% higher than the reference blocks.

Table 2 Repair material compression resistance

Type of material	Load (kN)	Tension (MPa)	Average Tension (MPa)
C20	303.41	38.6	39.1
	310.31	39.5	
Graute	540.64	68.9	62.0
	432.09	55.0	

Table 3 Concrete Block Compression Resistances

Material	Ø (mm)	Tension (MPa)	Potential Tension (MPa)	Ø (mm	Tension (MPa)	Potential Tension (MPa)	Ø (mm	Tension (MPa)	Potential Tension (MPa)
Reference	-	11.0 8.3	11.0	-	10.1 13.5	13.5	-	9.5 12.1	12.1
C20		8.0 8.4	8.4		10.0 10.6	10.6		7.5 6.5	7.5
Grout	100	10.1 11.1	11.1	75	7.2 8.1	8.1	50	6.6 7.3	7.3
Dry pack		8.6 11.9	11.9		9.6 12.9	12.9		9.1 9.1	9.1

Comparisons of the performance of the repaired blocks and reference blocks are shown in Figure 6. Blocks with 100 mm diameter extractions repaired with grout and dry pack were able to resist compression levels higher than the reference blocks. As extraction size decreased, repaired blocks underperformed with respect to reference blocks. The worst performance was obtained with the 75 mm diameter extraction block repaired with grout: a 40% reduction with respect to the reference block.
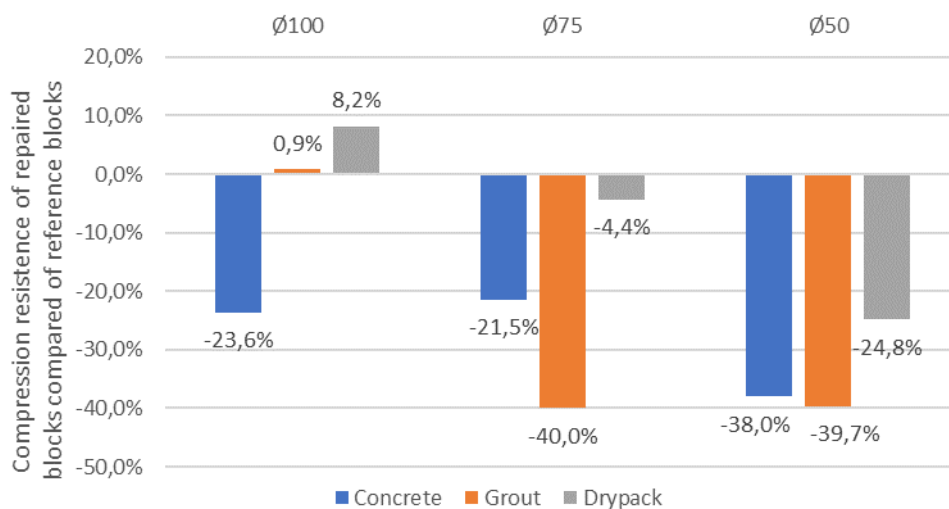
Figure 6 – Compression resistance of repaired blocks compared to reference blocks

IBRACON Struct. Mater. J., vol. 13, no. 4, e13413, 2020

6/9

Figure 7 shows the effect of diameter of the extracted region on the compression resistance of each repair material. Overall, it can be stated that a 50 mm diameter extraction compromised the mechanical resistance of the repaired block the most regardless of the repair material. This was likely a result of damage to the concrete block in the extraction of this smallest sample. If the concrete itself was less resistant, core extraction could lead to the appearance of micro-fractures and flaking of aggregates. In this case, a core sample with a higher area/volume ratio became a relevant factor in the loss of mechanical properties.
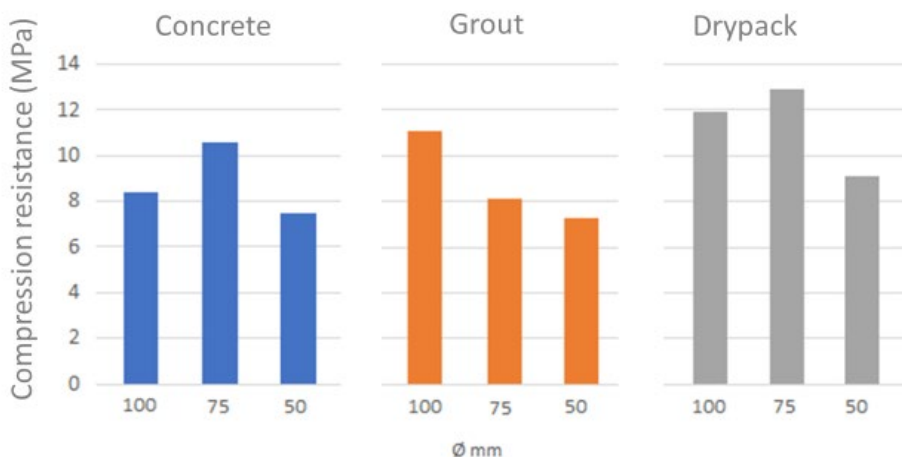
Figure 7 – Relative effect of diameter in repair material

Overall, dry pack presented the best efficiency in recovering the mechanical properties of the repaired blocks. This might be related to the water/cement ratio in this type of material. Smaller water content in the mixture leads to less shrinkage which is highly important in the structural repair of concrete. A shrinking repair material might leave gaps between the original material and filled volume so that the block would tend to fracture under compression before it can incorporate the resistance of the repair material. This phenomenon can be observed in the fracture characteristics of each block in Figure 8, with the fracture occurring in the interface between the repaired core and the block. While this may explain dry pack performance, comparison of the water/solid ratio between dry pack and grout showed minimal differences insufficient to cause such difference in performance (0.13 for dry pack and 0.12 for grout). In this case, compaction effects associated with the filling technique were likely to have influenced the results. In the case of grout, repair material was poured in with no special compaction executed. Dry pack, in the other hand, was filled in several packed layers and the energy of compaction could have induced greater adhesiveness and left fewer gaps in the interface with the block.

Figure 8 – Fracture characteristics of each repaired block (left to right: C20, grout and dry pack)

4 CONCLUSIONS

Results of this study demonstrated that dry pack was the most efficient filling material to repair core sample extraction volumes in concrete elements. Concrete itself was shown to be an inefficient repair material with the repaired block having a 38% reduction in compression resistance. Water content in the repair material might be considered an important factor in the performance of repaired blocks.

The diameter of core samples also influenced the results. Large core diameters resulted in repaired blocks that could exceed reference results. In the other hand small core diameters, which contain a higher surface/volume ratio, performed poorly probably due to damages to the concrete block structure caused during extraction.

REFERÊNCIAS

[1] A. Neville, "Core tests: easy to perform, not easy to interpret," *Concr. Int.*, vol. 23, no. 11, pp. 59–68, 2001.

[2] A. F. Domínguez and J. J. H. Albear, "Relación entre laresistencia a compresión de testigos y probetas de hormigón: estado del arte y propuestas para actualización de la normativa cubana," in *Ann. 11ª Conf. Cient. Téc. Construc.*, Havana, 2016.

[3] A. R. Grubbs, A. C. Carroll, A. K. Schindler, and R. W. Barnes, *Evaluation of In-place Concrete Strength by Core Testing* (Research Report 2). Alabama: Alabama Depart. Transp., Nov. 2016, ALDOT Project 930-828.

[4] American Concrete Institute, *Guide for Obtaining Cores and Interpreting Compressive Strength Results*, 214.4R-100, 2010.

[5] A. Masi and M. Vona, "Prove distruttive e non distruttive su materialie delementi strutturali di edificie sistenti in cemento armato," in *Conv. 12° Nazio. AIPnD*," Potenza, 2007.

[6] M. Tuncan, O. Arioz, K. Ramyar, and B. Karasu, "Assessing concrete strength by means of small diameter cores," *Constr. Build. Mater.*, vol. 22, no. 5, pp. 981–988, 2008, http://dx.doi.org/10.1016/j.conbuildmat.2006.11.020.

[7] A. S. F. D. S. Martins and H. M. Maia Fo., "Verificação da resistência do concreto in loco: métodos de ensaios mais usuais," *Vetor*, vol. 25, no. 2, pp. 25–40, 2015.

[8] H. J. N. Lima, R. L. Silva, J. M. Silva, and G. S. S. A. Melo, "Avaliação da resistência à compressão do concreto: comparativo entre corpo de provas de moldados e testemunhos extraídos," *InterScientia*, vol. 6, no. 2, pp. 2–11, 2018, http://dx.doi.org/10.26843/interscientia.v6i2.881.

[9] M. H. C. Sahuinco, "Utilização de métodos não destrutivos e semi-destrutivos na avaliação de pontes de concreto," Ph.D. dissertation, Esc. Politéc., Univ. São Paulo, São Paulo, SP, 2011.

[10] B. Kasal, M. Drdacky, and I. Jirovski, "Semi-destructive methods for evaluation of timber structures," *Trans. Built Environ.*, vol. 66, no. 8, 2003.

[11] J. L. R. Ortiz and J. M. B. Díaz, "Evaluación de laresistencia de pilares de hormigón por medio de testigos cortados: nuevasaportaciones," *Rev. Ing. Constr.*, vol. 28, no. 276, pp. 57–69, 1975.

[12] M. Vona and D. Nigro, "Evaluation of the predictive ability of the in situ concrete strength through core drilling and its effects on the capacity of the RC columns," *Mater. Struct.*, vol. 48, no. 4, pp. 1043–1059, 2015, http://dx.doi.org/10.1617/s11527-013-0214-2.

[13] American Concrete Institute, *Guide to Concrete Repair*, 546-14, 2014.

[14] International Organization for Standardization, *Testing of Concrete – Part 4: Strength of Hardened Concrete*, ISO 1920-4, 2005.

[15] American Society for Testing and Materials, *Standard Specification for Packaged, Dry, Rapid-Hardening Cementitious Materials for Concrete Repairs*, ASTM C928/C928M-13, 2013.

[16] American Society for Testing and Materials, *Standard Specification for Packaged Dry, Hydraulic-Cement Grout (Nonshrink)*, ASTM C1107/C1107M-17, 2017.

[17] Associação Brasileira de Normas Técnicas. *Concreto: Extração, Preparo, Ensaio e Análise de Testemunhos de Estruturas de Concreto – Parte 1: Resistência à Compressão Axial*, ABNT NBR 7680-1, 2015.

[18] D. R. Morgan, "Compatibility of concrete repair materials and systems," *Constr. Build. Mater.*, vol. 10, no. 1, pp. 57–67, 1996, http://dx.doi.org/10.1016/0950-0618(95)00060-7.

[19] S. C. Fagury and J. B. L. Liborios, "A utilização de concretos e pastas, com adição de sílica ativa e aditivo superplastificante, como material de reparo para estruturas de concreto," in *An. Cong. Bras. Eng. Ciên. Mat.*, Natal, 2002.

[20] F. L. Gondim, "Estudo da interface entre o concreto e o material de reparo mediante microscopia," M.S. thesis, Univ. Fed. Uberlândia, Uberlândia, MG, 2005.

[21] L. Tula, P. S. F. Oliveira, and P. Helene, "Grautes para reparo," in *VII Cong. Lat. Ame. Patol. Constr.*, Madrid, 2003, pp.139-152.

[22] P. D. Krauss and D. J. Naus, "Repair materials and techniques for concrete structures in nuclear power plants," *Nucl. Eng. Des.*, vol. 181, no. 1-3, pp. 71–89, 1998, http://dx.doi.org/10.1016/S0029-5493(97)00336-1.

[23] J. H. Paul, "Repair, renovation and strengthening of concrete structures," in *Eval. Rehabil. Concr. Struct.: Proc. ACI Int. Conf.*, Mexico City, Sept. 2002.

[24] M. Z. B. Jumaat, M. H. Kabir, and M. Obaydullah, "Structural performance of reinforced concrete beams repairing from spalling," *Eur. J. Sci. Res.*, vol. 45, no. 1, pp. 89–102, 2010.

[25] J. S. C. Astorqui, "Patología de lasestructuras de hormigón," in *Manual de Patología de Laedificación*, V. Rodríguez, Ed., Madri: Univ. Politéc. Madri, 2004, chap. 1, pp. 6-84.

[26] M. Marcelli, *Sinistros na Construção Civil: Causas e Soluções Para Danos e Prejuízos em Obras*, 1st ed. São Paulo: PINI, 2007.

[27] J. Nakamura, "Reparo, reforço e recuperação de concreto," *Rev. Techne*, vol. 146, 2009.

[28] B. M. B. Albergaria, "Inspeção e reabilitação de estruturas de betão armado," M.S. thesis, Inst. Sup. Eng. Porto, Porto, 2013.

[29] F. Pacheco, R. Christ, A. M. Gil, and B. F. Tutikian, "Aplicação de MEV e microtomografia 3D na investigação da distribuição de fibras em compósitos cimentícios avançados," *Rev. IBRACON Estrut. Mater.*, vol. 9, no. 6, pp. 824–841, Dec 2016.

[30] J. J. O. Andrade and B. F. Tutikian, "Resistência mecânica do concreto," in *Concreto: Ciência e Tecnologia*, G. C. Isaia, Ed., São Paulo: IBRACON, 2011, chap. 17, pp. 615-651.

[31] E. A. Silva, "Técnicas de recuperação e reforço de estruturas de concreto armado," Undergraduate thesis, Univ. Anhembi Morumbi, 2006.

[32] M. V. Z. Stotz, "Métodos de recuperação de estruturas de concreto armado deterioradas pela corrosão nas armaduras," *Rev. Especialize*, vol. 10, no. 10, pp. 1–14, 2015.

[33] L. R. Fernandes, "Metodologias para produção de pré-fabricados em concreto armado e protendido com abordagem das manifestações patológicas que surgem na fabricação e montagem," Undergraduate thesis, Esc. Eng., Univ. Fed. Minas Gerais, Belo Horizonte, MG, 2015.

[34] H. Beushausen, B. Höhlig, and M. Talotti, "The influence of substrate moisture preparation on bond strength of concrete overlays and the microstructure of the OTZ," *Cement Concr. Res.*, vol. 92, pp. 84–91, 2017, http://dx.doi.org/10.1016/j.cemconres.2016.11.017.

[35] M. D. Graeser and M. C. Jensen, "South channel dam rehabilitation project-successfully addressing dam rehabilitation challenges," in *Proc. 6th IAHR International Symposium on Hydraulic Structures*, Portland, 2016.

[36] J. O. Vieira Fo., "Avaliação da resistência à compressão do concreto através de testemunhos extraídos: contribuição à estimativa do coeficiente de correção devido aos efeitos broqueamento," Ph.D. dissertation, Esc. Politéc., Univ. São Paulo, São Paulo, SP, 2007.

[37] E. Castro, "Estudo da resistência à compressão do concreto por meio de testemunhos de pequeno diâmetro e esclerometria," Master thesis, Prog. Pós-grad. Eng. Civ., Univ. Fed. Uberlândia, Uberlândia, MG, 2009.

[38] J. M. A. Almeida, B. V. Silva, and J. M. Désir, "Resistência à compressão simples de concretos através da extração de testemunhos com pequenas dimensões," in *An. 56° Cong. Bras. Concr.*, Natal, 2014.

[39] L. C. P. Silva Fo. and P. Helene, "Análise de estruturas de concreto com problemas de resistência e fissuração," in *Concreto: Ciência e Tecnologia*, G. C. Isaia, Ed., São Paulo: IBRACON, 2011. chap. 32, pp. 1129-1174.

[40] F. M. Bartlett and J. G. MacGregor, "Effect of core diameter on concrete core strengths," *Mater. J.*, vol. 91, no. 5, pp. 460–470, 1994.

[41] M. H. F. Medeiros and A. P. B. Capraro, "Resistência a compressão em testemunho de concreto: influência do fator de esbeltez, diâmetro da amostra e método de extração," *Rev. Eletronica Eng. Civ. Goias*, vol. 13, no. 1, pp. 240–250, 2017.

[42] American Association of State Highway and Transportation Officials, *Obtaining and Testing Drilled Cores and Sawed Beams of Concrete*, T24, 2009.

[43] P. C. Bilesk and C. E. S. Tango, "Avaliação do concreto de peças estruturais pequenas pelo método dos cilindros montados," *Rev. Tecnol. Constr.*, vol. 121, pp. 92–98, 2007.

[44] A. C. Carroll, A. R. Grubbs, A. K. Schindler, and R. W. Barnes, *Effect of Core Geometry and Size on Concrete Compressive Strength* (Research Report 1). Alabama: Alabama Depart. Transp., Jul. 2016, ALDOT Project 930-828.

[45] British Standards, *Testing Concrete in Structures – Cored Specimens: Taking, Examining and Testing in Compression*, BS EN 12504-1, 2009.

[46] B. F. Tutikian and P. Helene, "Dosagem dos concretos de cimento Portland," in *Concreto: Ciência e Tecnologia*, G. C. Isaia, Ed., São Paulo: IBRACON, 2011, 2v., chap. 12, pp. 415-451.

[47] A. M. Gil, K. H. Khayat, and B. F. Tutikian, "An experimental approach to design self-consolidating concrete," *Constr. Build. Mater.*, vol. 229, no. 30, pp. 116939, 2019, http://dx.doi.org/10.1016/j.conbuildmat.2019.116939.

[48] J. S. Lapa, "Patologia, recuperação e reparo das estruturas de concreto," Undergraduate thesis, Esc. Eng., Univ. Fed. Minas Gerais, Belo Horizonte, 2008.

[49] I. De la Varga, J. F. Munoz, D. P. Bentz, R. P. Spragg, P. E. Stutzman, and B. A. Graybeal, "Grout-concrete interface bond performance: effect of interface moisture on the tensile bond strength and grout microstructure," *Constr. Build. Mater.*, vol. 170, pp. 747–756, 2018, http://dx.doi.org/10.1016/j.conbuildmat.2018.03.076.

[50] Associação Brasileira de Normas Técnicas, *Versão Corrigida: 2015 – Concreto de Cimento Portland – Preparo, Controle, Recebimento e Aceitação – Procedimento*, ABNT NBR 12655:2015, 2015.

ORIGINAL ARTICLE

Three-dimensional modelling of wall-beam interaction in structural masonry buildings

Modelagem tridimensional da interação parede-viga em edifícios de alvenaria estrutural

Anna Christinna Secundo Lopes[a] (iD)
Joel Araújo do Nascimento Neto[a] (iD)
Klaus André de Sousa Medeiros[b] (iD)
Daniel Nelson Maciel[a] (iD)

[a]Universidade Federal do Rio Grande do Norte – UFRN, Programa de Pós-graduação em Engenharia Civil, Natal, RN, Brasil
[b]Universidade Federal Rural do Semi-Árido – UFERSA, Departamento de Engenharias, Angicos, RN, Brasil

Abstract: Wall-beam interaction (wall-beam system) is a phenomenon that requires further investigation in order to be consistently incorporated into structural building analysis. Researchers such as Wood, Rosenhaupt, Burhouse, Stafford Smith, Navaratnarajah, Davies, Riddington and Armed conducted tests on specimens to develop simplified analysis models, emphasizing the behavior of walls without openings under one span beams. The present study performed computational analysis using an specific equivalent frame model in order to study the behavior of the wall-beam system in more complex wall and beam arrangements. The examples considered the linear elastic behavior of materials and consisted of assessing stress distribution and displacements on support beams, in addition to stresses at the bottom of the walls, for panels in a real structural masonry building. Two- and three-dimensional analyses were used and the results showed the importance of three-dimensional analysis of wall interconnections. The effects of eccentricity between the vertical plane of the wall and horizontal support beam axis were also evaluated, showing the strong influence of twisting moments in support beam design .

Keywords: structural masonry, wall-beam composite behavior, computational modeling, equivalent frame, wall-beam eccentricity.

Resumo: A interação entre paredes estruturais e vigas de transição (sistema parede-viga) é um fenômeno que ainda carece de estudos para se realizar sua consideração de forma sistemática na análise de edifícios. No passado, pesquisadores como Wood, Rosenhaupt, Burhouse, Stafford Smith, Navaratnarajah, Davies, Riddington e Armed, realizaram experimentos e buscaram desenvolver modelos de cálculo simplificados para representar esse fenômeno. Entretanto, os estudos se limitaram ao caso de vigas biapoidas e paredes sem aberturas. O estudo apresentado neste artigo teve como objetivo realizar análises por meio de modelagem computacional do sistema parede-viga em situações mais complexas de comportamento, empregando-se um específico modelo de barras equivalentes. Os exemplos elaborados consideraram comportamento elástico linear para os materiais e consistiram na avaliação dos esforços e deslocamentos verticais nas vigas de apoio, além das tensões na base das paredes, para painéis de um edifício real de alvenaria estrutural. A modelagem computacional foi elaborada segundo abordagens bidimensionais e tridimensionais da estrutura. Dentre os resultados obtidos, destaca-se a importância da consideração do efeito das amarrações entre painéis de alvenaria via modelo tridimensional devido à intensa redistribuição de esforços verificada. Também foi realizada a análise de uma possível excentricidade no sistema parede-viga, o que permitiu verificar que a consideração dos momentos de torção influenciou consideravelmente no dimensionamento das vigas de suporte.

Palavras-chave: alvenaria estrutural, interação parede-viga, modelagem computacional, modelo de barras equivalentes, excentricidade parede-viga.

1 INTRODUCTION

Although structural masonry is a widely used system in the Brazilian construction industry, new studies are needed to enhance knowledge of its structural behavior. One example is the interaction between masonry walls and the corresponding support structures, where there is a need to develop simple and consistent calculation models to determine internal forces and stresses. In addition, designing taller buildings, making architecture layouts more flexible and the use of subsoils and ground floors as common areas for residents highlight the need for support structures, thereby justifying in-depth studies on wall-beam interaction, also known as the arching effect.

The arch effect, or flow stress arching inside structural walls, is only one of the aspects for engineers to assess. Thus, for the purposes of this study, the authors preferred to refer to this phenomenon as wall-beam interaction or wall-beam system.

According to Barbosa [1], interaction changes the distribution of wall stresses and support beam forces that must be considered in the design. The transfer of vertical loads from a masonry wall to its foundations depends on the type of support. Walls can be supported by strip footings, or simply supported such as regularly spaced pilotis or foundation piles. Walls on strip footings exhibit nearly uniform distribution at the bottom, causing small direct load transfers to the ends of the span. For simply supported beams, the load on the wall tends to travel to the sections near the supports since they are regions of greater stiffness.

Paes [2] reported that this effect is relevant when the interaction between the masonry wall and its support structure is analyzed. This behavior influences vertical load transfer, resulting in some of the load at the center of the beam traveling to the supports as an arch (Figure 1). Thus, the internal forces of the beam, especially the bending moments, tend to decline, with stress concentration at the extremities of the walls and normal vertical tensile stress in the central part of the deep beam (Figure 1). If these tensile stresses reach the tensile strength of the block-mortar interface, the wall and beam may separate. In the case of single-span beams, this separation generally occurs in the middle of the span, where vertical tensile stress is greater, accentuating the direct transfer of loads to the supports, as reported by Nascimento et al. [4], Barbosa [1] and Medeiros [5].
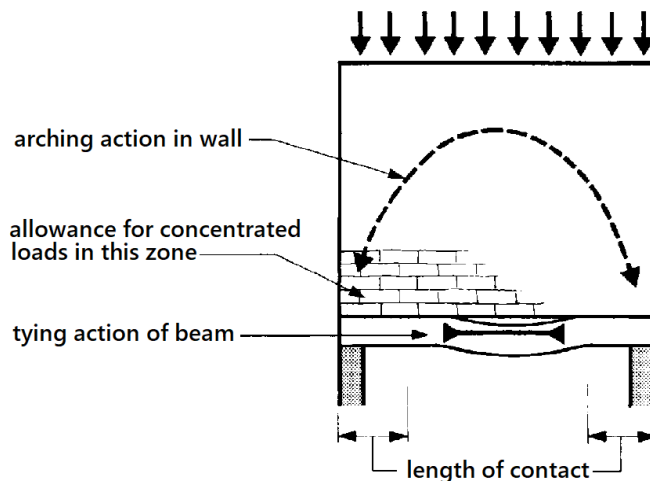
Figure 1. Joint action of the wall-beam system. Adapted: Haseltine, Moore [3].

Silva [6] states that typical structural masonry buildings normally have a ceiling height of 2.80 m, requiring spans of more than 4.0 m to compensate for the abovementioned behavior. In this case, studies using numerical modeling of only one ceiling height is sufficient to assess the phenomenon and its consequences in terms of beam forces and wall stresses.

2 COMPUTATIONAL MODELING OF STRUCTURAL MASONRY WALLS

Numerical simulations are essential to understanding structural behavior and developing efficient formulations that enhance the design. However, to obtain reliable numerical models, a complete description of the materials is required as well as validation by comparing with experimental results.

Given that the properties of the materials are represented, masonry can be simulated in three ways: micromodeling; simplified micromodeling; and macromodeling. According to Rots [7], Lourenço [8] and Holanda [9], each of these methods requires a set of material characteristics and should be applied for a distinct problem.

In detailed and simplified micromodeling, continuous elements are considered for discontinuous units and elements for the unit/mortar interface. The detailed method considers the stand-alone discretization of the masonry components, taking into account the modulus of elasticity, Poisson's coefficient and optionally, the inelastic properties of both the unit and the mortar, according to Nascimento [10]. The author also states that in simplified modeling each joint is associated with an average interface, while the units are expanded to maintain the geometry. Masonry is considered a group of elastic units adhered to the joints by potential fracture lines and/or slipping, such that all the linearity of the problem is attributed to the joint. Both micromodeling methods can be applied to analyses of computational models with small-scale geometry, where the local behavior must be more accurately verified.

According to Holanda [9], in macromodeling, there is no distinction between block and mortar, with masonry classified as a composite that can be considered isotropic, orthotropic or anisotropic depending on the data available. This global modeling of masonry is suitable for analyzing large structures, where masonry panels are large compared to the units and joint thickness. Thus, macromodeling is the most appropriate method to numerically model wall-beam systems in a building because it addresses the behavior of the structural system. Several authors have proposed models along this same line, such as Nascimento et al. [4], Barbosa [1], Paes [2] and Medeiros [5], a procedure adopted here.

With respect to the elements, several models analyze and design structural walls of reinforced concrete and masonry, strut-and-tie models, truss analogies, use of linear or flat finite elements and equivalent frame models.

According to Testoni [11], the flat finite element model encompasses several behavioral traits of walls in structural analysis. However, to obtain more detailed results, the number of computational modeling unknowns and parameters become considerably refined and numerous, as well as the results obtained, requiring the user to have specific knowledge. As a result, the modeling process and analysis of results may become cumbersome and arduous. Thus, applying sophisticated structural models is no longer a viable alternative for conventional structural designs in structural engineering. This author also reports that equivalent frame models represent walls that use linear elements, and can be analyzed considering frames alone or linked to each other, forming plane frames. Different plane frames can be connected to make a three-dimensional frame. a model used to analyze structural cores and structural masonry buildings.

Nascimento et al. [4] proposed a variation of equivalent frame models to analyze wall-beam interaction. The difference in this modeling is that they use bar elements in both the support beam and the masonry wall, the latter discretized using a grid network with multiple vertical and horizontal bars instead of bars alone and connected only to the floor level. In order to enhance this computational model, Medeiros [5] made a number of changes, such that both investigations conduct an extensive study of the new modeling, comparing it with a model that discretizes walls with shell finite elements, in order to analyze the performance of the computational model proposed. Analyses demonstrated that the equivalent frame model was consistent in analyzing wall-beam interaction for any arrangement of openings, beam spans and support conditions.

It is important to underscore that Medeiros [5] also compared the equivalent frame model with the experimental results obtained by Rosenhaupt [12]. The experimental results were assessed for normal stresses at the bottom of the wall and support beam deflection. The analyses conducted indicated that the normal stress peaks were relatively superior to computational models, which was expected after the linear analysis carried out. However, considering an average normal stress value for two neighboring frames in the equivalent frame model, this difference declines substantially. The maximum beam axial force was significantly near that assessed in the experiment. Thus, excellent correlations were obtained, confirming the capacity of simulating wall-beam interaction using the proposed model.

In her study to perfect the equivalent frame model, Lopes [13] proposed calibrating the thickness and stiffness of grouted frames, in order to obtain easy-to-interpret results. A more suitable analysis of stresses is conducted using the net area of the elements. Nevertheless, the author also assessed a model considering the gross wall area, obtaining results consistent with those of modeling using the net area.

Another relevant aspect for analyses are the possible eccentricities between the walls and support beams. The lateral surface of masonry, primarily on the walls of building facades, is typically aligned with the beam surface, as illustrated in Figure 2, resulting in eccentricity and a twisting moment in the beam, which should be properly assessed. This study was initiated by Lopes [13] using planar models, showing the need for further analyses.

Thus, the need for studies and subsequent improvement of consistent, safe and simple alternative modeling justifies the present investigation, and is relevant for enhancing the equivalent frame model and in-depth analysis of the behavior of the structural masonry system.
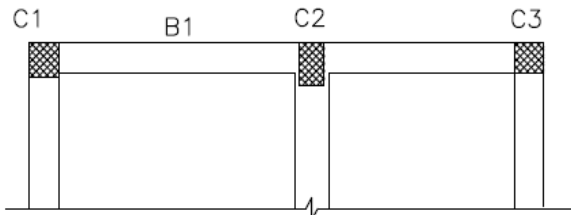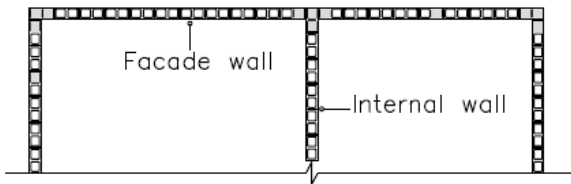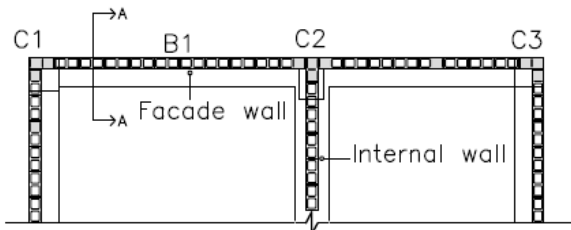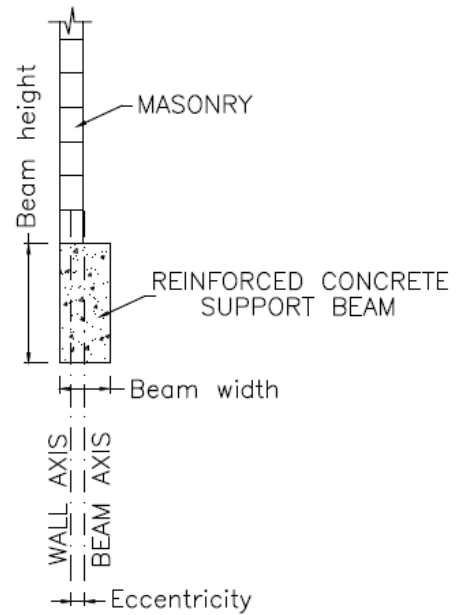
Figure 2. Layout of eccentricity between facade walls and support beam.

3 MODELS ADOPTED IN ANALYSES

This study proposes using the equivalent frame model described by Nascimento et al. [4], considering the calibrations developed by Medeiros [5] and Lopes [13], in order to analyze different configurations of the wall-beam system in a real structural masonry building. Analyses were conducted to compare transition structures, simulated by two and three-dimensional models, and reinforced concrete support beams were designed with and without considering the effects of torsion caused by eccentricity between the wall and beam.

The optimal grid proposed by Medeiros [5], who defined it after conducting numerous tests with different grids and support conditions, was used. Discretization consisted of arranging vertical and horizontal bars 15 and 20 cm apart in order to coincide with the axis of each hole in the blocks and the axis of each course, respecting the layout of the walls. Figure 3 illustrates discretization in the three-dimensional model of walls W30 and W31 with the respective transition structure, from which we can observe the distribution of vertical and horizontal bars to simulate the walls, and the horizontal and vertical bars corresponding to the transition structure, conducted according to the procedure described. The darker bars represent the grouted sections and their lighter counterparts the non-grouted sections.

The linear elastic behavior of the materials was assessed in all analyses and the following support beam forces were evaluated: shear force, axial force, bending moment, twisting moment and vertical displacements. In addition, normal and shear stresses at the bottom of the wall were also analyzed.

In the present study, the same building used by Medeiros [5] was adopted. Vertical loading was applied at the top of the walls, representing a 21-floor structural masonry building using concrete blocks. For transition structure beams, the sections varied according to the floor plans presented in Figure 4 and the isotropic material with longitudinal and transverse moduli of deformation presented in Table 1 was considered. These were determined based on guideline NBR 6118 [14] for concrete with f_{ck} = 25 Mpa.

In the case of non-grouted masonry, the material was considered orthotropic, attributing half of the value of the vertical direction to the horizontal longitudinal modulus of elasticity. According to NBR 15961-1 [15] and Parsekian et al. [16], compressive strength parallel to the horizontal laying joint in hollow blocks is 50% lower than

compression perpendicular to the joint, which generated the ratio between the moduli in both directions, given that these values are obtained as a function of the characteristic strength of prisms. Isotropic material was considered in both the vertical and horizontal sections of grouted masonry. The values adopted for specific gravity and the longitudinal and transverse moduli of elasticity for masonry are shown in Table 1, determined based on NBR 15961-1 [15] for a prism with f_{pk} = 12 MPa.

Table 1. Physical properties of the materials used in modeling [5].

Material	Specific weight Υ (kN/m³)	Modulus of elasticity (MPa)	
		Longitudinal	**Transverse**
Beam concrete	25	23800	9917
Grouted masonry	22	16320	8160
Ungrouted masonry	14	9600	4800
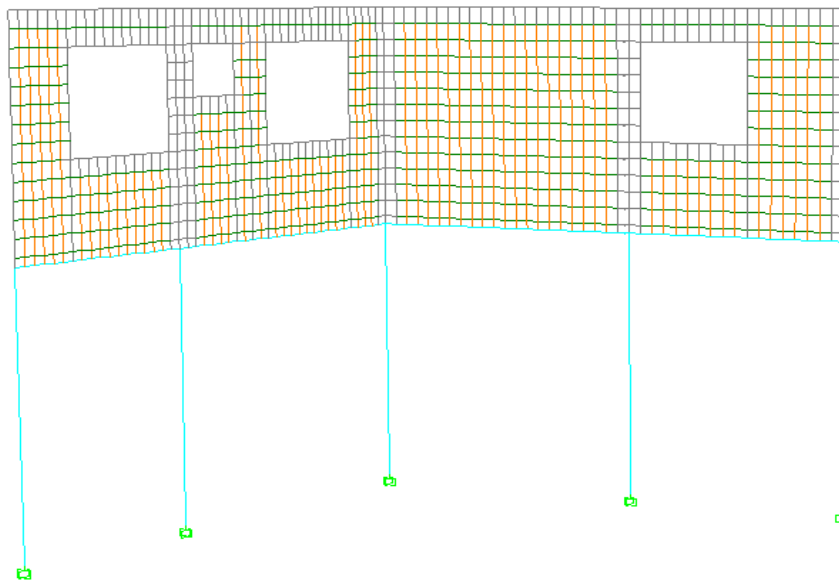
Figure 3. W30 and W1 discretization in the three-dimensional model.

It is important to underscore that the ratio between the characteristic simple compressive strength of a prism and a block (f_{pk}/f_{bk}) was 60%, resulting in a block with f_{bk} = 20 MPa, and the ratio between the grouted and hollow prism was 1.7. These efficiency values are considered reasonable and achievable for high-strength blocks, as shown in the experimental study of Fortes [17]. However, before executing the construction project, tests should be conducted to determine prism strength and when the appropriate levels are not achieved, a higher-strength block should be used to guarantee the prism strength stipulated in the design. Further details on this issue can be found in Parsekian et al. [16] and Fortes [17].

In the panels assessed by Medeiros [5], the thickness of the transverse section of the grouted frames was doubled to take into account the larger area of these elements. Simultaneously, the longitudinal modulus of elasticity of grouted elements was attributed to these same frames, which, if not duly assessed, leads to a duplicate effect.

In her study to perfect the equivalent frame model, Lopes [13] proposed calibrating thickness and stiffness of grouted frames, in order to obtain easy-to-interpret results. After the variations were assessed, a more adequate analysis of stresses was carried out using the net area of the elements, and Model 3, presented in Table 2, was considered the most suitable for analysis. Nevertheless, the author also assessed a model considering the gross wall area, obtaining results consistent with those of modeling using the net area. Thus, all the analyses in this study considered the characteristics of Model 2 presented in Table 2.
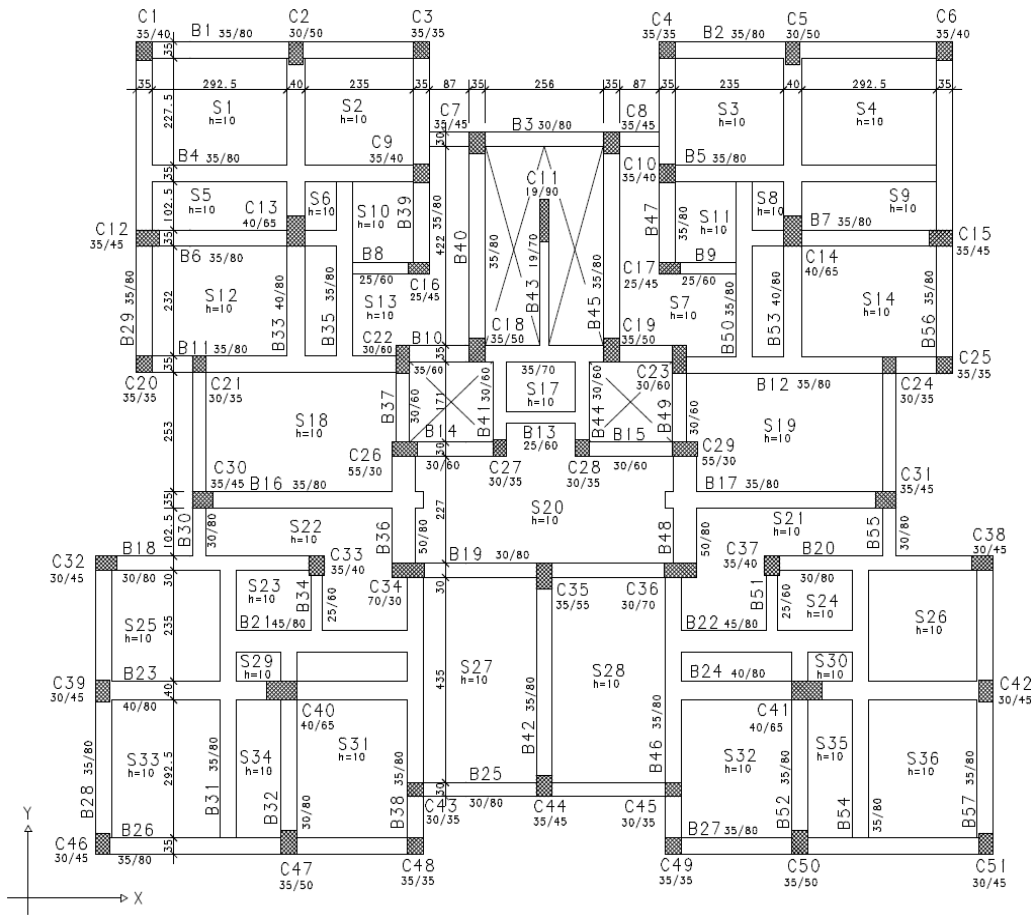
Figure 4. Formwork plan of the support concrete structure. Adapted: Medeiros [5].

Table 2. Variations adopted for the model [13].

Models	Modulus of elasticity (MPa)			Element thickness (cm)	
	Grouted Masonry	Ungrouted masonry		Grouted	Ungrouted
		Longitudinal	Transverse		
Reference	16320	9600	4800	28	14
1	9600	9600	4800	1.7x14	14
2	16320	9600	4800	14	14
3	16320	19200	9600	14	7

Analyses were conducted for four walls of the building, whose selection criteria were the following:

− Walls 1 and 30 were selected for exhibiting several openings in their geometry and interconnections between them at one of the ends; in addition, the transition structure beams that support them are continuous, with beam B1 for wall 1 and B29 for wall 30;
− Walls 41 and 3 were selected for the interconnection between them and primarily because the former is an important vertical shear panel in the building; beam V3, which supports wall 3, is continuous, while beam B40, which supports wall 41, has only one span.
The models that generated the results were denominated as follows:
− 2D model - Planar model with total permanent and accidental load action, without considering equivalent wind loads;
− 3D model – Three-dimensional model with total permanent and accidental load action, without considering equivalent wind loads;
− 3DV model – Three-dimensional model with total permanent, accidental and equivalent wind load action, through combinations of actions.

It is important to underscore that wind action was incorporated into the models by applying equivalent vertical loads to the top of the walls, in order to create the corresponding binaries according to the direction of the wind. Moreover, the effect of slabs (rigid diaphragms) was incorporated into modeling in order to guarantee that restraint straps were securely fit to the top of the structural walls.

The twisting moment, corresponding to the eccentricity between the vertical plane of the wall and the longitudinal axis of the beam, was applied to the model after previous processing to determine the vertical forces at the bottom of the walls. Once the vertical forces were determined, the intensity of the twisting moment to apply was obtained by multiplying the eccentricity of the corresponding vertical frame, and the resulting values were applied directly to the horizontal frames corresponding to the support beams of the structural walls.

Figure 5 illustrates the structural wall plan of the building, while the geometric characteristics of the walls under study (walls 1, 30, 41 and 3) are depicted in Figure 6. For further clarification, the results of 3DV Models for walls 1 and 30 correspond to wind action in direction X on the plan, while walls 3 and 41 correspond to wind action in direction Y on the plan.

4. RESULTS AND DISCUSSION

4.1 Comparison between planar and three-dimensional modeling

4.1.1 Wall 1

Figure 7a illustrates normal stresses at the bottom of the wall, showing similar behavior for the three models analyzed. Despite the proximity between curves, the three-dimensional models exhibited more pronounced peak stress than that of the planar model. Medeiros [5] reported that this increase in peak stress may be due to the effect of the intersection between the walls, not considered in the planar model, given that in three-dimensional modeling, a single frame represents the intersection between walls, receiving load from all those that converge on the intersection. In addition, Figure 7a shows that the intensity of the stresses around the peaks are also greater, notably in the sections on columns C2 and C3, which may also be attributed to the three-dimensional effect of the assembly. It is important to underscore that stress distribution associated with the 3DW Model, illustrated in the following figures, represent the envelope, considering the reversed wind direction, which explains the tendency for increases to always occur in three-dimensional models.

In the case of shear stress distribution at the bottom of the wall (Figure 7b), the planar model exhibited slightly higher peak intensities at the ends of the panel compared to three-dimensional models, in the center. In the intermediate sections, far from the regions on columns, the stresses obtained with the 2D and 3D models exhibited similar intensities, and those obtained with the 3DW model were slightly lower.

These results are illustrated in Table 3, showing considerable increases in peak stress with the three-dimensional model, notably in the regions of columns C2 and C3, with differences of up to 112% in relation to the planar model when considering wind action. These results indicate the real need for three-dimensional modeling and underscore the influence that the wind can exert on the distribution of normal stresses at the bottom of the wall. This suggests, for example, the possible need for grouting reinforcement in the corresponding region and/or a prism with greater compressive strength.

With respect to shear stress peak intensities, the three-dimensional models displayed lower values than those of their planar counterpart, in contrast to what occurred with normal stresses.

In relation to the support beam, Figure 8 shows the distribution of axial force, shear force, bending moment and displacements along its length, demonstrating similar behavior between the 3 models assessed. Table 4 contains the most significant graph values and the percentage differences. Figure 8a shows the differences obtained for maximum axial force intensity with the 3DW model, where the increasing trend was maintained on practically the entire length of the support beam. This behavior in the 3DW model may be associated with higher shear stress along the bottom of the wall, since this stress corresponds to the axial load acting on the beam. Likewise, shear stress at approximately the 1.8 m coordinate exhibits null intensity and maximum axial force. This could be due to the same shear stress signals (acting in the same direction) up to this coordinate, after which the signal changes (opposite direction), resulting in a decline in axial force in the section.
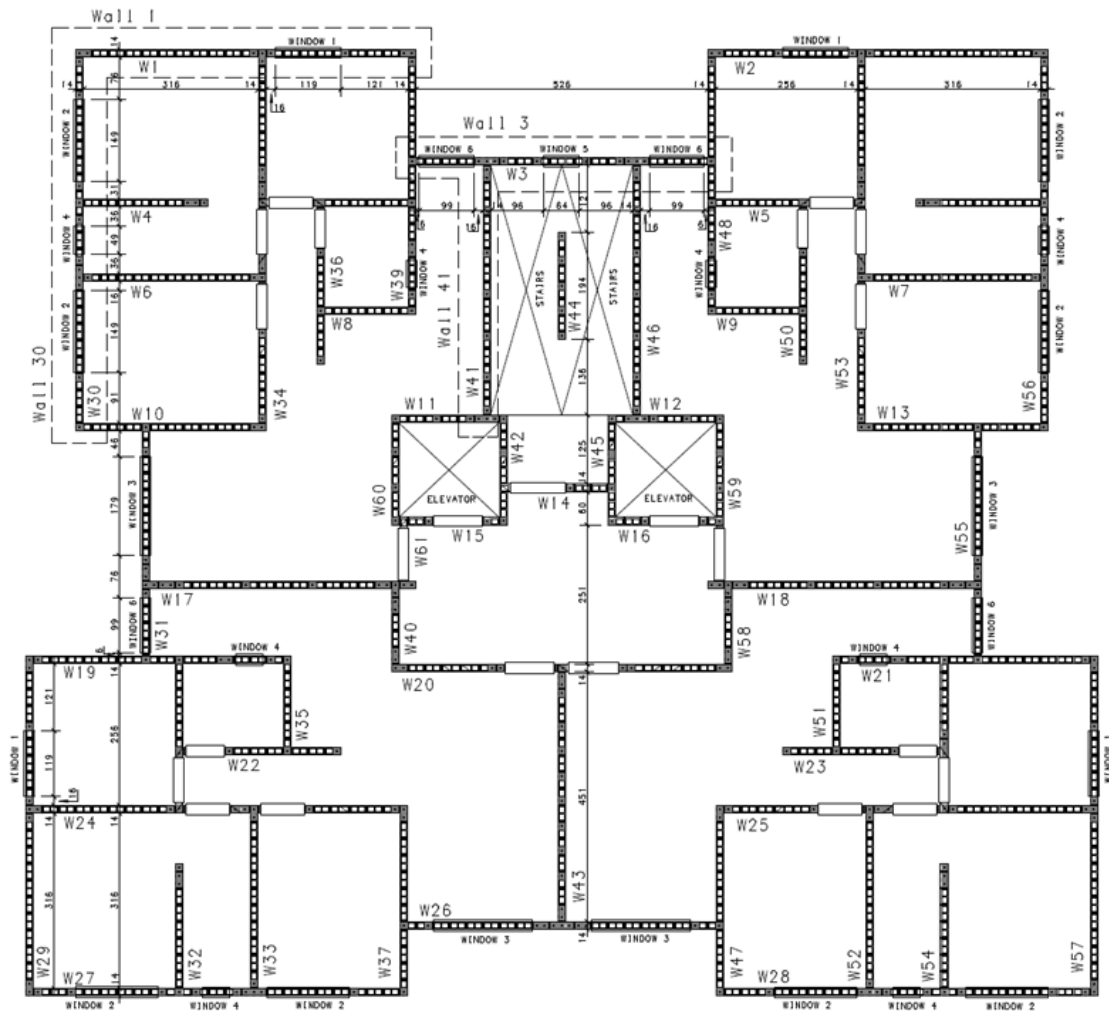
Figure 5. Wall layout, highlighting the walls under study. Adapted: Medeiros [5].

Table 3. Normal and shear stresses at the bottom of Wall 1.

Model	Normal stress (MPa) – Maximum values								
	Region C1	Δ_{2D}	Δ_{3D}	Region C2	Δ_{2D}	Δ_{3D}	Region C2	Δ_{2D}	Δ_{3D}
2D	7.03	-	-	3.28	-	-	3.36	-	-
3D	8.77	25%	-	5.18	58%	-	5.33	59%	-
3DW	10.52	50%	20%	6.17	88%	19%	7.13	112%	34%
Model	Shear stress (MPa) – Maximum values								
	Region C1	Δ_{2D}	Δ_{3D}	Region C2	Δ_{2D}	Δ_{3D}	Region C2	Δ_{2D}	Δ_{3D}
2D	0.60	-	-	0.40	-	-	0.16	-	-
3D	0.47	-22%	-	0.40	0%	-	0.11	-31%	-
3DW	0.51	-15%	9%	0.40	0%	0%	0.17	6%	55%

With respect to shear force, Figure 8b shows significant differences in intensities only in the supports, resulting in an 18% rise from changing the type of model and 11% when including wind action in analyses. Once again, this result can be explained by the three-dimensional effect of the assembly, where part of the load acting on a wall migrates to the intersecting wall.

With respect to bending moments, three-dimensional models are also associated with greater intensities when compared to the planar model, resulting in a 6% higher negative bending moment with three-dimensional modeling, and 17% higher than when the effect of wind is considered. In the case of positive bending moments, an increase (38%)

occurred only in the section between columns C2 and C3, corresponding to the result of the 3DW model. This behavior is due to the distribution of normal stress at the bottom of the wall, where the action of higher-intensity stress was observed on the beam spans of the 3DW model.

(a)

(b)

(c)

(d)
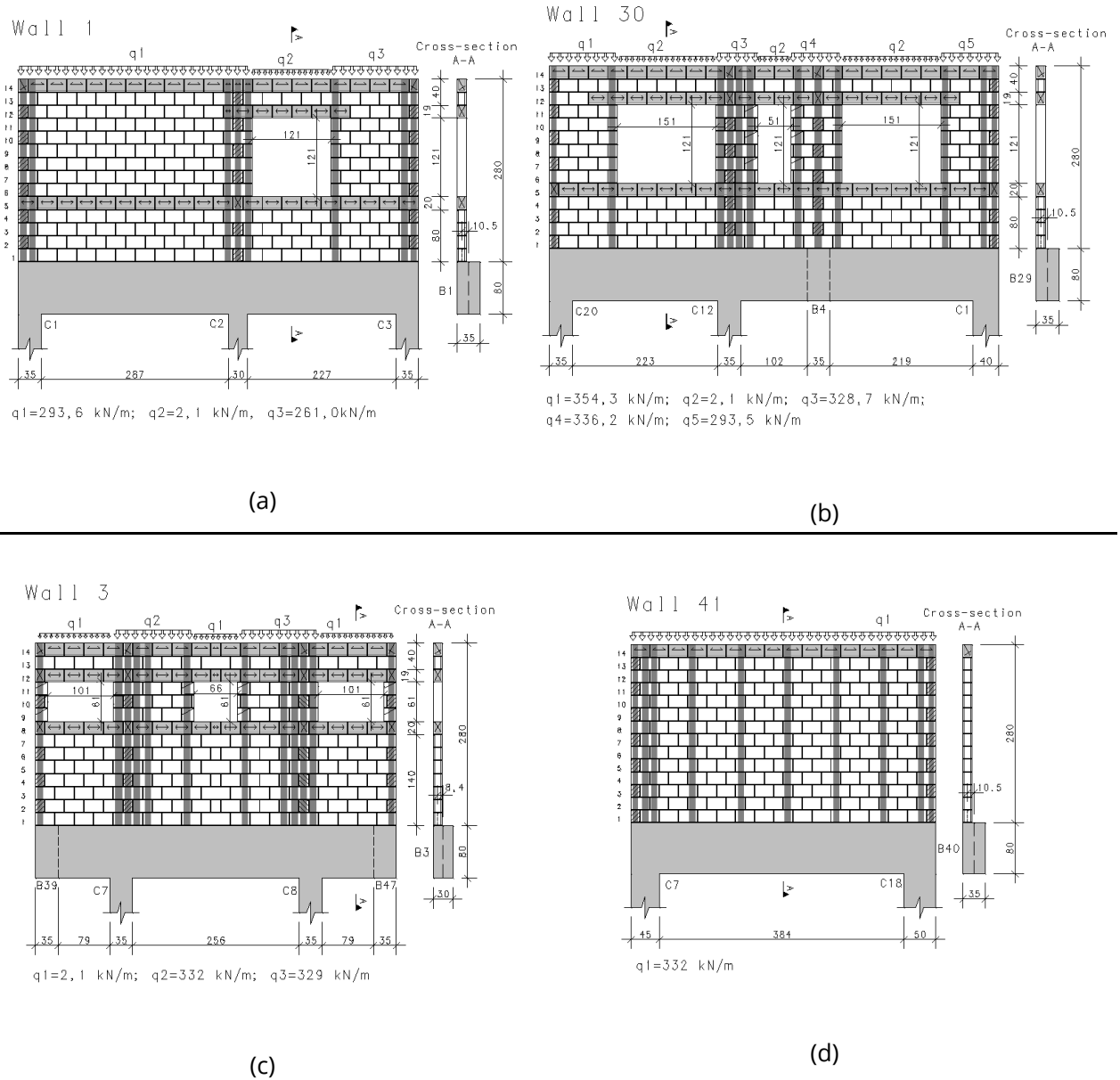
Figure 6. Walls details. (a) Wall 1; (b) Wall 30; (c) Wall 3; (d) Wall 41.

Table 4. Maximum forces and displacements in the support beam of Wall 1.

Model	Axial force (kN)			Shear force (kN)			Bending moment (kN·m)			Displacements (cm)		
	Maximum	Δ_{2D}	Δ_{3D}	Maximum	Δ_{2D}	Δ_{3D}	Maximum	Δ_{2D}	Δ_{3D}	Maximum	Δ_{2D}	Δ_{3D}
2D	57.83	-	-	396.68	-	-	183.50	-	-	0.11	-	-
3D	65.89	14%	-	467.57	18%	-	194.70	6%	-	0.16	45%	-
3DW	85.69	48%	30%	519.26	31%	11%	228.09	24%	17%	0.17	55%	6%
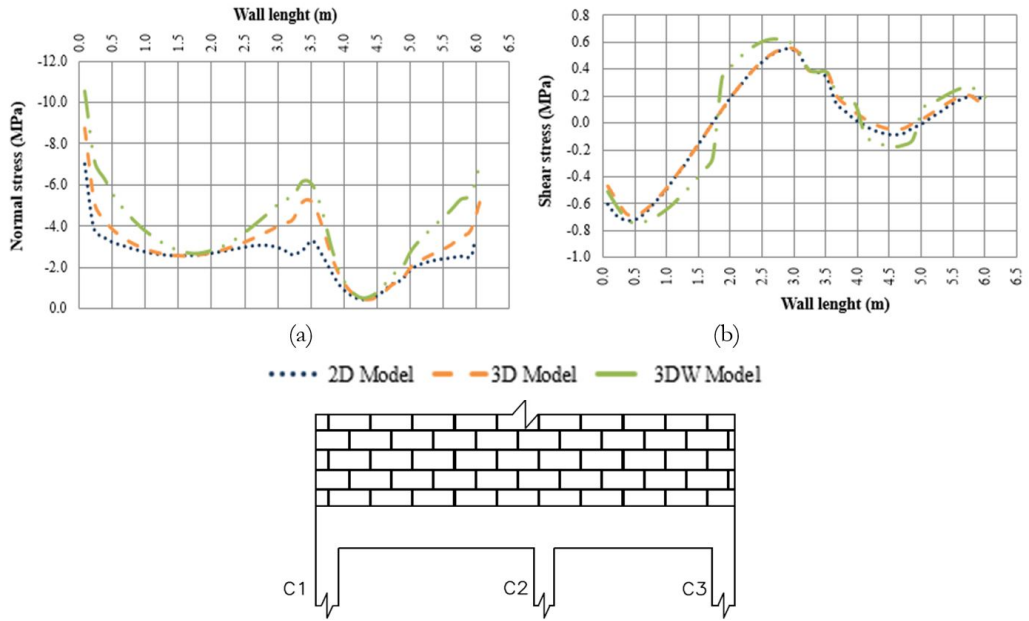
Figure 7. Stress distribution at the bottom of Wall 1: (a) Normal stress; (b) Shear stress
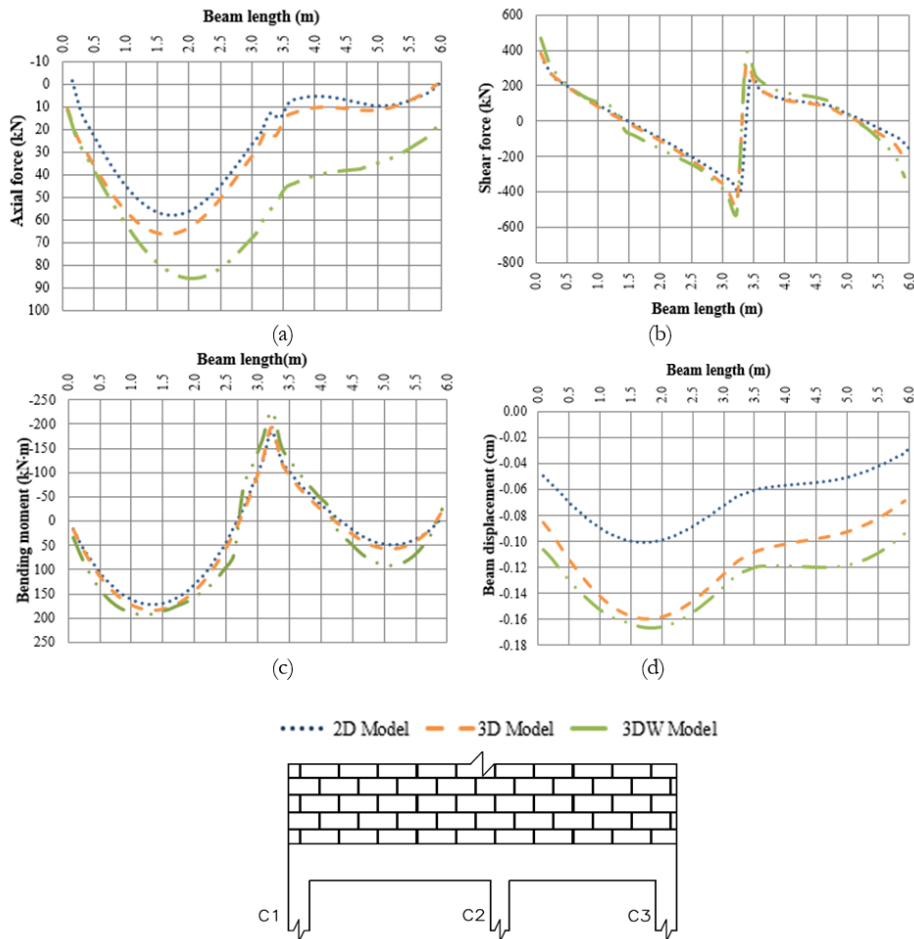
Figure 8. Forces on the support beam of wall 1: (a) Axial force; (b) Shear force; (c) Bending moment; (d) Vertical displacement.

In regard to beam displacement shown in Figure 8d, the significant difference between 3D and 3DW models and the 2D model, may be due to axial deformation in the support columns submitted to greater vertical load in these models. With respect to the results obtained, the absolute values are considered small in relation to the beam spans, and well below the service limits established in Brazilian guideline NBR 6118 [14].

Despite the importance of wall 1 for bracing the building, compared to the 3D model, the 3DW model exhibited stresses at the bottom of the wall, with significant differences only in the peaks and small increases in the support beam, except for axial force. This behavioral trend is due to the fact that wind distributes variable stresses along the length of the wall. Maximum stresses occur at the extremities, where vertical load stresses are concentrated. However, it is important to emphasize that despite being small, these increases may significantly change beam design since it is a support beam subjected to bending and traction.

4.1.2 Wall 30

Figure 6b illustrates the geometry of wall 30, arranged perpendicularly to wall 1 at its left end in the equivalent frame model. Figure 9 shows the distribution of normal and shear stresses at the bottom of the wall, exhibiting similarity in the curves for the results of the three models assessed, except the peak at the 2.75 m coordinate. This effect, observed only in the three-dimensional models, refers to the end of the transverse wall interconnected with Wall 30 in this section, as depicted in Figure 5. Despite the similar overall aspect in the 3D and 3DW models, significantly higher intensities occurred, resulting in differences in the region of column C1, of 47 and 76%, respectively, in relation to the 2D model. Considering wind action in the analyses caused an 20% increase in maximum normal stress in this region (Table 5) indicating the importance of considering it in the analyses. Moreover, due to the redistribution of stresses emanating from the interconnecting walls, three-dimensional models always exhibit higher intensities than those of the planar model.
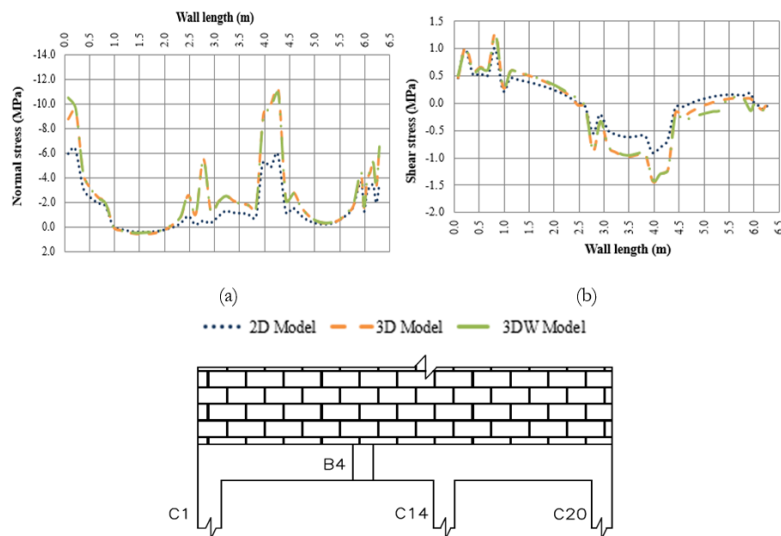
Figure 9. Stress distribution at the bottom of Wall 30: (a) Normal stress; (b) Shear stress.

Table 5. Normal and shear stresses at the bottom of Wall 30.

Modelo	Normal stress (MPa) – Maximum values								
	Region C1	Δ_{2D}	Δ_{3D}	Região C14	Δ_{2D}	Δ_{3D}	Região C20	Δ_{2D}	Δ_{3D}
2D	5.97	-	-	5.91	-	-	3.56	-	-
3D	8.77	47%	-	11.14	88%	-	6.64	87%	-
3DW	10.52	76%	20%	10.82	83%	-3%	6.54	84%	-2%
Modelo	**Shear stress (MPa) – Maximum values**								
	Region C1	Δ_{2D}	Δ_{3D}	Região C14	Δ_{2D}	Δ_{3D}	Região C20	Δ_{2D}	Δ_{3D}
2D	0.46	-	-	0.91	-	-	0.07	-	-
3D	0.44	-4%	-	1.43	57%	-	0.06	-14%	-
3DW	0.42	-9%	-5%	1.42	56%	-1%	0.08	14%	33%

Column C1, a common support for support beams B1 and B29 of walls 1 and 30, respectively, shows coincident maximum normal stress values at the bottom of these walls of 8.77 MPa, obtained using the 3D model, as depicted in Tables 3 and 5. In the case of the 2D model, maximum stress on the frame on top of column C1 is 7.03 MPa in wall 1 and 5.97 MPa in wall 30. Since modeling considered linear elastic behavior, overlapping effects were assessed, resulting in an intensity of 13.0 MPa, corresponding to a difference of 48% in relation to the 3D model. The 3D model obtained a lower intensity because analysis was conducted on a single vertical frame that interacts with two walls in this model, and only one in the 2D model, causing stress distribution along a smaller region. This indicates that using planar modeling could result in overestimating maximum normal stresses, demonstrating the need to use three-dimensional modeling in the analyses.

In relation to shear stresses at the bottom of the wall, Figure 9b illustrates their distribution and Table 5 the highest values. The same behavioral trend was observed in the three models evaluated, with more intense peaks in the 3D models, and significant differences associated only with the section of column C14, slightly different from what occurred for normal stresses. This difference in increasing trend is related to the several openings in the wall, especially that located between columns P14 and P20, where one of the sides is coincident with the end of the beam span. This hinders the formation of a stressed arch in this span, significantly changing the behavioral trend expected for stress distribution. Beam continuity and the section of masonry below the smallest opening near column C14 should also be considered, as shown in Figure 6b.

With respect to the support beam, Figure 10a presents the axial force diagram, where higher intensities in the three-dimensional models can be observed, with maximum values of 69.97 kN, 98.80 kN and 98.67 kN, for the 2D, 3D and 3DW models, respectively, and corresponding to differences of 41% in relation to the 2D model, as illustrated in Table 6. All the models exhibited tensile forces in the section between columns C1 and C14. For the section between C14 and C20, compressive forces occurred along the entire length only with the 3D and 3DW models, while in the 2D model, in the section after coordinate 5.75 m, practically no acting force was observed. This result corroborates the trend of the opening on the side of column C14, eliminating the formation of a stressed arch in the section between P14 and P20, as well as the trend of beam continuity and sections of masonry below the window openings changing shear stress distribution.

Table 6. Maximum forces and displacements in the support beam of Wall 30.

Model	Axial force (kN)			Shear force (kN)			Bending moment (kN·m)			Displacements (cm)		
	Maximum	Δ_{2D}	Δ_{3D}	Maximum	Δ_{2D}	Δ_{3D}	Maximum	Δ_{2D}	Δ_{3D}	Maximum	Δ_{2D}	Δ_{3D}
2D	69.97	-	-	380.73	-	-	182.94	-	-	0.12	-	-
3D	98.80	41%	-	577.77	52%	-	255.12	39%	-	0.21	72%	-
3DW	98.67	41%	0%	571.62	50%	-1%	252.70	38%	-1%	0.20	71%	-1%

With respect to shear forces and bending moments, the trend to consider wind action did not change these forces and the 3D models displayed higher intensities in relation to the planar model, with significant differences in maximum values, as shown in Table 6. These results may be due to the action of higher normal stresses at the bottom of the walls in the three-dimensional models.

Finally, Figure 10d shows that the vertical displacements of the support beam were significantly higher in the three-dimensional models, with differences of around 72% in relation to the planar model. A large part of this difference can be attributed to greater axial deformation of the columns in 3D models, due to the loading acting on the transverse walls that intersect with Wall 30. In addition, the higher shear forces and bending moments indicate greater loading on the beams of three-dimensional models, which also contributes to increasing vertical displacements. Nevertheless, small values were obtained, far below the guidelines established for service limit states.

Figure 4 shows that beam B4, which is supported by beam B29, is located between columns C1 and C14, on top of wall 30. The effect of this interaction between beams is considered in three-dimensional models, but not the planar model. However, the corresponding load on the beam was manually introduced into the 2D model and all the results presented until then refer to this condition. To illustrate the effect of not including this loading, Figure 11 shows the force diagrams of beam B29, where the total inconsistency in the trend of the results obtained with the 2D model can be observed in the section between P1 and P14, especially shear forces and bending moments.
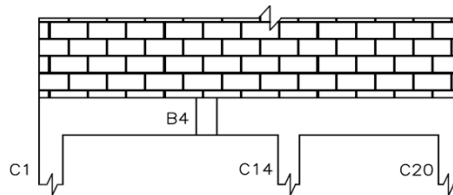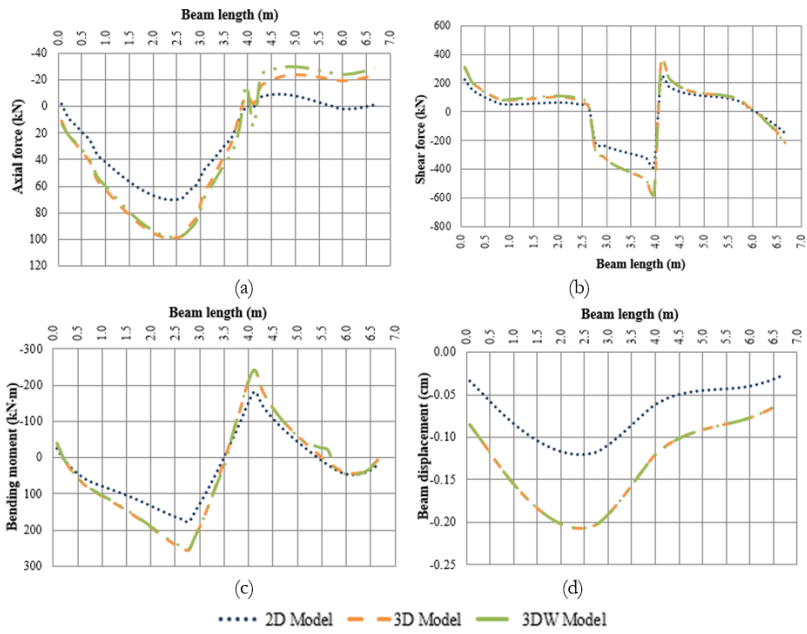
Figure 10. Forces on the support beam of Wall 30: (a) Axial force; (b) Shear force; (c) Bending moment; (d) Vertical displacement.
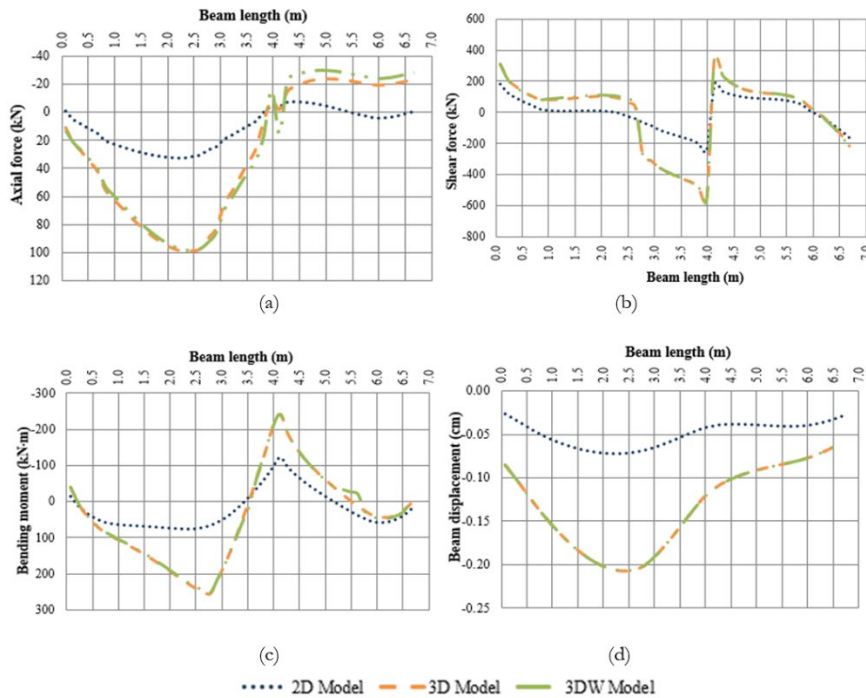

Figure 11. Forces on the support beam of Wall 30 disregarding the load of Beam B4 in the 2D model: (a) Axial force; (b) Shear force; (c) Bending moment; and (d) Vertical displacement.

4.1.3 Wall 3

Figures 6c and 5 illustrate the geometry of wall 3, demonstrating its interconnection with walls 41 and 46. In the case of the 2D model, due to the proximity of columns C10 and C11 (Figure 4), the intersections of beam B3 with beams B39 and B47 were considered simple supports. This condition was defined after the vertical displacements obtained with the 3D model were assessed.

Figure 12a shows the normal stresses at the bottom of the wall, where, despite the same curve behavior, the 3D models exhibited significantly higher stresses along the entire length of the wall, with peaks occurring in the column C7 region multiplied by 2.4, which increased by 11% when wind action was taken into account, as depicted in Table 7. This aspect can be explained by the interconnection with walls 41 and 46, which reveals higher vertical loading, redistributed in the corresponding section of wall 3 and only incorporated into in three-dimensional models.
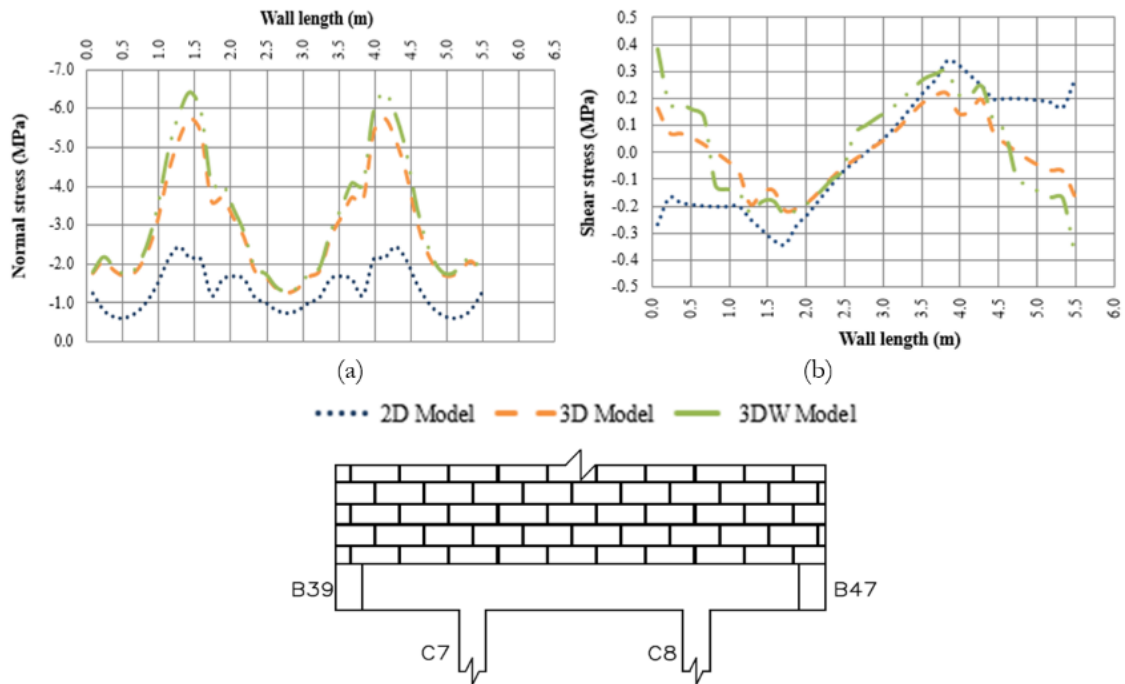
Figure 12. Stress distribution at the bottom of Wall 3: (a) Normal stress; (b) Shear stress.

Table 7. Normal and shear stress at the bottom of Wall 3.

Modelo	Normal stress (MPa) – Maximum values					
	Region C7	Δ_{2D}	Δ_{3D}	Region C8	Δ_{2D}	Δ_{3D}
2D	2.43	-	-	2.43	-	-
3D	5.75	137%	-	5.75	137%	-
3DW	6.40	163%	11%	6.40	163%	11%
Modelo	**Shear stress (MPa) – Maximum values**					
	Region C7	Δ_{2D}	Δ_{3D}	Region C8	Δ_{2D}	Δ_{3D}
2D	0.29	-	-	0.29	-	-
3D	0.19	-34%	-	0.19	-34%	-
3DW	0.22	-24%	16%	0.22	-24%	16%

With respect to shear stress distribution at the bottom of the wall, as illustrated in Figure 12b, in relation to the 2D, 3D exhibited reverse direction stresses in the end sections of the beam and always lower intensities in the central region. Unlike what occurred with normal stresses, the differences obtained in the region of column C7 resulted in decreases with far smaller variations (Table 7). With respect to the curves, it is important to underscore that the sections with constant intensities observed in the 2D model correspond to those below the window openings of wall 3, which was not characterized in the 3D and 3DW models. In addition, the maximum absolutes in the three-dimensional models did not occur on the supports of columns

C7 and C8, but on the supports at the ends, corresponding to beams B39 and B47. All of these changes in shear stress distribution reinforce the need for three-dimensional modeling in order to properly account for the effects of wall-beam interaction.

Considering the 2.75 m coordinate on the beam and the section to the left, a change in the direction of shear stresses can be observed in the 3D and 3DW models, evidenced by the change in signal, which did not occur in the 2D model. In this case, the vectors associated with the 2D model are arranged from right to left, while in the 3D and 3DW models the same direction can be observed from the 2.75 m to the 0.75 m coordinate, delimiting a 2.0 m section, and reversing direction between the 0.75 m and 0.0 m coordinates. This will affect axial force distribution in the beam due to its direct relation with shear stresses at the bottom of the wall.

Figure 13a presents the axial force distribution in the support beam, showing the exclusive occurrence of compressive forces along the entire beam, with higher intensities in the 3D model, while according to the results of the 2D model, the beam is submitted solely to tensile forces. This discrepant result is due to the change in direction of shear stresses at the bottom of the wall, as described before. Taking the middle section between pillars P7 and P8 as reference, and the part of the beam to the left of this section, the integration of shear stresses distributed to the left of the sections defined in this part leads to the axial force value in the section. In addition, when the vectors are arranged from left to right and right to left, compressive and tensile forces, respectively, are induced. Thus, the integration of these stresses only generates tensile forces on the beam of the 2D model. In the 3D and 3DW models, compressive forces are induced from the left end to approximately the 0.75 m coordinate, and thereafter tensile forces up to the 1.75 m coordinate, which reduces the initially induced compression. Thus, as illustrated in Figure 13a, the relief in compressive forces was insufficient to induce tensile forces in the sections of the beam in the 3D and 3DW models. This causes radical changes in beam design, where bending-traction forces become bending-compression forces, which, in turn, significantly changes the amount of reinforcement needed to obtain balanced sections in the service limit state. Finally, as occurred in the previously assessed walls, the 2.75 m coordinate at which the axial force reaches its minimum intensity in the three-dimensional models and maximum in the planar model, corresponds to the coordinate at which shear stresses are annulled at the bottom of the wall. The maximum compressive intensities in the three-dimensional models also correspond to sections with null shear stresses.
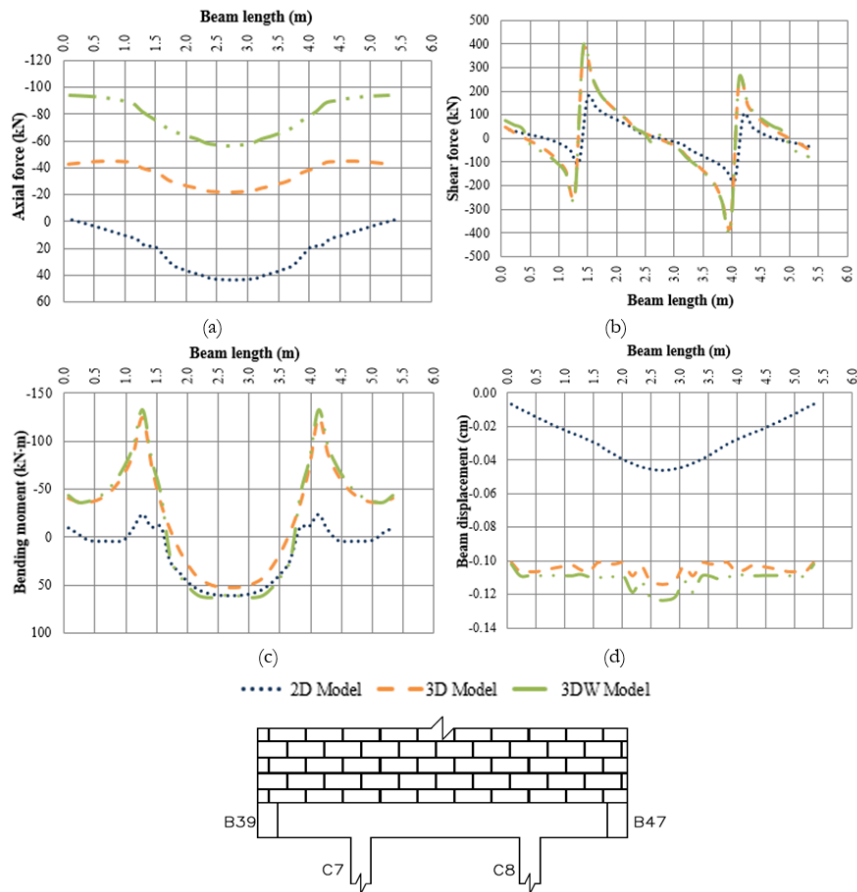

Figure 13. Forces on the support beam of Wall 3: (a) Axial force; (b) Shear force; (c) Bending moment; (d) Vertical displacement.

The graphs of shear forces, illustrated in Figure 13b show the significant rise in the values obtained with the three-dimensional models, whose intensities resulted in more than twice the amount compared to the 2D model (Table 8). These differences may be attributed to normal stress distribution at the bottom of the wall, which represents vertical loading on the beam. According to the three-dimensional models, considerably higher normal stress intensities will increase shear forces in the same order of magnitude. It is also important to underscore that only the distribution of normal stresses outside the section of the column contributes to loading on the beam, not contributing to the maximum normal stress that occurs.

Table 8. Maximum forces and displacements in the support beam of Wall 3.

Model	Axial force (kN)			Shear force (kN)			Negative bending moment (kN.m)			Displacements (cm)		
	Maximum	Δ_{2D}	Δ_{3D}	Maximum	Δ_{2D}	Δ_{3D}	Maximum	Δ_{2D}	Δ_{3D}	Maximum	Δ_{2D}	Δ_{3D}
2D	43.16	-	-	175.65	-	-	61.18	-	-	0.05	-	-
3D	-45.11	105%	-	373.63	113%	-	124.89	104%	-	0.11	120%	-
3DW	-94.02	218%	108%	388.91	121%	4%	132.41	116%	6%	0.12	140%	9%

Figure 13d shows the significant differences in beam displacements of the three-dimensional models. This result may be due to the axial deformations of columns submitted to significantly higher axial forces, since the loading of interconnecting transverse walls are taken into account. Nevertheless, the absolute values obtained with all the models are very low and below the displacement limits prescribed in NBR 6118 [14], indicating that this aspect is not a complicating factor in the analysis of this type of structure.

With respect to bending moments, Figure 13c indicates significant increases only for negative bending moments, whose intensities are also more than double those of the 2D model (Table 8). Likewise, this can be explained by the distribution of normal stresses at the bottom of the wall, which exhibited considerable increases in the regions near the supports, thereby inducing greater changes in negative bending moments, with little influence on their positive counterparts. It is important to underscore that the increase in negative bending moments in the supports means this same type of moment occurs along the end spans of the beam, in contrast to the 2D model, where a positive bending moment is observed in these sections, albeit not intense. This substantially changes the design of this beam, with an increase in negative reinforcement and a longer span.

4.1.4 Wall 41

The results at the bottom of the wall in Figure 14a depict the distribution of normal stresses for the three models analyzed. At the two ends, the 2D model exhibited a more pronounced peak than those of the other models, where the 3D and 3VD models resulted in a 50% decline in the region of column C7 (Table 9). In addition, at this same location, the 3DW model increased by 11% in relation to its 3D counterpart, highlighting the importance of considering the effects of wind in analysis. Column C7 is common to walls 41 and 3, and there is a tendency to overlap the normal stresses obtained with the respective planar models, whose values are presented in Tables 7 and 9. This overlapping resulted in a stress intensity of 13.83 MPa, 2.4 times greater than that obtained with the 3D model. Once again normal stresses were redistributed in the three-dimensional models which, in this case, resulted in a significant decline in maximum normal stress at the bottom of the wall. It is important to emphasize that this decrease was only possible due to the sections of masonry on the interconnecting transverse walls. Another important point refers to the links that promote this interconnection, which must provide sufficient strength to guarantee this redistribution. If this is not possible, redistribution will not be certain, and maximum stresses will increase, as observed in the results of the 2D model. This result underscores the need for 3D modeling in order to determine the interaction between the structural walls and transition structures of the building, as well as the importance of using procedures that guarantee the mobilization of limit forces in the connecting device capable of redistributing the stresses determined. However, in more central sections of the wall, the three-dimensional models exhibited slightly higher normal stresses than in the planar model, notably the localized peaks. This aspect characterizes behavior intrinsic to the wall-beam system, where the decline in maximum normal stresses in the region of support beams is accompanied by a rise in these stresses on the beam span. It is important to underscore that these increases were far lower than the significant declines at the ends of the wall. This corroborates the redistribution of stresses to the transverse walls, especially because the shorter span means the support beams of these walls are stiffer (Figure 4).
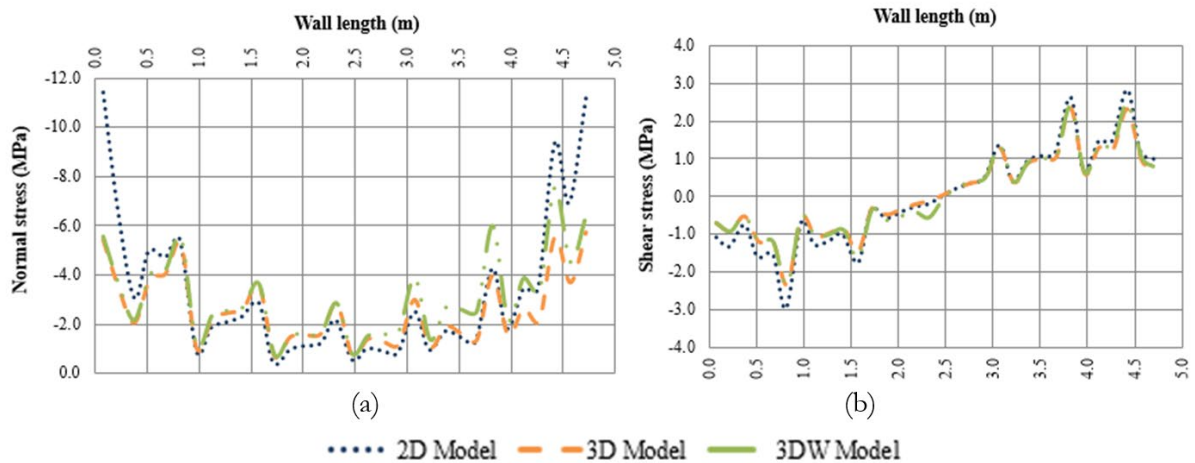
Rev. IBRACON Estrut. Mater., vol. 13, no. 4, e13414, 2020

16/24

Figure 14. Stress distribution at the bottom of wall 41: (a) Normal stress; (b) Shear stress.

Table 9. Normal and shear stress at the bottom of Wall 41.

Model	Normal stress (MPa) – Maximum values					
	Region C18	Δ_{2D}	Δ_{3D}	Region C7	Δ_{2D}	Δ_{3D}
2D	11.4	-	-	11.17	-	-
3D	5.44	-52%	-	5.75	-49%	-
3DW	5.57	-51%	2%	6.40	-43%	11%
Model	Shear stress (MPa) – Maximum values					
	Region C18	Δ_{2D}	Δ_{3D}	Region C7	Δ_{2D}	Δ_{3D}
2D	1.07	-	-	1.00	-	-
3D	0.70	-35%	-	0.71	-29%	-
3DW	0.70	-35%	0%	0.77	-23%	8%

With respect to the shear stresses illustrated in Figure 14b, the intensities obtained with the 3D models tended to decline, albeit with slightly smaller differences (Table 9). As expected for this type of stress in wall-beam interaction, the maximum intensities did not occur at the ends of the walls, but in the internal sections.

The axial forces on the support beam illustrated in Figure 15a show that the three-dimensional models obtained higher values than in the planar model, of around 15% in the central region (Table 10). In contrast to what occurred in the support beam of wall 3, all the models indicated that tensile forces occurred along the entire beam. Another relevant point is the coincident location of the maximum axial force and the null shear stresses at the bottom of the wall, at the 2.5 m coordinate.

In regard to the shear force and bending moments, the 3D and 3DW models obtained lower maximum values than those of the 2D model, of around 9 and 15%, respectively, as shown in Table 10. This greater difference in maximum positive bending moment was observed in the values of the other sections. This result is in line with the lower normal stress intensities at the bottom of the wall, near the columns, obtained with the 3D, as illustrated in Figure 14a.

In regard to displacements, illustrated in Figure 15d, the three-dimensional models displayed higher values than those of planar modeling. However, displacements at the ends, which correspond to axial deformation of the columns, were higher in the 3D models and if this difference was disregarded in the displacement diagram, the curves would be practically equal.
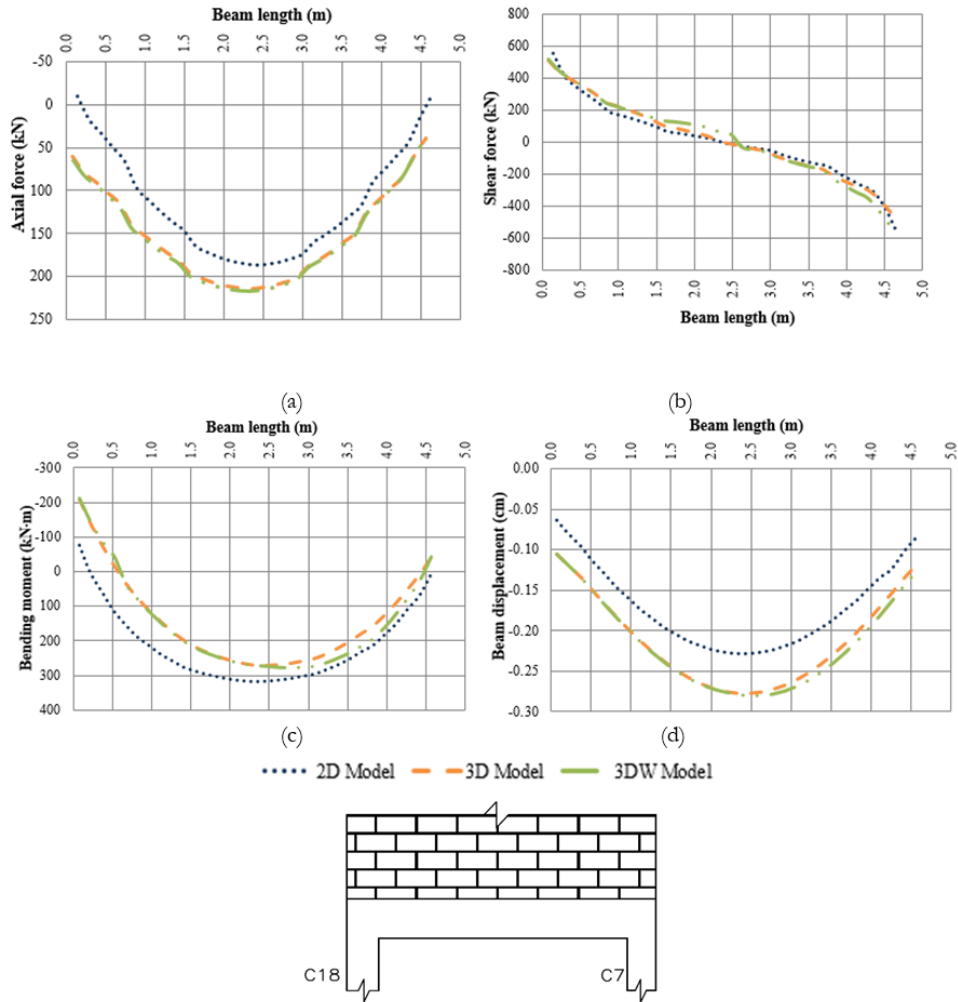
Figure 15. Forces on the support beam of wall 41: (a) Axial force; (b) Shear force; (c) Bending moment; (d) Vertical displacement.

Table 10. Maximum forces and displacements in the support beam of Wall 41.

Model	Axial force (kN)			Shear force (kN)			Bending moment (kN.m)			Displacements (cm)		
	Maximum	Δ_{2D}	Δ_{3D}	Maximum	Δ_{2D}	Δ_{3D}	Maximum	Δ_{2D}	Δ_{3D}	Maximum	Δ_{2D}	Δ_{3D}
2D	187.04	-	-	555.46	-	-	318.63	-	-	0.23	-	-
3D	214.56	15%	-	505.54	-9%	-	270.67	-15%	-	0.28	22%	-
3DW	216.23	16%	1%	525.97	-5%	4%	277.63	-13%	3%	0.28	22%	0%

4.2 Assessment of torsion and support beam design in reinforced concrete

As described in item 3, after the structure was processed without considering eccentricity, the vertical forces for each frame at the bottom of the wall were multiplied by the corresponding eccentricity – 10.5 cm for walls 1, 30 and 41, and 8 cm for wall 3 –, in relation to the longitudinal support beam axis, in order to obtain the torsion load on the beam. Figure 16 illustrates the twisting moment applied, underscoring the higher intensities in the sections near the columns and the discontinuities corresponding to the dimensions of the respective transverse sections of the columns. This figure shows the complexity of this loading, which is intrinsic to the behavior of the wall-beam system itself, making its inclusion in simple manual calculation models impractical and demonstrating the need for computational analysis of the problem.
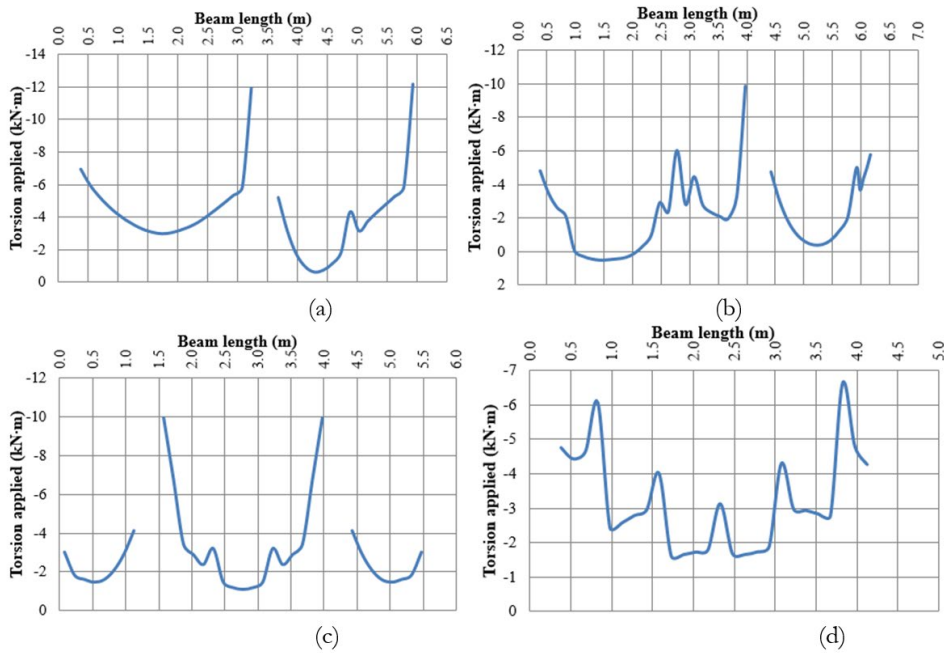
Figure 16. Torsion applied to reinforced concrete support beams without considering wind action: (a) Wall 1; (b) Wall 30; (c) Wall 3; (d) Wall 41.

Figure 17 illustrates the twisting moment diagrams of the planar and three-dimensional models for the four walls studied. The torsion compatibility values refer to the load applied without considering the twisting moments depicted in Figure 16, represent the reconciliation between the negative bending and twisting moments of the beams without regarding the eccentricity between the longitudinal axis and the vertical bars of the equivalent frame model. Figure 17 shows that including eccentric loading resulted in significant increases of maximum twisting moments, when compared to compatibility torsion. Likewise, the 3D and 3DW models exhibited similar values, but considerably different from the 2D model, except for wall 41. The twisting moment applied to this wall was the least intense (Figure 16), which may explain the smaller difference.

Table 11 contains the maximum twisting moments acting on the beams, which increases when wall eccentricity is considered in relation to the longitudinal axis of the beam and when three-dimensional modeling of the structure is performed. Maximum intensities more than tripled when eccentricity was considered for beams B1 and B29. In the case of B40, the 25-fold increase in values is due to the non-occurrence of the twisting moment when eccentricity is not included, which, in turn, may be associated with the low intensity of the negative bending moments of beam B3. Even the lower increases in the twisting moment of 21 and 23% in beam B3 could not be disregarded in the design.

Table 11. Intensities and maximum twisting moments in the support beams.

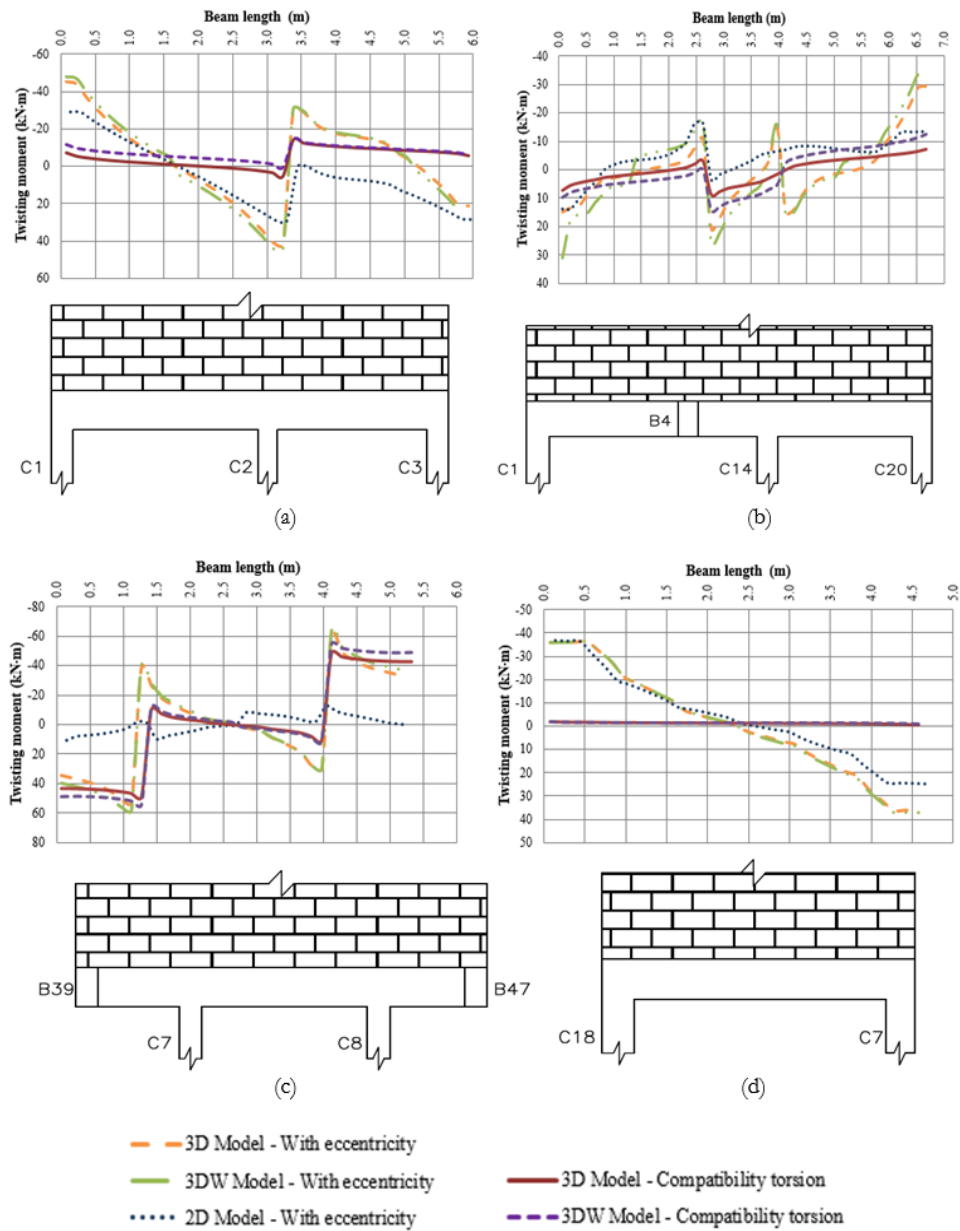| WALL/ BEAM (section)	MODEL	MAXIMUM TWISTING MOMENT (kN·m)		VARIATION	
		Disregarding eccentricity (1)	Considering eccentricity (2)	$\Delta_{(2)-(1)}$	Δ_{3D-2D}
W1/B1 (35x80)	2D	--	38.39	--	--
	3D	13.91	51.09	267%	33%
	3DW	14.23	53.94	279%	40%
W30/B29 (35x80)	2D	--	25.83	--	--
	3D	8.78	35.90	309%	39%
	3DW	14.31	41.36	189%	60%
W3/B3 (30x80)	2D	--	12.48	--	--
	3D	48.94	60.29	23%	383%
	3DW	54.38	65.70	21%	426%
W41/B40 (35x80)	2D	--	63.06	--	--
	3D	2.02	56.33	2689%	-11%
	3DW	2.12	56.43	2562%	-11%

Figure 17. Twisting moments in reinforced concrete support beams: (a) Wall 1; (b) Wall 30; (c) Wall 3; (d) Wall 41.

Given the different types of modeling, except for beam B40, three-dimensional modeling resulted in increases in maximum twisting moments, notably in beam B3, whose intensity was multiplied by 4.83 and 5.26 in the models without and with the wind, respectively. By contrast, the maximum intensities of B40 declined by 11% in the two three-dimensional models. Both the significant increase in B3 and the reduction in B40 were due to the interaction between walls 3 and 41 in the three-dimensional model. This interaction relieves normal stresses at the bottom of wall 41 and substantially raises them at the bottom of wall 3 as a result of their redistribution in the 3D model, which is not included in the planar modeling of the walls, as observed in Figures 7a.

Considering the twisting moments in Table 11, the normal stresses acting on the beams and the guidelines of NBR 6118 [14] regarding the design of beams submitted to simple bending and torsion, the corresponding designs were applied for the support beams, whose results are summarized in Table 12. Concrete with $f_{ck} = 25$ MPa was used in the calculations and the distance from the center of gravity of the reinforcement to the face of the beam (d') was 3.5 cm.

Rev. IBRACON Estrut. Mater., vol. 13, no. 4, e13414, 2020

20/24

Table 12 – Support beam design for vertical loading with and without eccentricity.

| Wall/ Beam (section)	Model	Non-eccentric loading			Eccentric loading		
		Long. Reinf. (flexo-tensile + torsion)	Trans. Reinf. (shear force + torsion)		Long. Reinf. (flexo-tensile + torsion)	Trans. Reinf. (shear force + torsion)	
		As (cm^2)	Strut colapse	As (cm^2)	As (cm^2)	Strut colapse	As (cm^2)
W1/B1 (35x80)	2D	8.07	No	11.67	15.38	No	14.85
	3D	11.24	No	16.14	18.00	Yes	--
	3DW	12.81	No	18.58	19.56	Yes	--
W30/B29 (35x80)	2D	8.05	No	10.92	12.97	No	13.06
	3D	13.13	No	20.87	18.27	No	22.49
	3DW	14.08	No	21.04	19.20	Yes	--
W3/B3 (30x80)	2D	3.60	No	2.32	5.41	No	3.58
	3D	16.40	Yes	--	18.69	Yes	--
	3DW	17.95	Yes	--	20.10	Yes	--
W41/B40 (35x80)	2D	14.52	No	19.10	26.53	Yes	--
	3D	12.58	No	16.93	22.65	Yes	--
	3DW	12.96	No	17.89	22.86	Yes	--

Initial analysis showed non-compliance with the strut stress criterion in beam B3, for the 3D and 3DW models in the two loading situations, and in B1, for the 3DW model for eccentric loading, indicating the need to change the geometry of the section of these beams. Once again, this underscores the need to include wind action, vertical eccentric loads on the beam and three-dimensional modeling, given that both shear force and maximum twisting moment are far less intense with planar modeling, as shown in Figures 13b and 17c. With respect to modeling conditions, the results of beam B3 should serve as a warning to masonry structure designers, who usually do not consider the effects of wall-beam eccentricity, typically using planar models when modeling wall-beam interaction.

Another relevant aspect of these results is the increase in horizontal reinforcement (bending-traction and torsion) in the three-dimensional models, initially due to non-eccentric loading. Differences of 51% were obtained for beam B29 and notably B3, where the amount of reinforcement was obtained with the 2D model multiplied by 2.9 and 3.1 for the 3D and 3DW models, respectively. This considerable increase in reinforcement in B3 underscores the high intensity of the forces obtained with three-dimensional modeling, corroborated by the fracture of struts. By contrast, horizontal reinforcement declined in B40, obtained with the three-dimensional models. Both results may be associated with stress redistribution between the walls, causing a significant rise in forces on B3 and a decline in B40.

Considerable increases were also observed in shear reinforcement. The results of beam B1 indicated differences of 38 and 59% between the 3D and 3DW models, respectively, and the 2D model. In B29, the transverse reinforcement obtained from the 2D model was multiplied by 1.9 when determined using the forces obtained with the 3D and 3DW models. These increases in reinforcement may be due to stress redistribution between the walls, demonstrating the greater influence on shear behavior. Figure 18a shows this behavioral trend, underscoring the highest differences in beam B29.

Considering eccentric beam loading for cases where shear reinforcement can be determined, the results of beam B29 obtained 78.5 and 79.8% increases in transverse reinforcement with the 3D and 3DW models, respectively, in relation to the 2D model. For this same beam, longitudinal reinforcements 47.1 and 50.7% higher were obtained with the three-dimensional models, once again confirming the greater influence of stress redistribution on shear behavior, which can be explained by the high eccentricity values. If non-eccentric loading is considered, the trend remains unchanged, albeit with higher differences, as illustrated in Figures 18a and 18b. Compared to the change in modeling type adopted in analyses, this result indicates that including wall-beam eccentricity had a smaller impact on the increase in reinforcement. Likewise, Figure 19 demonstrates that incorporating eccentricity exerted greater influence on the increase in longitudinal reinforcements, as shown in the results of beams B1 and B40.

Given the brittle nature of the fracture for this type of load, this result is another example of the importance of three-dimensional modeling and considering the eccentricity between the structural wall axes and the support beam in the design of support beams.
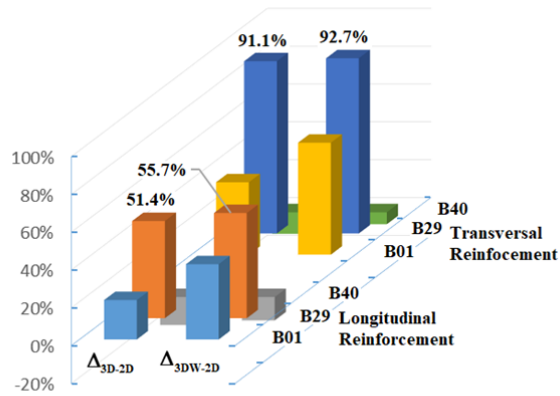
(a)
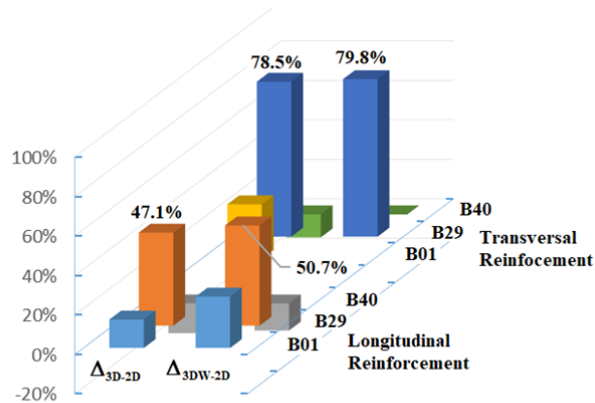
(b)

Figure 18. Differences between design results according to the analysis models: (a) Non-eccentric loading and (b) Eccentric loading.
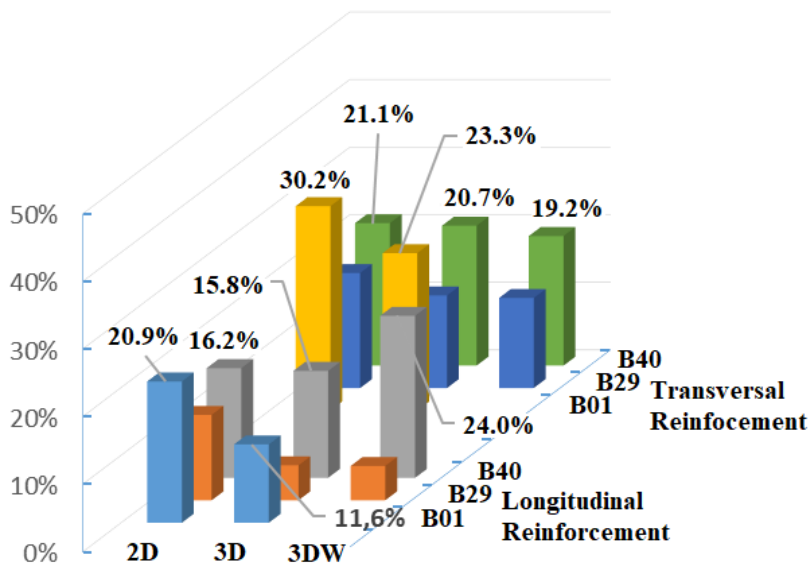

Figure 19. Difference between design results for eccentric and non-eccentric loading.

Rev. IBRACON Estrut. Mater., vol. 13, no. 4, e13414, 2020

22/24

5 CONCLUSIONS

The present study consisted of analyzing stress distribution in the structural walls of masonry buildings over a transition structure of reinforced concrete. Planar and three-dimensional modeling of the wall-beam system was performed, considering a possible eccentricity between the plane of the wall and the longitudinal axis of the beam. The analyses led to the following conclusions:

- A comparison between the planar and three-dimensional models confirmed the importance of interconnecting masonry walls, given that three-dimensional modeling revealed significant redistributions of normal vertical stresses at the bottom of the walls and shear stresses at the horizontal base joints, precluding planar modeling in the structural analysis of the wall-beam system in real situations. Overlapping the effects of planar models to determine the interconnection between wall proved to be inadequate;
- The stress redistribution observed in three-dimensional modeling resulted in significant changes in support beam forces, whose values were more than double those observed for the bending moment and shear force, reversing the direction of axial forces by changing from traction to compression;
- The flow of stresses to inside the wall is strongly influenced by openings in the masonry arranged near the columns of the support structure, and beam continuity, which can affect horizontal shear stress distribution at the bottom of the wall;
- The horizontal coordinate at the bottom of the wall, where horizontal shear stresses annul each other, corresponded to the cross-section of the beam, where axial force was either maximum or minimum;
- Wind action showed that both stresses at the bottom of the wall and forces on the support beams increased in intensity. The magnitude of the increases was influenced by different geometry and loading conditions. Thus, in order to ensure an adequate computational simulation of the wall-beam system, it is recommended that wind action always be taken into account;
- Calculating the torsion caused by eccentricity between the wall and the beam is no easy task and should be performed exclusively by computational modeling. The intensities obtained for the twisting moment indicated substantial increases in relation to those from the condition that does not consider this eccentricity;
- The effects caused by eccentric vertical loading in the studies conducted showed crushed struts in some of the beams analyzed, considering the criteria established in the Brazilian guideline. In addition, in cases where the necessary reinforcement was obtained, a considerable increase was observed in both longitudinal reinforcement, obtained for the combined effects of bending and torsion, and transverse reinforcement, obtained for the combined effects of shear force and twisting moment, demonstrating the need to include it in the design of support beams.

It is important to underscore that our findings correspond to the typology of the building selected for analysis, and should therefore not be generalized for any building. The results associated with the model that considers wind action cannot be extrapolated, for example, to low-rise buildings.

Finally, considering the guidelines of NBR 6118 [14] for the use of minimum shear reinforcement in order to prevent brittle fractures, the effects of wall-beam eccentricity should be carefully evaluated in the analysis of structural masonry buildings. If this analysis cannot be carried out, it is recommended that this eccentricity be eliminated to minimize torsion in the support concrete structure.

REFERENCES

[1] P. C. Barbosa, "Estudo da interação entre paredes de alvenaria estrutural com vigas de concreto armado," M.S. Dissertation, Esc. Eng. São Carlos, Univ. São Paulo, São Carlos, SP, 2000.

[2] M. S. Paes, "Interação entre edifício de alvenaria estrutural e pavimento em concreto armado considerando-se o efeito arco com a atuação de cargas verticais e ações horizontais," M.S. Dissertation, Esc. Eng. São Carlos, Univ. São Paulo, São Carlos, SP, 2008.

[3] B. A. Haseltine and J. F. A. Moore, *Handbook to BS-5628: Structural Use of Masonry. Part1: Unreinforced Masonry*. Windsor, Berkshire: The Brick Development Association, 1981.

[4] J. A. Nascimento Neto., K. A. S. Medeiros, and F. Quim, "Nova modelagem para análise da interação entre painéis de alvenaria e estrutura de suporte," *Rev. Prisma*, no. 52, pp. 1–20, 2014.

[5] K. A. S. Medeiros, "Modelagem computacional para avaliação da interação entre painéis de alvenaria e estrutura de suporte em concreto armado," M.S. Dissertation, Prog. Pós-grad. Eng. Civil, Univ. Fed. Rio Grande do Norte, Natal, RN, 2015.

[6] T. F. T. Silva, "Estudo da interação entre edifícios de alvenaria estrutural e pavimentos em concreto armado," M.S. Dissertation, Esc. Eng. São Carlos, Univ. São Paulo, São Carlos, SP, 2005.

[7] J. G. Rots, "Numerical simulation of cracking in structural masonry," *Heron*, vol. 36, no. 2, pp. 49–63, 1991.

[8] P. B. Lourenço, "Computational strategies for masonry structures," M.S. Dissertation, Delft Univ. Technol., Delft, 1996.

[9] O. G. Holanda Jr., "Influência de recalques em edifícios de alvenaria estrutural," Ph.D. Thesis, Esc. Eng. São Carlos, Univ. São Paulo, São Carlos, SP, 2002.

[10] J. A. Nascimento Neto., "Estudo de painéis com abertura constituídos por alvenaria estrutural de blocos," Ph.D. Thesis, Esc. Eng. São Carlos, Univ. São Paulo, São Carlos, SP, 2003.

[11] E. Testoni, "Análise estrutural de edifícios de paredes de concreto por meio de pórtico tridimensional sobre apoios elásticos," M.S. Dissertation, Esc. Eng. São Carlos, Univ. São Paulo, São Carlos, SP, 2013.

[12] S. Rosenhaupt, "Experimental study of masonry walls on beams," *J. Struct. Div.*, vol. 88, no. ST3, pp. 137–166, 1962.

[13] A. C. S. Lopes, "Aperfeiçoamento de modelagem computacional para análise da interação entre painéis de alvenaria e estrutura de suporte em concreto armado," Undergraduate Dissertation, Depart. Engenharia Civil, Univ. Fed. Rio Grande do Norte, Natal, RN, 2016.

[14] Associação Brasileira de Normas Técnicas, *Projeto de Estruturas de Concreto – Procedimento*, NBR 6118, 2014.

[15] Associação Brasileira de Normas Técnicas, *Alvenaria Estrutural – Blocos de Concreto. Parte 1: Projeto*, NBR 15961-1, 2011.

[16] G. A. Parsekian, A. A. Hamid, and R. G. Drysdale, *Comportamento e Dimensionamento de Alvenaria Estrutural*, 2nd ed. São Carlos: EdUFSCar, 2014.

[17] E. S. Fortes, "Influência do capeamento e caracterização da resistência à compressão de alvenaria estrutural de blocos de concreto," M.S. Dissertation, Prog. Pós-grad. Eng. Estrut. Constr. Civ., Univ. Fed. São Carlos, São Carlos, SP, 2012.

ORIGINAL ARTICLE

Ultrasonic measurement and elastic properties of the PbO-SrO-B₂O₃ glass system

Medidas ultrassônicas e propriedades elásticas do sistema vítreo PbO-SrO-B₂O₃

Bianca Reis Moya[a]
Idalci Cruvinel dos Reis[a]
Victor Ciro Solano Reynoso[b]
Mariana da Silva Barros[a]
Kamila Ruthielle Silva Gomes[a]

[a]Instituto Federal Goiano – IF Goiano, Rio Verde, GO, Brasil
[b]Universidade Estadual Paulista "Júlio de Mesquita Filho" – UNESP, Ilha Solteira, SP, Brasil

Abstract: The PbO-SrO-B₂O₃ glass system with the of molar ratio of R (= PbO/B₂O₃) were prepared by fusion method. The elastic properties have been investigated using longitudinal and transversal ultrasonic wave velocity. Measurements were performed at room temperature and using pulse-echo technique at frequency of 5 MHz. The results indicate that, when increasing R value, the glass network stability decreases. This decrease indicates, of the increase the number of borate structures with non bridging oxygen (NBOs) at the expense of the decrease of borate units with tetrahedral structures. This feature may lead to the more open glass network structures and lower stiffness of the samples studied.

Palavras-chave: vidro, método de fusão, densidade, medidas ultrassônicas.

Resumo: Vidros do sistema PbO-SrO-B₂O₃, em função da razão molar R (=PbO/ B₂O₃), foram preparados usando a técnica de fusão. As propriedades elásticas tem sido investigadas a partir das medições das velocidades longitudinais e transversais das ondas ultrassônicas. As medidas foram realizadas a temperatura ambiente usando a técnica de pulso-eco a 5 MHz. Os resultados indicam que, com o aumento do valor de R, a estabilidade da rede do vidro diminui. A diminuição da estabilidade da rede vítrea indica o aumento do número de estruturas boratos com oxigênios não ligados às expensas da diminuição das unidades boratos com estruturas tetraédricas. Esta característica pode levar à ter no vidro estruturas mais abertas e a ter menor rigidez das amostras estudadas.

Keywords: glass, fusion method, density, ultrasonic measurements.

1 INTRODUCTION

Oxide glasses containing boron, lead and strontium have a history of glass formation, showing good properties such as high refractive index, density and infrared transmission. Lead-oxide (PbO) containing glasses provide low melting glasses [1].

There are wide applications of different types of glass, with lead oxide and silica content, among many others, being the quality control of the final properties of the product of paramount importance, since high quality controlled glass is applied in the fields of nanotechnology and optics such as lasers, sensors, semiconductors, etc [2], [3].

Borate glasses have been widely studied for their interesting properties, have high optical transparency and thermal stability. Luminescent borate glasses gain importance in application as a laser amplifier due to their high transparency

over a wide range of the electromagnetic spectrum in the visible region, which is extremely important for glass application in many optical devices as most of them act by light transmission.

The interest in the B_2O_3-PbO-SrO glass system was due to the fact that boron oxide and strontium oxide are network forming in the glass structure; in small additions of lead oxide, it acts as a network modifier and in larger additions PbO plays a network forming role, being a double behavior component in glass.

The propagation of the ultrasonic wave in solids, such as glass, provides valuable information on the mechanical properties and overall solid state molecular motion in the material [4]. Sonic waves are classified as ultrasound waves at frequencies exceeding 20 kHz. The measurement technique is based on the analysis of ultrasound wave propagation at 5 MHz and its relationship with the elastic properties of the material [5]-[6].

The objective of this work is to correlate the microstructure with the elastic properties of the investigated glass samples. For this, the samples were characterized by measurements of longitudinal and transverse ultrasonic wave propagation velocities, density and infrared absorption spectroscopy (FTIR).

2 CHARACTERIZATION TECHNIQUES

2.1 Sample preparation

For the preparation of glass based on boron, lead and strontium oxides, the melt fusion technique was used. The amounts of each powdered reagent have been carefully mixed to give the glass homogeneity; The material was then placed in a porcelain crucible to make the melting process in an electric oven up to 1000 ° C for one hour. After melting, the viscous mass was poured into a preheated steel mold at a temperature of 60 ° C for the molding process. After being placed in another oven for annealing at a temperature of 300 ° C for three hours, this procedure serves to remove the internal stresses of the glass. All samples followed the same procedure at the same temperature to have a similar history and to make a useful comparison between the different structures. After cooling, the samples were cut in the form of slabs, sanded, polished and also crushed to be subsequently subjected to proper characterization.

2.2 Density and molar volume

The density of the samples was estimated by the Archimedes principle method, using a scale whit precision of 0,0001g and a pycnometer, where the pieces (splinters of glass) of the samples were immersed in acetone solution, applying the expression 1.0:

$$\rho = \rho_H \left(\frac{m_a}{m_d} \right)$$

(Eq. 1.0)

Where, ρ is the density, ρ_H is the density of the water, m_a and m_d are the mass of the sample in the air and the mass of the submerged sample, respectively. The molar volume of the glass can preferably be used to describe the structure of the network and the disposition of the constructive units, since it deals directly with the spatial structure of the Oxygen network [7].

The measurement was made three times to obtain an average, this being a value with greater precision for calculating the density. The molar volume was calculated from the expression. 1.1:

$$V_m = \frac{\sum x_i M_i}{\rho}$$

(Eq. 1.1)

In which x_i is the molar fraction and M_i, the molar mass of the glass component. Table 1 illustrates the glasses compositions and values obtained for the different properties.

2.3 Ultrasonic measurements

The elastic modules of glass are influenced by many physical parameters, which in turn can be studied by measuring ultrasonic velocities. The variation of the ultrasonic velocity in the glass samples indicates the various changes in the structural configuration between the network former and the modifiers, directly and indirectly affecting other properties [8].

Table 1 Chemical composition (% molar), proportion of the content of PbO/ B_2O_3 (R), thickness, density (ρ), molar volume (Vm) and glass sample packaging density (V_T).

Glasses	B_2O_3 (%)	SrO (%)	PbO (%)	R (=PbO/ B_2O_3)	Thickness (mm)	ρ (g/ cm^3)	Vm (cm^3)	V_T (cm^3)
BPS-1	60	25	15	0,25	0,6	4,26	23,75	61,03
BPS-2	60	20	20	0,33	0,9	4,35	24,63	60,34
BPS-3	60	15	25	0,42	0,96	4,43	25,53	59,64
BPS-4	60	10	30	0,50	1,18	4,52	26,35	59,20
BPS-5	60	5	35	0,58	0,94	4,68	26,72	59,75
BPS-6	60	0	40	0,67	0,64	4,82	27,19	60,08

Source: the autors (2018).

For ultrasonic measurements, samples were used in a rectangular slabs and thickness varying from 0.6 to 1.18 cm (Table 1). The measurement was performed using an equipment that uses the pulse-echo technique for ultrasonic speed measurements, this measures the sound velocity in the samples with a given thickness with the pulse-echo system working at a frequency of 5 MHz, with the Transverse (Vs) and longitudinal (VL) velocities were calculated using the Equation 1.2:

$$V_s = \frac{2x}{\Delta t} \quad V_L = \frac{2x}{\Delta t}$$

(Eq. 1.2)

Having x as the sample thickness in (mm) and the time interval given as Δt. The other elastic properties of the studied glass were measured using the following relationships:

Longitudinal Module: $L = \rho V_L^2$,

Shear Module: $G = \rho V_s^2$,

Bulk Module: $K = L - \frac{4}{3}G$,

Young's Module: $E = (1 + \sigma)2G$,

Poisson Coefficient: $\sigma = \frac{(L - 2G)}{2(L - G)}$, e

Debye Temperature: $\theta_d = \left(\frac{h}{k}\right) \cdot \left(\frac{9N_A}{4\pi V_m}\right)^{\frac{1}{3}} V_{ms}$

Where L, G, K and E are the longitudinal, shear, bulk and Young modulus modules, respectively. The ρ is the density of the samples, σ is the Poisson coefficient, θ_d is the temperature of Debye, V_{ms} is the average speed of sound, V_m is the molar volume, h is the Plank constant, k is the Boltzmann constant and N_A is the Avogadro number.

The average sound velocity (V_{ms}) is defined by the relationship 1.3:

$$V_{ms} = [\frac{1}{3}\left(\frac{2}{Vs^3}\left(\frac{1}{V_L^3}\right)\right)]^3$$

(Eq. 1.3)

Other properties can be calculated as the acoustic impedance (Z) and the coefficient of thermal expansion (A) [6]. Acoustic impedance is: $Z = \rho V_L$.

2.4 FTIR infrared spectroscopy

For infrared measurements, a Fourier transform Nicolet Nexus 670 FTIR spectrometer was used, which measures from the near-infrared region of 4000 cm^{-1} to 400 cm^{-1} in the mid-infrared. The powdered samples were mixed with potassium bromide (KBr) and prepared as a pellet; these were prepared using the ratio of 1 mg of powder sample and 150 mg of KBr, this mixture was subjected to a loading of 3 t / cm^2 resulting in a thin and compact tablet shape.

This is a structural characterization technique that qualitatively and quantitatively determines different molecular groups.

Rev. IBRACON Estrut. Mater., vol. 13, no. 4, e13415, 2020

3/7

3 RESULTS AND DISCUSSION

3.1 Density and volume molar

As the substitution of strontium oxide by lead oxide in the samples, there is an increase in the density provided by the high molecular weight of lead oxide, when compared to the other components of the glass system studied. The increase in density is also explained considering the formation of BO_4 units in the network of glass by the introduction of lead oxide in the sample.

The molar volume of the samples, Figure 1, showed unexpected behavior, since as the density increases, the molar volume also increases. The expansion in the structure of the vitreous matrix can be explained by the formation of non-bridging oxygen in the material during the substitution of the glass components [9].
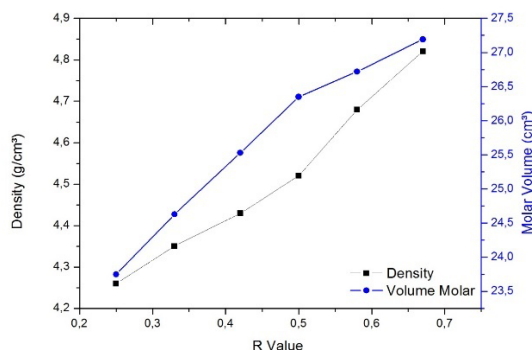

Figure 1. Density variation in R function of vitreous system and molar volume. Source: the autors (2018).

3.2 Ultrasonic study

Pulse-echo thickness measurement has a high sensitivity in detecting small internal discontinuities, so measurements were made at room temperature using a 5 MHz frequency ultrasonic meter.

Table 2 shows the variation of longitudinal ultrasonic velocities in the prepared samples. It is observed that velocities decrease as the value of the ratio R is increased. The longitudinal modulus (L) of the samples are calculated by the expression 1.4:

$$V_L{}^2 = \sqrt{\frac{k}{\rho}}$$

(Eq. 1.4)

Having k as volumetric modulus of elasticity, V_L as longitudinal velocity of sound and ρ as glass sample density.

When the substitution of components in the glass matrix occurs, new bonds between the ions are formed, causing the network expansion, which increases the molar volume, leading to a decrease in the packaging volume. Non-bridging oxygen formation decreases the peak pulse resistance, consequently contributing to the decrease in ultrasonic velocity [9]. Table 2 shows the results of ultrasonic velocity measurements and the various elastic modules.

Table 2 Longitudinal Velocity (V_L), Transverse velocity (V_s), Average sound velocity (V_{ms}), Longitudinal Module (L), Transversal Modulus (G), Bulk Module (K) e Young's Module (E).

Glasses	V_L (m/s)	V_S (m/s)	V_{ms} (m/s)	L (10^{10} N/m²)	G (10^{10} N/m²)	K (GPa)	E
BPS-1	4918,67	2951,20	3264,75	103,06	37,10	53,59	75,42
BPS-2	4626,00	2775,60	3070,49	93,09	33,51	48,41	68,24
BPS-3	4541,33	2724,80	3014,29	91,36	32,89	47,51	66,99
BPS-4	4361,00	2616,60	2894,60	85,96	30,95	44,69	63,12
BPS-5	4209,00	2525,40	2793,71	82,91	29,85	43,11	60,92
BPS-6	4104,00	2462,40	2724,01	81,18	29,23	42,21	59,68

Source: the autors (2018).

Rev. IBRACON Estrut. Mater., vol. 13, no. 4, e13415, 2020

4/7

Elastic modules allow a macroscopic view of material rigidity from inter atomic bonding energies and material connectivity. Figure 2 shows a decreasing trend in elastic modulus which may be associated with the number of unit bonds per glass unit formula and the average strength of these bonds, which are related to the values of the forces between cations and anions. Thus, both decreasing average bond strength and number of bonds explain the decrease values in elastic modulus [10].
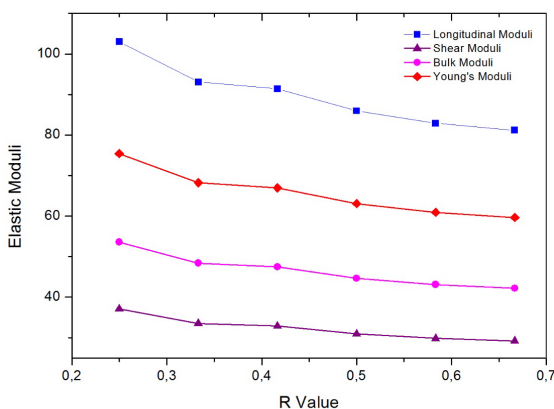

Figure 2. Variation of elastic modules for the BPS glass system. Source: the autors (2018).

Debye temperature is the value at which all vibration modes in a solid are excited, which is directly proportional to the average speed of sound [11]. The decrease is observed in the average speed of sound and the temperature Debye values, Table 3; that can be attributed to the formation of non-bridging oxygen due to the substitution of the components in the glass matrix, leading to a decrease in the stiffness of the glass [4], [12].

Table 3 Debye Temperature (θ_d), Poisson Coefficient (σ), Acoustic Impedance (Z) and Coefficient of Thermal Expansion (A).

Glasses	θ_d	σ	Z $(10^{-7}$ kg / m^2.s$)$	A
BPS-1	411,7409	0,21879	2,09	114099,81
BPS-2	382,5736	0,21878	2,01	107309,87
BPS-3	371,1051	0,21874	2,01	105345,53
BPS-4	352,6334	0,21869	1,97	101161,87
BPS-5	338,7643	0,21872	1,96	97635,47
BPS-6	328,3990	0,21867	1,98	95199,47

Source: the autors (2018).

The increasing behavior of acoustic impedance indicates that we have increased resistance to ultrasonic wave propagation in the sample, which can be verified by decreasing velocity as glass increases its density [13].

3.3 FTIR infrared spectroscopy

The properties that certain glass provide us can be analyzed by the structural study conducted by spectroscopy techniques. Infrared absorption spectroscopy allows us to verify if the material has presented significant structural changes, so it is important to know what are the peaks of the characteristic absorption bands of each structure. Table 4 shows the positions of the spectra absorption peaks obtained for each sample. It is possible to verify the displacement of some bands by the insertion of the network modifier in the matrix, such as lead oxide, and by the formation of tetrahedral units of BO$_4$; It is possible to verify the displacement of some bands by the insertion of the network modifier in the matrix, such as lead oxide and by formation of tetrahedral units of BO$_4$; therefore the increase of non-bridging oxygen to bridging oxygen's in the 800 to 1200 cm^{-1} range [13].

Table 4 position of the peaks for the FTIR spectra of the vitreous systems.

| Glasses | Vitreous system B_2O_3 - SrO – PbO | | | | |
	Peaks in the middle infrared (cm^{-1})				
BPS-1	2350	1640	1360	1030	682
BPS-2	2370	1640	1370	993	682
BPS-3	2360	1640	1420	1050	682
BPS-4	2360	1640	1430	1100	661
BPS-5	2350	1640	1390	1050	661
BPS-6	2350	1640	1390	1000	682

Source: the autors (2018).

Figure 3 shows the infrared absorption spectra for all samples of the glass system B_2O_3 – PbO – SrO, most peaks are in the same position.
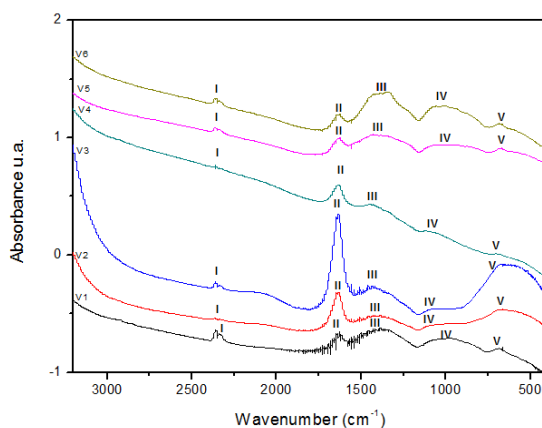

Figure 3. Samples absorption spectra in infrared. Source: the autors (2018).

For qualitative analysis, the spectrum was divided into five regions: (I) 2300-2350 cm^{-1}; (II) 1500-1700 cm^{-1}; (III) 1200-1550 cm^{-1}; (IV) 800-1200 cm^{-1} and (V) 700-1000 cm^{-1} respectively.

The spectrum in region (I) has bands close to 2300-2350 cm^{-1}, the vibrations of different C-O bonds or ambient CO2 concentrations in the Infrared [14] are attributed, these are not part of the glass structures. In region (II), bands between 1500-1700 cm^{-1} are attributed to molecular vibrations of hydroxyl (water) [15]. In region (III), the bands found between 1200-1500 cm^{-1} are attributed to molecular vibrations of borate group units with non-bridging oxygen [15]. In region (IV), bands between 800-1200 cm^{-1} are assigned to borate groups with BO4 tetra borate structures, extending in the range 1200-1600 cm^{-1} are related to BO3 triborate groups [16]–[17]. In the last region, region (V), bands close to 700 cm^{-1} are assigned to borate group bonds [15]-[18]. From 700 to 400 cm^{-1} the bands do not appear explicitly, but there may be bonds due to the Sr-O and Pb-O of the heavy atoms in the glass.

3 CONCLUSIONS

PbO-SrO-B_2O_3 glass samples are potential candidates for transparent ultraviolet and gamma ray protection materials [1]. The results of the ultrasonic velocity measurements of the PbO-SrO-B_2O_3 glass system indicate non-bridging oxygen formation with increasing PbO to B_2O_3 ratio. In addition, the glass structure becomes less rigid at higher R ratio values. On the contrary, the gamma ray protection properties improve with increasing PbO / B_2O_3 ratio of the glass samples.

FTIR spectral studies indicated the conversion of BO3 to BO4 structural units, caused by the addition of PbO in the matrix. These changes contributed significantly to obtaining denser glasses, a fact confirmed by the ultrasonic study. For these reasons, the characterization of the samples through ultrasonic and spectroscopic studies was presented as a powerful tool to explore the structural characterization of the glass type.

THANKS

We thank the whole team of the Department of Physics and Chemistry of UNESP-Ilha Solteira-SP for the use of their laboratories for measurements.

REFERENCES

[1] R. S. Kaundal, S. Kaur, N. Singh, and K. J. Singh, "Investigation of structural properties of lead strontium borate glasses for gamma-ray shielding applications," *J. Phys. Chem. Solids*, vol. 71, no. 9, pp. 1191–1195, Sep 2010, http://dx.doi.org/10.1016/j.jpcs.2010.04.016.

[2] W. D. Callister Jr., *Materials Science and Engineering an Introduction*, 5th ed. New York: John Wiley & Sons, 2000, pp. 18-31.

[3] F. Torres, K. Narita, Y. Benino, T. Fujiwara, and T. Komatsu, "Elastic and mechanical properties of transparente nanocrystallized KNbGeO5 glass," *J. Appl. Phys. Jpn.*, vol. 94, no. 8, 2003.

[4] S. V. Pakade and S. P. Yawale, "Ultrasonic velocity and elastic constant measurement in some borate glasses," *J. Pure Appl. Ultrason.*, vol. 18, pp. 74, 1996.

[5] J. C. Gonçalez, A. T. Valle, and A. F. Costa, "Estimativas das constantes elásticas da madeira por meio de ondas ultrassonoras (ultrassom)," *Cerne*, vol. 7, no. 2, pp. 81–92, 2001.

[6] V. Rajendran and H. A. El-Batal, "Behaviour of acoustical parameters of mixed alkali silicate glasses," *Indian J. Pure Appl. Phy.*, vol. 33, pp. 29, 1995.

[7] K. Sathish and S. Thirumaran, "Spectroscopic and ultrasonic investigations on structural characterization of borate glass specimen doped with transition metal ions," *Spectrochim. Acta A Mol. Biomol. Spectrosc.*, vol. 147, pp. 163–172, 2015, http://dx.doi.org/10.1016/j.saa.2015.02.031.

[8] S. P. Yawale, S. V. Pakade, and C. S. Adgaonkar, "Ultrasonic velocity and absorption measurement in xZno–(90–x)B2O3–10Bi2O3 glasses," *Acoustica*, vol. 76, pp. 103, 1992.

[9] Y. B. Saddeek and M. S. Gaafar, "Physical and structural properties of some bismuth borate glasses," *Mater. Chem. Phys.*, vol. 115, no. 1, pp. 280–286, May 2009, http://dx.doi.org/10.1016/j.matchemphys.2008.12.004.

[10] W. H. Wang, "The elastic properties, elastic models and elastic perspectives of metallic glasses," *Prog. Mater. Sci.*, vol. 57, no. 3, pp. 487–656, Apr 2012, http://dx.doi.org/10.1016/j.pmatsci.2011.07.001.

[11] M. A. Sidkey, A. Abd El-Moneim, and L. Abd El-Latif, "Ultrasonic studies on ternary Te2O2–V2O5–Sn2O3 glasses," *Mater. Chem. Phys.*, vol. 61, no. 2, pp. 103–109, 1999, http://dx.doi.org/10.1016/S0254-0584(99)00067-X.

[12] C. Bootjomchai, R. Laopaiboon, S. Pencharee, and J. Laopaiboon, "Elastic moduli of borosilicate glasses doped with heavy metal oxides," *J. Non-Cryst. Solids*, vol. 388, pp. 37–45, Mar 2014, http://dx.doi.org/10.1016/j.jnoncrysol.2014.01.039.

[13] R. P. R. D. Nardi "Vidros e vitrocerâmicas luminescentes de fluorofosfatos de chumbo e tungstênio," M.S. thesis, Prog. Pós-grad. Cienc. Eng. Mater., Univ. Fed. Alfenas, Poços de Caldas, MG, 2016.

[14] H. Yin et al., "Fabrication and characterization of strontium-doped borate-based bioactive glass scaffolds for bone tissue engineering," *J. Alloys Compd.*, vol. 743, pp. 564–569, Apr 2018, http://dx.doi.org/10.1016/j.jallcom.2018.01.099.

[15] S. Baccaro, Monika, G. Sharma, K. S. Thind, D. Singh, and A. Cecillia, "Analysis of structural modifications in γ-irradiated PbO–B2O3–SiO2 glasses by FTIR spectroscopy," *Nucl. Instrum. Methods Phys. Res. B*, vol. 260, no. 2, pp. 613–618, Jul 2007, http://dx.doi.org/10.1016/j.nimb.2007.04.214.

[16] N. A. Ghoneim, H. A. ElBatal, A. M. Abdelghany, and I. S. Ali, "Shielding behavior of V2O5 doped lead borate glasses towards gamma irradiation," *J. Alloys Compd.*, vol. 509, no. 24, pp. 6913–6919, Jun 2011, http://dx.doi.org/10.1016/j.jallcom.2011.03.180.

[17] N. Srisittipokakun, J. Kaewkhao, W. Chewpraditkul, and P. Limsuwan, "Comparative study of optical and spectroscopic properties of lead and bismuth on borosilicate glasses," *Procedia Eng.*, vol. 32, pp. 699–705, 2012, http://dx.doi.org/10.1016/j.proeng.2012.01.1329.

[18] M. S. Gaafar, N. S. A. El-Aal, O. W. Gerges, and G. El-Amir, "Elastic properties and structural studies on some zinc-borate glasses derived from ultrasonic, FT-IR and X-ray techniques," *J. Alloys Compd.*, vol. 475, no. 1-2, pp. 535–542, May 2009, http://dx.doi.org/10.1016/j.jallcom.2008.07.114.

Author contributions: Bianca Reis Moya: PhD student responsible for the project, has participated in all the planning, execution and production of the manuscript. Idalci Cruvinel dos Reis: Profº. Drº. - Project advisor and supervisor. Victor Ciro Solano Reynoso: Profº. Drº. - Project co-supervisor and supervisor. Mariana da Silva Barros: Academic of the undergraduate course in Civil Engineering, where she accompanied the laboratory activities. Kamila Ruthielle Silva Gomes: Academic of the undergraduate course in Civil Engineering, where she accompanied the laboratory activities. Note: All the authors used the scientific construction of the manuscript, considering the stages of reading and reviewing.

Editors: Jose Tadeu Balbo, José Luiz Antunes de Oliveira e Sousa, Guilherme Aris Parsekian.